## *Aerodynamic Effects of the Salient Flow Features in Grand Prix Car Wakes*

NEWBON, JOSHUA,JAMES

# Aerodynamic Effects of the Salient Flow Features in Grand Prix Car Wakes

by
Joshua James Newbon

Supervisors

Dr. D.B. Sims-Williams,
Prof R.G. Dominy


**School of Engineering**
**and Computing Sciences**

Submitted in conformity with the requirements
for the degree of Doctor of Philosophy

2016

# Aerodynamic Effects of the Salient Flow Features in Grand Prix Car Wakes


**Abstract**

Grand Prix cars are the fastest circuit racing cars in production, a large part of this is due to the high downforce generated by the car's aerodynamic surfaces, in excess of the car's own weight above 150kph. It is well known that a race-car operating in the wake of an upstream vehicle experiences a reduction of aerodynamic drag, and a corresponding increase of ultimate straight line speed. There is also a loss of aerodynamic downforce, predominately from surfaces acting on the front axle. The effect of the reduced downforce is an increase of lap-time and degraded handling characteristics, thereby reducing tyre life and the ability to follow the lead car or affect an overtake.

The wake of a generic Formula 1 car is shown to be characterized by a counter-rotating vortex pair, with centreline up-wash and a region of total pressure deficit, which is predominately a dynamic pressure deficit, with $C_{P_O} < 0$. The streamwise vorticity is dominated by the tip vortex pair emanating from the rear wing, which merges with other vortices, forming a coherent structure by just half a car length behind the rear of the car. The vortices have an influence on the location and strength of the total pressure deficit, sweeping the loss to the centreline, and upwards to surround the vortex cores, forming a 'mushroom' shaped wake.

The effect of an upstream vehicle wake has been measured in the wind tunnel and computationally, with downforce and drag losses of up to 67% and 29% respectively. The use of a short axial length bluff-bodied wake generator allows for a longer axial separation to be achieved with a complete downstream vehicle, in a conventional length wind tunnel working section, without further compromising the downstream model scale.

The sensitivity of the downstream car to the various salient flow features in the upstream wake have been investigated using the method of imposing the wake on the inlet of a CFD simulation. Imposing the wake has meant that the wake can be altered without the need to modify the upstream vehicle surfaces. The key wake feature has been shown to be the axial velocity deficit, which accounts for up to 90% of the downforce loss experienced by the following vehicle. While secondary flows in the wake do result in downforce loss for the following vehicle, they are also beneficial in diverting the dynamic pressure deficit over the following vehicle, thereby introducing higher energy flow onto the following vehicle.

# Contents

# List of Figures

# List of Tables

# Nomenclature

## Roman Symbols

| | |
|---|---|
| $A$ | Frontal area – $[m^2]$ |
| $a$ | Lift slope – $[1/^\circ]$ |
| $b$ | Wing span – $[m]$ |
| $C_D$ | Aerodynamic drag coefficient – [1] |
| $C_L$ | Aerodynamic lift coefficient – [1] |
| $C_{LF}$ | Aerodynamic lift coefficient acting at front axle – [1] |
| $C_{LR}$ | Aerodynamic lift coefficient acting at rear axle – [1] |
| $C_P$ | Static pressure coefficient – [1] |
| $C_{P_O}$ | Total pressure coefficient – [1] |
| $[C]$ | 6-Component balance $6 \times 6$ calibration matrix – $[N/V]$ or $[Nm/V]$ |
| $c$ | Wing chord – $[m]$ |
| $D$ | Aerodynamic drag force – $[N]$ |
| $d$ | Diameter – $[m]$ |
| $F$ | Force – $[N]$ |
| $\{F\}$ | 6-Component balance force/moment $6 \times 1$ column vector – $[N]$ or $[Nm]$ |
| $H_C$ | Car height dimension – $[m]$ |
| $h$ | Car ground clearance – $[m]$ |
| $h_{min}$ | Nominal car ground clearance – $[m]$ |
| $I$ | Second moment of area – $[mm^4]$ |
| $L$ | Aerodynamic lift force – $[N]$ |
| $L_C$ | Car length dimension – $[m]$ |
| $\dot{m}$ | Mass flow rate – $[kg/s]$ |
| $P$ | Static pressure – $[Pa]$ |
| $P_o$ | Total pressure – $[Pa]$ |
| $q$ | Dynamic pressure – $[Pa]$ |
| $R_o$ | Vortex core radius – $[m]$ |
| $r$ | Radius – $[m]$ |

| | |
|---|---|
| $[S]$ | 6-Component balances $6 \times 6$ sensitivity matrix – $[V/N]$ or $[V/Nm]$ |
| $TI$ | Turbulence intensity – [1] |
| $t$ | Time – $[s]$ |
| $u$ | Velocity – $[m/s]$ |
| $U_\infty$ | Freestream velocity – $[m/s]$ |
| $u_X, u_Y, u_Z$ | Component velocities – $[m/s]$ |
| $u_{Y,Z}$ | Secondary flows $= \sqrt{{u_Y}^2 + {u_Z}^2}$ – $[m/s]$ |
| $u_\Theta$ | Tangential velocity – $[m/s]$ |
| $\{V\}$ | 6-Component balance voltage $6 \times 1$ column vector – $[V]$ |
| $W_C$ | Car width dimension – $[m]$ |

## Subscripts

| | |
|---|---|
| FA | Front axle |
| FW | Front wing |
| Min | Minimum quantity |
| Max | Maximum quantity |
| RA | Rear axle |
| RW | Rear wing |
| Total | Total quantity |
| Wheels | Related to car wheels |
| WB | Wheelbase |
| X– | Related to front wheels (Cartesian aligned wind tunnel reference) |
| X+ | Related to rear wheels (Cartesian aligned wind tunnel reference) |
| Y– | Related to driver left wheels (Cartesian aligned wind tunnel reference) |
| Y+ | Related to driver right wheels (Cartesian aligned wind tunnel reference) |
| $\infty$ | Freestream |

## Greek Symbols

| | |
|---|---|
| $\alpha$ | Wing Incidence – $[1^\circ]$ |
| $\Gamma$ | Circulation – $[m^2/s]$ |
| $\Gamma_o$ | Total vortex circulation – $[m^2/s]$ |
| $\Delta$ | Change / delta – [1] |
| $\theta$ | Car pitch / rake angle – $[1^\circ]$ |
| $\lambda$ | Wing aspect ratio – [1] |
| $\nu$ | Kinematic viscosity – $[m^2/s]$ |

| | |
|---|---|
| $\rho$ | Density – $[kg/m^3]$ |
| $\Omega$ | Vorticity – $[1/s]$ |

## Acronyms

| | |
|---|---|
| BBWG | Bluff bodied wake generator |
| BL | Baseline |
| COP | Centre of pressure |
| COG | Centre of gravity |
| FST | Freestream turbulence |
| FWEP | Front wing end-plate |
| IW | Imposed wake case |
| PIV | Particle imaging velocimetry |
| RWDF | Rear wing downforce |
| TGS | Turbulence generation system |
| TVF | Two vehicle following case |
| WIG | Wing in ground-effect |

# Key Definitions

Throughout this thesis velocity, forces and moments are referred to using Cartesian aligned axes, shown below.

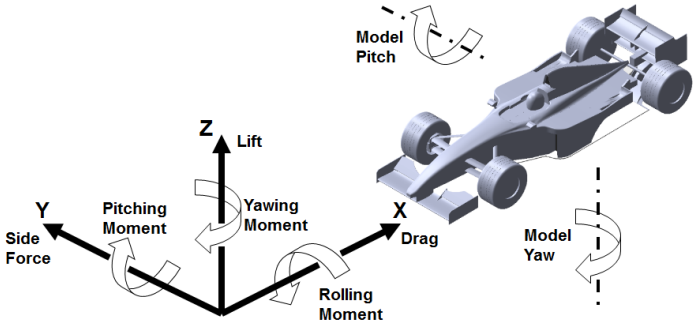


Another key definition used throughout this thesis is the car **reference plane**. The underbody of a modern Formula 1 car is split over 2 parallel planes, the reference plane is the lowest face on the sprung component of the vehicle as defined by the FIA regulations and may be $< 500mm$ wide, extending from $330mm$ behind the front axle line to the rear of the car. The rest of the underbody is on the **step plane** which is mandated to be $50mm$ above the reference plane at full scale. The only geometry which is allowed below the reference plane is the FIA mandated wooden skid block which has a thickness of $10mm$ at full scale. The skid block is used to control ride-height as excessive wear can be grounds for disqualification.

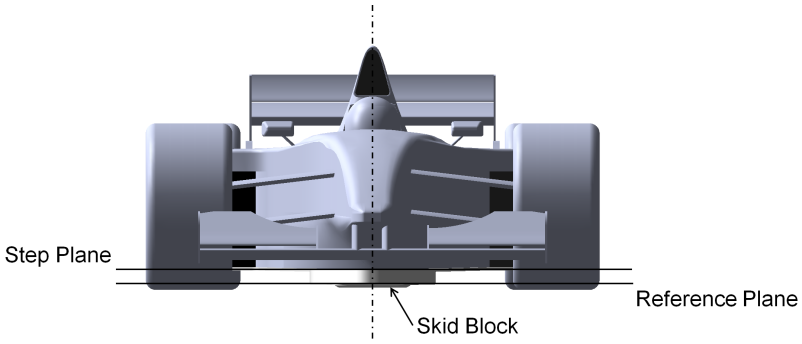

# Declaration

The work in this thesis is based on research carried out at the School of Engineering and Computing Sciences, Durham University, UK. No part of this thesis has been submitted elsewhere for any other degree or qualification and it all my own work unless otherwise referenced in the text.

# Acknowledgements

I would like to thank my supervisors Dr David Sims-Williams and Professor Robert Dominy for their support and guidance through the duration of this research.

I would also like to thank the members of staff in the School of Engineering who provided technical support towards the progress of this PhD. In particular Mr Gary Parker in the thermofluid lab, Mr Colin Wintrip and the rest of the staff in the mechanical workshop, Mr Ian Hutchinson and Mr Neil Clarey in the electronics workshop and Mr Stephen Richardson in the civil engineering lab.

I am also grateful to Jaguar Land Rover and the EXA corporation for the use and continued renewal of the PowerFLOW software licence, and the assistance of Dr Joaquin Gargoloff from the EXA corporation in defining some of the less straightforward CFD simulations.

This research would not have been possible without funding from the Engineering and Physical Sciences Research Council (EPSRC).

# Chapter 1

# Introduction

## 1.1 Project Motivation

> *"...Catching is one thing, passing is quite another..."*
> Murray Walker, motorsports commentator.

It is well known in motorsports that when one car follows another the trailing vehicle suffers from decreased grip associated with a loss of peak downforce, a key variable in lap time performance. The loss of downforce is greater at the front axle [1] resulting in understeer which increases tyre wear, making it more difficult to follow the leading vehicle. Regulation changes in 2009 [2, 3] were made in order to reduce the negative effect of following in the wake of a leading vehicle while also reducing overall downforce. These changes have not necessarily had the desired effect and the rear wing drag reduction system (DRS), whereby the slot gap the rear wing of the trailing vehicle opens to 50mm to reduce drag in prescribed zones, was introduced in 2011 to increase overtaking frequency [4].

It has been postulated that since most of the performance loss occurs on the front axle that the front mounted wing in ground effect loses the most downforce, and a number of studies have investigated the effect of wake flows on single element wings in ground effect [5, 6, 7]. To this point very little research has been published on the effect of wake flows on a full Formula 1 car [1, 8] and that which has found that large vehicle separations are not possible without compromising vehicle Reynolds number. Part of the motivation of this project is to fill the gap in research on the effect of an upstream vehicle on a Formula 1 car.

The wake of a Formula 1 car is dominated by a counter-rotating vortex pair emanating from the rear wing tips, with a strong centreline upwash which is enhanced by the rear diffuser [9, 4]. The location

and strength of these vortices is largely determined by the regulations regarding the size of the rear wing. The primary motivation for this study is to guide future regulations by determining the processes by which a Formula 1 car loses aerodynamic downforce and removing or reducing the unwanted features from the wake.

## 1.2 Literature Review

The following is a review of the existing literature. This review is split into four sections detailing the processes by which open-wheeled race cars generate downforce, the composition of wakes along with how they behave and decay, recreating a wake using a short body and the impact of wakes on a downstream car.

### 1.2.1 Race Car Aerodynamics

Much of a Formula 1, or any winged race-car's lap-time advantage is the result of the cornering performance of the car, where lateral acceleration in excess of 4.0g is possible. As Katz [10] and Zhang, Toet & Zerihan [11] among others summarise, by increasing the normal load on the tyres the side force generated for a given slip angle can be increased. In other words the maximum lateral force is equal to the frictional coefficient of the tyre multiplied by the vertical force. The effect of various vehicle parameters on lap-time are shown in table 1.1; of these variables the key performance differentiators between teams are downforce and drag; as a minimum car weight is defined in the rules, and identical tyres are supplied to all of the teams.

**Table 1.1:** Key F1 car parameter effects on lap time and top speed around a typical circuit.

| Reference | Agathangelou & Gascoyne [12] | | Toet [13] | Nakagawa et al [14] |
|---|---|---|---|---|
| | $\Delta$ Lap-time (s) | $\Delta$ Top Speed ($kph$) | $\Delta$ Lap-time (s) | $\Delta$ Lap-time (s) |
| Downforce +10% | -0.71 | 0.0 | -0.90 | - |
| Drag -10% | -0.68 | +8.8 | - | - |
| Power +10% | -1.23 | +9.3 | -1.4 | -1.20 |
| Tyre Grip +10% | -3.09 | +0.1 | -3.0 | -1.72 |
| Weight +10% | +2.03 | -1.3 | +1.7 | +1.93 |

The primary focus for the Formula 1 aerodynamicist as a means of reducing lap-time is the production of downforce (or negative lift). Downforce greater than three times the car weight is possible [11], or -3.5 to -4.5 on $C_L$, based on a full scale reference area (frontal) of $\sim 1.5m^2$, depending on the car configuration and regulations enforced, figure 1.1. Due to the open-cockpit, open-wheel geometry of Formula 1 cars aerodynamic the drag of the cars is very high, varying between $0.8 \leq C_D \leq 1.2$ over the past decade [15, 16]. Aerodynamic characteristics of the cars are tailored to specific circuits throughout a season, a high speed circuit, such as Monza, will require a very different aerodynamic package to a low speed circuit, like Monte Carlo. The regulations of the time also impact the aerodynamic configuration, e.g. the championship winning car in 2004 had an ${}^{L}/_{D} \approx -2.6$ (where ${}^{L}/_{D}$ is the lift to drag ratio) whereas by 2014 overall efficiency became more important when a limit of 100kg was placed on race fuel, and ${}^{L}/_{D}$ increased to over -4.5 [17].

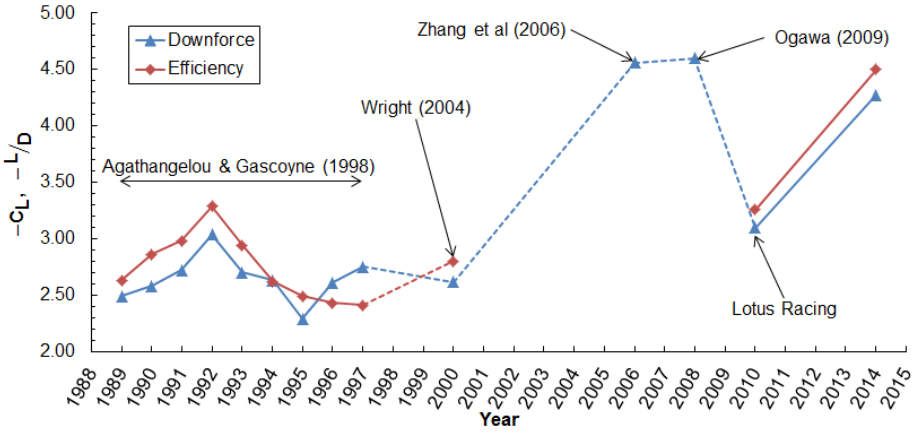


**Figure 1.1:** Average Formula 1 downforce and lift to drag ratio over the past quarter of a century, from Agathangelou & Gascoyne [12], Wright [16], Zhang, Toet & Zerihan [11], Ogawa et al [18] and Force India vs Lotus [19].

There is little published research from Formula 1 teams, and that which exists is either technologically outdated [20] or tends toward a general overview of techniques and equipment [21, 3, 22], rather than specifics of downforce production or wake flows [18, 14]. Published research related to Formula 1 aerodynamics tends to come from academic institutions, using generic geometries and concentrating on the sub-systems, figure 1.2, of a Formula 1 car rather than the whole car. This section of the literature review summarizes the current research for the different sub-systems of a Formula 1 car, from wings to wheels.

#### 1.2.1.1 Summary of Key Aerodynamic Surfaces

**Front Wing (Red):** The front wing is arguably the most important aerodynamic device on a Formula 1 car. As the only component of the car operating in undisturbed airflow, the front wing is not only responsible for generating downforce, it generates between $25\%$ and $30\%$ of the total car downforce, but also for the quality of airflow to the rest of the car. The front wing wake will reduce the performance of downstream components like the underbody so must be carefully controlled, too much downforce and the wake up-wash will alter the effective angle of attack downstream of surfaces [18].

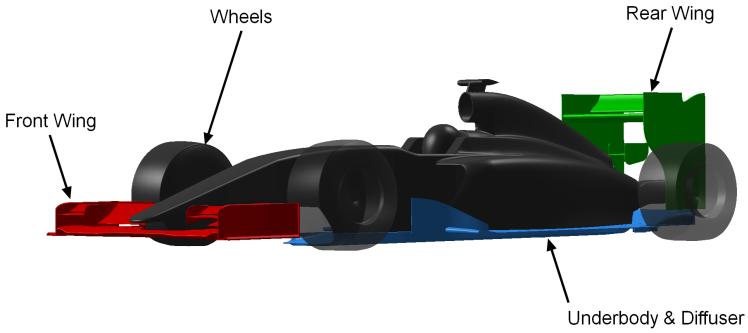


**Figure 1.2:** Generic 2014/15 specification Formula 1 car.

The interactions between the front wing and wheels are particularly important, figure 1.3, and the complex wing endplate vortex system can be used to minimize the effect of the static pressure discrepancy between

the front and rear face of the front tyres, reducing wheel drag [23, 24]. The span, volumetric envelope, and height of the front wing above the ground is determined by the regulations at the time [25, 26] rather than necessarily the optimal solution.

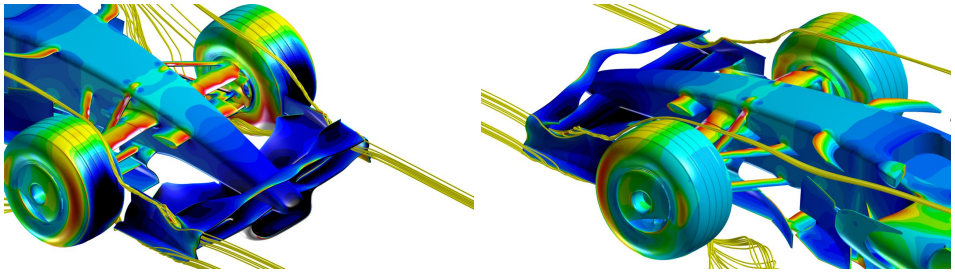

**Figure 1.3:** 2008 Renault R28 F1 front wing vortex/front wheel interaction, from CD Adapco [27].

**Rear Wing (Green):** The first case of a Formula 1 car using an inverted wing purely for downforce was in the late 1960's [28], initially they were mounted to the sprung part of the car but quickly moved to the unsprung corners in order to directly apply load onto the tyre contact patch. However limitations in manufacture at the time led to a number of accidents caused by failures of the wheel hubs, and suspension travel resulted in breaking of wing mounts, and the wings themselves. In 1969 the rule which, in essence, lasts to this day was introduced and stated the wings be fixed to the sprung part of the car [29].

The rear wing of a modern Formula 1 car is used in conjunction with the front wing to balance the car. The rear wing is a multiple element component, with elements ranging from the 'Venetian blind' style wings of the 1990s to the 2-element designs dictated by the 2014 rules. The rear wing is responsible for a large proportion of the total car drag and the angle of attack will be reduced to decrease frontal area [28] on circuits where higher top speeds are desired. The rear wing also works in conjunction with the underfloor and rear diffuser [30] to improve flow extraction from under the car (diffuser pumping) by helping to reduce the static pressure at the base of the car. Like the front wing the envelope in which the rear wing must fit is tightly controlled, rather than free for the most efficient design.

**Underbody (Blue):** The first use of a contoured underbody to generate downforce was in the late 1970s with the Lotus 78 (though arguably the 1970 March 701 came close with its wing shaped fuel tanks), which featured sidepods shaped like the lower surface of a downforce generating wing, commonly known as Venturi tunnels, and sealed with a flexible 'skirt'. Earlier attempts at ground effect aerodynamics, the Chaparral 2J and Brabham BT46B which used fans to extract air and generate a low static pressure region under the car, were quickly banned by rule-makers. Since the mid 1980s the underbody has been regulated as a flat surface with a rear up-swept diffuser. The downforce generated by the underbody is upwards of a third the total vehicle downforce [11], and is distributed approximately equally between the front and rear axles, with the balance driven by a combination of car rake angle and regulations regarding the location of the start of the diffuser ramp.

**Wheels:** Wheels are the largest source of drag on a Formula 1 car, typically contributing up to $40\%$ of

the total vehicle drag [11, 12]. Wheels do not contribute positively to the aerodynamic performance of the car and are only left exposed by regulation and tradition, with other 'open-wheel' racing series using front (Formula E) and rear (Indy Car and Formula E) fenders to reduce wheel wakes. As well as increasing total drag, the effect of wheels on other aerodynamic surfaces is predominantly negative, creating strong cross flows where axially aligned flow is desired [12]. A lot of effort is spent reducing the undesirable impact of the wheel wakes [18], with barge boards and turning vanes utilized to divert the front wheel wake outboard of the underbody as shown in figure 1.4, which serves to increase the effective width of the car.

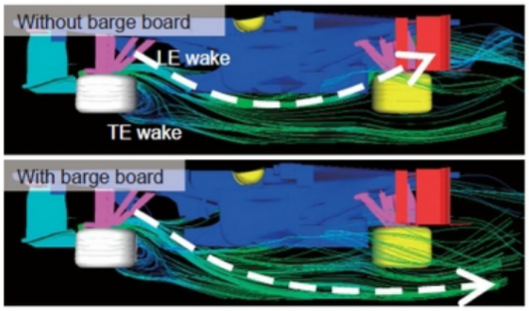


**Figure 1.4:** Path of front wing and wheel wake, with and without flow conditioners, from Ogawa et al [18].

#### 1.2.1.2 Single Element Wings in Ground-Effect

The 'ground-effect' can be simply defined as the increase, relative to freestream conditions, of vertical aerodynamic force (either lift or downforce) experienced by a body operating in proximity to the ground [31]. The force enhancement behaviour of wings operating in ground-effect differs depending on whether the wing is upright (lift generating) or inverted (downforce generating), figure 1.5. An upright wing experiences an asymptotic increase of aerodynamic lift, typically starting when operating less than a chord length from the ground, which is coupled with a reduction of the aerodynamic drag of the wing, significantly improving the lift-to-drag ratio ($^{L}/_{D}$).

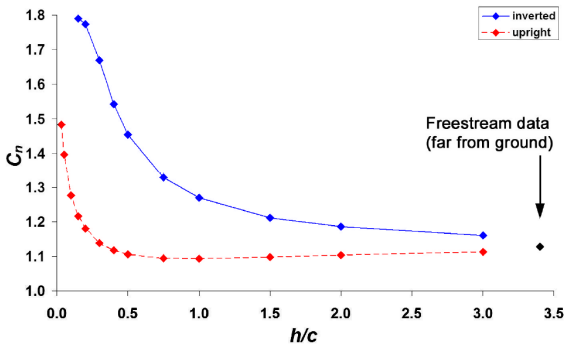


**(a)** Vertical force coefficient ($C_L$ or $-C_L$).

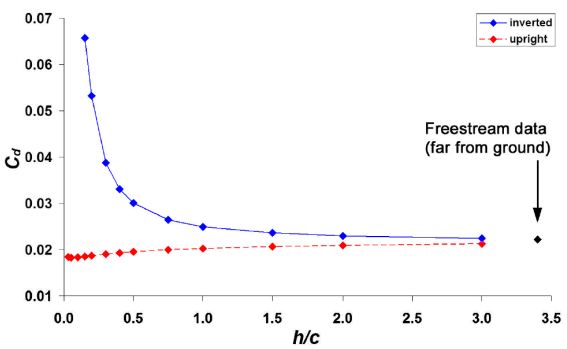


**(b)** Drag coefficient ($C_D$).

**Figure 1.5:** Comparison of force enhancement due to ground effect for upright and inverted wings in ground effect, from Vogt et al [32].

An inverted wing in ground-effect, such as the front-mounted wing of a Formula 1 car, experiences an

increase of vertical force over a greater range of ground clearances, with peak downforce in excess of the peak lift of an upright wing. Downforce does not increase infinitely with reduced ground clearance though, and reaches a local maximum which is followed by force reduction [33, 32, 34] at very low ground clearances. The ground clearance for which the force reduction occurs will depend on Reynolds number, the aerofoil profile, and incidence. Contrary to an upright wing, the aerodynamic drag of the inverted wing in ground-effect also increases with proximity to the ground, figure 1.5b, serving to reduce the lift-to-drag ratio. In the case of a modified GA(W)-01 aerofoil (the 'Tyrrell wing' [33]) in ground effect, used in many studies of wings in ground-effect, the $^{L}/_{D}$ reduction is a similar magnitude to the increase of $^{L}/_{D}$ experienced by an identical upright wing [32] at an incidence of $\alpha = 6°$. Part of this is due to the change of induced drag of the wing, which is known to decrease for an upright wing, but increases for an inverted wing [35].

A large part of the difference between upright and inverted wings in ground-effect is the effect the ground plane has on the pressure distribution of the pressure and suction surfaces [32]. In the case of an inverted wing the suction surface and ground plane form half of a Venturi, whereby the airflow is accelerated in the contraction [33] raising the dynamic pressure under the wing. The increased velocity from the Venturi effect in turn increases loading on the suction surface (i.e. reduces static pressure). Sub-atmospheric static pressure ($-C_P$) on the suction surface can increase significantly at very small ground clearances, figure 1.6, while the pressure surface remains relatively unaffected by ground proximity. The significant downforce increase is therefore primarily the result of the suction surface pressures. The radically increased loading on the suction surface increases the relative pressure difference between the upper and lower surfaces, increasing tip vorticity and induced drag.

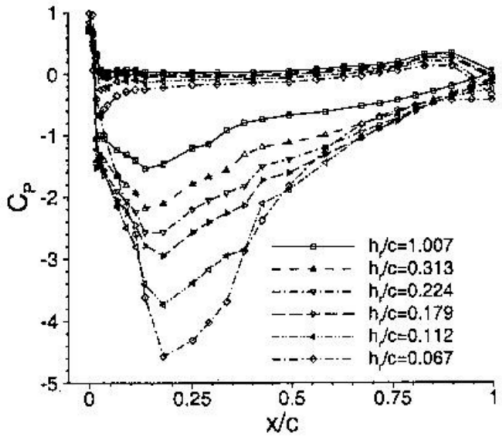


**Figure 1.6:** Effect of grond clearence on centreline pressure distribution of wing in ground effect, from Zerihan & Zhang [33].

Similarly to an inverted wing, vertical force for an upright wing in ground-effect increases primarily as a result of the lower surface pressure. However pressure increases on the underside due to a ramming effect, where the air under the wing stagnates (approaches $C_P = 1$) [36] as the wing approaches the ground.

Interestingly the lower surface can also be subject to the venturi effect due to a convergent-divergent path under the wing. This would normally be the case for symmetric aerofoils and aerofoils with low camber at small incidences, where the point of the aerofoil closest to the ground is the location of maximum thickness of the wing [36]. Whereas for a heavily cambered wing at high incidence the lowest point is at the trailing edge [37, 32], and the venturi effect is negated.

The aerodynamic behaviour of upright and inverted wings operating in close proximity to the ground plane is very different. While lifting wings are used in Formula 1 to generate localized down-wash and streamwise vorticity, particularly under the chassis [18]. As downforce, generated by inverted wings, is the primary interest to motorsport applications the rest of this review will focus on the behaviour of inverted wings in ground-effect.

It is well known that proximity to the ground reduces the angle of up-wash in the wake of a wing [38, 18], figure 1.7. The result of a theoretical mirror image of the wing, reacted by the ground plane, the circulation of which cancels the circulation of the wing. The wake up-wash of the front wing is important in the development of Formula 1 cars, as it is the incidence of onset flow to downstream geometries [18].

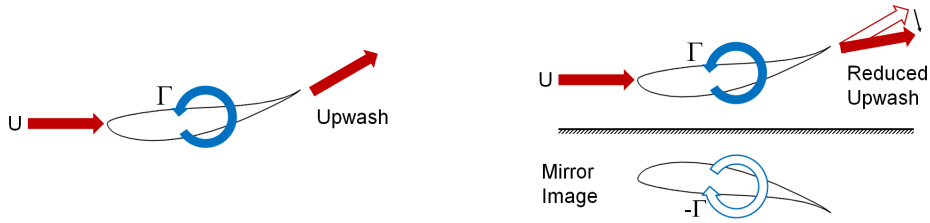


**(a)** Out of ground effect. **(b)** In ground effect.

**Figure 1.7:** Theoretical effect of ground effect on wake up-wash.

As the ground clearance is reduced the dynamic pressure under the wing increases, which in turn increases peak suction loading on the lower surface of the wing. The increased peak pressure creates a steeper adverse pressure gradient, thickening the boundary layer [38, 32]. The increased thickness of the lower surface boundary layer leads to a thicker wake downstream of the wing, figure 1.8, which for very low ground clearances merges with the ground plane (figure 1.8b).

Part of the downforce reduction experienced by an inverted wing in ground-effect, operating in very close proximity to the ground, can be attributed to separation of the suction surface boundary layer. Separation begins from the trailing edge of the wing [33, 38, 39, 34] and increases in length, moving up the chord of the wing as the ground plane is approached. Boundary layer separation can be attributed to the increased adverse pressure gradient resulting from the large increase in peak loading on the suction surface (figure 1.6). The separated region increases the wake thickness further and is responsible in part for the increase of drag seen for an inverted wing at low ground clearances, figure 1.5b.

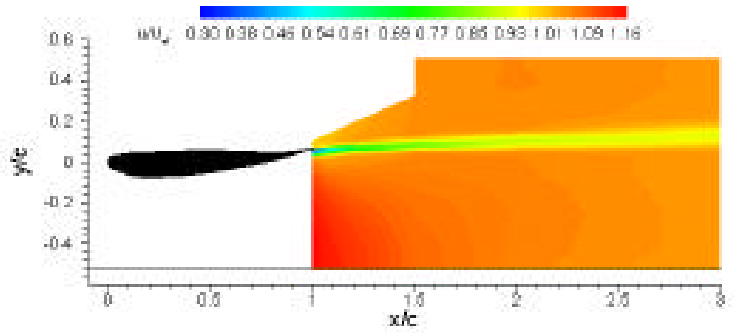


**(a)** High ground clearance.

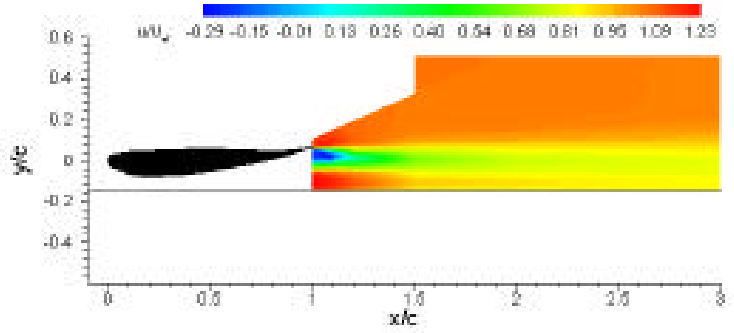


**(b)** Low ground clearance.

**Figure 1.8:** Effect of ground clearance on 2-D wake thickness and direction, from Zhang & Zerhian [38].

Separation of the boundary layer does not immediately result in the region of downforce reduction, seen in figure 1.5a, with the peak suction on the lower surface increasing for ground clearances lower than the height at which force reduction is seen to begin [33]. Instead the trailing edge separation acts against the increased dynamic pressure under the wing to retard the downforce to ground clearance slope. At peak downforce the suction surface boundary layer separates at $\approx 80\%$ of the chord[33, 38, 32], with force reduction then occurring as a greater chordwise fraction of the boundary layer separates, until total stall occurs.

As mentioned previously part of the increase of drag experienced by an inverted wing in ground-effect is from an increase of the induced drag, relative to freestream [35, 38], with the venturi effect under the wing increasing vertical load over a greater range of ground clearances to a higher peak force than an identical upright wing (figure 1.5a [32]). The increased suction results in a greater pressure difference between upper and lower surfaces, creating a strong tip vortex. Surface flow near the endplate is dominated by this main vortex with a highly 3-dimensional flow, where near the centreline the flow can be considered as 2D.

For wings with endplates, most applicable to Formula 1 cars, the main Front Wing End-Plate vortex (FWEP) starts to roll-up from the point of peak suction on the lower surface of the wing, and remains attached to the inner face of the endplate. On a conventional rectangular endplate a secondary co-rotating vortex forms at the upper edge [40, 41, 23, 42], which depending on wing height and peak suction pressure can be stronger than the main FWEP vortex.

In the force enhancement region, up to peak downforce, the size of the vortex core is relatively unaffected by ground clearance [41, 42], with the suction generated by the vortex maintaining flow attachment and reducing the static pressure towards the tips, aiding generation of downforce. The circulation of the FWEP continues to increase in strength as ride height is reduced [23]. At ride heights below maximum downforce the vortex begins to break down and core diameter increases and moves inboard (towards the wing centreline). In the force reduction region, the vortex bursts resulting in the rapid reduction of downforce (and drag) seen at very low ground clearances, figure 1.5.

Literature found for wings in ground effect is often base on Reynolds numbers an order of magnitude below a Formula 1 car at full scale and representative speed ($Re \approx 2.5 \times 10^6$ for a Formula 1 front wing at 240km/hr), owing to limitations in wind tunnel velocity and model scale ($Re \approx 4.4 \times 10^5$ from Zerihan & Zhang [33], Zhang & Zerihan [41] and Mahon & Zhang [39], and $Re = 2.0 \times 10^5$ from Roberts et al [43] based on aerofoil lengths), meaning the boundary layer of most studies is either fully laminar or in the transitional regime at the trailing edge (see fig 1.27 top), based on the assumption that the boundary layer is laminar on a flat plate up to $Re = 5.0 \times 10^5$. Transition fixing is a method of forcing the suction surface boundary layer to prematurely transition to turbulence through use of a grit strip placed across the span. Placed near the leading edge the effect of forcing transition is to reduce downforce for all ground clearances [33, 43], with force reduction and trailing edge boundary layer separation occurring at higher ground clearances than the transition free wing. Roberts et al [43] asserts that the location of the boundary layer trip has an important effect on the results. Moving the trip rearwards into the pressure recovery gradient has a similar effect to introducing vortex generators at mid chord [44], in that downforce increases beyond peak downforce in the transition free case. Roberts postulates that this is due to the laminar separation bubble [45] ahead of the turbulent transition. In the transition-free case the bubble serves to increase the effective camber of the suction surface, while with fixed transition near the leading edge the boundary layer transitions without a separation bubble. Moving the trip aft of the peak suction, but still ahead of the location of the laminar bubble in the transition free case, moves the bubble upstream into a favourable location along the chord. This increases $C_{L\,Max}$, but increases wake thickness and is likely geometry specific.

#### 1.2.1.3 Multiple Element Wings

The use of multiple element wings is essentially a means of enhancing the normal force on the wing by increasing camber, while also increasing the incidence at which stall occurs. Benzing [28] explains the delayed stall by the flow through the slot re-energising the lower surface boundary layer. Smith [46] though asserts that the flow through the slot explanation is a simplification and describes five effects of adding one or multiple flaps:

1. **Fresh boundary layer effect** each element introduces a fresh boundary layer, which being thinner is capable of remaining attached to the adverse pressure gradient than a thicker boundary layer. Though if the slot is too narrow the boundary layers of the up and downstream elements can merge forming a thicker boundary layer and resulting in greater drag.

2. **Slat effect** whereby the velocity and circulation at the trailing edge of the upstream element reduce peak pressure at the leading edge of the downstream element.

3. **Circulation effect** whereby the circulation of the downstream element increases the velocity at the trailing edge of the upstream element, in turn increasing the circulation of the upstream aerofoil, where circulation ($\Gamma$) is directly proportional to lift.

4. **Dumping effect** where the higher velocity boundary layer at the trailing edge of the upstream element is discharged into a region of higher local velocity, reducing the adverse pressure gradient and the likelihood of separation.

5. **Off-surface pressure recovery** where the deceleration of the wake back to freestream occurs in a separated boundary layer, with less skin friction drag than an attached boundary layer.

The types of multiple element wing fall into four categories [28], the Fowler flap, NACA multiple slotted, Junkers flaps and the most extreme being the Venetian blind. Fowler flaps are a derivative of the plain flap commonly used in aeronautics to alter camber with the flap displaced to introduce a slot. The NACA multiple slotted are similar to the Fowler flap with multiple slots and normally a short leading edge slat typically 10-20% of the main aerofoil chord. Venetian blind type wings can feature upward of eight aerofoils stacked above one another, and in the simplest form is used by biplanes. The flap type normally used in Formula 1 is the Junkers flap, where a pair of aerofoils with desirable pressure profiles are paired with a slot between them to increase downforce. Current Formula 1 regulations [26] allow the rear wing out of ground effect to be constructed of only two elements, commonly named the mainplane and flap, with a slot at least 15mm between them [30].

Wenzinger [47] investigated the effect of a NACA23012 aerofoil flap, 20% the chord of the mainplane, with a NACA23012 mainplane. Both flap and mainplane lifts were seen to increase relative to their isolated values, which can be attributed to circulation effects, as described above. The majority of lift is produced by the mainplane and load was seen to increase rapidly even at small flap incidences. As both the flap and mainplane were the same profile the pressure profiles are similar, featuring a low pressure spike at the leading edge on the suction surface. The magnitude of both increases with flap angle, though more so for the mainplane than the flap. Pressure was also seen to incrementally increase on the mainplane pressure surface with increased flap incidence. Wenzinger [47] also note that a further influence of the flap is a reduction the adverse pressure gradient, figure 1.9, increasing the incidence at which stall occurs. Smith

[46] also presents a velocity plot for a Leibeck high lift double-element Indianapolis 500 race car rear wing, as the angle of the wing was changed the velocity profile of the flap suction surface remained relatively constant while the mainplane suction surface velocity increased.

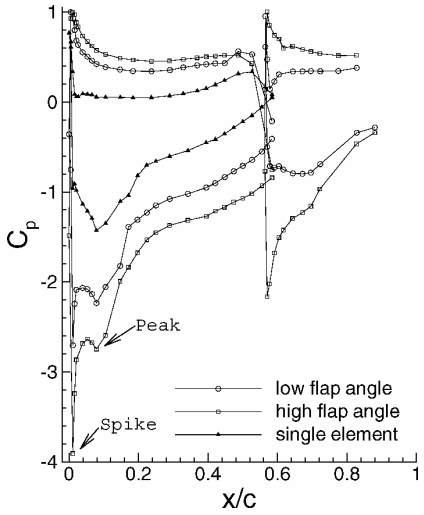


**Figure 1.9:** Centre span surface pressure distibutions for multiple element wing in ground effect, from Zhang & Zerihan [48].

Zhang & Zerihan [48, 41] and Mahon & Zhang [49] investigated the same rectangular double element wing in ground effect experimentally and in CFD. The mainplane was identical to the single element wing used by Zerhian & Zhang [33], Jeffrey, Zhang & Hurst [50] and Zhang, Senior & Ruhrmann [51] with the addition of a 41% chord flap. Like single single element wings in ground effect, figure 1.5, downforce increases with reduced proximity to the ground. Unlike the single element wing though, downforce produced with reduced height can be split into three distinct regions [48, 41], figure 1.10, at high clearances downforce increases rapidly, there is then a discontinuity after which downforce increases more gradually to stall. The discontinuity and stall occur further out of ground effect with a greater flap incidence, though peak downforce is higher with the higher flap incidence. Mahon & Zhang [49] notes that the contribution to the increased downforce from the flap is relatively constant for all ride heights, and much of the force increase results from the mainplane which is attributed to the flap being further out of ground effect than the mainplane. The earlier stall with the high flap incidence is attributed to the increased circulation of the wing creating a thicker boundary layer, which separates more readily at a greater ground clearances. Like downforce, drag also increases with reduced ground clearance similarly to the single element wing in ground-effect up to the discontinuity. After which the rate of drag increase slows with downforce before rapidly increasing after stall. Drag is greater with a higher flap angle, which can be resulting from increased blockage and circulation and thus induced wake drag.

A secondary effect of the vertical force development is the tip vortex [51]. The vortex behaviour is seen to change with the three distinct gradients of lift (against ride height) seen in figure 1.10 and can be said to have a role in force generation. During region 'a' the vortex gains strength as lift increases. During region

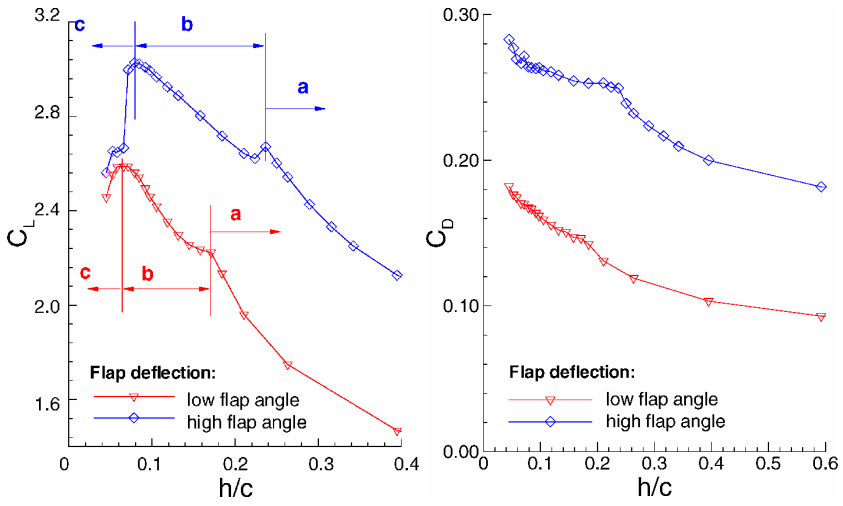


**(a)** Downforce. **(b)** Drag.

**Figure 1.10:** Effect of ground clearance on forces generated by multiple element wing in ground effect, from Zhang & Zerihan [48].

'b' the vortex loses strength and begins to breakdown at the lowest 'b' heights, in region 'c' the vortex has broken down as the wing stalls. With planar endplates, as used by Zhang, Senior & Ruhrmann [51] and Jasinksi & Selig [40], a secondary vortex is present at the top of the endplate. The vortex rotation is opposite to the main tip vortex resulting in a "figure of 8" shaped wake. More complicated endplates, like those used in Formula 1, result in a more complicated vortex system in the wake, figure 1.11.

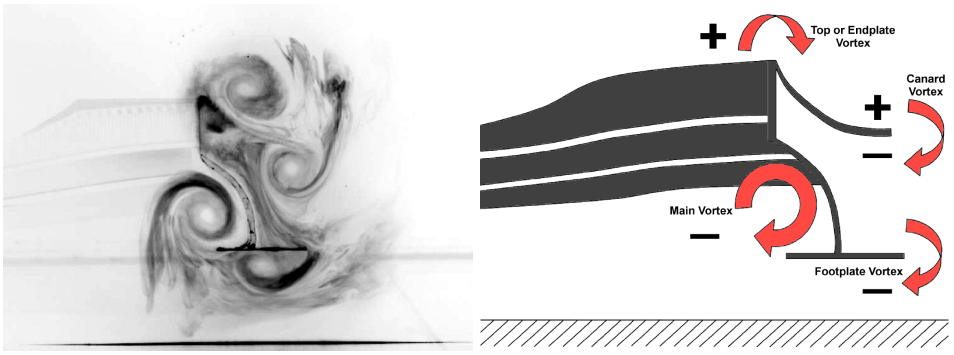


**Figure 1.11:** Complex endplate vortex system for a front wing in ground effect, from Pegrum [23].

Flap style has also been shown to have an impact on downforce generated by the double element wing, where Zhang & Zerihan [48, 41] and Mahon & Zhang [49] used a rectangular planform flap, Jasinkski & Selig [40] compared two full-width flaps similar to the Champ Car and Formula 1 designs of the time. While both had an identical shorter chord at the centreline and longer chord towards the endplate, the short chord in the middle of the car used to reduce blockage and wake up-wash onset to the radiator inlets [52]. The Champ Car design featured a sharp cut-out while the Formula 1 flap featured a gradual sweep from minor to major chord. The sharp cut out on the Champ Car design promoted a third vortex to form at the discontinuity. The flap vortex rotates in the same direction as the upper endplate vortex, but is significantly weaker. When using the same mainplane and endplates, the Champ Car design consistently produced $0.15$ on $C_L$ less downforce than the Formula 1 design. More interestingly the endplate also has

an impact on downforce and drag generated. With a longer Champ Car design generating $0.1$ on $C_L$ more downforce than a Formula 1 design, with 13% less drag.

#### 1.2.1.4 Gurney Flaps

As well as the multiple element wing, another commonly used high-lift device in motor-sports is the Gurney flap. The Gurney flap became synonymous with the American racing driver Dan Gurney after its introduction to American oval racing in the 1970's [28]. The Gurney flap is simply a short right-angled strip, typically measuring $1-5\%$ of the wing chord, affixed to the trailing edge of a wing perpendicular to the wing's pressure surface, figure 1.12.

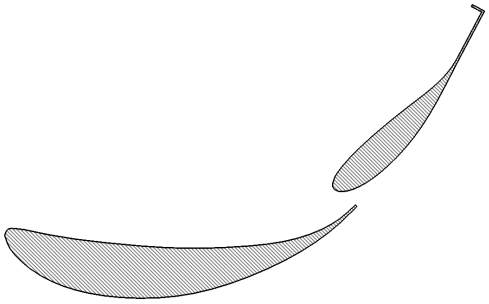

**Figure 1.12:** Two element, high camber, Formula 1 style aerofoil with Gurney flap with height of 5% wing chord attached to flap trailing edge.

What makes the Gurney flap a useful tool for motor-sport applications is the increase of downforce, therefore cornering velocity, for relatively little effort. Affixing a Gurney flap at the trailing edge of a single element wing serves to increase $C_L$ along the linear region of the incidence-lift slope, figure 1.13a, thereby increasing peak downforce ($C_{L\,Max}$) [53, 50, 54]. The $C_L$ gain does increase with Gurney flap height, though the $C_L$ increase is disproportionately higher with shorter Gurney flaps [54]. While the incidence of stall is not significantly affected, stall does occur at a lower incidence with a Gurney flap, with a greater force loss occuring. Placing a Gurney flap on an inverted wing in ground effect [54] also increases $C_L$ over a range of wing incidences, with stall behaviour occurring at higher ground clearances.

The addition of a Gurney flap increases loading on both suction and pressure surfaces of a wing [53, 55, 50], in both the chord and span-wise directions. The increased magnitude of pressures on upper and lower surfaces leaves a finite discontinuity in the pressure distribution at the trailing edge of the the wing, figure 1.13b, which increases with Gurney flap height, increasing the wake thickness and velocity deficit [54]. Stall incidence with the Gurney flap is reduced, due to the increased peak loading near the leading edge on the suction side, which increases the adverse pressure gradient, making the wing more susceptible to separation at lower incidence or higher ground clearances.

The wake of the Gurney flap behaves as a flat plate normal to the airflow, with a pair of recirculated

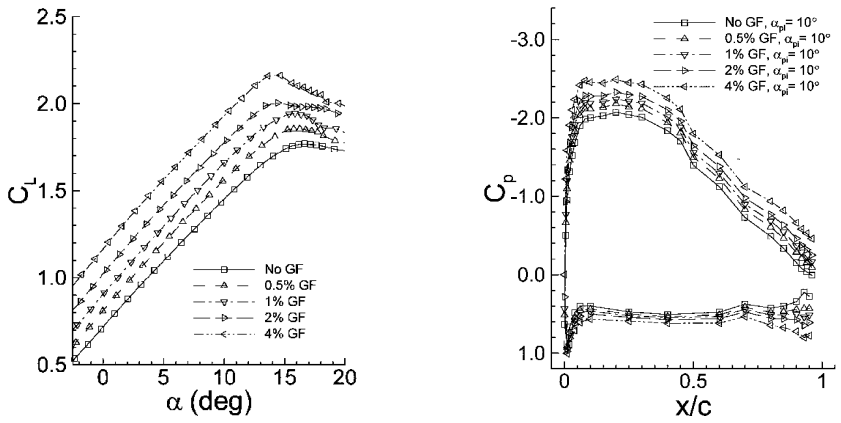


**(a)** Wing incidence ($\alpha$) vs $C_L$. **(b)** Chordwise surface pressure ($\alpha = 10°$).

**Figure 1.13:** Effect of Gurney flap height on aerofoil, from Jeffrey, Zhang & Hurst [50].

counter-rotating vortices formed directly behind the flap. The size of the vortices are not dependent on the flap height, but are instead a function of velocity gradient upstream of the flap, meaning the suction side vortex is disproportionately large [50]. From a time averaged view point these vortices remain behind the wing, with the wake closing at some point downstream of the Gurney flap. In reality the vortices are shed into a von Kármán vortex street, figure 1.14, Strouhal number of the shed vortices is dependant on flap height but is in the region of $0.15 < Sr < 0.19$ for Gurney flaps measuring $1 - 4\%$ of the wing chord in height [56, 50, 54].

**Figure 1.14:** Smoke flow visualization of wing wake with a Gurney flap, from Jeffrey, Zhang & Hurst [50].

A summary of wing in ground-effect studies referenced in this literature review is shown in table 1.2.

**Table 1.2:** Summary of wing in ground-effect studies referenced in this literature review.

| Reference | No. of Elements | Re Number | CFD/ Exp | Ground Simulation | Result Types |
|---|---|---|---|---|---|
| Jasinski & Selig [40] | Double | $4.9 \times 10^6$ | Exp | Fixed | Forces, 7-hole |
| Zerihan & Zhang [33] | Single | $2.0 \times 10^6$ | Exp | Moving | Forces, Surface Pressures & Oil Streaklines |
| Zhang et al [57] | Single | $4.5 \times 10^5$ | Exp | Moving | Forces, Oil Streaklines, LDA & PIV |
| Zhang & Zerihan [38] | Single | $4.5 \times 10^5$ | Exp | Moving | LDA & PIV |
| Zhang & Zerihan [48] | Double | $7.5 \times 10^5$ | Exp | Moving | Forces, Oil, Surface pressure, PIV & LDA |
| Zhang & Zerihan [51] | Double | $7.5 \times 10^5$ | Exp | Moving | Forces, Oil Streaklines, Surface Pressure, PIV & LDA |
| Mahon & Zhang [39] | Double | $7.9 \times 10^5$ | CFD | Moving | Forces, Surface Pressures & CFD Fluid |
| Ahmed & Sharma [36] | Single | $2.4 \times 10^5$ | Exp | Fixed | Surface Pressure & Forces |
| Pegrum [23] | Triple | $2.0 \times 10^5$ | Exp | Moving | PIV & LDA |
| | | $5.7 \times 10^5$ | CFD | | CFD Fluid |
| Vogt et al [32] | Single | $4.6 \times 10^5$ | CFD | Moving | Forces, Surface Pressure & CFD Fluid |
| Genua [34] | Single | $4.6 \times 10^5$ | CFD | Moving | Forces, Surface Pressure & CFD Fluid |
| Diasinos et al [58] | Single | $4.6 \times 10^5$ | CFD | Moving | Forces & CFD Fluid |

#### 1.2.1.5 Under-Body and Rear Diffuser

The rear diffuser of a modern Formula 1 car, figure 1.15, is a compromise between generating the maximum load and the relatively small volume allowed by the regulations. The shape of the diffuser itself is free to interpretation, provided it remains within the volume defined by the regulations. The short diffuser length ($350mm$) and height ($125mm$) means that instead of being planar, the diffuser profile is an aggressive kick and multiple inflected ramp defined in such a way to generate a high peak suction at the diffuser throat [18]. A series of strakes are then used to maintain a uniform pressure distribution across the width of the rear diffuser, while also flattening the adverse pressure gradient to prevent separation along the length of the diffuser. Static pressure at the diffuser exit is further enhanced by the low pressure under the suction peak of the lower rear wing [18]. Since 2009 the underfloor must be flat up to the rear wheel centre line; placing the diffuser kick relatively close to the inner face of the rear wheels, reducing the effective sectional area of the the diffuser thereby limiting peak performance.

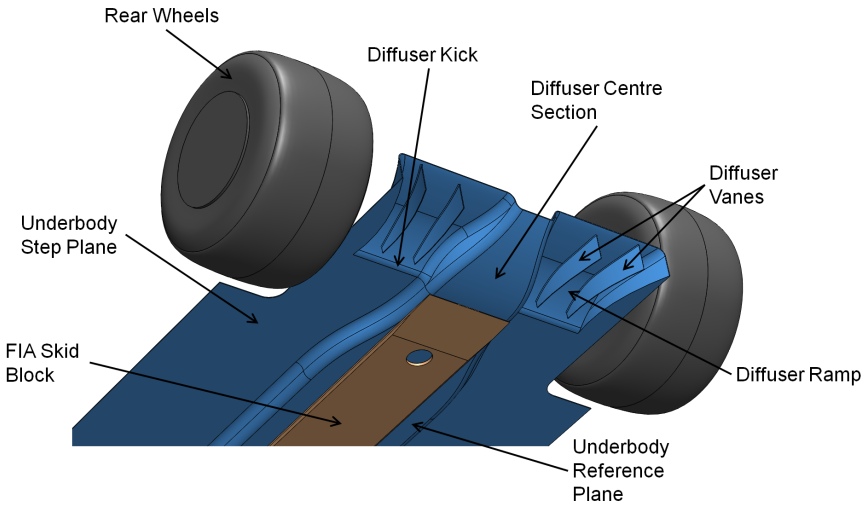


**Figure 1.15:** 2015 style Formula 1 rear diffuser.

All of the published research found for diffuser flows utilize a reference bluff body with a rounded front end and a planar up-swept rear diffuser of various lengths and ramp angles, as shown in figure 1.16.

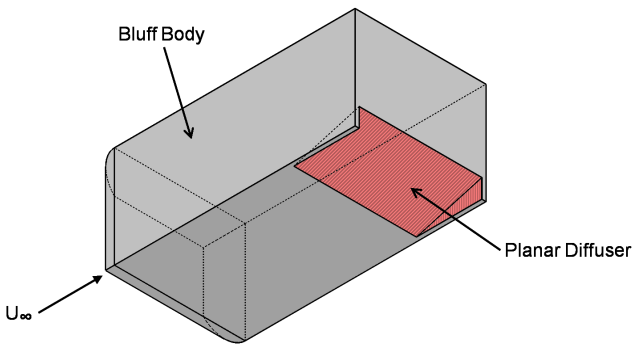


**Figure 1.16:** Reference bluff body with planar diffuser.

The force behaviour of a diffuser equipped bluff body in ground effect is similar [59, 60, 61, 51] to that seen for wings operating in ground effect. Reducing the ground clearance increases the suction peak ($-C_P$) at the diffuser throat, for high to moderate ground clearances downforce and drag increase as the ground is approached. At low ground clearances, the downforce enhancement retards while drag continues to increase, up to peak downforce. For very low ground clearances there is an abrupt stall, with drag and downforce reducing rapidly. The increased suction peak at the diffuser throat is disproportionate from the reduced pressure in the diffuser, increasing the adverse pressure gradient along the diffuser length.

Downforce generated by the diffuser can be increased by lowering the vehicle base pressure, known as diffuser pumping. In Formula 1 this is achieved using the lowest element of the rear wing, or "beam wing" [30], which lowers pressure at the diffuser exit, thereby lowering pressure along the floor.

For each region of force behaviour, a distinct surface flow behaviour occurs [59, 51], figure 1.17. In the force enhancement region (figure 1.17a) the flow is attached across the width of the diffuser, with a pair of counter-rotating streamwise vortices forming at the diffuser throat and constrained by the end-fence [62], which detach from the surface of the diffuser along the length [61]. In the plateau region, figure 1.17b, the vortices increase in strength and size [51], aiding force production. The centre of the diffuser begins to separate as the adverse pressure gradient increases, though flow remains symmetric about the centreline. In the final region (figure 1.17c) there is 3-dimensional separation at the diffuser throat. Either vortex will breakdown, leaving a single, significantly weakened, end-fence vortex occupying much of the width of the diffuser. Asymmetry is attributed to imperfections in set up of model height and tunnel alignment, or surface finish [59].

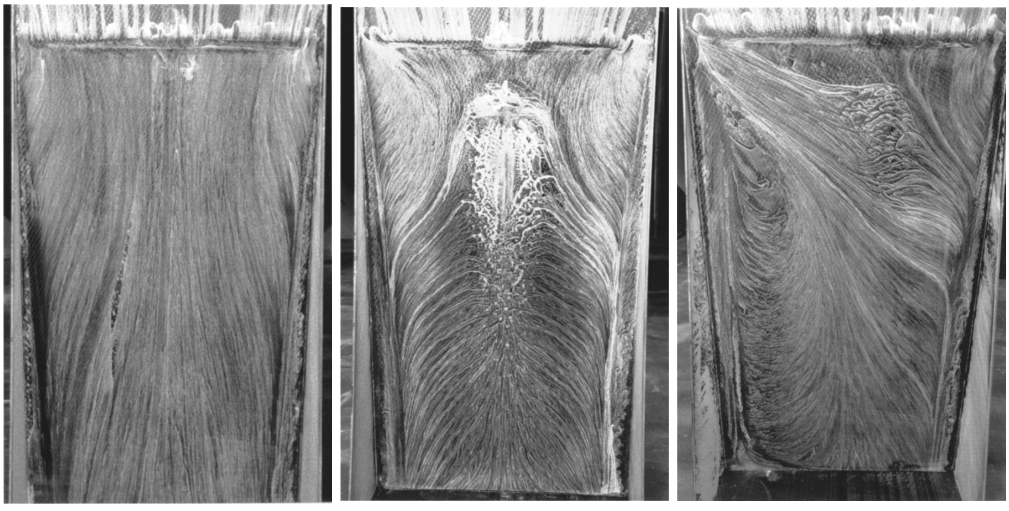

**(a)** Force enhancement. **(b)** Plateau to peak force. **(c)** Stall and force reduction.

**Figure 1.17:** Planar diffuser surface streaklines highlighting flow regime changes (flow from top to bottom), from Senior & Zhang [59].

Increasing the angle of the diffuser ramp has the effect of increasing the suction peak at the diffuser kick [60, 63]. The increased pressure increases the adverse pressure gradient, resulting in separation at

higher ground clearances. Downforce increases up to a critical angle, beyond which the effect is to induce separation at ever higher ground clearances.

The planar diffuser can be transformed into a multiple channel diffuser with the addition of a number of triangular vanes, set perpendicular to the ground plane [63, 64]. Under the optimal ramp angle of a single plane diffuser ($\theta = 13^{\circ}$) multi-channel diffusers do not appreciably increase downforce generated. Though the vanes tested [64] were seen to reduce the effective area of the diffuser, with each channel generating more downforce in the active area. For moderate ramp angles, $16^{\circ} < \theta < 19^{\circ}$, downforce is seen to increase with only a minimal increase of drag. While for extreme angles, where the single channel diffuser would experience flow separation, the downforce generated increases significantly.

Force enhancement is facilitated by a moderate increase of pressure at the diffuser throat, which in turn improves diffuser pumping and suction to the leading edge. The lower pressure and increased downforce increases the end-fence vortex strength, which aids flow attachment along the diffuser [51]. With a higher number of vanes, downforce generation is further aided by a secondary vortex forming on a central vane. The delayed stall at higher ramp angles is aided by a reduction of the adverse pressure gradient, and a reduction of base pressure.

#### 1.2.1.6 Isolated Wheels

The abiding rule throughout the history of Formula 1 is that the wheels remain exposed (open-wheel), with the wheels forming a large percentage of the frontal area of the car [28]. As such drag generated by the wheels is high, between $30\%$ to $40\%$ of the total vehicle drag [16, 11]. The characteristics of isolated cylinders are well documented, with flow separation and recirculation from the upper and lower surfaces. Wheels are in actuality in contact with the ground plane in normal operation, which significantly alters the flow around the wheel, and the wheels actually generate lift instead of downforce. So this section of the review will focus on literature relevant to wheels in contact with the ground.

The wake of both static and rotating wheels in contact with the ground plane takes the form of an inverted T ($\perp$) [65, 66, 67, 68], with a pair of streamwise vortices shed from the lower edge of the tyre, where the fluid jets around the front of the contact patch and is diverted by the freestream surrounding [69, 70], figure 1.18. McManus & Zhang [67] among others [71, 70] performed comparison of static and rotating wheels in contact with the ground, showing significant differences in the wake above the axle line, figure 1.18. In the stationary case flow over the top of the wheel remains attached, with a high velocity down-wash, while the wheel rotation causes a separation to occur from the upper surface with a resulting large recirculation region. Below the axle line, while the wakes are similar, perhaps counter-intuitively the lower wake in the static case is larger than with the rotating wheel. Forces generated by stationary and rotating

wheels are different, and drag and lift generated by the wheel reduces with rotation, $\Delta C_D = -0.05$ and $\Delta C_L = -0.20$.

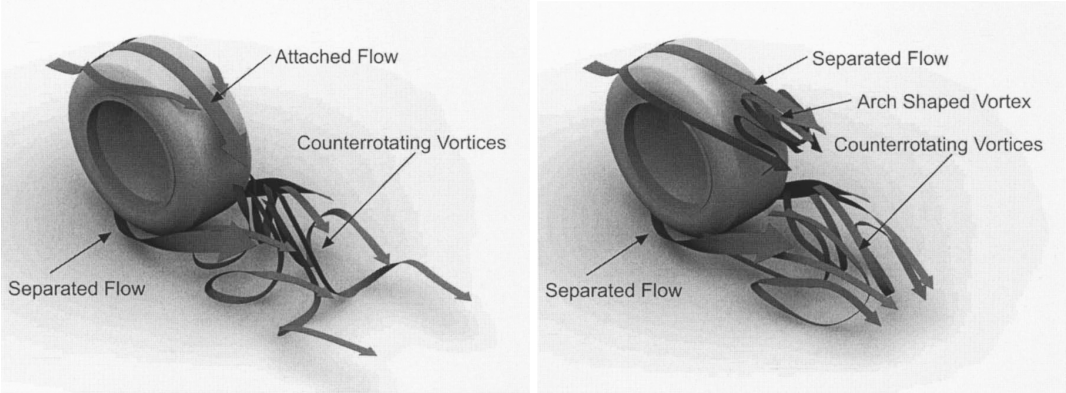


**Figure 1.18:** Comparison of static (left) and rotating (right) wheel wakes, from McManus & Zhang [67].

The very near wake of isolated and rotating wheels, ${}^{x}/_{D} < 1$ (where $D$ is the wheel diameter), features two pairs of counter-rotating vortices [65, 66, 68], an upper and lower pair. Both pairs have their centres within the projected frontal area of the wheel and rotate with centreline down-wash. The lower, ground co-incident, pair is stronger than the upper pair, and is dominant in the wake behind ${}^{x}/_{D} = 1$ (figure 1.19), with high turbulence intensity around the cores in excess of $TI_X > 30\%$ [66].

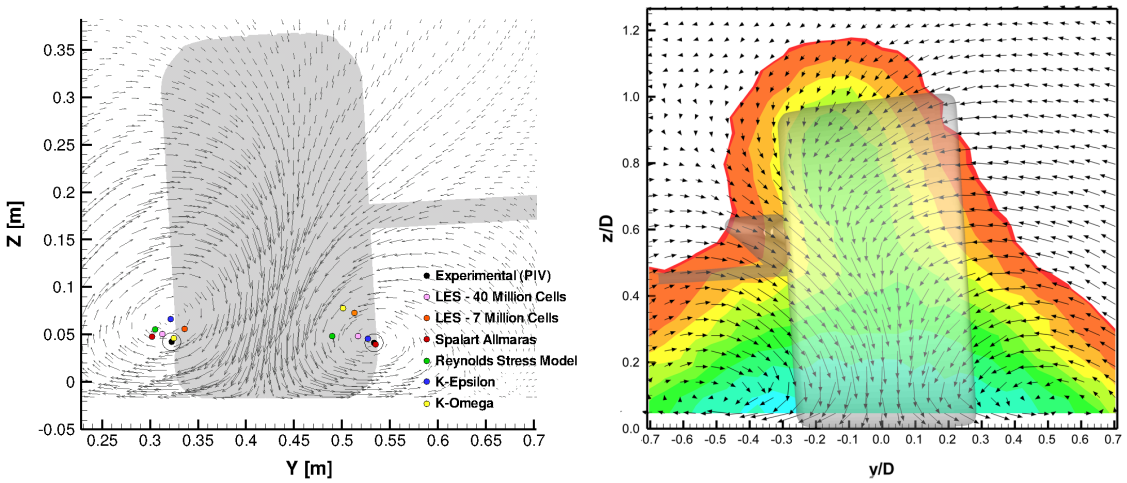


**(a)** $x/D = 1.12$ from axle line, from Axerio et al [72]. **(b)** $x/D = 2.0$ from axle line, from Sprot [73].

**Figure 1.19:** Secondary velocity vectors in wake of cambered wheel and tyre.

Formula 1 and other open-wheel race-cars tend to run with extreme negative camber angles, especially on the front axle where cambers in excess of $-3.5°$ [73] (i.e. the top leaning in towards the chassis) are common, while rear cambers are closer to $-1°$ to $-1.5°$. To simulate camber angles in experimental studies (using rigid wheels) conical cross-section wheels (figure 1.19b) were used in Formula 1 through the early 2000s [70, 73]. In computational simulations, where a support strut is not required, wheel camber angle is not shown to have a significant impact on the surface flow and wake [70]. While in physical experiments, the support strut is shown to affect the wake [66, 74]. In figure 1.19a, the inboard vortex is

larger and persists further downstream of the wheel. This is likely due to disruption of the outer vortex by the support strut, which is connected to the outboard side of the wheel. While in figure 1.19b, the strut is on the chassis side (in a similar position to the front suspension) and the outer vortex is slightly larger. Other parameters such as side-wall profile, through-hub flow, brake ducts with or without blanking [75, 73], solid or spoked wheels, will all make a difference to the accuracy of the wake.

While camber angle is simulated by conical wheels, they do not accurately simulate the contact patch deformation under load as is experienced on-track [76]. Since the mid 2000s [14], in Formula 1, the preferred means of simulating wheel and tyre wakes in experiments is pneumatic tyres [69, 77, 23, 78, 73]; and teams are provided with pneumatic tyres from the official FIA tyre supplier [79] for the purpose of wind tunnel testing.

Deformation of the tyre contact patch due to downforce and yaw will alter the wake of the tyre, and can affect downforce generated by the underbody, figure 1.20a. Under normal conditions the vertical displacement of the axle can be as much as 25mm [22]. Simulating the tyre squash under load is therefore important for teams trying to understand the minutiae of the flow structures around the car. Contact patch deformation can be achieved in wind tunnel tests a number of ways; with wheels mounted on stings, pre-load can be applied via the lever arm [73]. Alternatively, with the wheels mounted to the chassis, pre-load can be applied through the suspension arms [22], though this requires the suspension to be load bearing. Alternatively the contact patch can be deformed by a pusher inside the wheel (figure 1.20b), this has the advantage that no added download is required. With deformation due to yaw applied, the separation from the front of the contact patch moves rearward on the outboard side [22, 73] (windward i.e. top to bottom in figure 1.20a). Likewise vertical displacement of the axle, due to downforce, can create a distinct wake structure [73].

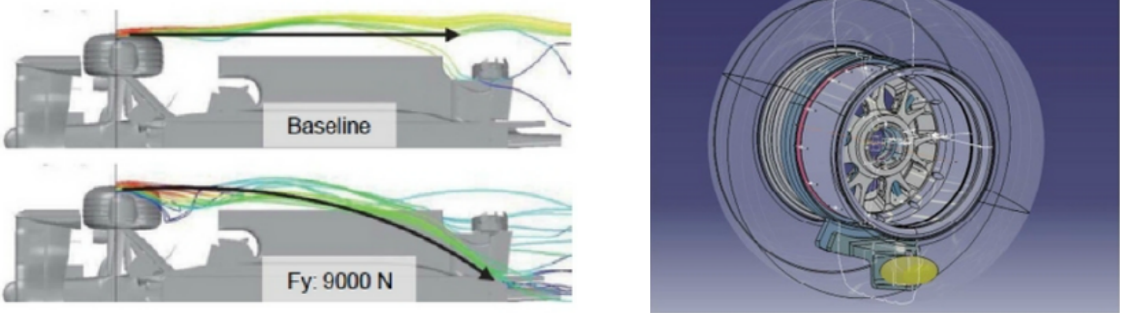


**(a)** Effect of tyre deformation on wheel wake. **(b)** Contact patch deformation mechanism

**Figure 1.20:** F1 tyre contact patch deformation due to side-force, from Ogawa et al[22].

#### 1.2.1.7 Wing - Wheel Interactions

Modern Formula 1 front wings are flow conditioners just as much as they are downforce generators. Endplates are no longer used solely to constrain the tip vortex and instead feature a number of turning vanes and vortex generators in order to direct airflow around the front wheels, shown in figure 1.21, to minimize both wheel drag and the wheel wake. In 2009 the FIA mandated that the central 500mm span of the wing be a prescribed profile [2], the teams have since used the vortex formed between the 'neutral section' and downforce generating surface to generate a strong vortex (or "Y250 vortex", figure 1.21) which is manipulated downstream in order to divert the front tyre wake outboard of the the underfloor.

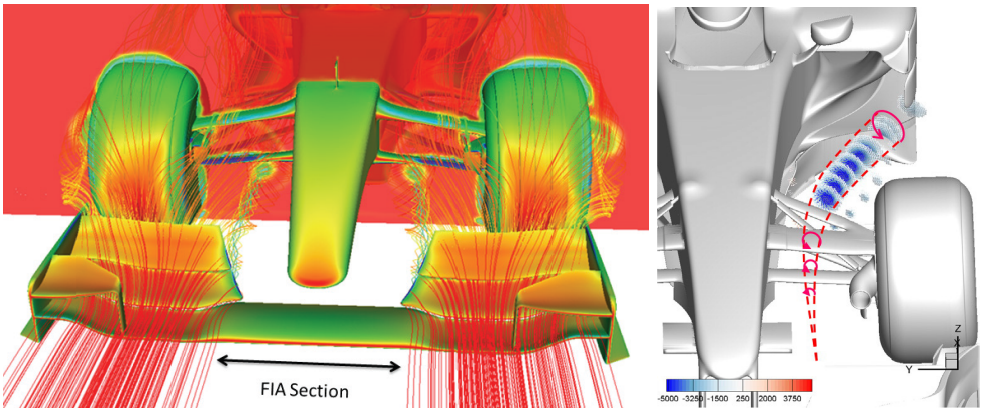


**Figure 1.21:** Front wing and wheel interactions and the "Y250" Vortex, from Larsson [3] and Nakagawa et al [14].

The behaviour of an inverted wing in the presence of a rotating tyre has been investigated by numerous sources. In 2D the presence of a rotating cylinder behind an aerofoil significantly affects the force generated by both cylinder and aerofoil [80]. The aerofoil was found to reduce the cylinder lift by affecting a reduction of the high pressure region on the front of the cylinder from stagnation pressure, with the best case at high angle of attack where the blockage effect is greatest. This model is insufficient though as in reality the wing may only overlap part of the wheel and wing tip wake flows are highly 3-dimensional in the region of interaction, figure 1.22.

The general effect on wheel drag due to an upstream wing is a reduction of drag for the wheel, seen for both stationary [81] and rotating [24] wheels, when the wing is close to the ground. Wheel drag is seen to increase relative to an isolated wheel when the wing is at high ground clearances [24, 70], with a sharp reduction of drag as wing ride height is reduced between $^{h}/_{c} = 0.3$ and $^{h}/_{c} = 0.4$. Like the 2D rotating cylinder the high pressure region on the front face of the tyre is reduced from stagnation pressure, $C_P < 1.0$, when the wing is upstream. The static pressure reduces further when the wing ground clearance is lower; the channel effect reduces pressure under the wing and the low pressure region extends rearward to the contact patch. Towards the top of the wheel, the separation point is delayed by the presence of the upstream wing [24], the separation point moves rearward around the tyre with increasing wing ground clearance and can be seen in figure 1.22 (labelled E). Van den Berg [24] asserts that this delayed separation

at high ride heights is the result of the circulation of the wing wake which, being of opposite sign to the wheel circulation, serves to postpone separation. Van den Berg also notes that this effect is strongest when the trailing edge of the wing is at axle height, when the gap between wheel and wing is smallest, and that at higher ride heights the delayed separation can be explained by the increased flow directed over the wheel by the wing.

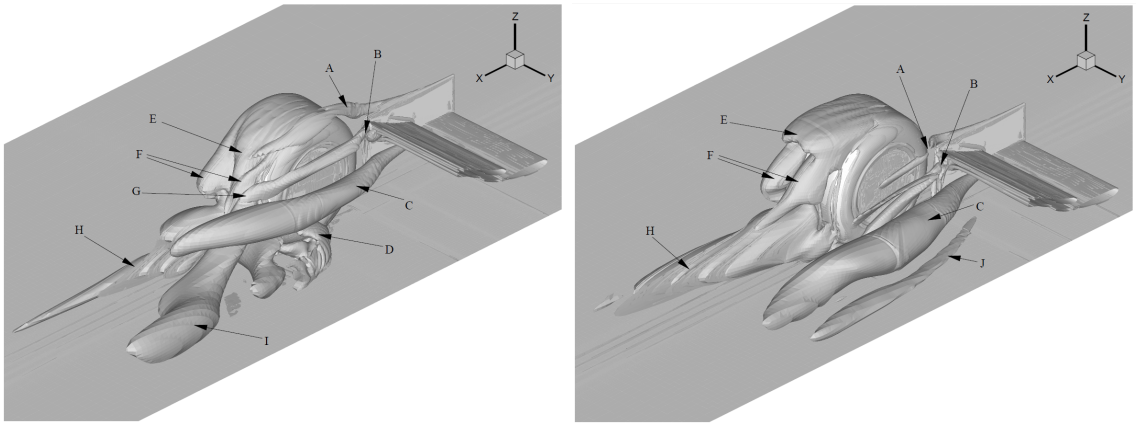


**(a)** High wing, high wheel drag. **(b)** Low wing, low wheel drag

**Figure 1.22:** Effect of wing ground clearance on combined wing and wheel wake, from Van den Berg [24].

The effect of the wheel on the wing downforce is similar to the effect of the wing on wheel drag, downforce is seen to increase at low ground clearances ($^{h}/_{c} < 0.15$ [24, 70]) but at most ground clearances downforce is reduced compared to an isolated wing. Force increase follows the same behaviour as an isolated wing, with a gradual force increase as ride height reduces, becoming more rapid before plateauing, and finally a force reduction at very low ground clearances. In the presence of the wheel the peak force is higher magnitude ($16.2\%$ at $^{h}/_{c} = 0.067$), however the force plateau occurs for a smaller range of heights [24]. Wing drag is greater than freestream for ride heights lower than $^{h}/_{c} = 0.35$, incidentally the same ride height that wheel drag is seen to reduce below the isolated wheel drag [24]. Where the wing wake circulation has a negative effect on the wheel separation point, Van den Berg asserts that the increased downforce at low ride heights is the result of the wheel circulation; the flow under the wing is actually faster than for an isolated wing [70]. The wheel circulation also results in a third endplate vortex to form, along with the main tip vortex and upper endplate vortex, originating at the separation point of the flap [24]. Like the wheel, the effect of the combined circulation on the wing is negative when the trailing edge is at or near axle height on the wheel, hence the reduction of downforce compared to an isolated wing.

The effect of the wheel on the wing wake, and vice versa, can be difficult to measure experimentally as the physical blockage of the wheel makes probe and PIV planes difficult to collect [23, 14], so CFD has been the preferred tool to visualise the wake [81, 24, 70]. For high wing ride heights the combined wake is similar to a static wheel [70], while for low wing ground clearances the wake resembles the wake of a rotating wheel. Depending on wing span the effect on the combined wake varies. In isolation increasing wing (WIG) span will also result in increased downforce due to the reduced proportion of the surface subject

to 3-dimensional flow, as the size of the tip vortex remains constant [58].

The main wing tip vortex has the greatest effect on both wing and wheel drag, if the endplates are designed such that the vortex does not pass the wheel either inside or outside then wheel drag is significantly increased [81]. Diasinos & Gatto [82] and Diasinos [83] showed that there are three potential flow paths for the wing tip vortices, for full width wings (like pictured in figure 1.21) either both the vortices pass outside the front wheels, or the endplate vortex passes outside the wheel with the tip vortex inside. The main vortex tended to pass inside the wheel for high angles of attack, where downforce was greater. The third path was that both vortices passed the inside face of the front tyre, which occurs with narrower span wings.

At full span (and low angles of attack) the high pressure on the front face of the tyre limits the pressure under the wing, reducing downforce by as much as $40\%$. The strength of the main vortex also reduced, which has been shown to be strongly linked to downforce production, but also results in a drag reduction of up to $70\%$ [83]. The main vortex passes around the outside of the wheel [14], though the effect on the combined wake is minimal. Increasing the angle of attack of the wing, i.e. increasing the downforce, reduces the pressure on the front face of the tyre while also allowing the main vortex to pass inside the wheel. This then merges with the inboard lower vortex of the wheel (figure 1.22) reducing wheel drag while decreasing the downforce deficit to the isolated wing by $30\%$. In this configuration the endplate is outboard of the wheel stagnation point, so the upper endplate vortex passes around the outside of the wheel, as per figure 1.21. Reducing the span the suction under the wing which was required to drag the main vortex inboard of the wheel was reduced. With short span wings the endplate vortex also travels inboard of the wheel, although the static pressure ahead of the front face of the wheel increases the static pressure on the outside of the endplate, thus the rotation is reversed compared to an isolated wing. The endplate and main vortices travelling inboard means that downwash in the wheel wake is reduced, reducing wheel lift and drag by $45\%$ and $25\%$ respectively. Where Diasinos [83] and Diasinos, Barber & Doig [58] only tested maximum span and a span to the inner face of the wheel, Van Den Berg [24] tested a number of overlaps, finding that an overlap between $65\%$ and $75\%$ performed best, with greater downforce (at the lowest ride heights) and reduced drag compared to an isolated wing.

### 1.2.2 Wake Composition

#### 1.2.2.1 Formula 1 Wake

The Formula 1 wake combines elements of the generic lifting and bluff body wakes; with a counter-rotating vortex pair originating from the high camber, low aspect ratio, inverted rear wing end-plates coupled with a large region of stagnation pressure deficit. The rear wing vortices rotate with centreline up-wash [7, 15] and remain present in the wake for many car lengths downstream of the car. Closer than $x = 0.25L_C$ from

the rear of the car stagnation pressure deficit peaks in excess of $90\%$ [7] are present in the wake behind the wheels and diffuser. As the wake continues downstream, beyond $0.5L_C$, the tip vortices become more dominant forcing the velocity and pressure deficits in the wake to surround the vortex cores; the pressure and velocity deficits become more homogeneous and also concentrate on the centreline due to in-wash near the ground, forming a "mushroom" shaped wake, figure 1.23a & 1.23b. Wilson, Dominy & Straker [7] found turbulence intensity ($TI$) peaks in excess of 45% in the wing vortex cores, figure 1.23e, $TI_X$ is 35% over much of the projected area of the car, while Watts & Watkins [4] found peak turbulence intensity to be 30% and concentrated on the wake centreline, with $TI_X$ of 25% in the wing tip vortices. This discrepancy could be due to a number of differences, Wilson, Dominy & Straker used a moving ground plane with rotating tyres, while Watts & Watkins [4] used a fixed ground which severely limits the generation of downforce by the underfloor, the up-wash from which adds to the centreline up-wash from the rear wing vortices. As a result of the moving ground Wilson, Dominy & Straker [7] required an overhead strut to mount the vehicle, which can be seen in the stretching of the axial velocity deficit and increased turbulence on the centreline above the rear wing of the car. There is also a difference in the Reynolds number of experiments, Wilson, Dominy & Straker [7] $Re = 6 \times 10^5$ and Watts & Waktins [4] $Re = 2.4 \times 10^6$, and model scale affects the accuracy of components, where Wilson, Dominy & Straker used a $^1/_6$ scale model and Watts & Watkins used a $30\%$ scale model. Finally any differences could be geometry specific, as well as the regulations the models were designed for (Wilson, Dominy & Straker used a pre-2009 specification car, while Watts & Watkins designed their car based on the 2010 regulations), differences in wing pressure distribution and car shape can affect the shape of the wake.

In 2009 the Formula 1 technical regulations [2] were changed with the intention of increasing overtaking frequency. To achieve this it was decided that downforce needed to be reduced by as much as 50% [3] by removing the numerous flaps, turning vanes and winglets which had become prevalent on the cars by the end of 2008. The rear wing span was reduced and also moved further out of ground effect, with the diffuser shortened to reduce the interactions between the two components (this was further achieved in 2014 with the banning of the lowest 'beam' wing element [26]). The effect of the changes on the wake, as can be seen in figure 1.23, is an increase of centreline velocity deficit and turbulence intensity, with a migration of the vortices upwards and inwards which increases the crossflow at front wing height for a following vehicle.

After the 2009 regulation change did not have the desired effect on the frequency of overtakes the rear wing drag reduction system, or DRS, was introduced for 2011 [28, 4]. The system allows the rear wing slot gap to be opened to 50mm when within 1 second of a leading vehicle at prescribed locations around a circuit. The effect of DRS activation on a vehicle wake is shown by Watts [4] to be reduced vorticity coupled with a decrease of turbulence intensity of around 10-15%. The reduction of induced drag leads to a higher top speed for the trailing vehicle making it easier to effect a pass at the end of a straight, though the ease of some overtakes has led to some fans regarding the system as a gimmick.

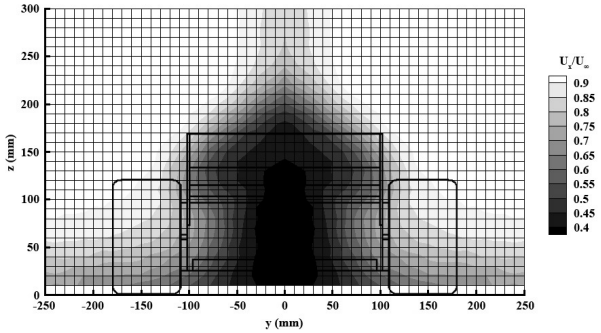


**(a)** ${}^{u_X}/_U$ pre-2009, from Wilson, Dominy & Straker[7].

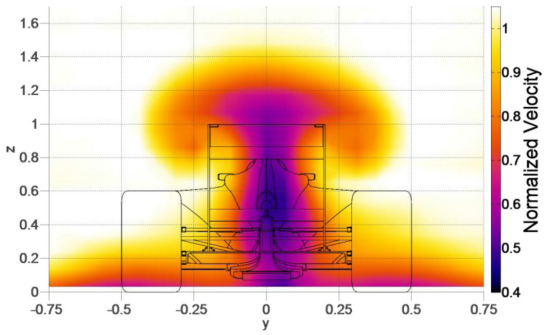


**(b)** ${}^{u_X}/_U$ post-2009, from Watts & Watkins [4].

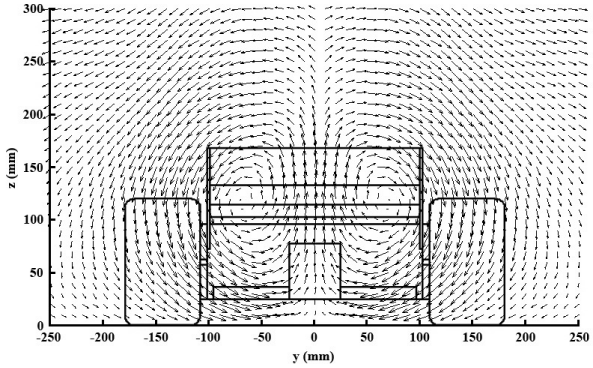


**(c)** Vectors pre-2009.

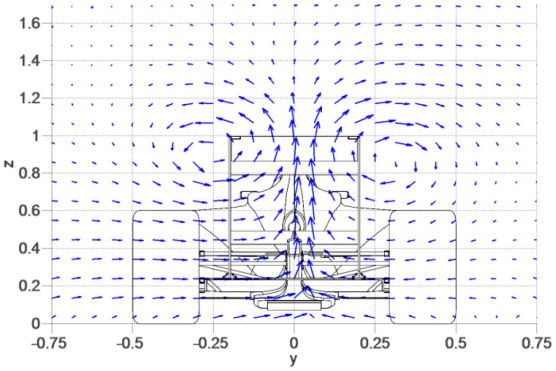


**(d)** Vectors post-2009.

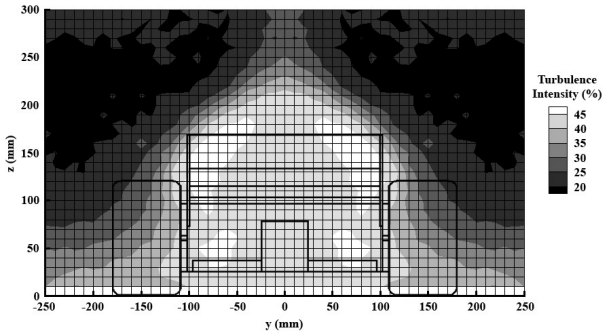


**(e)** $TI_X$ pre-2009.

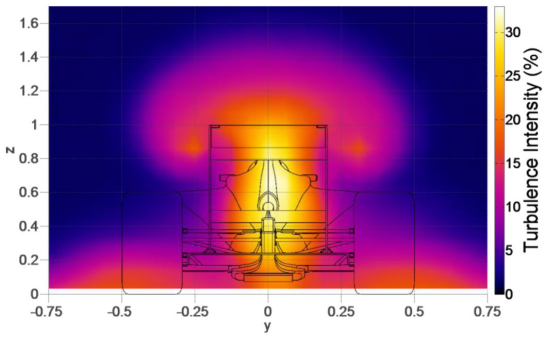


**(f)** $TI_X$ post-2009.

**Figure 1.23:** Wake contours at $x = 0.5L_C$ downstream of 16% & 30% scale Formula 1 cars.

#### 1.2.2.2 Generating Formula 1 Wake with Bluff Body

One of the key obstacles to using a pair of representative vehicles in a wind tunnel is the length of the models, reducing the potential axial separation. Figure 1.24 shows a pair of identical scaled Formula 1 cars in the Fondtech FT1 wind tunnel, the facility features a 4.1m long rolling road [84] so assuming a model scale of 40% (length $\approx 1.9m$) the maximum separation possible is only between 0.25 and 0.5 car lengths, which is not a representative offset for a slipstreaming manoeuvre. Model scale can be reduced to increase the separation, though this approach can reduce the accuracy of results. The lead model can also be placed upstream of the moving belt, as per Dominy [1] but this can reduce the accuracy of the upstream wake as rotating tyres and underfloor flow are important factors in wake development and strength.

Soso [5, 85, 9] hypothesised that the use of a generic, diffuser-equipped, bluff-body would recreate the

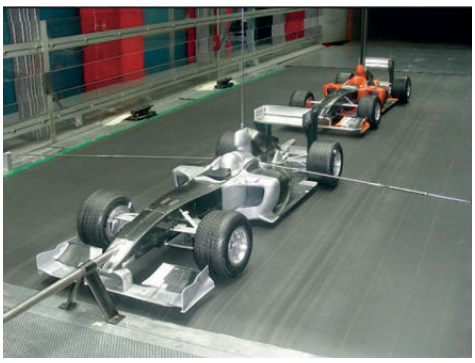

**Figure 1.24:** A pair of 50% scale Formula 1 cars in the Fondtech wind tunnel.

key features of the wake while also being shorter than a scale model to increase the potential offset while maintaining a larger scale for the trailing body (discussed later). The wake generator is quite long, at around 40% of the length of a full vehicle and is still placed on a ground board with sharp leading edge ahead of the rolling road. The wake generator also features a rear wing out of ground effect to strengthen the vorticity created by the underfloor. In the very near wake two pairs of counter-rotating vortices are created, a small pair at the rear wing tips and a large pair from the underfloor. By the downstream vehicle the co-rotating pairs on each side merge to form a large counter-rotating pair representative of a Formula 1 car wake. No data is presented on the velocity and pressure deficits in the wake to compare.

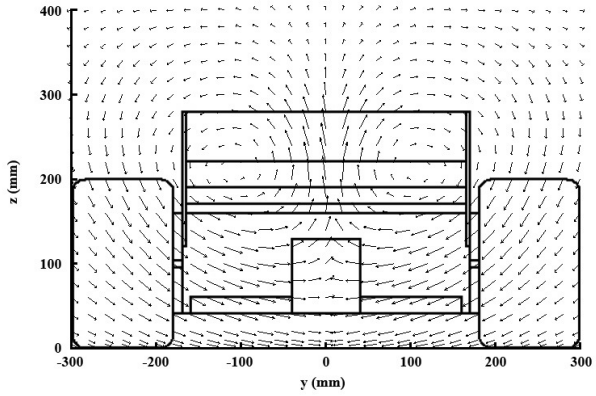


**(a)** Vectors, from Wilson, Dominy & Straker [7].

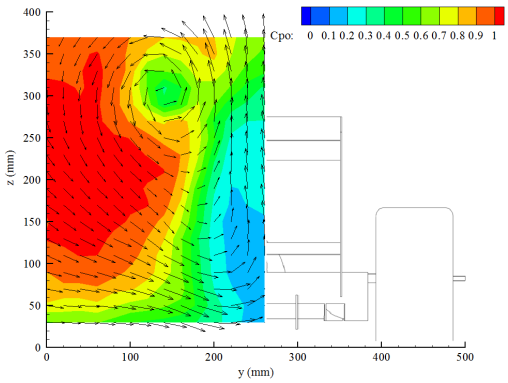


**(b)** Vectors & $C_{P_O}$ deficit. from McClintock [8].

**Figure 1.25:** Secondary velocity vectors at $x = 0.5L_C$ downstream of bluff bodied wake generator.

Wilson, Dominy & Straker [7] and Straker [6] carried on from Soso and Soso & Wilson with the creation of a bespoke bluff bodied wake generator. With further generations designed at Durham University by Barrett [86] and McClintock [8] and at Cranfield by Correia et al [87]. The wake generator must generate the strong vorticity and pressure and velocity deficits in the wake while possessing a shortened body with upswept floor, albeit significantly shorter than that used by Soso. As shown in figure 1.25 the vector plots of both the pre-2009 and post-2009 wake generators show good correlation to the wakes in figure 1.23 in both size and location of the vortex cores. It must be noted that shortening the body, and particularly the underfloor, of the wake generator will reduce the downforce generated by the body, as lift (and negative lift) is equal to the integral of surface static pressure with respect to the surface area.

The wake generator designed by McClintock is 15% of the length of a full vehicle. The reduction of lift means that the strength of the vortices is reduced, and rate of decay is increased compared to the full vehicle. Corriea shows turbulence intensity on the centreline to be only 25%, 5% and 10% lower that the Formula 1 wakes shown in Watts & Watkins [4] and Wilson, Dominy & Straker [7] respectively. Wilson, Dominy & Straker and Barrett [86] show the high stagnation pressure deficit at rear wing height of a similar magnitude to the Formula 1 wake, though without the centreline deficit lower in the wake. This can be a result of the loss of underfloor upwash and the smaller blockage of the shortened bluff body.

Outside of Formula 1, a similar bluff bodied wake generator has been utilized to generate a NASCAR (Stock Car) wake [88] with similar results. The vorticity is recreated, while the short axial length of the wake generator means turbulence, and velocity and pressure deficits are not perfectly recreated, although the magnitudes are similar.

### 1.2.3 Wake Interactions

#### 1.2.3.1 Race Cars in Wake Flows

Recent sporting regulations [79] restrict Formula 1 teams to the use of only one model in both wind tunnel testing and CFD simulations, which prevents the use of both two vehicles or a bluff bodied wake generator as described above. The only published work on a Formula 1 car in a wake is from Dominy [1] and McClintock [8], while both used 25% scale Formula 1 models, Dominy used a second model placed upstream of the rolling road on a ground board so was only able to achieve a single axial separation, in this case 1 wheelbase $(L_{WB})$. While McClintock used a bluff body placed on the rolling road and moved upstream from 0.25 to 1 car length $(L_C)$.

Instead of moving the upstream car axially Dominy instead introduced an offset from 0 to 1.25 car widths $(W_C)$ laterally. The biggest effect of the upstream wake was seen with no offset, with a 36% loss of downforce and 23% drop of drag, while the aerodynamic centre of pressure shifted rearwards by 22%. As lap-time can be improved by increasing downforce (figure 1.1) it is clear a 36% loss would increase lap-time, while the centre of pressure moved to 90% along the length of the wheelbase, which would have a catastrophic effect on the handling balance towards understeer. As the lateral offset was introduced downforce recovered to freestream more rapidly than drag, the losses cross over at $y = 0.2W_C$, after which drag loss is greater than downforce. Downforce recovery is roughly asymptotic and is 98% of freestream at $y = 1.25W_C$, while drag recovery is almost linear. Using a simple steady-state lap-time simulation it was determined than a constant offset of $0.3W_C$ would result in a faster lap-time, as the cornering performance loss is offset by the increased straight line speed due to lower drag; though as the author surmises, driving at a constant offset around a lap would be difficult for a driver to maintain.

Using a bluff body McClintock [8] was able to increase the axial spacing relative to Dominy [1] to one car length with the bluff body moving toward the test car up to $0.25L_C$. The biggest losses were seen at the shortest separation as a 60% loss of downforce with a 17% rearward shift of the centre of pressure. Like the lateral offset downforce recovery is more rapid at short axial separations and the loss is only 28% at $1L_C$. At $0.75L_C$, roughly the same axial separation as Dominy, the downforce loss is 32% which is similar to the loss seen by Dominy with no lateral offset. The rearwards shift of the centre of pressure is only 10% rather than the 22% seen by Dominy. This could be geometry related (a 1990's Formula car compared to a late 2000s geometry) or because the centre of pressure for McClintock is 10% more rearward in freestream conditions which limits how rearwards the centre of pressure can move without the front wing also generating lift.

The effect of vehicle proximity on sports-cars was also investigated by Howell [89] and Dominy, Ryan & Sims-Williams [90] both of which after cases of cars overturning as in figure 1.26. Both vehicles feature a flat bottom with rear wing placed out of ground effect and produce a wake featuring low static pressure in the vortex cores from the rear wing and a cerntreline upwash, in Howell in excess of 20% of $U_\infty$. Both studies saw a decrease in downforce when following behind a lead car, in the case of Howell this became a lift force. Both studies also introduced a lateral offset which served to increase downforce relative to the freestrem, perhaps as the car centreline was operating in the downwash from the wing vortices. Where the studies differ is the change in centre of pressure as a result of the upstream vehicle, Howell saw a pitching moment large enough that front lift exceeded the mass on the front axle. Whereas Dominy, Ryan & Sims-Williams saw an increase in front axle load. Where the cars differ is the use of ground effect to aid downforce, with the CanAm (1966-1987) cars in Howell none is used, while with the LMGTP (Le Mans Grand Touring Prototype, 1997-2003) car in Dominy, Ryan & Sims-Williams a front and rear diffuser is present. Dominy, Ryan & Sims-Williams explain the forward shift, while still losing downforce, as the presence of faster velocity below the up-wash in the upstream wake. This coupled with the front splitter extending close to the ground than a Formula 1 car leads to the front diffuser being less sensitive to the wake than the rear wing. Dominy, Ryan & Sims-Williams also only tested a nose down pitch of $0.7^\circ$ where Howell tested angles from $1^\circ$ nose down to $1^\circ$ nose up, seeing a smaller influence from the wake in the nose down configuration.

#### 1.2.3.2 Wing in Ground Effect In Wake Flows

As the furthest forward geometry on the car, the front mounted wing in ground effect is the first component to be affected by the onset wake. As such wings in ground effect have been the subject of more studies to date than the whole car. As described earlier, the wing in ground effect in freestream is subject to force enhancement as the ground is approached, though stall occurs at lower angles of attack for lower

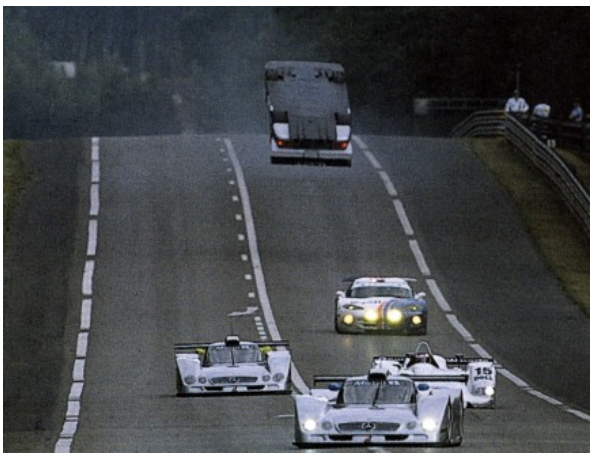

**Figure 1.26:** Mercedes CLR LMGTP overturning at 1999 Le Mans 24 hour race, from Mulsanne Corner [91].

ride heights. This is due to the increased loading of static pressure on the suction surface increasing the adverse pressure gradient between the suction peak and trailing edge of the wing, leading to separated flow.

The effect of a vehicle wake on front wing forces has been investigated by Soso [5], Soso & Wilson [85, 9], Wilson, Dominy & Straker [7], Straker [6], and Correia et al [87]. All used a rectangular and unswept single element GA(W)-01 aerofoil with rectilinear endplates, with the exception of Correia et al who added a pair of flaps. For all cases the wing stall incidence is increased at all wing heights tested, by between $5^\circ$ and $10^\circ$, while the ride height at which the peak downforce is achieved increases. Drag is also seen to reduce by between 20% and 50% depending on height and incidence. Straker tested two bluff body locations and saw that in the near wake $(0.5L_C)$ the peak downforce was 30% lower than freestream at a height $1.5\times$ the freestream maximum. In the very near wake $(0.25L_C)$ peak downforce was reduced by 35% but the the height at which this occurs was five times the freestream. Soso [5] tested a range of wing heights and incidences wide enough to see a second, more abrupt, stall in the freestream case. This hard stall disappeared with the upstream wake and was replaced by a less rapid force loss. Soso & Wilson [9] also tested a number of upstream body diffuser angles between $5^\circ$ and $16.7^\circ$ with little effect on the downforce produced by the wing. The lift to drag of the wing did improve with decreased ramp incidence at greater ride heights, though still significantly lower than the freestream, which was attributed to a change of the upwash incidence at low ramp angles.

The effect of the wake generator on surface flows is shown by both Soso & Wilson [85] and Correia et al [87]. Despite Soso & Wilson using a single element and Correia et al a two element wing, and the height at which the streaklines were generated being $0.153c$ and $0.089c$, the mainplane suction surface streaklines are remarkably consistent. Both show a separation bubble, owing to the low Reynolds numbers of $3 \times 10^5$ and $4.5 \times 10^5$ respectively, spanning most of the wing at around 50-60% chord in the freestream cases with turbulent reattachment behind, shown in figure 1.27 top. While the presence of the wake generator

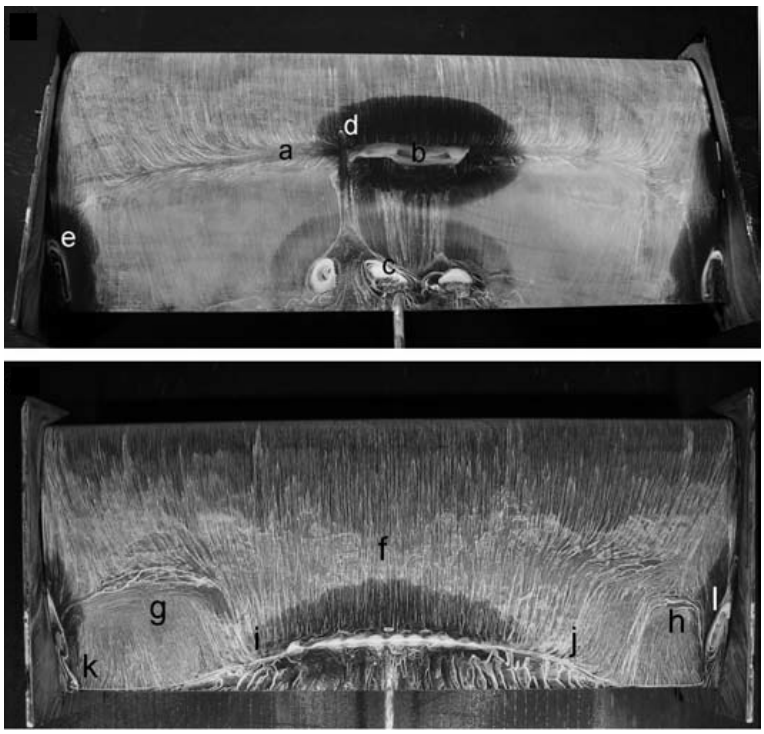


**Figure 1.27:** Change in surface flow structures in wake (flow from top to bottom), from Soso & Wilson [85].

results in a fully turbulent boundary layer from the leading edge with turbulent separation occurring at the trailing edge, near the centreline, figure 1.27 bottom. The forward shift and burst of the separation bubble is indicative of a higher Reynolds number, though the incident dynamic pressure is lower in the wake due to the axial velocity deficit. The loss of the separation bubble also acts to effectively reduce the camber of the wing which results in some of the downforce loss.

Soso [5] and Correia et al [87] also present the surface pressure distributions for the wing in and out of the wake flows. Both see a significant reduction of the centreline suction pressure coefficient, $-2.5C_P$ to $-1.1C_P$ for Correia et al. With reduced loss toward the wing tips and almost no effect seen on the pressure surface. As Soso notes, this could be a result of the centreline upwash emanating from the upstream wake generator, while the tips of the wing are in an incident downwash.

Where Soso [5] and Correia et al [87] disagree is the effect of the upstream wake on the WIG wake. Soso shows little effect on the size and intensity of the larger lower wing endplate vortex as a result of the wake, either at high or moderate ride heights nor as a result of the upstream diffuser angle. While the smaller upper endplate vortex is eradicated by the wake. The lower vortex also migrates inboard relative to the freestream case. Correia et al on the other hand sees a greater effect on the vorticity of the lower vortex, with the upper vortex less affected. As Correia et al used a pair of flaps with the wing a third vortex per side is present at the inboard edge of the flap, which is relatively unchanged by the wake. Correia et al attributes the endplate vortex reduction to the loss of suction on the lower surface of the wing resulting in a smaller pressure delta, while increased turbulence also reduces the vortex stability. Increased lift also

results in a larger and more stable vortex, as lift is reduced in the wake this seems to support the theory that vorticity would be reduced. Where the two studies agree is that the wake behind the WIG is thicker as a result of the upstream wake, this is due to the earlier transition to a turbulent boundary layer on the lower side of the wing and even turbulent separation in some conditions.

There is little research published investigating the effect of upstream vehicle wakes, a summary those which have been found are show in table 1.3, with the majority investigating the effect of wakes on isolated wings in ground effect.

**Table 1.3:** Summary of maximum force losses experienced with an upstream wake.

| Upstream | Downstream | Separation | $\Delta C_D$ (%) | $\Delta C_L$ (%) | Reference |
|---|---|---|---|---|---|
| Can-AM | Can-AM | 0 | -97.7 | -62.4 | Howell [89] |
| Formula 1 | Formula 1 | $L_{WB}$ | -36.0 | -23.0 | Dominy [1] |
| Formula 1 | Formula 1 | $2.4L_C$ | -10.2 | -17.3 | Perry & Marshall [92] |
| Wake Generator | Formula 1 | $0.25L_C$ | - | -60.0 | McLintock[8] |
| Bluff Body | WIG | $1.5L_C$ | -22.0 | - | Soso [5] and Soso & Wilson [85, 9] |
| Wake Generator | WIG | $0.5L_C$ | -35.0 | -50.0 | Wilson, Dominy & Straker [7] |
| Wake Generator | WIG | $0.5L_C$ | -51.0 | -42.0 | Correia et al [87] |

### 1.2.4 Freestream Turbulence

Background turbulence levels in wind tunnels are deliberately low, with the intention to improve repeatability by reducing random noise. However, the low turbulence intensities, usually less than 0.5%, are not representative of the turbulence levels found in normal on-road driving conditions, so the desire to reintroduce a repeatable source of turbulence into the freestream has grown in the recent past, where turbulence intensity is equal to the r.m.s. velocity divided by the average velocity.

Freestream turbulence intensities over 10% are termed 'high' by Bearman & Morel [93], while under 0.5% is termed 'low', and 'very low' is less than 0.1%. Bearman & Morel do not assign a classification for the turbulence intensities found in the wake of a Formula 1 car which was found to exceed 30% by both Wilson, Dominy & Straker [7] and Watts & Watkins [4], though perhaps 'very high' suffices.

#### 1.2.4.1 Effect due to Passive Turbulence Generation

Passive systems of introducing turbulence generally take the form of a grid or series of parallel bars, either of round or square section, placed in the nozzle of the wind tunnel. With grid generated turbulence the axial component of turbulence intensity ($TI_X$) is consistantly double that of the lateral intensities ($TI_Y$ and $TI_Z$) [94, 93]. The turbulence decays downstream of the grid at a rate proportional to the distance downstream and bars size to the power of $-5/7$ [94],

$$TI_X \propto (\frac{x}{b})^{-5/7}, \tag{1.1}$$

where $x$ is the distance downstream of the grid and $b$ is the bar diameter.

The effect of freestream turbulence on aerofoils out of ground effect has been investigated [95, 96, 97], these studies are primarily related to vertical axis wind turbines so the incidences tested $(\pm 90^{\circ})$ exceed mostorsports applications, but regions 1 and 2 in figure 1.28 are still of interest, i.e. up to the first stall. Even at low levels of turbulence, $0.2\% < TI_X < 0.65\%$ [95], there is an effect on force and surface flow behaviour. Most changes due to turbulence occur in region 2 where the boundary layer transitions from laminar to, laminar with a separation bubble and turbulent reattachment, to turbulent separation which migrates upstream on the chord to stall. The effect of freestream turbulence is similar to an increase of the Reynolds number leading to the term 'effective Reynolds number' [93], laminar separation bubbles shorten and move upstream on the chord [95] leading to a longer chordwise turbulent boundary layer, high $(> 10\%)$ freestream turbulence intensities will result in a turbulent boundary layer forming at the leading edge of the wing [96, 97]. The advantage of a turbulent boundary layer is that it is less susceptible to separation when subjected to an adverse pressure gradient, so the incidence at which stall occurs increases (by $5^{\circ}$ to $10^{\circ}$ [97]). The increased incidence before stall leads to reduced suction pressure on the suction surface [96] which serves to increase lift (20% to 60% [97]). With increased lift the sudden stall as shown in figure 1.28 becomes less abrupt and region 2 blends into region 3 at high turbulence intensities. Increased turbulence intensity does not have the same effect on lift generated by all geometries, Devinant, Laverne & Hureau [96] saw a decrease in lift between $TI_X = 9.7\%$ to $13\%$, though stall incidence was still retarded. Swalwell [97] saw more lift generated at high turbulence for a symmetric aerofoil (NACA0012, 160% $C_L$) than a cambered one (NACA4412, 120% $C_L$).

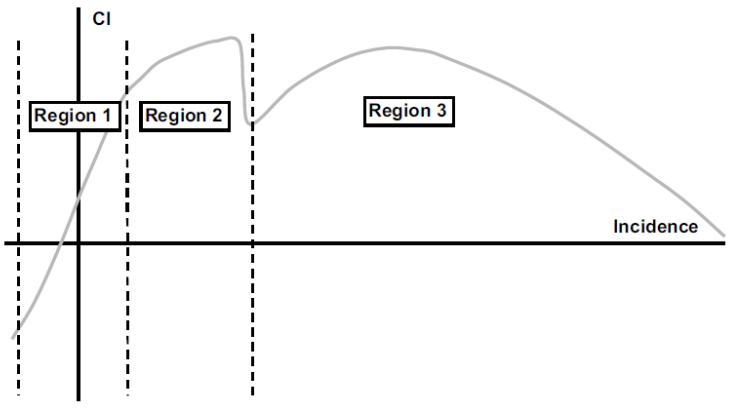


**Figure 1.28:** Typical incidence vs $C_L$ for turbine aerofoil, from Devinant, Laverne & Hureau [96].

In ground effect Wilson, Dominy & Straker [7] found that the effect of freestream turbulence was an increase of downforce generated compared to a wing in freestream; with the stall angle increasing owing to the turbulent boundary layer remaining attached to greater angles-of-attack. This could be Reynolds number related as Devinant, Laverne & Hureau [96] suggest the effect of freestream turbulence will be smaller at high Reynolds numbers, as the Reynolds number effect on force production becomes less critical

in a fully turbulent regime. The freestream turbulence generated of $TI_X = 8\%$ is significantly lower than the turbulence in the Formula 1 car wake, which from the above literature one would assume would increase downforce, so there may be multiple and conflicting effects in the Formula 1 wake.

The effect of freestream turbulence on aerodynamic drag is less dramatic than the effect on lift [96, 97]. Drag increases incrementally with turbulence intensity, and the jump in drag at the first stall becomes less abrupt, as does the decrease of lift. While the turbulent boundary layer separates less easily, skin friction owing to the turbulence will increase. This is the opposite effect to increased Reynolds number, where skin friction coefficient would decrease with increasing Reynolds number, and Bearman & Morel [93] and Newnham [98] suggest this is enough for the 'effective increase of Reynolds number' to be insufficient to describe the result of freestream turbulence. On top of increased skin friction the separated shear layer is more susceptible to unsteadiness as it transitions to turbulence earlier [93, 98] further increasing the wake drag. The effect of increased freestream turbulence on aerodynamic drag of bluff bodies is also not predictable, in some cases increasing and some decreasing.

In table 1.4 the intensities generated in a selection of the papers reviewed is collated. The maximum intensity found is only 16% which is less than half of the peak intensity found in a Formula 1 wake. It is clear another method of generating freestream turbulence would be required to simulate the turbulence in a Formula 1 car wake, which is only one constituent of the wake.

**Table 1.4:** Summary of turbulence intensities generated by passive grids, from literature in this review.

| Mesh Size (mm) | Bar Size (mm) | $TI_X$ (%) | Distance from Grid to Measurement Plane (mm) | Reference |
|---|---|---|---|---|
| 38.1<br>76.2<br>152.2<br>228.3 | 9.8<br>12.8<br>31.1<br>37.7 | 2.09<br>2.83<br>5.71<br>6.4 | 2682<br>2675<br>2679<br>2671 | Bearman & Morel [93] |
| $137.5 \times 141.6$ | 43.0 | 13<br>8<br>7 | 774.0<br>1048.0<br>1544.6 | Wilson, Dominy & Straker [7] |
| 0.7<br><br>0.3<br><br>0.09 | 0.3<br><br>0.1<br><br>0.04 | $< 3$<br><br>$< 7$<br><br>$< 13$ | 3550<br>4600<br>5600<br>7200<br>9600 | Swalwell [97] |
| 100<br>280<br>360 | 25<br>70<br>120 | 4.1<br>9.7<br>16 | 1900 | Devinant, Laverne & Hureau [96] |

#### 1.2.4.2 Active Turbulence Generation Systems

Active methods of generating turbulence, or turbulence generation systems (TGS), are used in the Durham University [99, 100], FKFS [101] and Pininfarina [102, 103, 104] wind tunnels. These systems consist of a number of vertical foils situated immediately after the contraction at the inlet to yaw the jet, figure 1.29, both statically and via numerically controlled time dependant oscillations to generate turbulence.

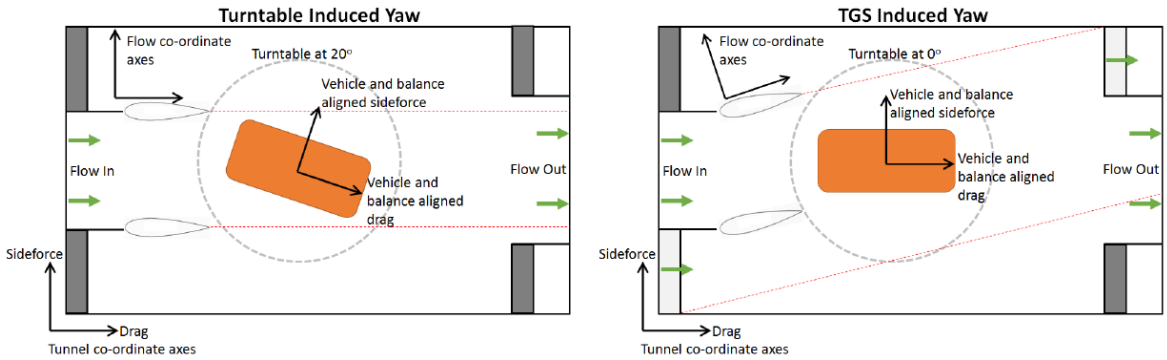


**Figure 1.29:** Inlet TGS crosswinds compared to urntable model yaw, from Mankowski [99]

In reality the 'turbulence generation system' is terminologically inexact, as the systems are primarily used to reproduce the cross-winds naturally found in on-road conditions [105, 106]. A lot of effort in automotive wind tunnels is spent minimizing the freestream turbulence intensity and creating flow uniformity in the jet, while this increases the repeatability of results, drag measurements can be different to on-road data. In the automotive sector there is a drive for improving drag predictions to improve accuracy of fuel consumption and emission predictions. The TGS allows realistic cross-winds to be generated in a reproducible manner to simulate on-road conditions. Matching the probability density function of the cross-wind angle, as well as the power spectrum of turbulent length scales.

Another method of generating cross-winds in wind tunnels has been tested by Docton [107], where a second jet was introduced along the side of the wind tunnel working section. While this generates suitable cross-winds and gusts it requires space along the working section to introduce the second jet, and is only applicable to open jet wind tunnels.

While these systems are beneficial in creating realistic conditions for road vehicles, like passive freestream turbulence generation by grids, they cannot generate sufficiently high turbulence intensities to simulate the peak $TI_X = 45\%$ found in the wake of Formula 1 cars, or even the $TI_X \approx 40\%$ found over much of the base [7]. The flapping of the inlet foils also generates $TI_Y$ at a similar intensity to the axial component ($TI_X$).

Generation of cross-winds has also been preformed in 2 and 3-dimensional CFD simulations [108, 109, 110, 111]. The requirement for this is a transient solver to compute the time-varying boundary conditions. While these studies used flow fields generated to match realistic on-road length scales and intensities, $TI_X, TI_Y, TI_Z$, there is no limit to the turbulence which can be created in CFD, though boundary layer prediction models may not accurately predict the effect of onset turbulence.

### 1.2.5 History of F1 Regulations Designed to Aid Overtaking

Throughout the history of Formula 1, revisions to the technical regulations have been used to reduce cornering speeds as a means of improving safety. However, the 2009 regulations [2] were specifically drafted with the intention of improving overtaking frequency. The FIA set out to reduce turbulence in the wake by reducing total vehicle downforce by as much as $50\%$ [3]. Downforce reductions were achieved by reducing the rear diffuser length and height, while the rear wing span was reduced from $1000mm$ to $750mm$ and the rear wing was disconnected from the diffuser by increasing its height above the reference plane from $750mm$ to $950mm$. In the central $500mm$ span of the front wing a 'downforce neutral' aerofoil was specified to minimize the effect of the centreline surface pressure loss experienced by the following car. While the higher frequency fluctuations of the velocity deficit were reduced by removing upper body elements, primarily used by teams to improve aerodynamic consistency, especially at yaw [18] (figure 1.30). The rule changes did not necessarily achieve the increase of overtaking frequency that was desired.

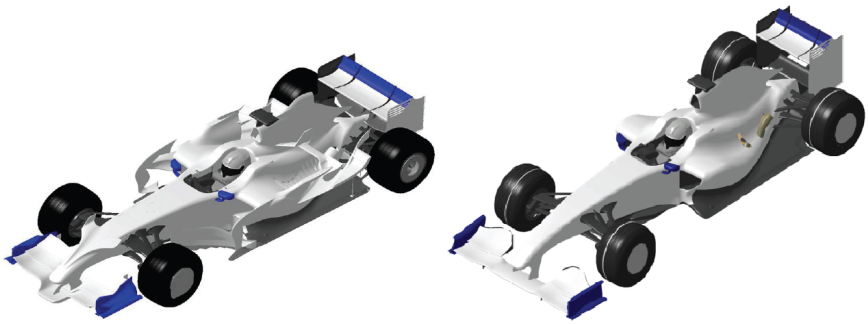

**Figure 1.30:** Comparison of 2008 and 2009 regulations, from Larsson [3].

A CFD investigation of the then proposed 2009 regulations by Perry & Marshall [92], compared to the 2008 rules, showed that only a $35\%$ reduction of total downforce was achieved. Contrary to the intent of the regulations, downforce loss for a vehicle following in the wake was also seen to increase for the 2009 style car, from $\Delta C_L = -17.4\%$ at 2.4 car lengths behind the lead car to $\Delta C_L = -25.7\%$. The authors [92] postulated that while the overall wake was 'cleaner' for the 2009 design, with reduced velocity deficit, up-wash, and vortex flows; the removal of upper bodywork elements, especially around the rear wheels (pictured in figure 1.30), increased the relative magnitude and impact of the rear wheel wakes on the front wing and underbody of the downstream vehicle. The increase of the velocity deficit near the ground more than doubled the downforce loss experienced by the trailing car's front wing and underbody.

### 1.2.6 Summary of Literature Review

In this literature review the sub-systems through which Formula 1 cars generate their downforce have been investigated, namely inverted wings, both in and out of ground-effect, and flat underbodies with up-swept

rear diffusers. Formula 1 cars also generate high levels of drag due to the exposed wheels, and the wakes of rotating wheels have also been reviewed. As a general rule publications regarding these sub-systems are considered in isolation, with little consideration given to the interactions between the sub-systems, which are important along the entire car, especially in the region of the rear diffuser, rear wing and wheels. The exception to this is the effect of interactions from the front wing span and endplate vortex system and the front wheels.

In practice no vehicle or generic geometries used in academic institutions will recreate the high peak loadings present on the wings and underbody of a modern Formula 1 car. Nor will the vortex systems be suitably developed to aid downforce production, shown in figure 1.31 where bargeboard vortices run along the underbody to assist flow attachment in the large adverse pressure gradient of the rear diffuser. Turbulence levels in the wake will therefore be lower than produced for a real car, though they still exceed 40% in the wake of generic vehicles.

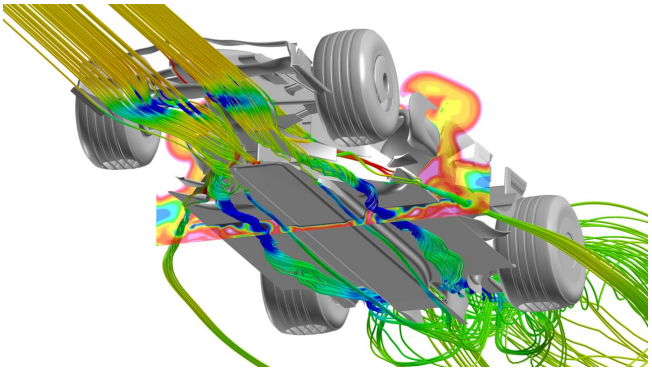

**Figure 1.31:** Complex underbody vortex systems, Renault R28 2008 Formula 1 car, from CD Adapco [112].

The effect of an upstream vehicle wake on a following car has been investigated, though very few publications present a complete upstream vehicle, in most cases owing to scale restrictions in the length of standard wind tunnels. The use of short axial length bluff bodied wake generators has therefore been preferred to test the effect of upstream wakes on wings operating in ground-effect, the short axial length allowing representative vehicle separations to be achieved. The subsystems of Formula 1 cars are so interconnected that investigating wings in ground-effect is insufficient to identify an upstream wake effect on a following vehicle.

Finally, literature regarding the effect of wake features, namely turbulence, on the forces generated by wings has been reviewed. Passive means of generating turbulence do not create the high levels of turbulence intensity as found in the wake of Formula 1 cars. Active means of generating turbulence can more readily and repeatability recreate turbulent length scales and intensities found in natural on-road conditions. Though freestream turbulence intensities generated are less than $30\%$ of the peak intensity found in the wake of Formula 1 car. Freestream turbulence generation systems will also not generate the non-uniform distribution of turbulence in the wake of a Formula 1 car.

## 1.3 Scope & Objectives

What is conspicuous from the preceding literature review is that there is little data available in the public domain regarding the effect of an upstream wake on the aerodynamic characteristics of a representative open-wheeled race-car (Formula 1/ GP2/ Indy Car/ F3). The primary objective is therefore to characterise the effect of an upstream wake on a downstream vehicle.

Utilizing the respective strengths of wind tunnel and CFD methodologies the objectives for this thesis are as follows:

### Measure Effect of an Upstream Vehicle

- Measure the effect of an upstream wake on a downstream vehicle for a number of downstream locations and vehicle postures.
- Use of bluff bodied wake generator in experimental studies to test the effect of a wake for greater axial length separations than have previously been published.

### Characterize Effect of the Upstream Wake

- Identify key flow features in the wake of a Formula 1 car.
- Analyse the relative effects of the various wake features on a downstream vehicle.
- Investigate methods of reducing the performance drop for a following vehicle, either within contemporary regulations or by suggesting new aerodynamic constraints

A list of publications made throughout the course of this thesis can be found in Appendix A.

# Chapter 2

# Experimental Methodology

## 2.1 Durham University 2m Wind Tunnel

All experimental tests were performed in the Durham University $2m^2$ low speed wind tunnel shown in figure 2.1. The tunnel is an open-return, $^3/_4$ open jet type wind tunnel with a 2:3 aspect ratio jet measuring $2m^2$; more information about the design and characteristics of the tunnel can be found in [113, 114]. The test section is $5.5m$ long and is housed inside a sub-atmospheric plenum chamber (not shown in figure 2.1) driven by a pair of centrifugal fans. The ground boundary layer is removed by suction at the leading knife edge of the test section, with the return ducted to exit under the collector into the diffuser. Total power used is $165kW$. Mean jet turbulence intensity is less than $0.7\%$.

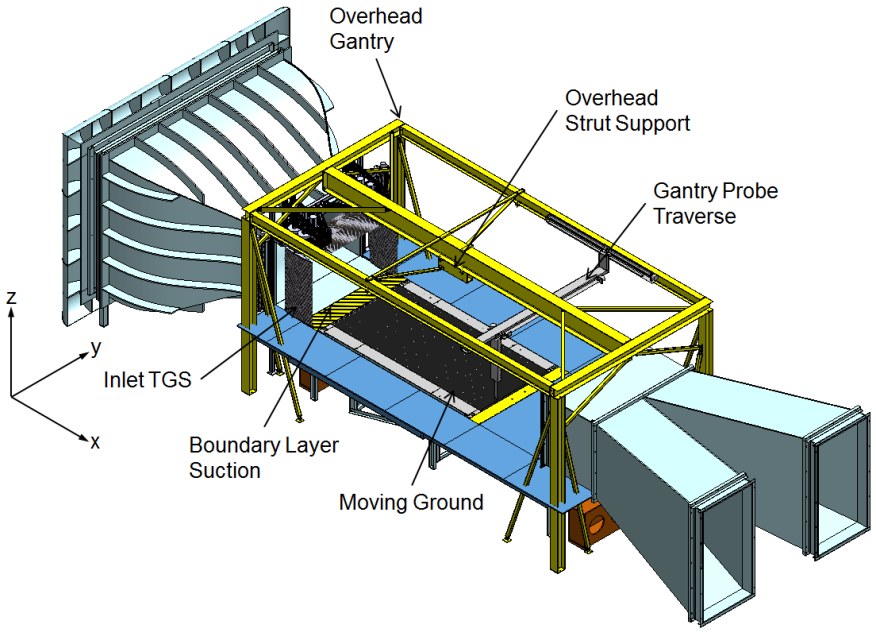


**Figure 2.1:** Durham University 2m low speed wind tunnel (plenum chamber hidden).

The wind tunnel can be operated either in fixed ground, with an underfloor balance and turntable, or with a moving ground plane, figure 2.2. For this study the $3.1m$ long by $1.4m$ wide rolling road was used for ground simulation and to drive wheel rotation up to a velocity of $25ms^{-1}$. The rolling road is prevented from lifting during operation by platen suction using three motors mounted under the aluminium platen. Model support with the rolling road in place is performed by an overhead, 2 degree-of-freedom, numerically controlled strut (figure 2.2), with ride height to an accuracy of $0.01mm$ and model pitch accuracy of $0.05°$.

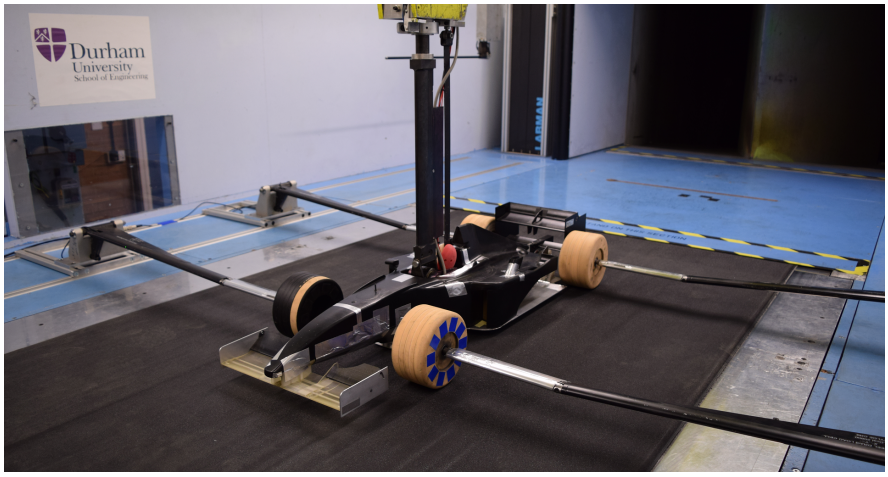


**Figure 2.2:** Internal view of Durham 2m wind tunnel with 25% F1 model installed.

The wind tunnel is also equipped with a 3-axis traverse system, whose primary function is the attainment of wake pressures measurements via a mounted 5 hole probe, though can also be used for other applications, e.g. hot wire measurements.

The tunnel also features a numerically controlled turbulence generation system (TGS) consisting of two vertical and one horizontal foil at the inlet which can be programmed to flap at up to $10Hz$ in or out of phase to create a realistic on-road cross winds or used to yaw the flow between $0°$ to $\pm 7°$ in the test section. For this experimental study the TGS was left in the default position for straight ahead flow, more information about the design and operation of the TGS can be found in [99, 108].

## 2.2 Wind Tunnel Models

### 2.2.1 Generic 25% Formula 1 Car

The model used for this study is a 25% generic formula 1 car, figure 2.3, contemporary to the 2006-2008 FIA technical regulations [25]. Since 2008 there have been multiple changes to the technical regulations, twice in the duration of this research with a further change planned for the 2017 season, though the means of generating downforce remain the front and rear wings and the underbody. It was decided that the best use of time was to evaluate the effect of the wake on these features rather than redesigning the car to match the changing regulations.

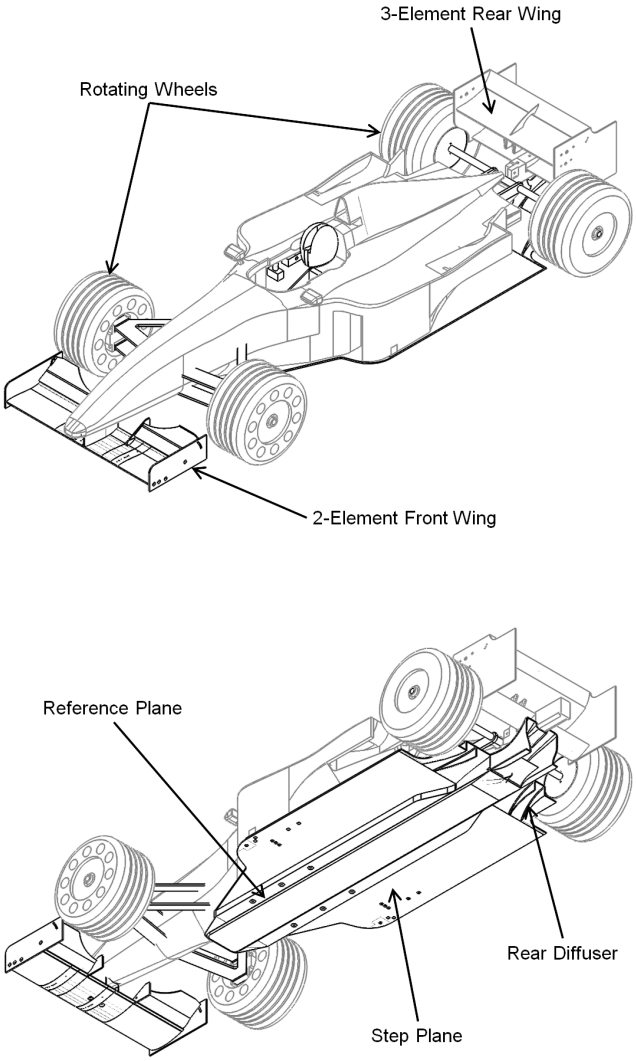


**Figure 2.3:** Generic 25% scale Formula 1 wind tunnel model.

The car features rapid prototyped two-element front wing and rear wings and an aluminium underfloor complete with rapid prototyped up-swept rear diffuser. The span and height above the ground of the front

and rear wings are mandated by regulation. The geometry of the underfloor is also tightly regulated, and features a $12.5mm$ step plane ($50mm$ at full scale) with skid block, used by the FIA to control ride height. There is an upswept rear diffuser starting from the front face of the rear-wheel and ending at the rear axle line, though the centre section continues beyond the rear wheels. The car has a wheelbase, $L_{WB}$, of $785mm$ and is $1200mm$ in length from from front to rear overhangs, $L_C$, key dimensions and their abbreviations as used throughout this thesis are shown in table 2.1.

**Table 2.1:** Key dimensions of generic Formula 1 vehicle.

| Dimension | Abbreviation | Model Scale (mm) | Full Scale (mm) |
|---|---|---|---|
| Car Length | $L_C$ | 1200 | 4800 |
| Wheelbase | $L_{WB}$ | 785 | 3140 |
| Car Width | $W_C$ | 450 | 1800 |
| Car Height | $H_C$ | 237.5 | 950 |
| Frontal Area | $A$ | 93750 $(mm^2)$ | 1.5 $(m^2)$ |
| Front Wing Chord | $c_{FW}$ | 130.7 | 522.6 |
| Front Wing Span | $b_{FW}$ | 350 | 1400 |
| Rear Wing Chord | $c_{RW}$ | 92.4 | 367 |
| Rear Wing Span | $b_{RW}$ | 250 | 1000 |
| Wheel Diameter | $d$ | 165 | 660 |

The rear wing and diffuser geometries were designed during a previous research project investigating the wake of the vehicle. However the front wing was not suitable to collect surface pressure measurements as was desired, and a new wing was designed. In order to fit pressure tappings on the surface, with the tubing routed internally, figure 2.4, a Wortmann FX63-137 aerofoil with chord $80.85mm$ was used for the mainplane. The FX63-137 is $14\%$ thick and optimized for low Reynolds number use ($Re_{FrontWing} = 2.2 \times 10^5$) with relatively high lift, low drag characteristics and though not designed for use in ground-effect was sufficiently thick as to allow 17 pressure tappings to be distributed on the upper and lower surfaces (tapping locations can be found in figure 2.12). To enable manufacture the trailing edge thickness was increased to a constant $1mm$.

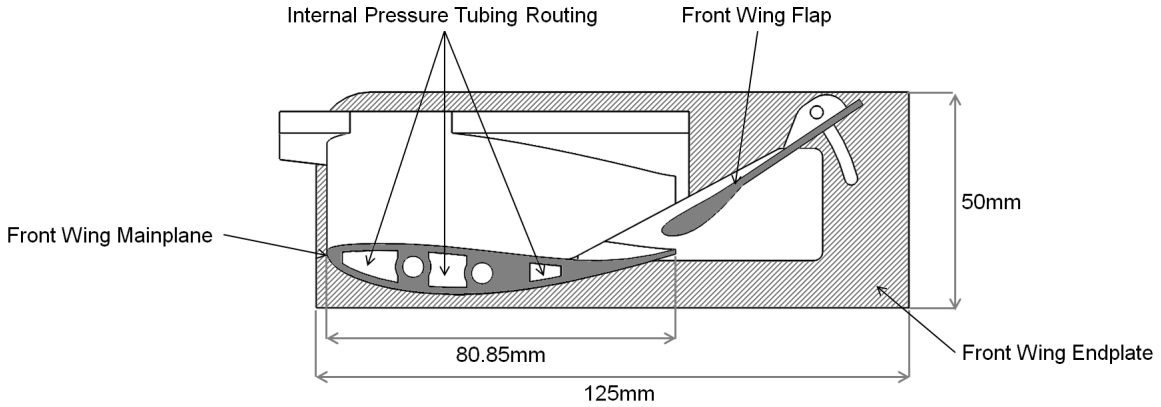


**Figure 2.4:** Section view of 2-element front wing in ground effect.

The scale of the model meant that no pressure tappings could be contained within the flaps. The flaps could be defined as constant thickness plates, however in order to shroud an M3 fastener used to form the pivot for angle adjustments, a Göttingen 702 aerofoil was used. The Göttingen 702 has maximum

thickness near the leading edge so the pivot could be placed close to the front, meaning that the slot gap and flap overlap would vary little with flap incidence. The slot gap was defined in such a way that the space between the flap and mainplane was convex [30], forming a throat at the mainplane trailing edge. With the flap angle ($\alpha$) variable between $9° \leq \alpha \leq 34°$ it proved impossible to maintain a constant slot gap ($\pm 0.15\%$ of $c_{FW}$) and overlap ($\pm 0.2\%$), though the slot remains convex. The flaps are of chord $55mm$ and split such that the rear half was a constant thickness of $1.5mm$. With variable flap angle the front wing chord ($c_{FW}$) varies $128.5mm \leq c_{FW} \leq 132.8mm$, an average of $130.7mm$.

The model is connected to the overhead gantry by a numerically controlled computer strut with 2 degrees-of-freedom, ride height and pitch. The comprehensive 48 point ride height map used for the experimental program is shown in figure 2.5. Minimum ride height ($h_{min}$) is given relative to the lowest point on the car, i.e. the bottom of the skid block, and ranges from $2mm$ to $7mm$ ($8mm$ to $28mm$ full scale) which was deemed a representative range for a variety of car set-ups and on-track conditions. Vehicle pitch was varied between $0°$ to $-1°$ (nose down) so that the height of the reference plane at the position of the front axle is $3.4mm \leq h_{FA} \leq 9.5mm$ from the ground, and at the rear axle position is $4.5mm \leq h_{RA} \leq 19.6mm$, which is in a similar range to that used in the both Toyota [115] and Honda [22] Formula 1 wind tunnels.

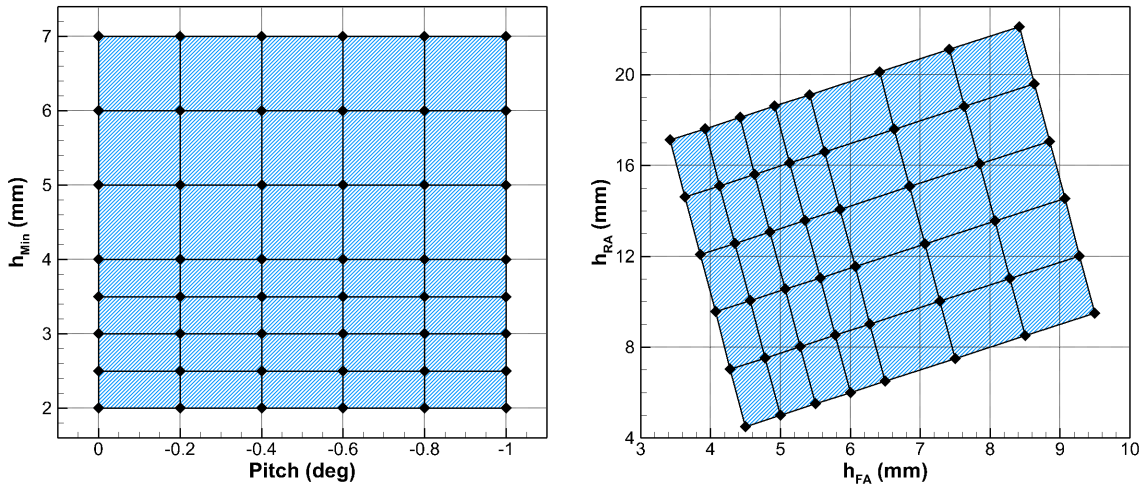


**Figure 2.5:** Car ride-height map.

### 2.2.2 Bluff Bodied Wake Generator

The wake generator used for this study is the fifth generation of bluff bodied wake generator, hereafter referred to as BBWG, designed at Durham University. The previous iterations were designed by Straker [6] and Wilson [7] both 33% scale, Barrett [86] $25\%$ scale, and also McLintock [8] 25% scale but designed based on the post-2009 regulations. A similar wake generator has also been used at Cranfield by Correia [87]. All the BBWG designs feature a short bluff body with a rounded leading edge and the same features as the rear of a Formula 1 car, namely wheels, a wing out of ground effect, and an up-swept planar diffuser.

BBWG have been shown to generate a wake similar to the full car although the reduced length means that the downforce produced is lower than would be the case for the full car. Increasing the axial length the bluff body could more accurately reproduce the wake, but the length of the possible separation between the BBWG and car would be reduced, defeating the purpose of the short body.

There was no wake generator of a suitable scale or length available so a new BBWG was manufactured based on the previous designs. The wake generator was made as short as reasonable, $0.2L_C$, meaning the maximum possible separation to the 25% Formula 1 car was $1L_C$. Unlike previous BBWG which were manufactured from foam the new design featured an aluminium spine and trailing arm suspension to better cope with extended use running on a moving belt.

The wake generator was mounted on a single degree of freedom ILA traverse attached to the overhead gantry, figure 2.6. The traverse allows a y-axis offset to be set to an accuracy of $\pm 0.025mm$. The mounting strut was of circular section, so was shrouded with a symmetrical $30\%$ thickness NACA series aerofoil to minimize the disruption to the wake.

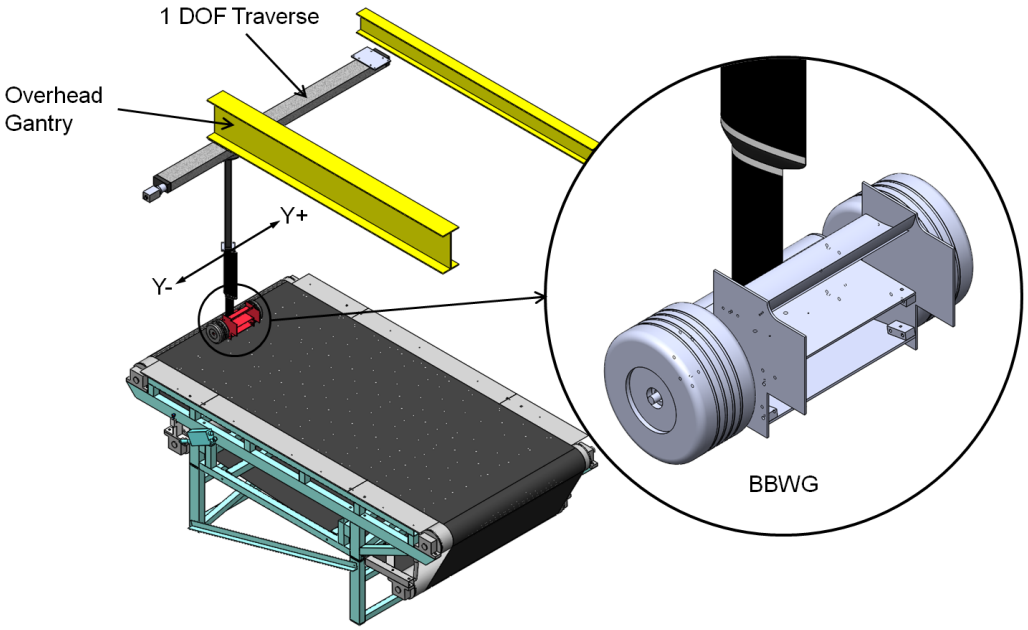


**Figure 2.6:** Setup of bluff bodied wake generator on moving ground.

## 2.3 Instrumentation

### 2.3.1 Force Measurements

#### 2.3.1.1 Vehicle Body Forces

Vehicle force and moment measurements were taken using a bespoke internal 6-component balance, the design of which is detailed in Chapter 3. The balance is rated to $150N$ in the X direction and $600N$ in the Z direction, which can be applied up to $400mm$ from the balance centre. The balance was logged for 32 seconds, the length of averaging gave a $95\%$ confidence interval of $\pm 0.0015$ on $C_D$ and $\pm 0.006$ on $C_L$, figure 2.7. Where the confidence interval was calculated based on the normal distribution of a number of samples, logged at $1kHz$ for $4s$ each.

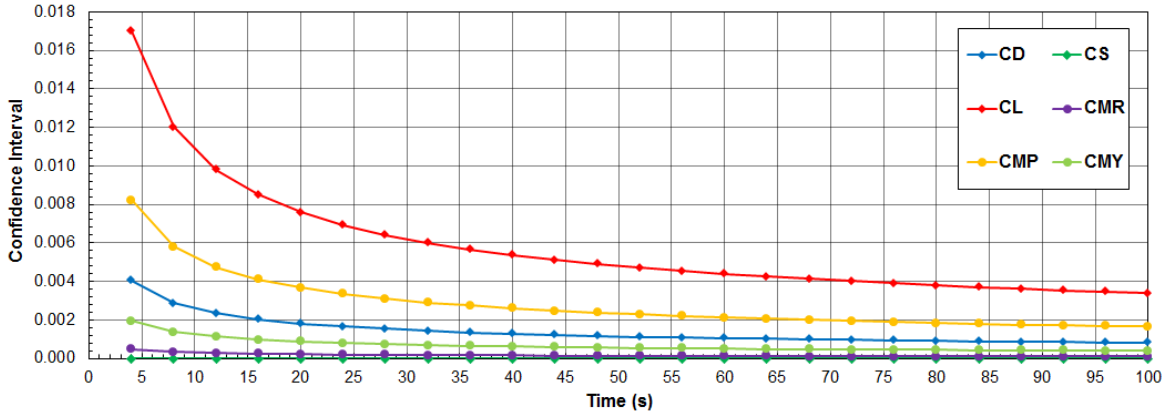


**Figure 2.7:** Effect of average measurement period on $95\%$ confidence interval of balance (B0008).

The balance was situated in the model such that the balance centre was at the same approximate length along the wheelbase as the desired centre of pressure, figure 2.8, this prevented the balance being loaded with a pitching moment in freestream conditions. The standard practice for motorsports applications is that the overhead support exits through the cockpit, and the balance assembly was designed to allow the pivot of the strut to be fully enclosed within the car, minimizing disruption.

#### 2.3.1.2 Wheel Drag Measurements

There are two methods of mounting model wheels in the wind tunnel; (1) 'wheels-on', where the wheels are connected to the body of the car and any drag force is measured by the internal force balance. (2) 'wheels-off', where the wheels are mounted on external stings (figure 2.2) isolating them from the rest of the car's forces. The trend in Formula 1 in the recent past is towards a wheels-on approach, though there are advantages to both solutions. In Formula 1 the change seems to have coincided with the almost

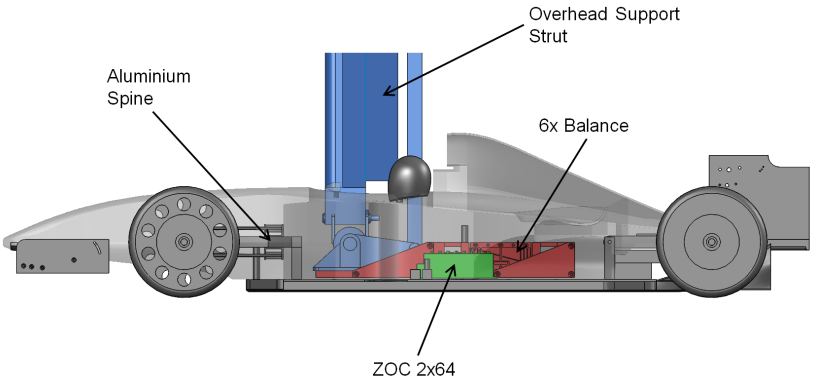


**Figure 2.8:** Representation of internal layout of 25% F1 model.

universal adoption of pneumatic tyres. Pneumatic tyres are used to accurately represent contact patch and centripetal deformation of the tyre, both of which alter the wheel wake and in turn affect flow to downstream components. Imperfections in the wheel and belt surfaces can also cause random vibrations which affect the repeatability of tests, or require long averaging intervals in order to become statistically negligible, pneumatic tyres will slightly damp these vibrations. In Formula 1, with "wind-on" tunnel time becoming so restricted [79], dynamic testing is utilized; i.e. the model forces and pressures are logged continuously over a pre-programmed ride-height, pitch, yaw, and roll sweep. Arguably for Formula 1 teams the absolute aerodynamic accuracy of a test is more important than the repeatability, with academic research more time can be committed to a study and repeatability and validation of results become more important; "*we found over time that the absolute accuracy of having wheels mounted on the model outweighs the slight measurement or repeatability problem you have*" Toet [116]. The effect of wheel stings on isolated wheels was tested in CFD by Knowles [66] showing the location of the wheel vortices, especially the upper counter-rotating pair, was altered by the presence of the sting. Mean velocity and turbulence intensity profiles were also affected by the sting. Wheel drag was found to increase by $1.3\%$ in the presence of the sting, and mass flow rate through the wheel hub increased by $58\%$. The effect of different sting designs was also tested experimentally, showing that different configurations of sting will also affect vortex location and strength. The magnitude of reversed flows in the wheel wake was also affected by sting design.

Experiments have also been performed at Durham University by Hetherington [74] to quantify the effect of struts and wheel stings on automotive models, of particular interest to this study is the open wheel race car tested. Forces on the vehicle were measured by an underfloor balance with dummy struts and stings placed in the working section. With the overhead strut, vehicle drag was found to decrease by 1%, while wheel stings increased vehicle drag by $0.1\%$; strut and stings combined resulted in a $0.8\%$ decrease in the vehicle drag. Downforce was more significantly affected by the strut and stings, with a $5\%$ loss of downforce, coupled with a $6\%$ shift of the centre of pressure (COP).

Considering model scale and the solid construction of the wheels, with no flow through the hub, it was

decided that the wheels-off approach was an acceptable compromise to improve accuracy and confidence in results.

To complete the experimental tests new flexible wheel stings were designed to accommodate the different models tested in the Durham University 2m wind tunnel, figure 2.9. The stings feature a pair of pivots allowing the height of the axle centre to be adjusted, and also allowing cambered wheels to be accommodated, wheel cambers in excess of $-3°$ are not uncommon in motorsport. To minimize the sting wake disrupting wheel wakes the chord is kept to $50mm$ using a $30\%$ thick NACA 4-digit symmetrical aerofoil. The $30\%$ thickness allows load cells to recess into the aerofoil profile with covers to further reduce flow disruption.

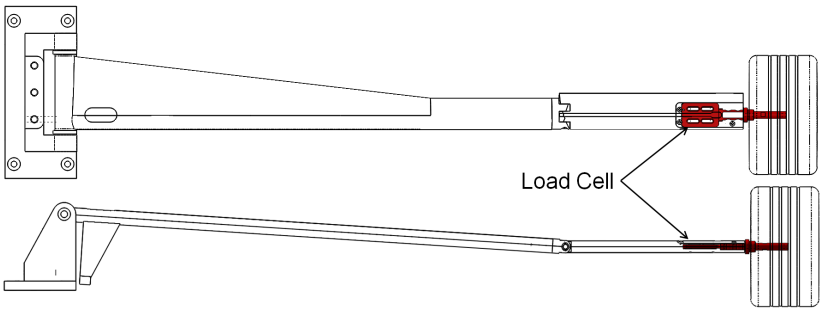


**Figure 2.9:** New Durham University wheel sting with 25% Formula 1 wheel.

Wheel drag measurements were collected using $4 \times 70N$ load cells (figure 2.10) shrouded by the wheel stings. Wheels are named using the tunnel co-ordinate system so the driver reference front left $= X-Y-$, front right $= X-Y+$, rear left $= X+Y-$, and the rear right $= X+Y+$. The $Y-$ load cells were connected to a pair of Fylde FE-579 transducer amplifiers while the $Y+$ were connected to a generic transducer amplifier constructed of RS 308-815 strain gauge amplifiers mounted in RS 435-692 PCBs. Calibration was performed by hanging masses from zero load up to $3kg$, then decreasing the load back to zero to confirm the absence of hysteresis and zero shift. Once performed for each load cell and amplifier combination a linear calibration was generated from the force-voltage slope for each corner. Wheel drag tare measurements were performed wind-off with the rolling road at $1ms^{-1}$. The same $32s$ averaging interval used for the internal force balance and repeatability for all corners is below $\pm 0.002$ on $C_D$.

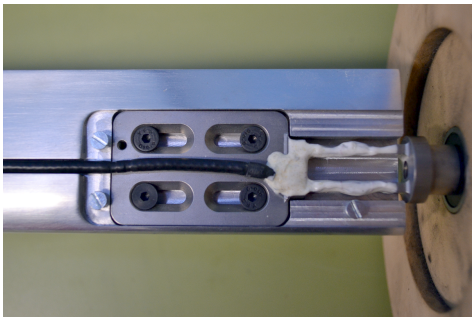

**Figure 2.10:** Benetton F1 70N wheel load cell.

### 2.3.2 Surface Pressure Measurement

Surface pressures were collected using a Scannivalve ZOC $64 \times 2$ electronically scanned pressure transducer bank. The scanner logs each bank of 64 ports simultaneously making it easy to collect large datasets relatively quickly, overall 119 pressure tappings were distributed in the front wing, upper body, underfloor, and diffuser. The Cartesian aligned co-ordinate of each tapping can be found in Appendix B. It was assumed that the time averaged surface pressures are symmetric about the the centreline so to improve measurement resolution the tappings were only present on the $Y-$ side of the car, figure 2.11, and could be mirrored in post-processing. Each bank of the scanner was logged at 100Hz for 3200 samples to average measurements for 32 seconds, the same interval as the force measurements.

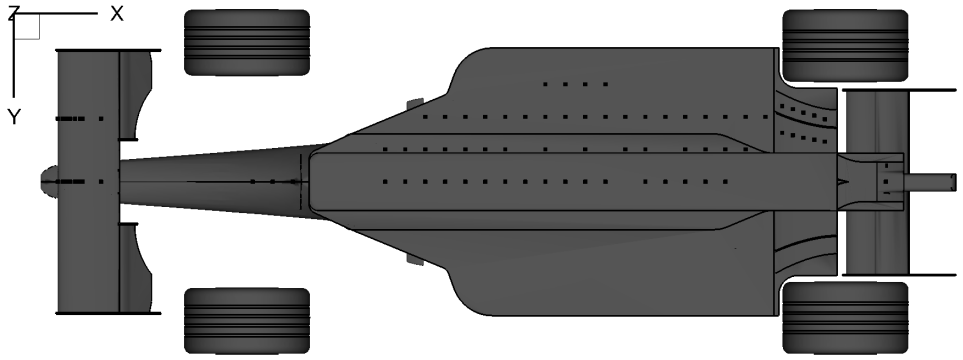


**Figure 2.11:** Underbody surface pressure tapping distribution.

The front wing contains a total of 34 pressure tappings split between the centreline and quarter-span. The tappings are evenly distributed with a leading edge tapping and 8 tappings each on the upper and lower surface of the mainplane, figure 2.12. The scale of the model meant that the thinness of the trailing edge prevented any tappings being present aft of 70% of the mainplane chord, and no tappings were present either on the flap or near the flap slot-gap.

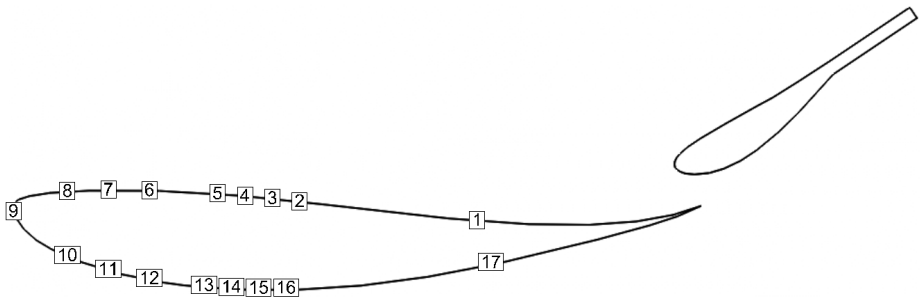


**Figure 2.12:** Front wing pressure tapping locations (shown for front wing quarter-span).

To prevent any pressure tubing passing into the airflow, which could potentially disrupt flow to key areas, the tubing for each tapped section in the front wing is fed through hollow sections of wing into one of the oversized front wing pylons, figure 2.13a, and through the nose of the car to the pressure scanner. The

rest of the tubing, with the exception of the diffuser shown in figure 2.13b, is contained within the body of the car. The tubing was then bound to prevent any movement changing the flow characteristics through the body of the car affecting the 'cooling' drag.

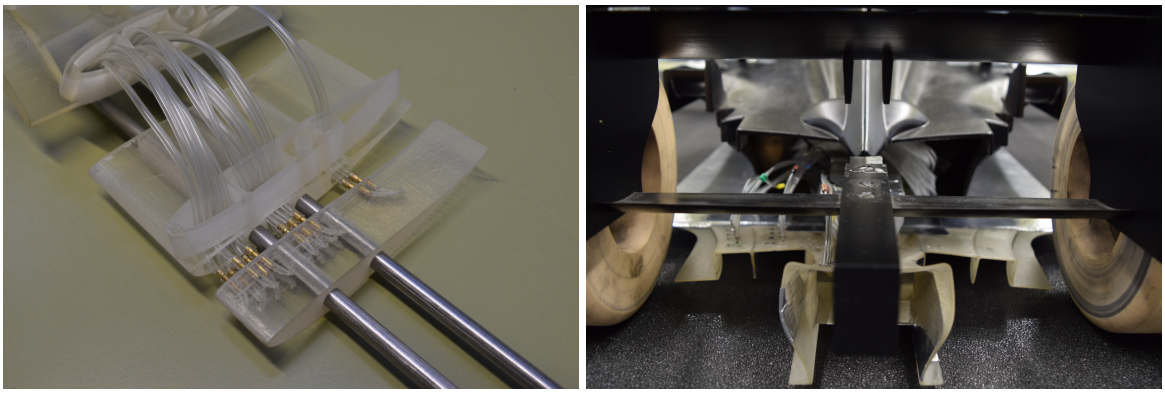

**(a)** Front wing. **(b)** Rear diffuser.

**Figure 2.13:** Internal pressure tubing routes.

The underbody features the greatest density of tappings, figure 2.11, with 54 tappings split between 4 rows; allowing contours to be drawn of the surface pressure. The floor features a step and a skid plank, as per the regulations, so the lowest tappings are on the centreline, with subsequent rows $2.5mm$ and $15mm$ further from the ground respectively. Unfortunately the geometry of the upper body is such that the furthest forward tapping is $\approx 100mm$ aft of the leading edge of the underfloor. Upstream of the underfloor there are 4 tappings on the keel, which plays a role in diverting air flow from under the nose to the underfloor. The rear diffuser is also well represented, figure 2.13b, with 5 tappings on each of the 2 outer channels and a further 6 in the centre-channel. The upper body shell is also represented with tappings present on the nose centreline, between the tip and the cockpit. There are a final 5 tappings on the upper surface of the sidepod, running parallel to the cockpit opening.

### 2.3.3 Wake Probe Measurements

Wake measurements were made with the use of a 5-hole probe, shown in figure 2.14, the position of which is numerically controlled with the 3-axis gantry traverse (figure 2.1). The 5-hole probe is commonly used in wind tunnel testing for the high accuracy, versatility and robustness of measurements. The tip features a hole at the centre with four holes around the tip sloping away at $45^\circ$ to measure flow yaw and pitch. Pressure and velocity vector measurements are determined from a calibration map, which was generated for angles up to $\pm 50^\circ$.

The wake was mapped with $4\times$ YZ planes at $0.1L_C$, $0.25L_C$, $0.5L_C$, and $0.75L_C$ downstream of the car, figure 2.15; these 2-D planes were also combined and used to generate 3-D ISO surfaces of the wake to compare to CFD. Other planes collected were XZ aligned on the centreline and behind the rear wheel, and

**Figure 2.14:** 5-hole probe.

a XY plane on the vehicle waistline. The 5-hole probe can be used to collect transient data, though in this case the steady-state wake was collected, each point was logged for a period of 4 seconds at 1kHz which was enough to remove unsteady effects. It was assumed that the time averaged wake is symmetric about the centreline so only half the wake was recorded to increase measurement resolution. The YZ planes have a grid resolution of $15 \times 15mm$ while the XY and XZ planes are doubled in the x direction to $30 \times 15mm$.

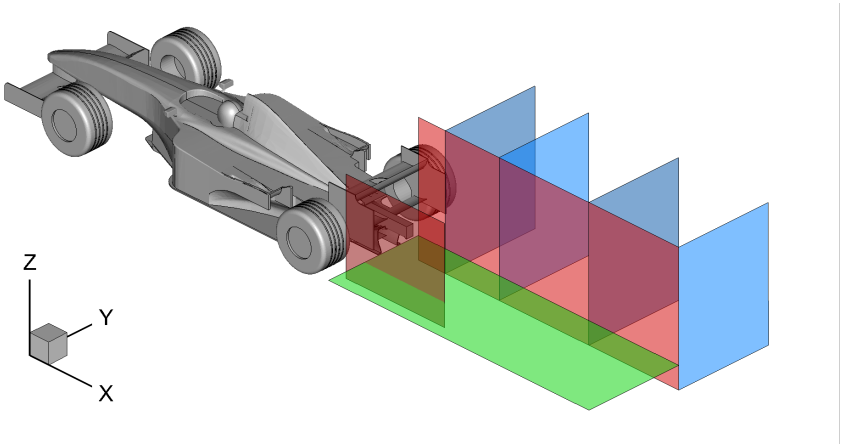


**Figure 2.15:** Wake probe measurement planes.

Sterken et al [117] showed that the probe traverse unit in a wind tunnel can have a not insignificant effect on the flow field behind a SUV. The authors found that vehicle forces with the probe in the wake flow field could change by as much as $\Delta C_D = 0.015$ and $\Delta C_L = -0.026$ depending on probe location as well as slightly altering the base pressure of the vehicle. This could be argued to result in a reduction in the accuracy of any wake measurements as the probe itself alters the wake. The probe traverse system in the Volvo Cars Aerodynamic Wind Tunnel is arguably more intrusive than the system in the Durham University 2m Tunnel, however for interest the force balance was also logged during wake measurements. Due to the reduced averaging period compared to force measurements, with the probe in the parked position, the force repeatability is reduced to $\pm 0.017 C_L$ $(1.4\%\ C_{LTotal})$ and $\pm 0.004 C_D$ $(1.1\%\ C_{DTotal})$. The probe does appear to decrease downforce in the near wake close to the centreline, albeit only by the 95% confidence interval, figure 2.16a. Downforce is slightly increased on the centreline with the probe above rear wing height, but again the reduced averaging could lead to aerodynamic unsteadiness corrupting the results. The effect of the probe on vehicle drag on both centreline and waistline is limited to noise in the order

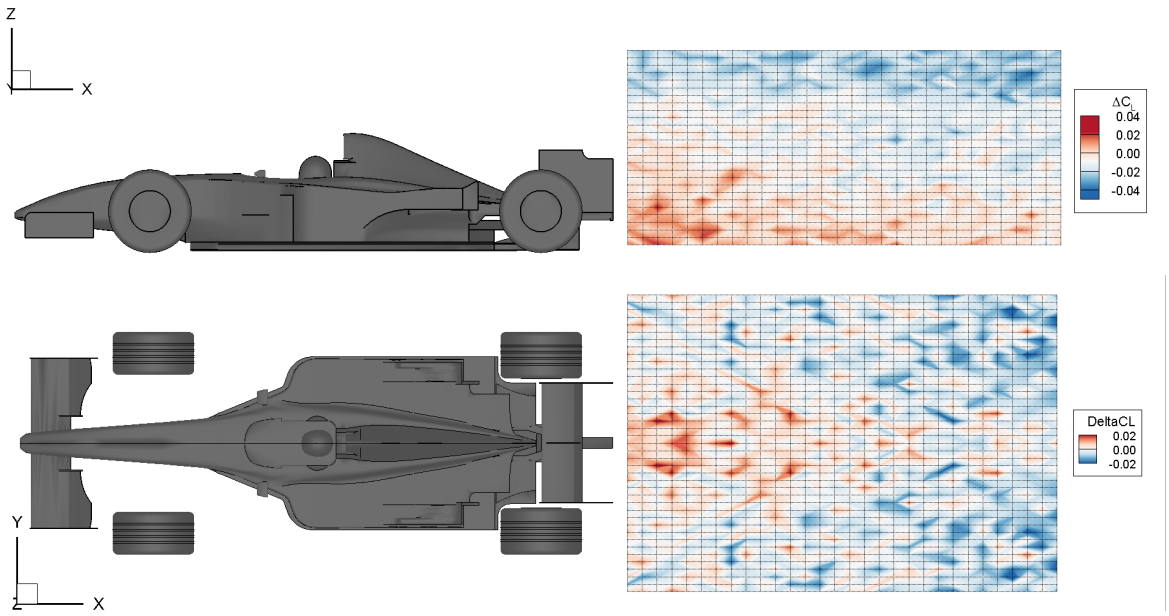


**Figure 2.16:** Effect of probe traverse on force measurements.

of the measurement repeatability. While the probe traverse does appear to affect force results it is only in the order of magnitude of the repeatability of the balance, considering the short logging period, so no definitive conclusions can be drawn as to whether the wake is significantly affected.

# Chapter 3

# Design of a Compact 6-Component Internal Balance

The following chapter details the design and manufacture of new internal 6-component force balance, shown in figure 3.1. The available volume inside the $25\%$ scale Formula 1 car is also limited, so the balance is required to have the smallest possible dimensions while still maintaining a relatively high rating necessary for measuring the high forces expected with a high performance race-car. The Durham University 2m Wind Tunnel was already equipped with a number of internal balances of different sizes and ratings. In creating a new compact balance it was desired that this would be suitable for both smaller scale vehicle models and aircraft models.

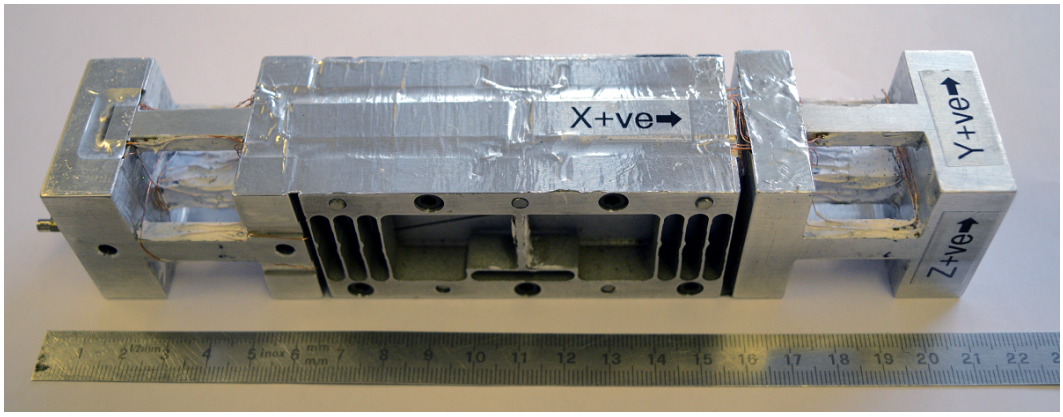


**Figure 3.1:** Compact 6-component internal wind tunnel balance.

## 3.1 Review of Literature Relevant to Balance Design

The intricacies of wind tunnel balance design are commercially sensitive and consequently not in the public domain, with individual companies having their own designs and preferences, and few available papers describing the minutiae of individual designs. There is however a reasonable volume of papers and documentation describing the general science of balance design, with the final details of the element dimensions left to the authors knowledge of bending beam theory and an iterative design process using FEA (Finite Element Analysis) software. The following review is related only to the literature associated with the sting mounted integral type internal strain gauge balance.

The simplest design for a two component, force and moment balance would be a single cantilever beam [118] clamped at one end and fixed to the model at the other, with strain gauges top and bottom at either extremity. Using a single Wheatstone bridge both force and moment can be independently determined from the difference in stress at either end of the cantilever. A longer cantilever will increase strain and thus increase force sensitivity, though as stress increases the peak load which can be carried by the load cell, before exceeding yield stress, decreases.

The perpendicular force can be measured by mirroring this set-up onto the sides of the beam, making a very simple four component balance. Assuming a square section the normal and transverse rated load and sensitivities will be the identical, however in motorsports, it is common for downforce to exceed side-force, so the vertical dimension of the beam can be increased; increasing peak measurable load at the expense of sensitivity. It is not essential that the cantilever be of rectangular section, Parker and De Loach [119] performed a FEA optimization on a number of elliptical sections, approximated by octagons for ease of manufacture.

Rolling moment causes a twisting of the cantilever which could be measured using a strain gauge rosette angled at $45^{\circ}$ to the moment axis, however the preference is for the strain gauges to be axially aligned. A higher sensitivity to roll can be achieved if the cantilever is split into one or two pairs of elastic elements, figure 3.2, situated away from the moment centre. Rolling moment will cause an S-shaped twisting of the beams, so with the strain gauges placed at the roots of the beams, the signal either side of the elastic elements will be equal in magnitude but opposite in sign. Moving the moment measurement away from the balance centre has the benefit of increasing stiffness and therefore reducing movement of the attached model, especially in pitch, while also allowing for vertical shearing to measure lift.

The final component to be measured is the axial force. Axial force, or drag, would result in a longitudinal stress on the beam, beam theory indicates that this stress on an axially aligned beam will be significantly lower than normal forces and moments. The universally adopted [120, 118, 121] method involves splitting

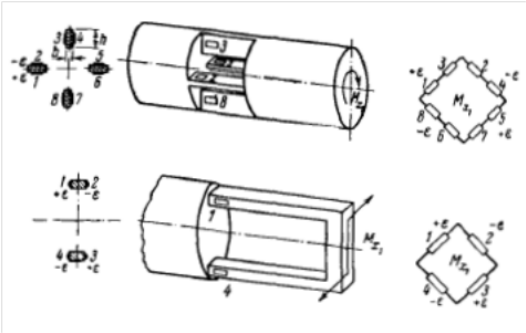

**Figure 3.2:** Multiple beam cage strain gauge placement, from Gorlin & Slezinger [120].

the balance into live (model mounted) and earthed (strut mounted) halves. The two halves are then linked by a number of thin flexures which are compliant axially, resulting in an elastic parallelogram, but stiff vertically to carry the lift and pitching moments. The webs must also have second moment of area suitably great that the balance is stiff when loaded in by normal and transverse forces. Drag is then measured by a final linking element situated at the balance centre, seen in figure 3.3. The two halves of the balance are typically split by an inclined cut which serves to increase the stiffness of the balance, but allows the elastic parallelogram to operate without interference.

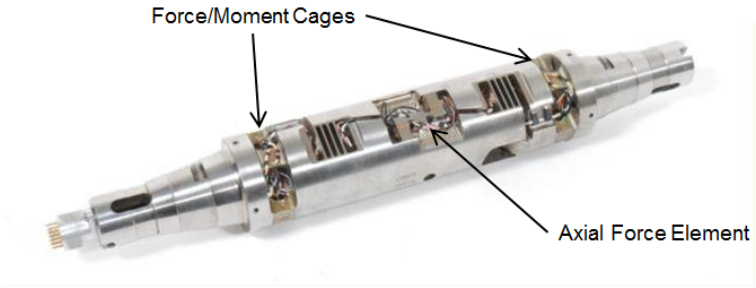


**Figure 3.3:** ARA wind tunnel balance with five-beam cages and axial force flexures, from ARA website [122].

The final step of the balance design is to combine all the different elastic elements described in this section into a single design. If the elements were combined modularly so that each component has its own elastic element there is a danger of the balance becoming very long so some compromises are made to keep the balance as compact as is reasonably possible. The ARA and Onera [120] designs use two cages similar to the elastic pairs shown in figure 3.2 topping and tailing an elastic parallelogram for longitudinal loads. Gorlin and Slezinger [120] describe how the use of five beams allows for the simultaneous measurement of forces and moments in the two perpendicular planes, with forces measured on a central beam and moments on the four outer beams. By moving the moment measurement away from the neutral axis the balance becomes stiff in bending, small section links means the beam pairs form elastic parallelograms which allows the central force link to carry peak load under a normal force. Finally the drag parallelogram is kept suitably long so that the two five-beam cages are separated by enough material so that the whole balance behaves as the cantilever described earlier.

There are alternatives to the five-beam cage design [119, 123] which use EDM (Electrical Discharge Machining) to machine complex shapes which are suitably stiff to withstand a variety of rated loads this method requires different cage designs to be optimized for individual load cases so is not universal in its application.

The selection of material is simply a balancing act between the mechanical properties, i.e. ductility, elastic strength, and fatigue life, and the environmental considerations of the wind tunnel, i.e. temperature variations. The material is selected at the outset of the design process [123] using a basic diameter and load calculations combined with past experience to determine the desirable material properties, i.e. a high ratio of yield strength to Young's modulus. The materials used by NASA [123], Onera [124] and VFW-Fokker [125] are shown in table 3.1, whereby the mechanical properties have been selected for either high load or cryogenic applications. For the more general use in wind tunnels either stainless steel or aluminium alloy is preferred for availability and machinability with the specific alloy selected by estimating the required mechanical properties to withstand the rated loading requirements.

**Table 3.1:** Summary of materials used in industrial balances from literature.

| Material | Alloy | Application | Reference |
|---|---|---|---|
| Stainless Steel | 15-5PH | General | Rhew [123] |
| | 17-7PH | General | NASA |
| Steel | C-200 18% Ni H900 | Cryogenic | NASA |
| | C-300 18% Ni H900 | High Capacity | NASA |
| | 45 SCD6 | General | Dubois [124] |
| | Air Hardened High alloy Martensite | General | Ewald [125] |
| Aluminium | 2024-T6 | General | NASA |
| | 7075-T6 | General | NASA |
| Copper Beryllium | 2% Be | Extreme Temperature | NASA/Onera |

## 3.2 Design of 6-Component Balance

Being a multi-purpose balance the design, with regard to size and mechanical properties, is in some small ways compromised for each use of the balance. The primary function of this balance is to measure the forces and moments acting on a $25\%$ scale Formula 1 car for use in the Durham University 2m wind tunnel, which runs at a maximum wind velocity of $30ms^{-1}$. As such the mechanical specifications are limited by the relatively low lift to drag ratio of an open-wheeled race car. However for the external dimensions the limiting factor is most likely to be the cylindrical shape of an aircraft fuselage, which requires a thin but long shape to fit within the model. The assumed minimum fuselage diameter for an aircraft with similar maximum lift force to a Formula 1 car is $70mm$, so to account for wall thickness the balance is designed to fit within a $50mm$ diameter cylinder. It was decided that a square cross-section would be both easier to manufacture than a circular or elliptical cross-section, and easier fit to a model so that both the wind tunnel

and model axes (at zero yaw) can be aligned. The chosen concept was similar to the Aircraft Research Association (ARA) design, shown in figure 3.3, the balance is split into two halves each with a '5-beam cage' of elastic elements.

Assuming a maximum downforce coefficient for a Formula type car, $C_L \approx -3.5$ and drag coefficient $C_D \approx 1$ at $30ms^{-1}$ the design loads of the balance, assuming a frontal area up to $2m^2$, full scale, and a safety factor of two, are as found in table 3.2. The approximate downforce centre of pressure of a Formula 1 car is between $60\%$ and $70\%$ along the wheelbase [11], however to generate a suitable safety factor for the pitching moment it was assumed that $100\%$ of the rated lift could occur up to the length of the wheelbase from the balance centre, $< 0.8m$ from the balance centre. A sensitivity of at least $0.001$ of rated load is desired.

**Table 3.2:** Design loads for 6-component balance.

| Drag (N) | Side (N) | Lift (N) | Roll (Nm) | Pitch (Nm) | Yaw (Nm) |
|---|---|---|---|---|---|
| 150 | 300 | 600 | 80 | 240 | 120 |

The central link in the 5-beam cage measures force in both the normal and transverse directions, while moments are attained using the outer links. There is a final element in the centre of the balance, oriented perpendicular to he plane of the 5-beam cages, for the measurement of drag force. Figure 3.4 shows the theoretical effect of altering the dimension of the elastic links in the 5-beam cages on both the load and the proportion of load carried by the centre link when loaded in the normal direction. Where the percentage of load is equal to the second moment of area of the centre link divided by the total 5-beam cage second moment of area, where the total second moment of area is the sum of the second moments of area of the centre and outer links,

$$\%Load = \frac{I_{Centre}}{I_{Total}} \times 100, \tag{3.1}$$

where,

$$I_{Total} = \left(\frac{B \times D^3}{12}\right)_{Centre} + 2 \times \left(\frac{b \times d^3}{12}\right)_{Upper,Lower} + 2 \times \left(\frac{d \times b^3}{12}\right)_{Left,Right} \tag{3.2}$$

and B is the base dimension and D is the depth dimension and B in figure 3.4 is 8mm.

Figure 3.4 is an analysis of load carried by the central link compared to the proportion of stress (with a lift force applied). As the beam increases it carries a greater percentage of the applied load, however, if the central beam is too large, above $\sim 8mm$, the proportion of total stress it carries will decrease, which in turn decreases the sensitivity to the applied force. For machining on a 3-axis mill the centre beam cannot be smaller in any dimension than the outer beams surrounding it i.e. if the outer beams of the 5-beam cage measure $10 \times 6mm$ the central beam must be at least $10 \times 10mm$. The dimensions of the outer beams will also affect the capacity of the central beam, larger outer beams carrying a larger proportion of

the force and lowering the peak stress of the centre beam. The graph shows that the centre beam is at peak stress when it carries around 35% of the force applied to the balance, regardless of the size and shape the outer links. Also shown, the centre link performs best when its cross section is rectangular rather than square, this increased lateral dimension for a lift force would reduce sensitivity to side force, which has a lower rated load, as such another design compromise is required whereby the centre link is eccentrically shaped but with the larger dimension in the direction of the lift force.

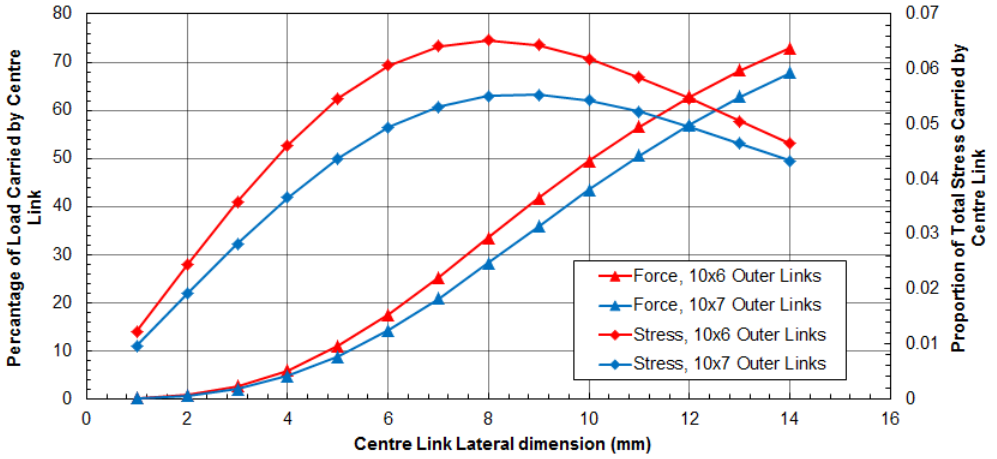


**Figure 3.4:** Beam 'D' dimension compared to load carried and stress on central beam in 5-beam cage.

For ease of manufacture the balance was machined in four pieces, a potential source of hysteresis due to slipping of mechanical components, so care was taken not to introduce any further sources of error. Due to the thinness of the elastic webs on the drag parallelograms, water jet cutting was selected. Water jet cutting creates no heat affected zone in the the thin material as it uses a mix of water and aggregate at pressure to cut the material. There is also no danger of small dimension end mills vibrating and elongating the channels. For a combination of its corrosion resistance properties and machinability aluminium alloy was selected as the balance material. The ratio between the yield strength of the material and the Youngs modulus is important, alloying tends to have little impact on the Young's modulus but can significantly alter the yield strength. The aluminium alloy 2024 features good characteristics of high strength, yield strength (414MPa) with ultimate tensile strength (469MPa), and elasticity, while also being readily available [126].

Following on from bending beam theory the balance was created in the Strand7 FEA package using a number of elastic and infinitely rigid elements, figure 3.5d and e. A number of load cases were simulated, including all the design loads and a combined load case. For most of the load cases the peak stress occurs at the location desired, with the exception of the yaw mode where peak stress occurs in the elastic web on the drag parallelograms (figure 3.5e).

For the final design the centre link measures $8 \times 10mm$ with outer links measuring $8 \times 6mm$, from figure 3.4 this means the centre link carries $60\%$ of force when loaded in lift. Finally a $5mm$ diameter hole was added through the centre link to allow cable egress. The hole reduces the second moment of area

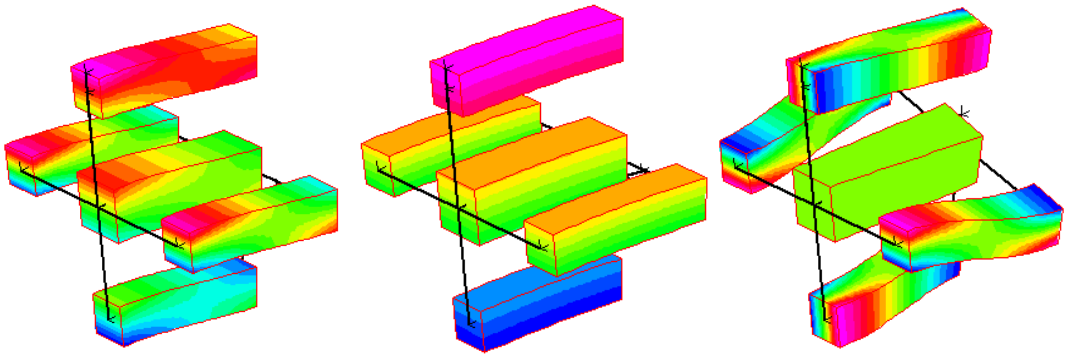

**(a)** Lift. **(b)** Pitch. **(c)** Roll.

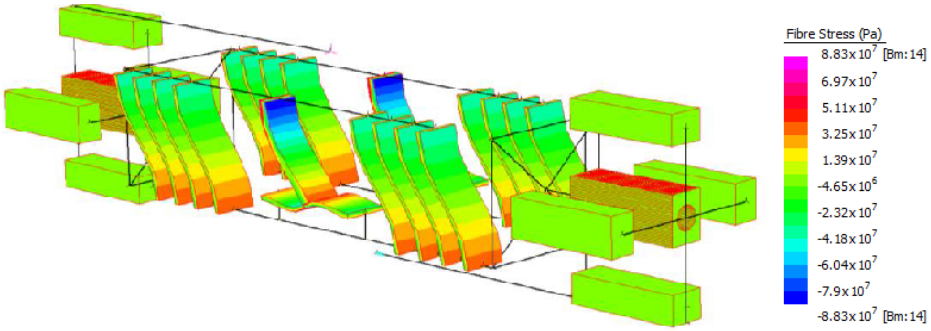


**(d)** Drag.

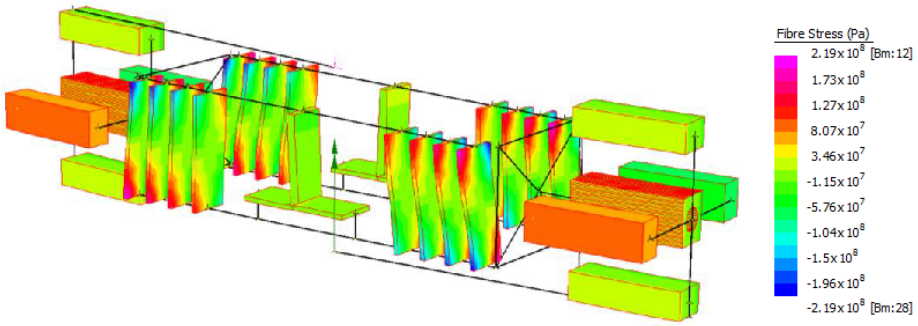


**(e)** Yaw.

**Figure 3.5:** 6-Component balance FEA stress distribuion for different load cases.

of the 5-beam cage by $2.1\%$ and slightly increases the peak stress on the centre link under normal loads compared to figure 3.4. The peak stress for each design case is shown in table 3.3, the table shows that the balance can just carry all the design loads in combination without reaching yield stress. The moments are the hardest to design for with factors of safety around 2, while the safety factor for the three forces is between 4.5 and 10. The actual rated loads of the balance are shown on the bottom row of table 3.3, only yaw fails to exceed the design load with peak stresses concentrated on the drag parallelogram web, figure 3.5e. This could be corrected by increasing the number of webs while decreasing their thickness, though the limitations of the manufacturing process prevents this, so the reduced rating was accepted.

To measure strain a total of forty eight TML FLA-3-350-23 $350\Omega$ strain gauges were bonded to the balance, figure 3.6, with paired strain gauges in each Wheatstone bridge. The paired gauges are used to isolate any thermal discrepancy from one end of the balance to the other [124]. Gauges are bonded to the 5-beam

**Table 3.3:** Predicted mechanical rating for 6-component balance.

| Component | Drag | Side-Force | Lift | Roll | Pitch | Yaw | Combined |
|---|---|---|---|---|---|---|---|
| Applied Load | 150N | 300N | 600N | 80Nm | 240Nm | 120Nm | All |
| Peak Stress (MPa) | 88.3 | 40.1 | 48.6 | 204.0 | 164.0 | 219.0 | 399.0 |
| % Yield | 21.3 | 9.69 | 11.7 | 49.3 | 39.6 | 52.9 | 96.4 |
| Safety Factor | 4.69 | 10.3 | 8.52 | 2.03 | 2.52 | 1.89 | 1.04 |
| Mechanical Rating (S.F. = 2) | 350N | 1550N | 2555N | 80Nm | 305Nm | 115Nm | - |

cages at the locations of maximum stress, figure 3.5. Lift and side force gauges are placed at the roots of the central elements. Gauges in the centre top and bottom elements measure pitch, while the side elements measure yaw. Roll is measured by gauges placed at the roots of the top and bottom elements. Finally the centre perpendicular element is used to measure drag, figure 3.5d.

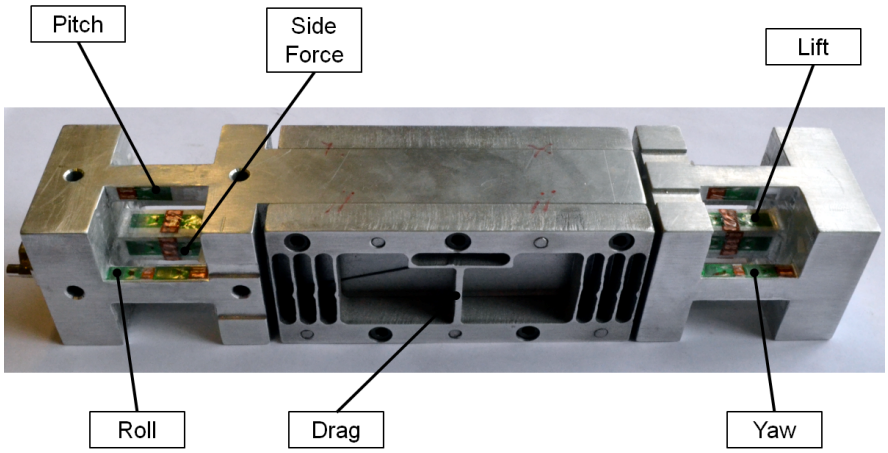


**Figure 3.6:** Strain gauges bonded to 6-component balance (before wiring).

The balance voltages were measured using a bank of six Fylde FE-579-TA [127] strain gauge transducer amplifiers, figure 3.7 capable of supplying a constant excitation voltage up to 10V. To improve individual component sensitivity the signal could be amplified with gains of $1$, $3$, $10$, $30$, $100$, $300$, $1000$, and $3000\times$. Each channels gain was selected to improve component sensitivity without exceeding peak voltage at the desired maximum loads.


**Figure 3.7:** Fylde FE-579-TA strain gauge transducer amplifiers.

## 3.3 Calibration

Gorlin and Slezinger [120] define two types of calibration typically performed for a wind tunnel balance. (1) Adjustment calibrations, which are carried out immediately after manufacture, where the calibration coefficients and component interactions are determined and documented. (2) Control calibrations, which are routinely performed during the life of the balance to check the condition of the balance, specifically for the presence of zero shift or hysteresis, figure 3.8.

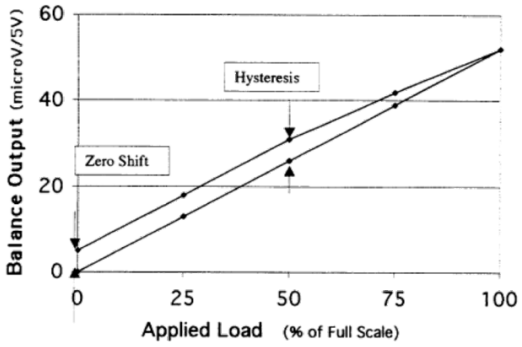


**Figure 3.8:** Example of hysteresis and zero shift, from Rhew [123].

Typically calibrations are performed by loading the balance, both directly and via hanging masses and pulleys, so that forces and moments can be applied in all directions. For each load condition the mass is incrementally increased to a maximum and the six output voltages measured, the mass is then incrementally removed to check for zero shift and hysteresis. The gradient of voltage and load for each load case is then used to create a $6 \times 6$ sensitivity matrix $[\mathbf{S}]$ in ${}^{V}/_{N}$ or ${}^{V}/_{Nm}$,

$$[\mathbf{S}] = \begin{bmatrix} \frac{\partial V_D}{\partial D} & \frac{\partial V_D}{\partial S} & \frac{\partial V_D}{\partial L} & \frac{\partial V_D}{\partial R} & \frac{\partial V_D}{\partial P} & \frac{\partial V_D}{\partial Y} \\ \frac{\partial V_S}{\partial D} & \frac{\partial V_S}{\partial S} & \frac{\partial V_S}{\partial L} & \frac{\partial V_S}{\partial R} & \frac{\partial V_S}{\partial P} & \frac{\partial V_S}{\partial Y} \\ \frac{\partial V_L}{\partial D} & \frac{\partial V_L}{\partial S} & \frac{\partial V_L}{\partial L} & \frac{\partial V_L}{\partial R} & \frac{\partial V_L}{\partial P} & \frac{\partial V_L}{\partial Y} \\ \frac{\partial V_R}{\partial D} & \frac{\partial V_R}{\partial S} & \frac{\partial V_D}{\partial L} & \frac{\partial V_R}{\partial R} & \frac{\partial V_R}{\partial P} & \frac{\partial V_R}{\partial Y} \\ \frac{\partial V_P}{\partial D} & \frac{\partial V_P}{\partial S} & \frac{\partial V_P}{\partial L} & \frac{\partial V_P}{\partial R} & \frac{\partial V_P}{\partial P} & \frac{\partial V_P}{\partial Y} \\ \frac{\partial V_Y}{\partial D} & \frac{\partial V_Y}{\partial S} & \frac{\partial V_Y}{\partial L} & \frac{\partial V_Y}{\partial R} & \frac{\partial V_Y}{\partial P} & \frac{\partial V_Y}{\partial Y} \end{bmatrix}. \tag{3.3}$$

The sensitivity matrix should be a diagonal matrix, though in reality no component is fully isolated. The inversion of the sensitivity matrix forms the calibration matrix of first order terms $[\mathbf{C}]$, so that the $6 \times 1$ column vector of forces and moments $\{\mathbf{F}\}$ is equal to the product of the $6 \times 6$ calibration matrix and $6 \times 1$

column vector of voltages output from the strain gauge transducer $\{\mathbf{V}\}$,

$$\{\mathbf{F}\} = [\mathbf{S}]^{-1}\{\mathbf{V}\} = [\mathbf{C}]\{\mathbf{V}\}. \tag{3.4}$$

By combining load cases 2nd order and higher calibration coefficients can be calculated [128], Smith [129] comments that these terms are significantly smaller than the first order coefficients. Tests performed during the calibration process showed the 2nd order effects to be sufficiently small to be ignored.

Rather than use pulleys, which can be vulnerable to hysteresis, calibration of the 6-component balance was performed using an ABB 3HAC-5761-1 7-axis robot and a calibration frame which allows force to be applied directly through the balance centre and moments to be applied via a pair of perpendicular arms, measuring $0.16m$ and $0.285m$ from the balance centre. The robot could move the balance spatially so that the balance was oriented with the axis of the desired load case perpendicular to the ground, figure 3.9. The calibration was then performed by incrementally hanging $5kg$ masses from the calibrations frame, up to $25kg$ depending on the load case, the masses were then incrementally removed to check for linearity (figure 3.8). The load cases for each balance orientation are as follows:

1. x-axis down: Drag (figure 3.9a)
2. y-axis down: Side Force and Side Force + Yaw
3. z-axis down: Lift (figure 3.9b), Lift + Pitch (figure 3.9c) , and Lift + Roll

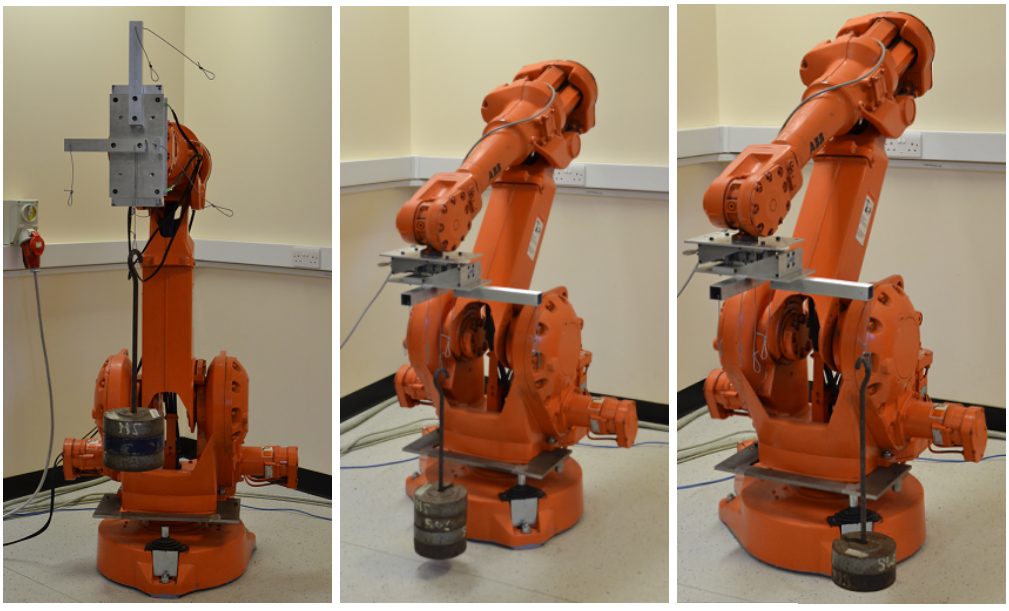

**(a)** Drag force. **(b)** Lift force. **(c)** Pitching moment.

**Figure 3.9:** Calibration of 6-component balance using 7-axis robot.

As can be seen in figure 3.10 each channel is individually sensitive to the applied load case, with minimal interactions. While no component is at peak voltage at the design load, increasing the channel gains would

result in an overload of the transducer/amplifier. So while sensitivity could be improved, it would be at the expense of reducing the peak measurable load. For some applications of the balance this would be advised, though would require a different calibration matrix, and therefore a new calibration to be performed.

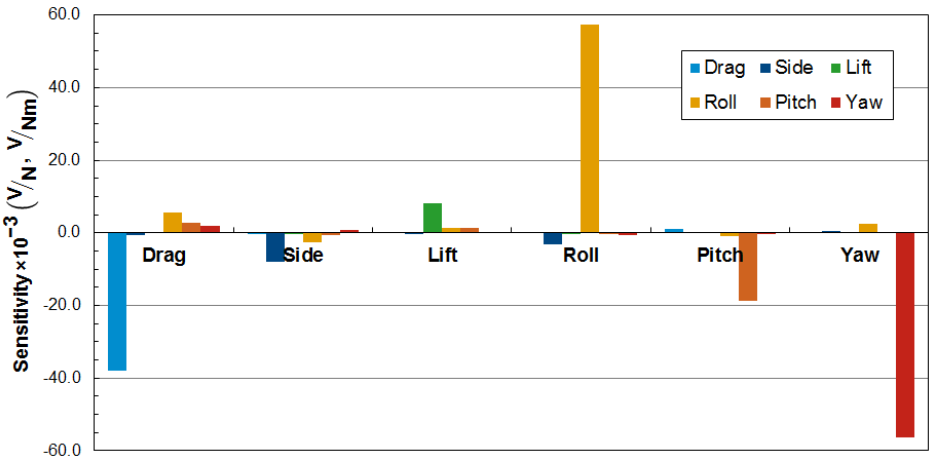


**Figure 3.10:** Graphical representation of balance B0008 sensitivity matrix.

From the inverse of the sensitivity matrix $[\mathbf{S}]^{-1}$ (figure 3.10) the calibration matrix $[\mathbf{C}]$ is constructed,

$$[\mathbf{C}] = \begin{bmatrix} -26.5 & 0.3 & 0.3 & 0.0 & -1.4 & 0.0 \\ 0.6 & -122.6 & -4.0 & -6.6 & 0.0 & -1.4 \\ 0.4 & -0.5 & 124.6 & 0.0 & 1.6 & 0.1 \\ 2.5 & -5.5 & -2.8 & 17.1 & -0.7 & 0.7 \\ -3.7 & 5.1 & 9.6 & 0.1 & -53.4 & -0.2 \\ -0.9 & -1.6 & 0.6 & -0.3 & 0.1 & 17.8 \end{bmatrix}$$

the calibration coefficients of the six forces and moments are the largest and lie on the main diagonal, with minimal cross-talk from the secondary terms off the main diagonal.

## 3.4 Summary

A multi-purpose 6-component balance has been designed and built for the measurement of forces and moments in the Durham University 2m Wind Tunnel. The balance is a sting type design comprising a pair of 5-beam cages at each end and a drag parallelogram at the balance centre. For the purpose of mounting in automotive bodies, a pair of brackets was added to attach to the model and overhead strut, figure 3.11. Rating for the design forces were achieved with a factor of safety of at least 4.5 before exceeding yield stress. Moments proved more difficult to design for and a factor of safety of just 1.89 on the design case was achieved for yaw moment.

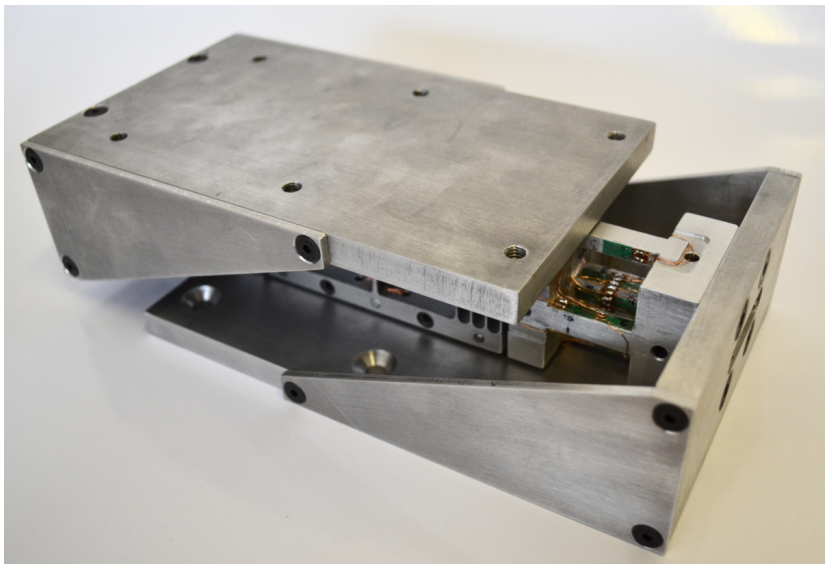

**Figure 3.11:** Assembled 6-component balance, complete with mounting brackets.

# Chapter 4

# Effects on a Following Vehicle (Experimental)

In this chapter the aerodynamic characteristics of the $25\%$ Formula 1 car are obtained empirically using the methodologies described in Chapter 2. The isolated forces, surface pressures and wake of the car are measured and compared to the forces and pressures gathered in the presence of the upstream wake generator. The experimental process made it relatively easy to collect a large dataset of upstream wake generator positions and car conditions.

## 4.1 Vehicle in Isolation (Car Set-up)

The aerodynamic set-up of a Formula 1 car refers to the parameters of the car which can be changed, within a given aerodynamic package. Primarily this refers to front and rear wing incidences ($\alpha$), and the static posture of the car, i.e. the ride height ($h_{min}$) and car pitch angle ($\theta$); with secondary consideration given to the blanking of brake and engine cooling ducts. An equilibrium must be achieved between maximizing downforce, while also maintaining a desirable handling balance, and minimizing drag for straight line speed.

Shifts in the handling balance, i.e. understeer vs oversteer, are achieved through the relative locations of the car's centre-of-gravity (COG) and the downforce centre-of-pressure (COP). Understeer is defined as the tendency for the car to 'push on' in a corner, i.e. the yaw rate is lower than the driver input, and occurs when the centre of pressure is behind the centre of gravity. While with oversteer the yaw rate is greater than the steered input, and occurs when the COP is ahead of the COG. Setting the car with the COP slightly behind the COG gives a more stable and predictable handling balance for the driver, as the low mass (595-702kg between 2008 and 2016) and high power ($>$1000bhp in 2005) construction of a Formula

1 car means the rear tyres can easily break traction under acceleration. Dominy [52] performed a simple cornering analysis for an early 1990s F1 car, finding that a neutral balance is achieved when the COP is $3\%$ of the wheelbase aft of the COG. Agathangelou and Gascoyne [12] quote a baseline aerodynamic balance of $64\%$ for the Tyrrell F1 team between 1989 and 1998, where the aerodynamic balance is defined as the percentage of downforce acting on the rear axle ($\frac{C_{LR}}{C_L} \times 100$).

As the desired outcome of the experimental campaign is to quantify the effect of the wake generator, firstly the car must be set-up in isolation. The current F1 [26] rules specify a rear weight distribution of $54\% \pm 0.5\%$, so it was judged that an aero-balance of $57.5\% \pm 2.5\%$ ($55$ to $60\%$) would give a neutral handing balance. To prevent the force and wake characteristics changing between isolated and affected cases the car was placed as far back on the moving ground plane as possible to allow the longest bluff body separation, however a $0.5m$ ($x = 0.42L_C$) length of belt was left aft of the car to allow the wake to propagate naturally. All experiments were performed at Reynolds number of $2.05 \times 10^6$ based on model length and the model blockage was $4.7\%$.

### 4.1.1 Effect of Front Wing Flap Angle

The front wing flap adjustment was performed during a wheels-on study, the results from which were used to define the set-up for the computational programme. The vehicle forces were measured with the same internal balance as the wheels-off test, but pressure measurements were made using a mechanical Scanivalve, with 47 ports instead of the 128 port electronic pressure scanner used in later wheels-off testing. Consequently there were insufficient underbody and upper body pressure tappings to draw definitive conclusions about the flaps effect on the surface pressure distribution of the rest of the car. The forces were recorded for $9^\circ$ (minimum), $22^\circ$, and $34^\circ$ (maximum) flap angles; with all three flap angles resulting in peak force at a posture of $h_{min} = 2.33mm$ and $\theta = -0.6^\circ$, figure 4.1.

Between $\alpha = 9^\circ$ and $34^\circ$ peak downforce increased by $16.7\%$ with peak downforce occurring with the maximum flap angle. The aerodynamic balance shifts forward with increasing flap angle from severe understeer, $\frac{C_{LR}}{C_L} = 73\%$ when $\alpha = 9^\circ$, to $\frac{C_{LR}}{C_L} = 62\%$ when $\alpha = 34^\circ$. Interestingly, while downforce increases with flap angle, vehicle drag actually reduces by $0.019$ on $C_D$ when the flap angle is increased between $22^\circ$ and $34^\circ$ (figure 4.1), which could be the result of the front wing and suspension wakes merging. There is insufficient data available from the wind tunnel study to show this, but it can been seen to occur in CFD, shown in figure 4.2.

The front wing surface pressure distributions for the optimal posture are shown in figure 4.3, for ease of visualization the leading edge tapping is grouped with the upper surface. The stagnation point is not captured by the pressure tappings on the front wing centreline, nor is any suction spike on the lower surface

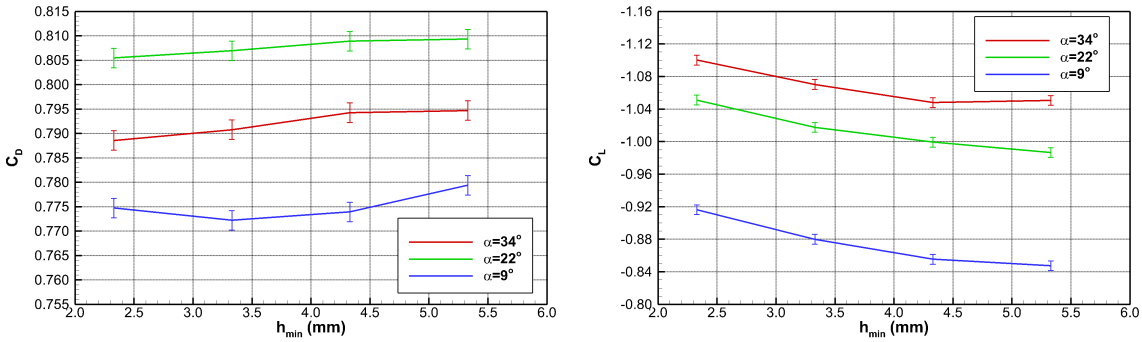


**(a)** Drag. **(b)** Downforce.

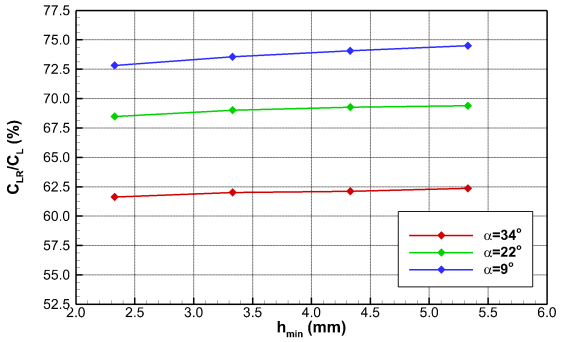


**(c)** Aero-balance.

**Figure 4.1:** Force variation with front wing flap angle ($\theta = -0.6°$ posture), reference area $= 1.5m^2$ (full scale).

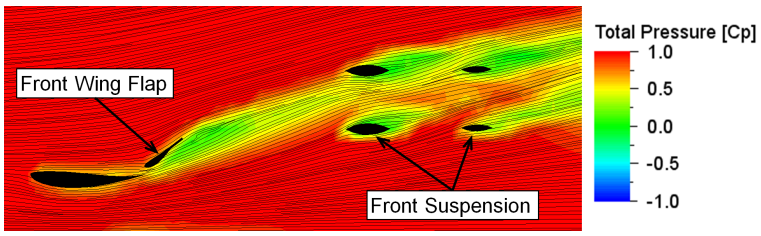


**Figure 4.2:** Front wing (flap at $\alpha = 34°$) and suspension wakes from isolated CFD case, flow from left to right.

near the leading edge. The effect of the flap on front wing is a systematic increase of the upper surface pressure with flap angle, $\Delta C_P = 0.14$ on average from minimum to maximum incidence ($\alpha$). The main difference occurs on the lower surface, especially at the quarter-span where the negative pressure on the lower surface doubles ($\Delta C_P = -0.6$) between minimum and maximum flap angles. The effect of the flap at the quarter-span location is also to move the suction peak ($-C_P$) rearward by as much as $8.5\%$ as flap angle increases. The effect on the centreline lower surface is less significant, though $\Delta C_P = -0.5$, and the location of peak pressure remains at $x = 0.18c$ on the mainplane chord. It is clear that the maximum flap angle results in the greatest downforce, lift-to-drag ($^L/_D$), and closest to the optimal aero-balance, so all future experiments were performed with the front flap set to an incidence of $\alpha = 34°$.

It can be assumed, at least for the isolated vehicle (section 4.1), that despite the adverse pressure gradient on the lower surface the boundary layer of the front wing will remain laminar up to the trailing edge; based on the Reynolds number at the trailing edge of the front wing being less than half ($Re = 2.2 \times 10^5$) the Reynolds number for laminar flow on a flat plate ($Re_X = 5.0 \times 10^5$). This is a well known consequence

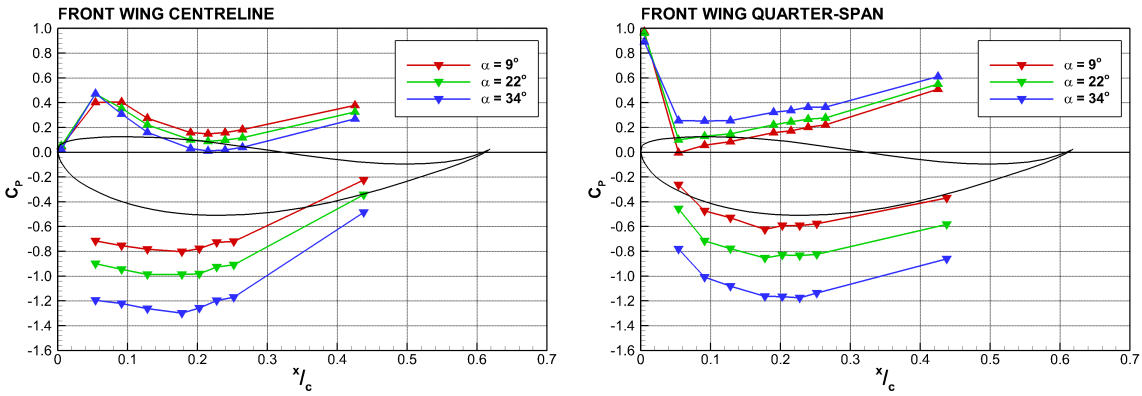


**Figure 4.3:** Front Wing Pressure Distribution with Varied Flap Angle (Up Arrows = Upper Surface, Down Arrows = Lower Surface).

of model scale testing of race cars, as the boundary layer at the trailing edge of a full scale front wing at racing speeds will be turbulent. Modern Formula 1 teams use 60% scale models (limited by the FIA to 50% or 60% scale models at tunnel velocities up to 60m/s [79]) for closer dynamic similarity and therefore better correlation to the full scale flow characteristics [14], however, increasing the model scale is not feasible in this study considering the working length of the wind tunnel, even using a short axial length wake generator.

### 4.1.2 Vehicle Forces

With wheel drags being measured by the wheel stings, aerodynamic drag can be split into body (figure 4.4) and wheel drag forces as measured by the corner load cells (figure 4.5). Drag is distributed relatively evenly between the body and wheels ($C_D \approx 0.38$ for each), the change of drag with ride hight and pitch is different for the body than the wheels, with bodywork drag increasing with ride height and wheel drag changing with pitch angle.

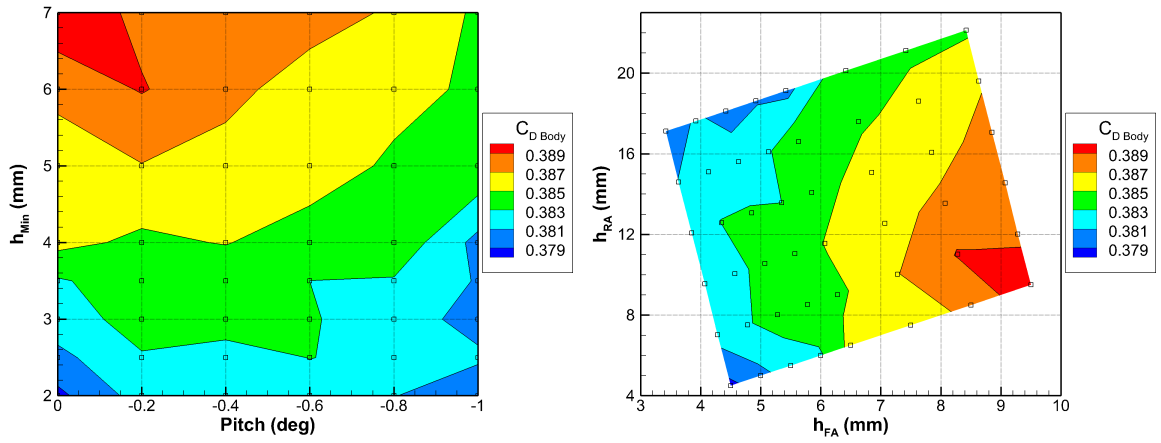


**Figure 4.4:** Freestream body drag, reference area = $1.5m^2$ (full scale).

The increase of body drag with ride height could be the result of increased effective frontal area of the car,

however that the rate of drag increase is retarded by increased pitch would oppose this assumption. At the $2mm, 0^\circ$ posture ($h_{min}, \theta$) the front and rear ride heights (relative to the reference plane) are both at $4.5mm$. When $\theta$ increases to $1^\circ$, $h_{FA}$ decreases to $3.20mm$ while $h_{RA}$ is $19.6mm$ or $15mm$ higher than at $\theta = 0^\circ$ at model scale. This would indicate that the blockage would be greater at high pitch angles, as the rear of the car is significantly higher. Comparing the drag contours instead to $h_{FA}$ and $h_{RA}$ shows a strong correlation between body drag and front ride height. This would instead point to a change in the interaction between the front wing and front wheels and figure 4.5a indeed shows that front wheel drag is lowest where body drag is highest. It should be noted, that the variation from minimum to maximum body drag is very small at only $0.01$ on $C_D$, or $\approx 1.3\%$ of the peak total drag.

As mentioned before, the combined wheel drag increases, almost linearly, with car pitch angle. The variation of wheel drag is even smaller ($0.006$ on $C_D$) than the vehicle body, which is not all that surprising as the only changes are due to subtle variations in the interactions with bodywork. Peak front wheel drag ($C_{D\,X-} = 0.196$) is $0.006$ on $C_D$ higher than rear wheel drag ($C_{D\,X+} = 0.190$). Front wheel drag is lowest at high ground clearances with no pitch on the car, and highest at low ground clearances with a lot of pitch on the car. This could be caused by interactions with the front wing wake and the area of the tyre which is blocked by the wing; at large pitch angles the front wing ground clearance reduces significantly increasing the thickness of the wake and exposing more of the front wheel to the onset airflow. The wing mainplane is also at a greater angle of attack, increasing the angle of the wake. On the contrary the rear wheel drag (figure 4.5b) is greatest at high pitch and ride height. While the rear bodywork will theoretically block more of the wheel at large rear ride heights, lowering drag, the increased interaction with the underbody wake will increase drag. The contour plot of rear wheel drag is very flat, with only $0.004$ of variation on $C_D$, perhaps as one interaction cancels another.

Total drag (figure 4.7c), the sum of wheel and body drags, increases with both ride height (as does the body) and pitch (as do the wheels). As the peak drag for the body and wheels occur at different conditions the range is not the sum of body ($0.01$ on $C_D$) and wheels ($0.006$ on $C_D$) but $< 0.008$ on $C_D$ from minimum to maximum. The range of downforce (figure 4.7a) is much greater at $0.1$ on $C_L$, predictably for a ground effect race car downforce is greatest at low ground clearances. In this aero map the ride height was not lowered sufficiently to see any force reduction due to low ground clearances, but downforce decreases by $< 8.5\%$ at the maximum ride height. Adding pitch to the car does result in a recovery of downforce, especially at higher ground clearances with greater pitch (shown in figure 4.6). With the drag contour being so flat the lift to drag ratio (figure 4.7d) is dominated by the change of downforce; as $C_{D\,Total} < 1$ the lift-to-drag ratio ($^L/_D$) is greater than 1. The car aero-balance for all postures tested for the aero map is in the optimal range, ranging between $56.5\%$ and $58.8\%$. The balance moves further forward with increasing pitch, as the front wing moves closer and the rear diffuser further from the ground. With no pitch on the car the balance changes little with ride height, figure 4.6b, though as pitch increases

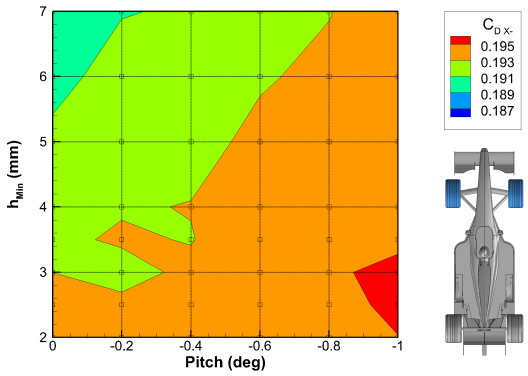


**(a)** Front wheel drag ($C_{D\,X-}$).

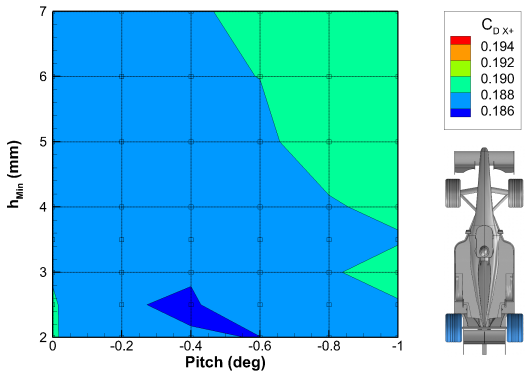


**(b)** Rear wheel drag ($C_{D\,X+}$).

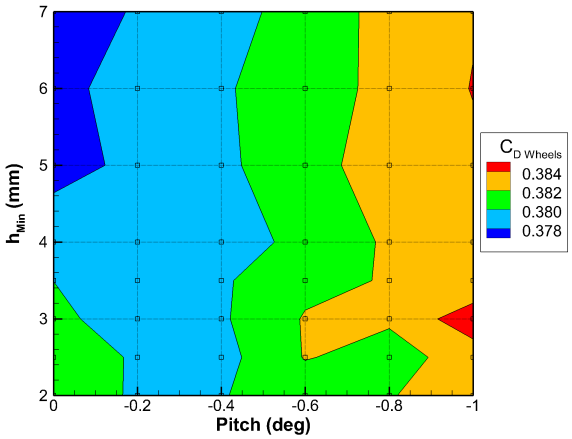


**(c)** Combined wheel drag ($C_{D\,Wheels}$).

**Figure 4.5:** Freestream wheel drag, reference area $= 1.5m^2$ (full scale).

so too does the gradient of the $h_{min}$, $\frac{C_{LR}}{C_L}$ slope.

The key vehicle set-up considerations are high downforce and low drag (i.e a high lift-to-drag ratio) with an aero-balance of $\frac{C_{LR}}{C_L} \approx 57.5\%$. In this case the optimum downforce and drag occur for the same posture $(2mm, 0°)$, while the optimum aero-balance occurs at the $7mm, 0°$ posture. The aero-balance for the $2mm, 0°$ posture falls within the same contour level $\frac{C_{LR}}{C_L} \pm 0.125\%$ as the balance at the $7mm, 0°$ posture (figure 4.7b), while downforce is $7.5\%$ greater. Another peak of downforce ($C_L = 1.19$) occurs for the $2mm, -1°$ posture, with a slightly further forward aero-balance of $\sim 56.5\%$, which is close to the FIA mandated centre of gravity and an oversteering handling balance.

The difference in peak downforce and aero-balance between the wheels-on (figure 4.1) and wheels-off (figure 4.6) studies can be attributed to the removal of the front suspension members, which generate both lift and drag. The reduction of lift on the front axle moves the centre of pressure forward by $\sim 5\%$ at the same car condition.

It should also be noted that the downforce generated is significantly below what would be expected for a car of this type, a modern Grand Prix car is expected to generate downforce in excess of three times its own weight, or $-4.0$ to $-4.5$ on $C_L$. There are numerous reasons that this could be the case, the camber

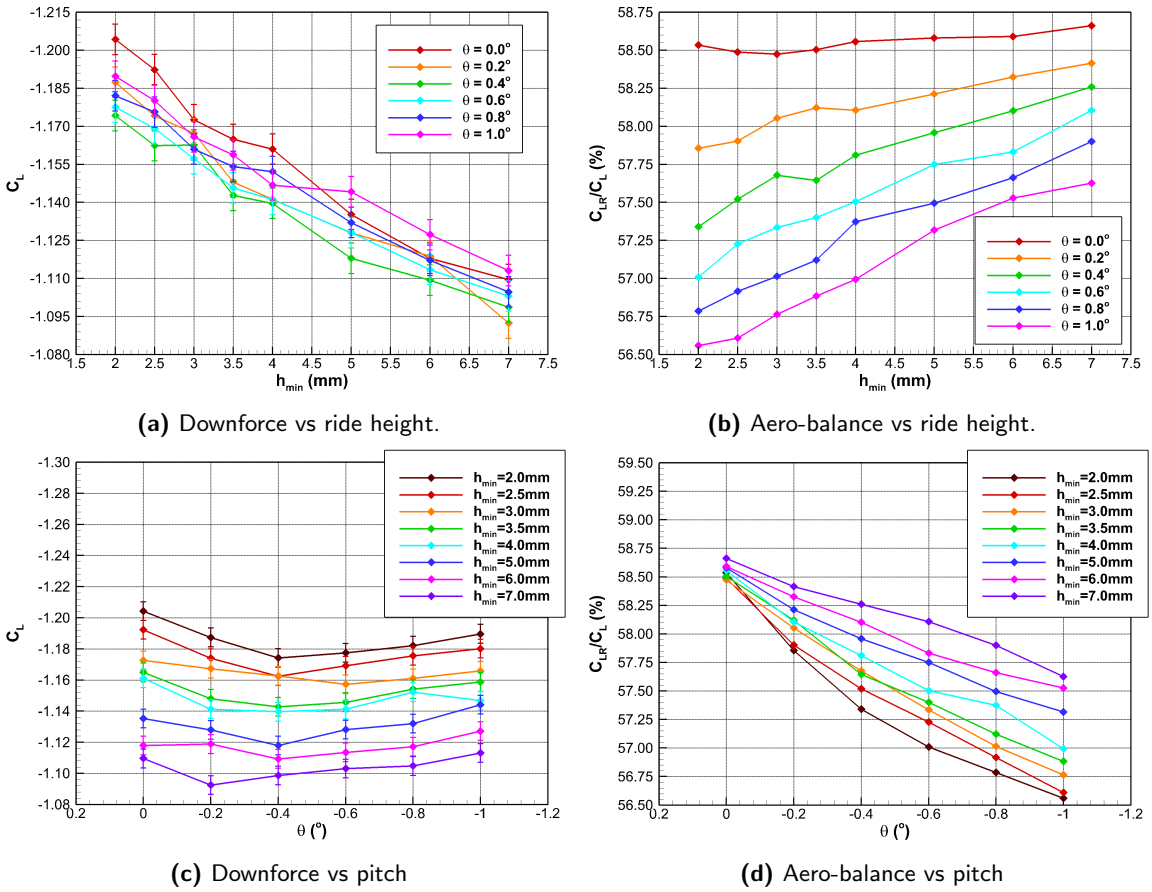


**(a)** Downforce vs ride height.

**(b)** Aero-balance vs ride height.

**(c)** Downforce vs pitch

**(d)** Aero-balance vs pitch

**Figure 4.6:** Freestream vehicle forces (lines), reference area $= 1.5m^2$ (full scale).

of the wing profiles and shape of the underbody, with $-C_P$ (as shown in figure 4.3) significantly lower than would be anticipated. The car has also not been optimized such that the wakes of upstream aerodynamic surfaces do not negatively affect downforce produced by the downstream geometries, figure 1.31. While the car could undoubtedly be improved with the inclusion of barge boards, turning vanes, vortex generators or higher camber wing profiles, it is unlikely that the author could create a car of similar performance to a full scale Formula 1 operation, without committing significant resources. So for the same reason the car was not updated to the latest set of regulations, namely that the function of this research is the evaluation of the effect of an upstream wake on the car, not the optimization of a car, it was decided that improving performance was an unnecessary diversion.

### 4.1.3 Vehicle Surface Pressure Distribution

Surface pressures were only measured for four car postures; the postures include the optimal freestream set-up $(2mm, 0°)$, with the lowest drag and maximum downforce, point A on figure 4.8. The other three postures cover the corners of the aero-map $(7mm, 0°/2mm, -1°$ & $7mm, -1°)$, and could be linked to a the change in car attitude during cornering, this is only an approximation as the load transfer in cornering is corner specific and dependant on the vehicle dynamics. During the braking phase, figure 4.8, the car

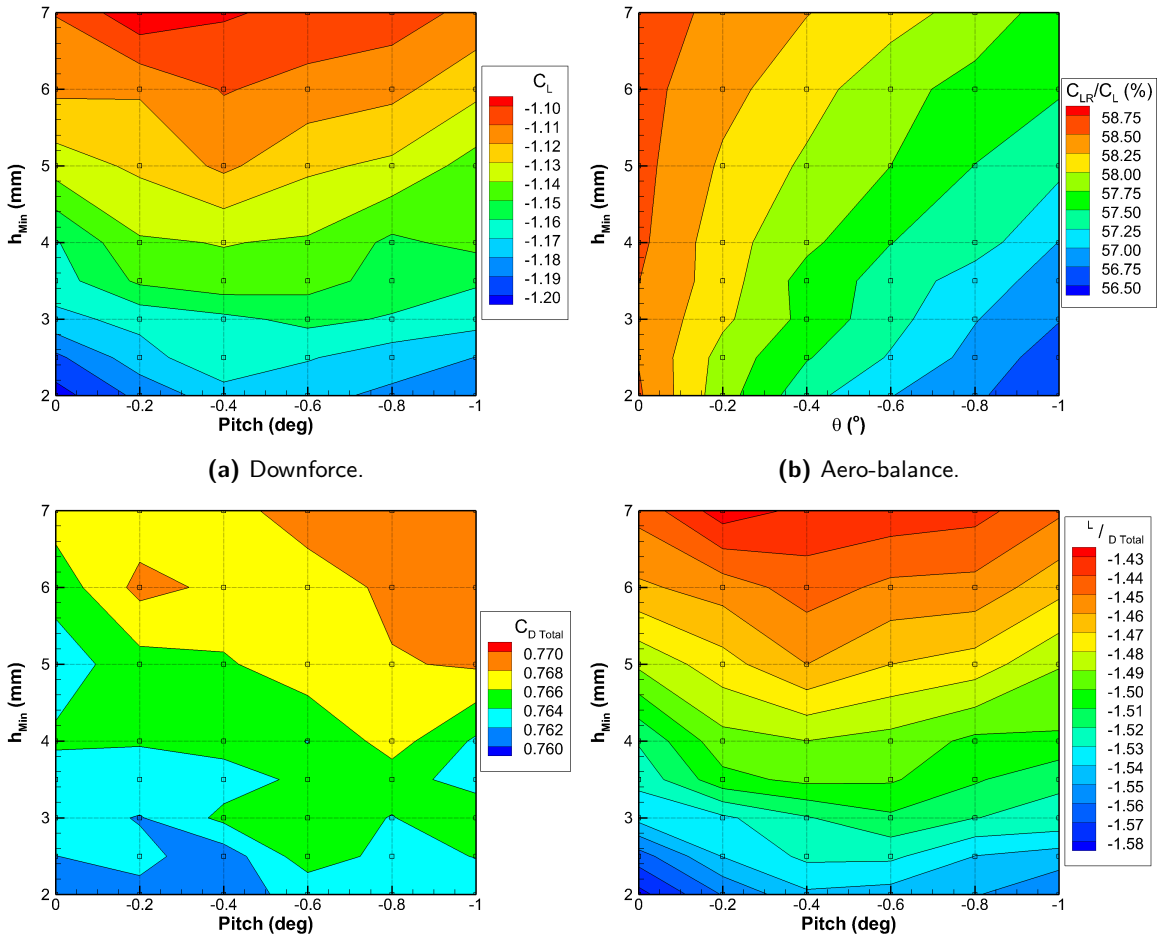


**(a)** Downforce. **(b)** Aero-balance.

**(c)** Total drag. **(d)** Lift-to-drag.

**Figure 4.7:** Freestream vehicle forces (contours), reference area $= 1.5m^2$ (full scale).

weight transfers to the front axle and rear ride height increases $(2mm, -1°)$, the overall ride height also increases as the downforce reduces with vehicle velocity $(7mm, -1°)$. In cornering the car ride height increases further to the minimum cornering velocity, during the final phase of cornering the load transfers back to the rear as the braking phase is complete and the driver begins to accelerate $(7mm, 0°)$.

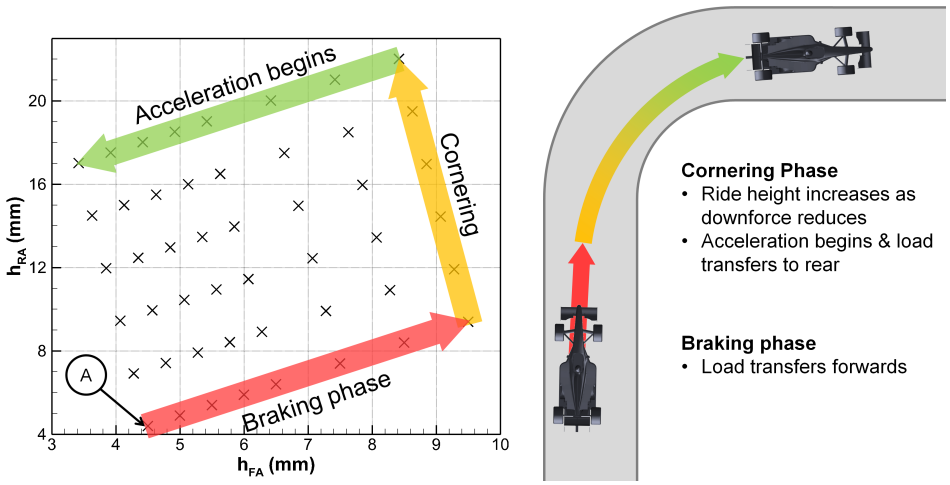


**Figure 4.8:** Approximate effect of cornering on vehicle posture.

#### 4.1.3.1 Front Wing Surface Pressure Distribution

The aerodynamic balance of the car has been shown to move forward with increased pitch (figure 4.7b) and the front wing pressure distribution, shown in figure 4.9, is at a lower static pressure at both centre and quarter-span locations when $\theta = -1°$, even at the maximum ride height. The centreline and quarter-span upper surfaces show little variation with ride height or pitch angle, with the exception of the leading edge on the centreline for the $2mm, 0°$ posture, which is very different than the other conditions tested. On the front wing centreline the leading edge lies underneath the nose of the car, which for most of the conditions shifts the stagnation point on the wing away from the leading edge pressure tapping. This does not happen to the same extent at the lowest condition with no pitch, perhaps as the ground clearance prevents the nose deflecting the onset airflow to the same extent, i.e. the positive $C_P$ in the stagnation region of the nose extends further in the Z direction. At the quarter-span there is no geometry upstream of the leading edge of the wing so the leading edge tapping is near the stagnation point for all conditions tested. The trailing edge of the upper surface is at a greater $C_P$ than the centreline, due to the leading edge pressure of the flap.

The shape of the lower surface, pressure distribution at both planes is unaffected by the vehicle ride height or pitch angle. On the centreline the negative pressure peaks at $x = 0.18c$ on the mainplane chord, while the suction peak is at $x = 0.23c$ on the mainplane chord at the quarter-span. Peak suction is greater on the centreline that on the quarter span, which would be anticipated for a 3D aerofoil. However the quarter-span lower surface pressure is more closely matched to the centreline due to the presence of the flap, the circulation of which increases downforce on the mainplane upstream. The flap also serves to reduce pressure at the trailing edge by $\Delta C_P = 0.4$ compared to the centreline.

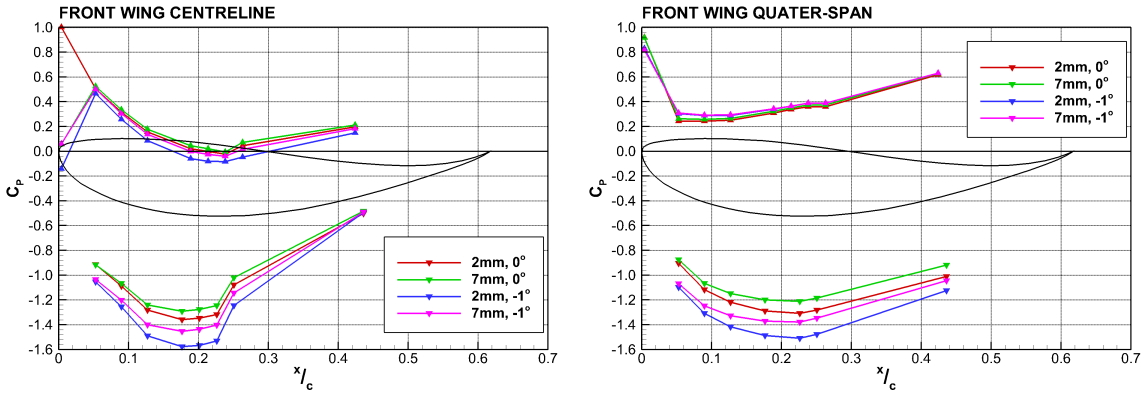


**Figure 4.9:** Freestream Front Wing Pressure Distribution (Up Arrows = Upper Surface, Down Arrows = Lower Surface)

From the front wing pressure distributions, despite the tappings only covering up $x = 0.44c$ (to 70% of the mainplane chord), the force generated by the front wing on the centreline and quarter-spans can be approximated from the integral of the pressure distributions, shown in figure 4.10.

As the pressure distribution indicates the front wing generates more downforce for the nose-down postures, at both the centreline and quarter-span locations (figure 4.10), with the greatest downforce generated for the $2mm, -1°$ posture, $-0.3$ on $C_L$ greater on the centreline than the $2mm, 0°$ posture. The ideal lift slope in 2D potential flow is $\frac{\pi^2}{90}$, a change of $C_L = -0.11$ for a incidence change of $\alpha = 1°$, so a significant portion of the downforce increase is a result of the reduced ground clearance of the wing resulting from the cars pitch; as $h_{min}$ is measured relative to the front of the floor, pitching the car moves the front wing closer to the ground even if the nominal ride height remains constant. For the flat postures the increase of ride height has little effect on the force created on the front wing centreline, $C_L = -0.85$, though this could be skewed by stagnation pressure at the first pressure tapping for the $2mm, 0°$ posture; the quarter-span is $0.1$ on $C_L$ lower at the higher ride height.

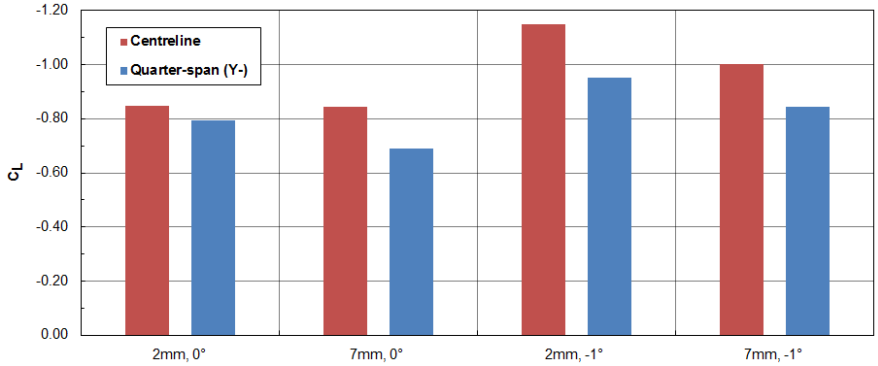


**Figure 4.10:** Freestream front wing centreline and quarter-span force approximation based on planform reference area $= 0.036m^2$.

#### 4.1.3.2 Body Surface Pressure Distribution

Like the front wing upper surface the upper bodywork (pictured in figure 4.11), nose and sidepod, are relatively unaffected by vehicle attitude. The nose pressure gradually reduces over the length, becoming negative near the cockpit opening. The sidepod, just to the side of the cockpit, shows a sharp adverse pressure gradient near the leading edge before reducing again at the final pair of tappings, possibly indicating a separation and reattachment region at the sharp leading edge of the sidepod. Formula 1 teams now use a series of vortex generators on the leading edge of the sidepod to maintain attached airflow along the top surface of the sidepod, and in turn increasing the mass flow to the rear diffuser.

Like the front wing, the underside of the car (figures 4.11 and 4.12) is where the significant differences between vehicle postures occur. The profile of the underbody static pressure distribution is notably different for each vehicle pitch tested, with the lower ride hight ($h_{min} = 2mm$) for each pitch angle at a lower pressure than the high ground clearances ($h_{min} = 7mm$). At the front of the floor the static pressure is visibly higher when $\theta = 0°$, this can be seen on the lower nose centreline and on the underfloor centreline. This is surprising as despite the car being at pitch the minimum ground clearance is the either $h_{min} = 2mm$

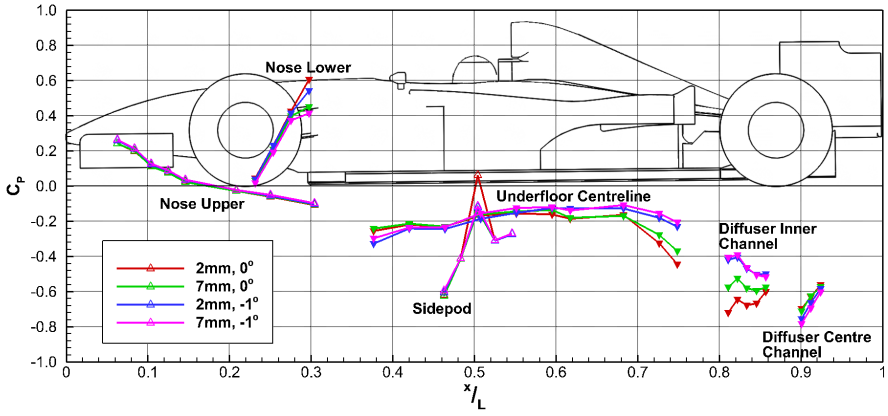


**Figure 4.11:** Comparison of Car Posture Surface Pressures (Up Arrows = Upper Body, Down Arrows = Underbody)

or $7mm$ and measured from the ground to the bottom of the skid block on the leading edge of the splitter.

At the rear of the floor and into the diffuser region the effect of pitch on the car is again striking. As the flow travels downstream on the underfloor the pressure normalizes with the ingress of flow from higher pressure regions, the start of the diffuser ramp then creates another low pressure region. When the car is at no pitch the pressure in this region is more negative as a result of the rear ground clearance causing a greater acceleration at the diffuser throat. This lower pressure continues into the diffuser but also generates lower pressure in the immediate upstream region. When the car is at $\theta = -1^\circ$ the pressure at the diffuser throat is higher, but the low base pressure in the near wake of the car (resulting from a combination of rear wing and diffuser flow) actually drives the pressure down over the diffuser length so that at the last tap the pressure is similar to when $\theta = 0^\circ$. The underfloor pressure distribution would lead to the conclusion that the change in vehicle balance with pitch is not just the result of the front wing, but also that the floor balance shifts toward the front axle.

Like the front wing, the downforce generated by the underbody can be approximated by integrating the surface pressure in the region populated by pressure tappings, shown in figure 4.13. While this region of the floor is sufficiently covered by tappings to generate contours, it only equals $79\%$ of the total area of the undertray and diffuser, even when mirrored, so this is only an approximation of the downforce generated by the underbody.

Contrary to the front wing, where downforce was greater for the nose-down postures, the underbody generates more downforce for the flat postures (figure 4.13). This is not a surprise as the pressure distributions (figure 4.12) show an increase of the static pressure just before the diffuser kick for the nose-down postures, indicating a loss of rear downforce. What is of note is that the downforce generated on the lower surface of the underbody is only $31.5\%$ of the total downforce generated by the car for the $2mm, 0^\circ$ posture, decreasing to $26.3\%$ for the $7mm, -1^\circ$ posture, possibly as the pressure tappings are insufficiently placed to capture all the significant features.

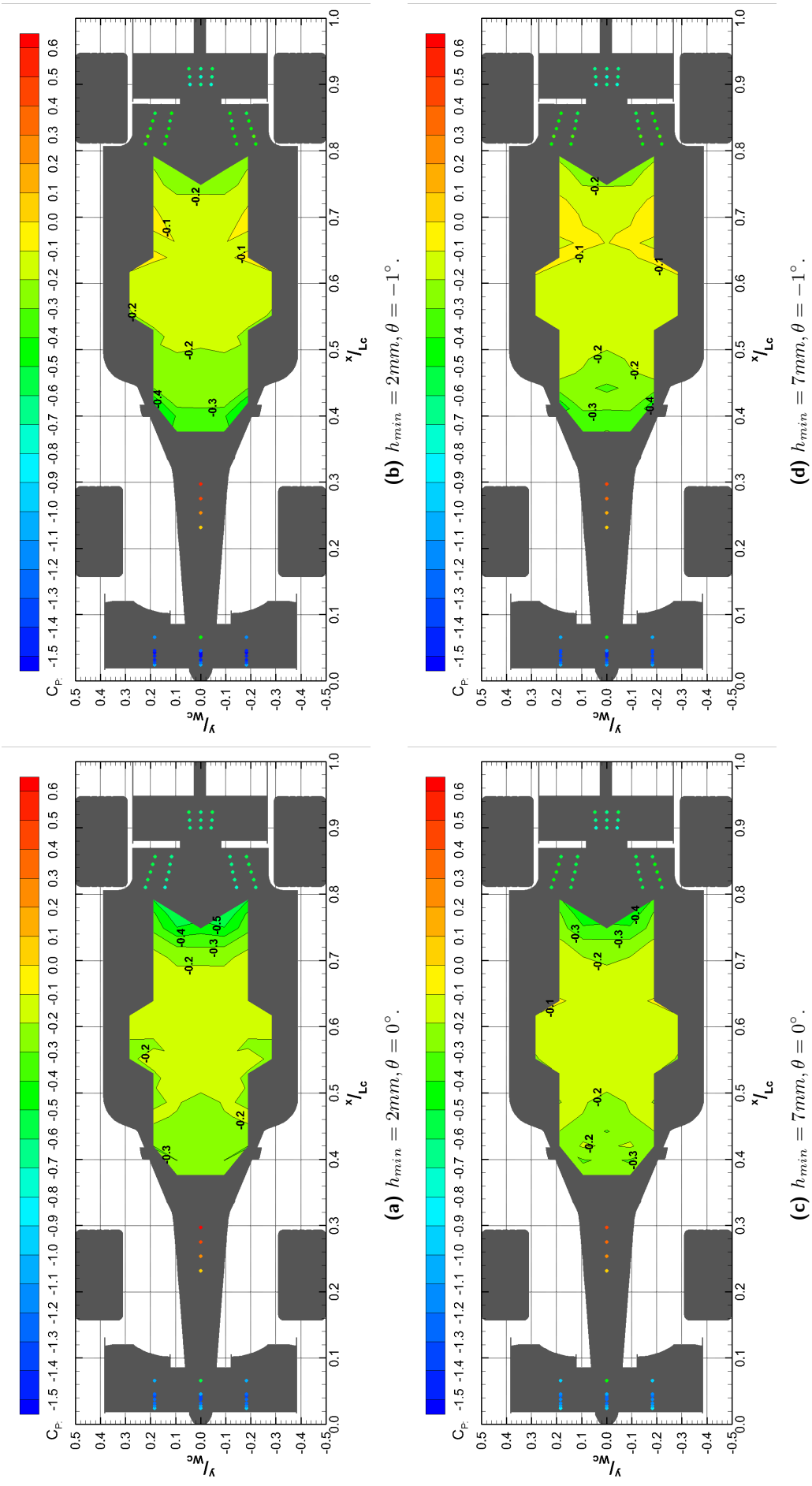


**Figure 4.12:** Contours of underbody pressure distribution.

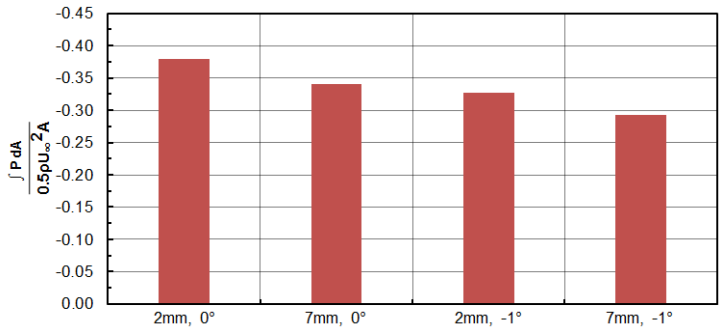


**Figure 4.13:** Freestream underbody contours integral pressure, reference area $= 1.5m^2$ (full scale).

In this section the aerodynamic characteristics of the 25% Formula 1 car operating in isolation have been investigated. Although total downforce is lower than anticipated for such a vehicle, the car behaves as expected with changes to the ride height, pitch angle, and front wing flap incidence. Increasing front wing flap incidence increases the front wing downforce, moving the overall aero-balance forwards, with the greatest flap incidence $\alpha_{flap} = 34°$ giving the best downforce, lift-to-drag, and aero-balance. Reducing ride height increased downforce, with the greatest downforce occurring for the lowest ride height tested. Car pitch also affects balance, with greater suction loading at the front of the floor with nose-down pitches, and at the rear of the floor for flat postures. Flatter pitch angles resulted in less of a shift of the aero-balance with reducing ride height, giving a more consistent handling for the driver.

## 4.2 Comparison of 25% Formula 1 and Bluff Body Wakes

A number of bluff bodied wake generators have been manufactured for previous projects [7, 6, 86, 8], none of which were suitable for this study, owing to differences in scale compared to the 25% Formula 1 wind tunnel model, or length making it difficult to achieve a suitable inter-vehicle separation. A new wake generator was created for this study, described in Chapter 2; in this section the wake of the bluff bodied wake generator is measured and compared to the wake of the 25% Formula 1 car. The wheels of the wake generator were supported off the model, figure 4.14, in order to improve the stability of the model for the duration of the wake measurements. The short length of the wake generator meant that vehicle centreline (figure 4.15) and waistline (figure 4.16) measurement planes could extend further downstream ($x \leq 2.0L_C$) than the F1 model ($x \leq 1.75L_C$). Unless stated, downstream XY and YZ wake planes are mirrored about the car centreline for the purpose of presentation.

Centreline (figure 4.15) and waistline (figure 4.16) wake plane measurements show relatively good correlation in the size, shape and magnitude of stagnation pressure deficits between the wakes of the 25% F1 and wake generator; while there are some notable differences in the very near wake, $x < 1.2L_C$, the accuracy of the BBWG wake increases further downstream, and is most accurate for realistic on-track following

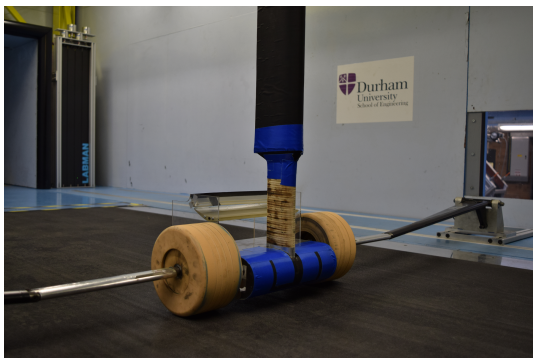


**Figure 4.14:** Bluff bodied wake generator in 2m wind tunnel.

separations (beyond $x \approx 1.5L_C$). Both the wakes are characterized by large regions of stagnation pressure deficit $C_{P_O} < 0.65$, with local regions of $C_{P_O} << 0.1$ in the near wake of both models. The region of $C_{P_O} < 0.65$ extends to the end of the centreline plane, increasing in height as it progresses from $z = H_C$ at the base to $z \sim 1.6H_C$ at $x = 1.75L_C$.

On the centreline, the near wake ($x < 1.2L_C$) of the Formula 1 car is dominated by the total pressure deficit from the body and underbody. The body of the wake generator does not appear to create the same magnitude pressure deficit, despite the relative bluffness of the geometry. The high total pressure below the bluff body would seem to indicate that the upswept floor of the wake generator accelerates the airflow on the underside. It is not entirely surprising that the wake generator does not generate the same stagnation pressure deficit at the base as the full Formula 1 car considering the relative lengths. The wing wake of the wake generator extends further than the Formula 1 model, up to $x < 1.2L_C$, and could result from the 'cleaner' onset airflow, compared to the F1 car. The rear wing of an F1 car is itself in the wakes of upstream geometries, such as the engine air intake, and will have onset up and downwash localized across the span [52, 18], reducing downforce generated by the wing.

The centreline wake is compared to the wake of the Perrinn Ltd open source Formula 1 car [130], figure 4.15c, designed by a Formula 1 engineer for the 2017 regulations. The model was released too late to be used in this study but allows a comparison to be made to a more developed vehicle. The car generates more downforce than the 25% generic model, albeit significantly less than a front of the grid car, $C_L = -2.4$ and $C_D = 0.8$ based on a frontal area of $1.5m^2$. However, despite the higher forces, the wake appears similar to the model used in this study. While it is difficult to give exact value to the differences owing to the wider contour range and lack of axes, peak total pressure deficit is in the same range as the generic 25% vehicle, $0 < C_{P_O} < 0.2$. The the wakes form a similar 'rooster tail' shape with $C_{P_O} < 0.8$ extending above the height of the car up to and beyond one car length downstream. This gives confidence that while the downforce created by the 25% scale vehicle is low the wake is broadly similar to a less generic vehicle.

The waistline, at wheel axle height $z = 0.5d$, wake measurement plane (figure 4.16) shows that the near wake of the BBWG is dominated by the wheels. Like the rear wing of the F1 car, the rear wheels operate

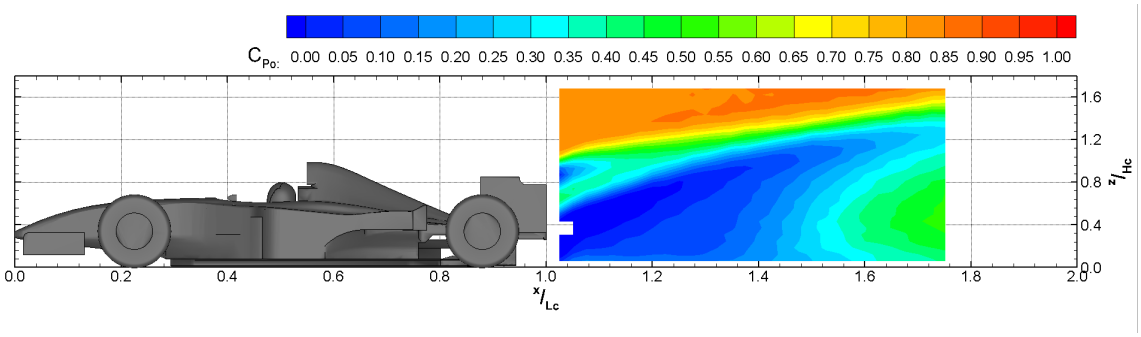


**(a)** 25% Formula 1.

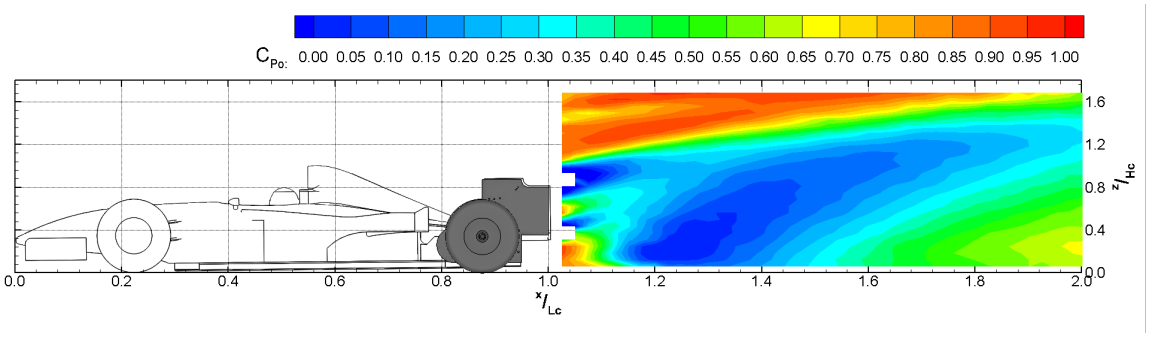


**(b)** Wake generator.

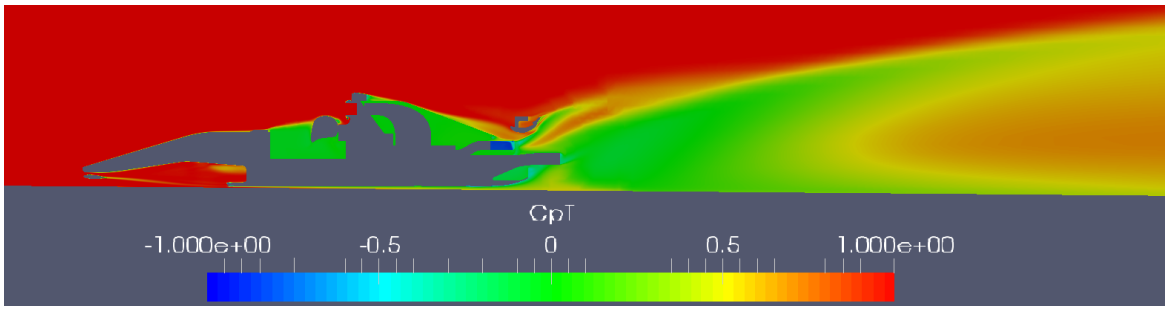


**(c)** Perrinn 2017 open source F1 car, from Perrin Ltd [130].

**Figure 4.15:** Wake contours of $C_{P_O}$, XZ plane on car centreline ($y = 0$).

in the wakes of the rest of the car, the clean onset flow to the wheels of the BBWG therefore results in a larger and more dominant wheel wake, also seen on a slice through the wheel centrelines (figure 4.17). The shapes of the wheel wakes are slightly different, with the BBWG wheel wake featuring a greater quantity of reversed flow behind the wheel which extends to $x \approx 1.2L_C$, where 25% Formula 1 car wheel wake closes by $x = 1.05L_C$. The wheel wake could perhaps be reduced with a flow conditioner in front of the wheel to reduce the static pressure discrepancy between the front and rear faces of the wheel. Both the full F1 car and BBWG wakes have inwash at axle height, sweeping the wake deficits towards the centreline, with similar deficits ($C_{P_O} \approx 0.6$) and width ($y \pm 0.2W_C$) by $x = 1.6L_C$.

Behind the full Formula 1 car the wake is dominated by the counter-rotating vortex pair emanating from the rear wing, figure 4.18a, with secondary flows present over a height of $z = 1.6H_C$. The vortices commence roll-up at the tips of the rear wing and are initially heavily concentrated, with high magnitude secondary flows around a low static pressure core, shown in figure 4.18b to be located at $(y, z) = (0.35W_C, 0.9H_C)$. Static pressure in the vortex cores peaks at $C_P = -0.5$ at $x = 1.1L_C$ downstream of the car and decreases

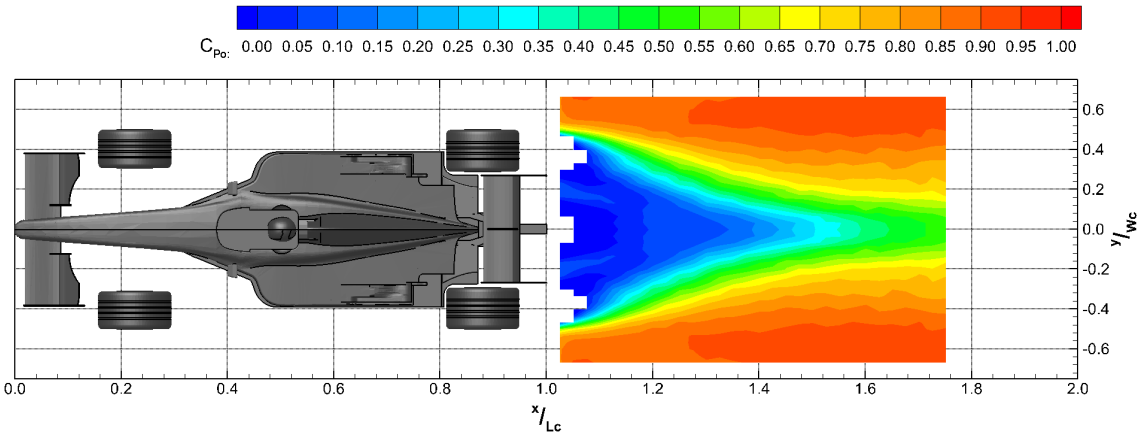


**(a)** 25% Formula 1.

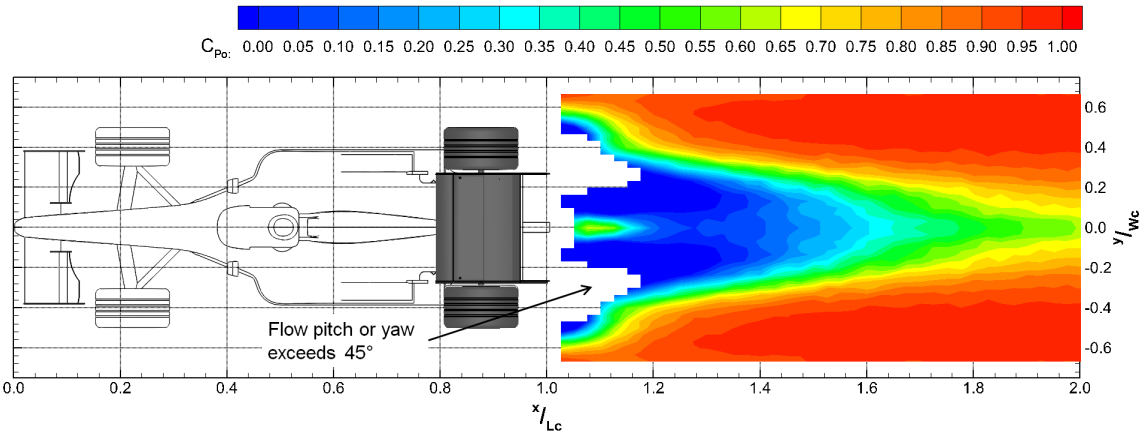


**(b)** Wake generator.

**Figure 4.16:** Wake contours of $C_{P_O}$, XY plane on waistline ($z = 0.5d_{Wheel}$).

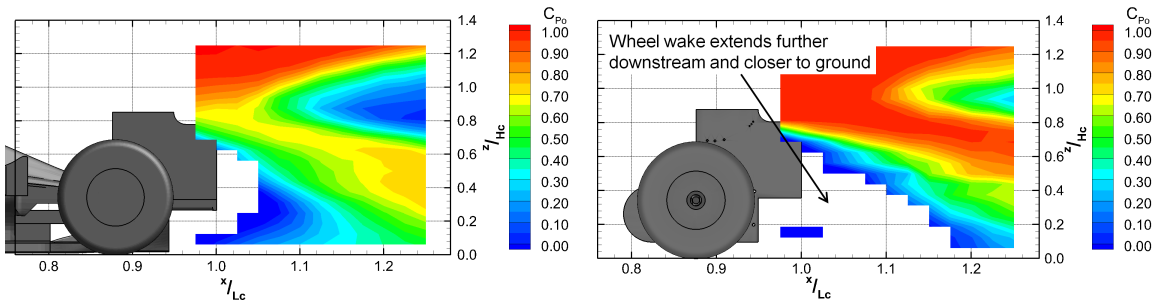


**(a)** 25% Formula 1. **(b)** Wake generator.

**Figure 4.17:** Wake contours of $C_{P_O}$, XZ plane on wheel centreline ($y = 0.4W_C$).

by half to $C_P - 0.25$ by just $x = 1.25L_C$ downstream of the car. The relatively short span of the rear wing means that a strong interaction occurs between the vortex pair, creating a strong centreline up-wash between the vortex centres, $0.4H_C < z < 0.8H_C$. In the near wake the vortices are also constrained by the ground plane, which increases the horizontal component of the secondary flows near the ground and the secondary flows are forces into an elliptical shape. Further downstream the centreline up-wash in the wake combined with the diffusion as the wake loses energy helps to divert the vortex centres away from the ground, with the secondary flows taking a more circular form and reducing the magnitude of the horizontal

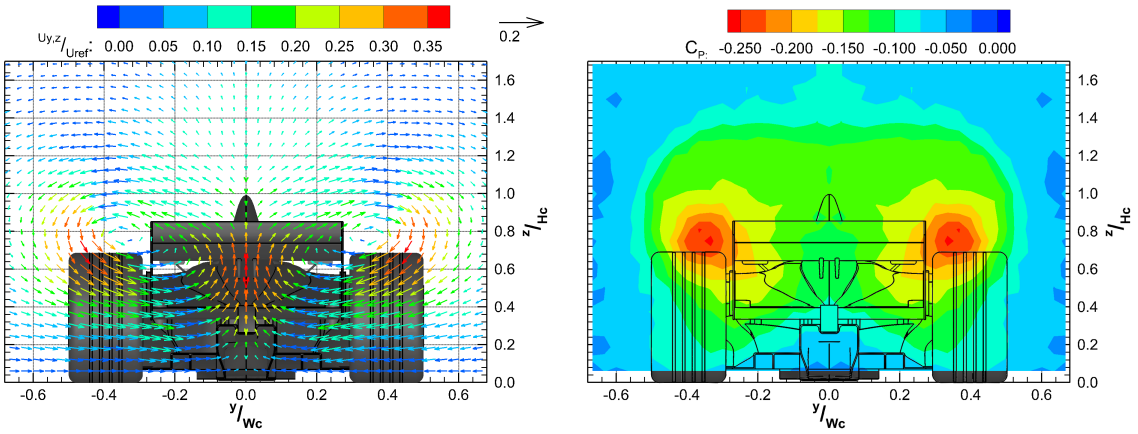


**(a)** $u_{Y,Z}$ vectors. **(b)** $C_P$ contours.

**Figure 4.18:** 25% Formula 1 YZ wake plane at $x = 1.25L_C$.

component of velocity near the ground (figure 4.19).

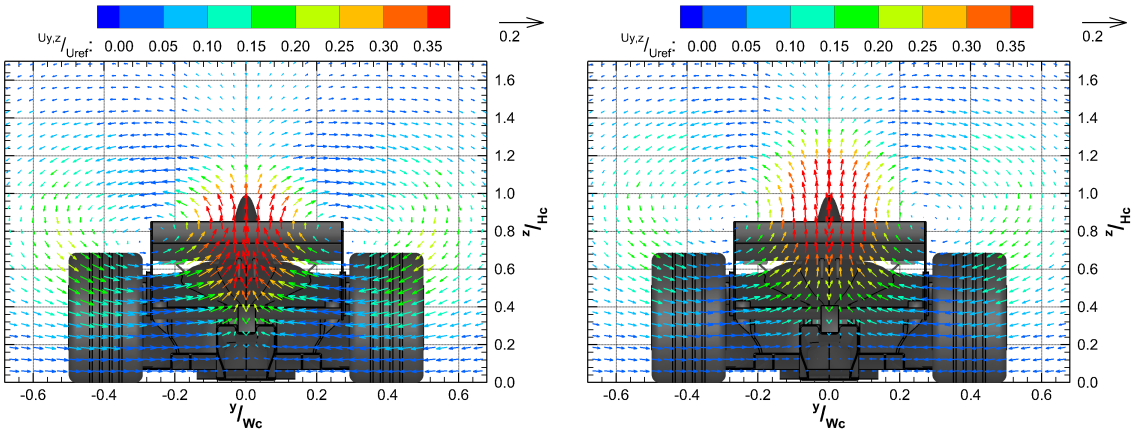


**(a)** $x = 1.50L_C$. **(b)** $x = 1.75L_C$.

**Figure 4.19:** Progression of 25% Formula 1 wake shown by $u_{Y,Z}$ vectors.

Peak vorticity in the wake in confined to the rear wing counter-rotating vortex pair, figure 4.20, though in the wake of the bluff body a lower magnitude vortex persists in the wake close the wheel axle height; as this rotates in the same direction as the rear wing tip vortex it is likely to originate from the bluff body diffuser end fences, though could also be related to the wheel wake. The exact location of the rear wing tip vortices of the 25% Formula 1 and BBWG wakes changes downstream of the vehicles, though they fall in the same approximate region outboard of the rear wing endplates (figure 4.20b). The vortex centre of the BBWG are slightly higher in the wake, possibly due to ride height differences or a difference of rear wing downforce level resulting from the more uniform onset condition, without any upstream bodywork. The position the vortex cores move with the rotation of the vortex, i.e. clockwise for the right endplate and counter-clockwise on the left.

Despite static pressure in the vortex cores in excess of $C_P = -0.5$ the static pressure deficit averaged over the base region of the car is relatively low, $\bar{C_P} = -0.11$ at $x = 1.10L_C$ falling to $\bar{C_P} = -0.071$ by

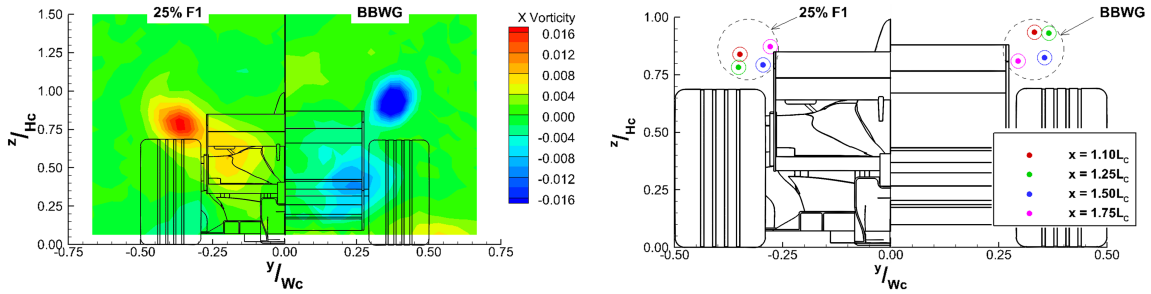


**(a)** Axial vorticity ($\Omega_X$) at $x = 1.25L_C$ **(b)** Vortex core locations.

**Figure 4.20:** Comparison of rear wing vortices.

$x = 1.75L_C$. Much of the total pressure deficit in the wake, figure 4.21, is therefore from dynamic pressure and initially results from the individual body wakes, i.e. wheels, body, and rear wing. The influence of the rear wing vorticity (both the low static pressure in the core and the secondary flows) on the pressure deficit is evident, with the dynamic pressure deficit swept to the centreline and becoming more homogeneous by just $x = 1.25L_C$ downstream. Further aft of the car the stagnation pressure deficit in the wake takes on a form which is sometimes termed 'mushroom' or 'T' shaped, as it is confined to a column on the centreline and the two vortices at rear wing height. As the wake further progresses (between $x = 1.5L_C$ and $x = 1.75L_C$) the peak pressure deficit reduces as wake the decays, while the 'cap' of the mushroom becomes larger with the diffusion of the rear wing vortex pair.

One dimensional plots of velocity deficit on the wake centrelines, figure 4.22, indicate the same improvement of accuracy downstream of the wake generator as the centreline contours of stagnation pressure (figure 4.15). At $x = 1.1L_C$ the difference is large, the BBWG wake is higher velocity by $u_X < 0.6U_\infty$ than the 25% Formula 1 car, under $z = 0.5H_C$. By $x = 1.5L_C$ to $1.75L_C$ the velocity deficits are remarkably similar in both profile and magnitude, despite differences in the near wake; possibly as the larger wheel wakes of the exposed wheels are swept to the centreline by the rear wing vorticity.

The difference in wake up-wash is much smaller at $x = 1.1L_C$ than axial velocity deficit, figure 4.23, though is still $u_Z = 0.2U_\infty$ higher in the BBWG wake. Downstream of $x = 1.25L_C$ the magnitude of peak up-wash is comparable between the vehicles, though the height at which peak up-wash occurs is initially greater in the BBWG case, and downstream of $x = 1.5L_C$ it is greater for the 25% Formula 1 car wake.

No hot wire measurements of turbulence intensity in the wake were made in this study; though turbulence intensity in the wake of a 2008 style Formula 1 car was measured by Wilson, Dominy & Straker [7], and was found to exceed 30% over much of the projected area of the car, at $x = 1.25L_C$, with local peaks up to 45% at the rear wing endplates and diffuser end fences (see figure 1.23e). The authors also found the effect of a uniform turbulence intensity on a wing in ground effect was an increase of peak downforce relative to an isolated wing due to delayed stall incidence resulting from the turbulent boundary layer,

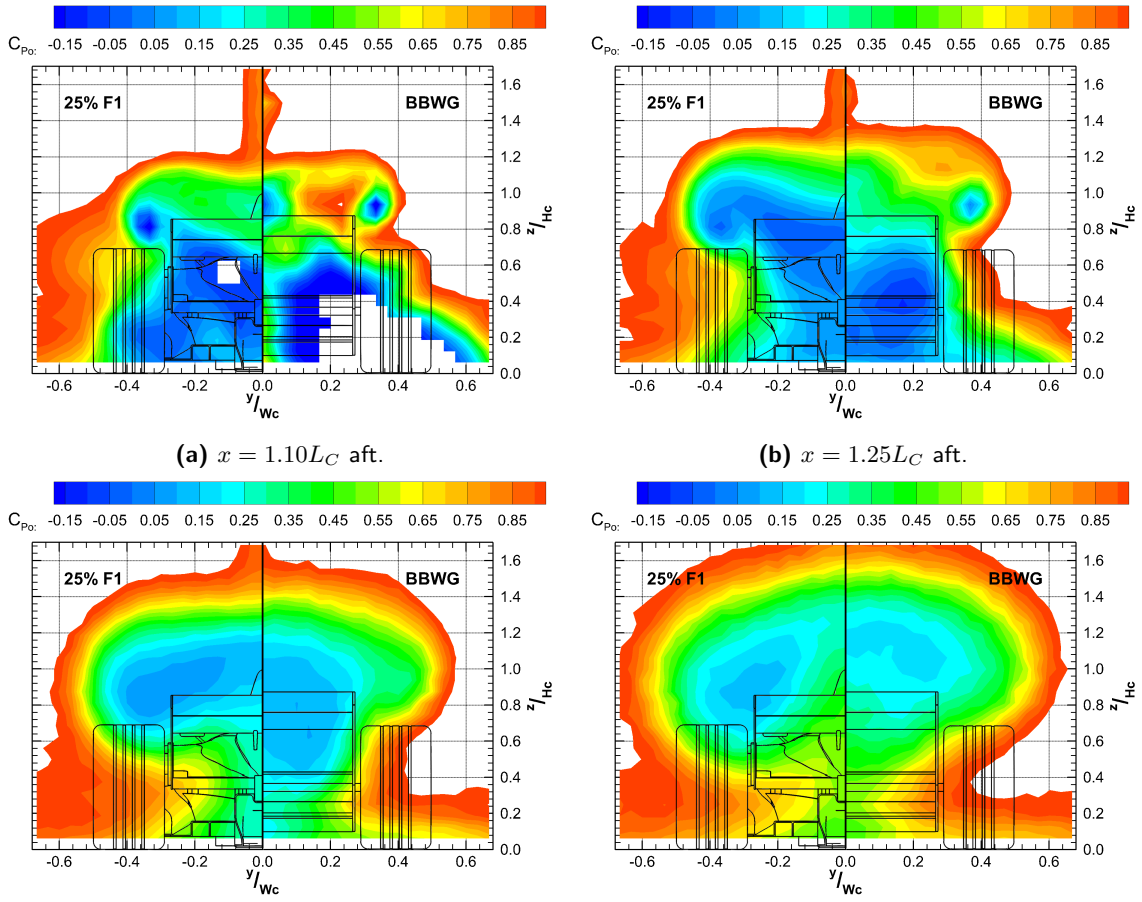


**(a)** $x = 1.10L_C$ aft. **(b)** $x = 1.25L_C$ aft.

**(c)** $x = 1.50L_C$ aft. **(d)** $x = 1.75L_C$ aft.

**Figure 4.21:** Wake contours of $C_{P_O}$ (hidden above $C_{P_O} = 0.95$), YZ planes comparing F1 (left) and BBWG (right) wakes.

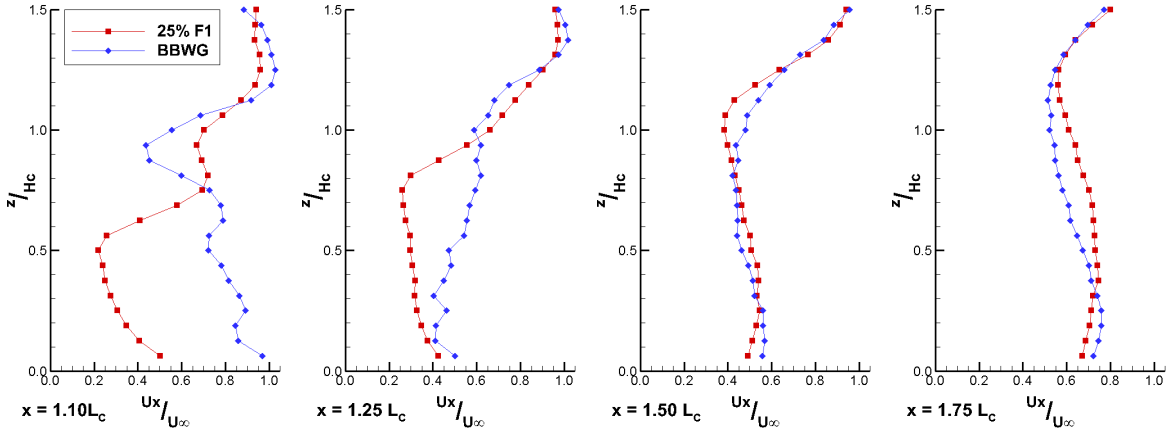


**(a)** $x = 1.10L_C$ **(b)** $x = 1.25L_C$ **(c)** $x = 1.50L_C$ **(d)** $x = 1.75L_C$

**Figure 4.22:** Normalised velocity profile on wake centreline comparing axial velocity deficit in the 25% F1 model and BBWG wakes.

suggesting that it is other features in the wake rather than turbulence intensity are responsible for the reduced downforce experienced by a following vehicle.

In spite of the differences present in the wake described above, the key wake variables, namely a counter-

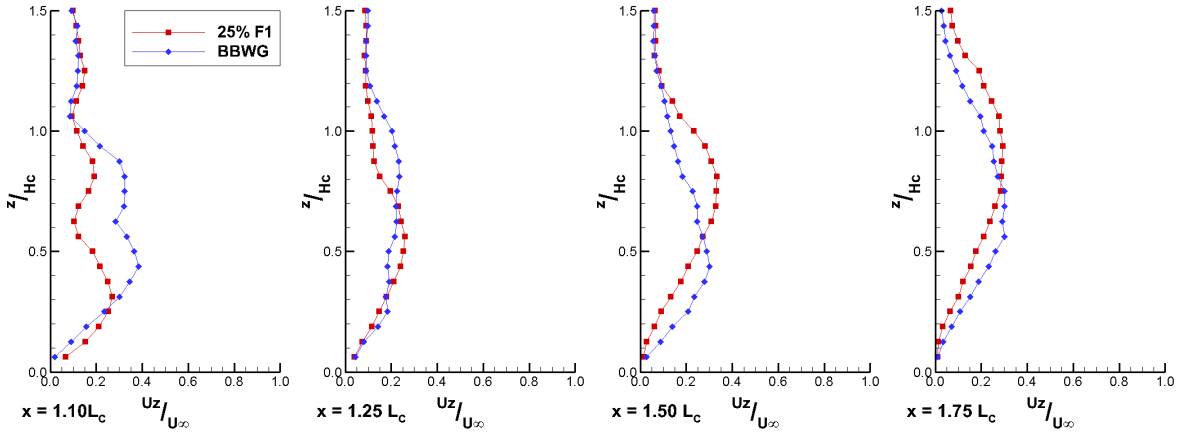


**(a)** $x = 1.10L_C$ **(b)** $x = 1.25L_C$ **(c)** $x = 1.50L_C$ **(d)** $x = 1.75L_C$

**Figure 4.23:** Normalised velocity profile on wake centreline comparing up-wash in the 25% F1 model and BBWG wakes.

rotating pair of vortices with a centreline up-wash, and a velocity deficit, which continues many car lengths downstairs of the wake generator are created. The accuracy of the wake gains improves with distance from the wake generator and is best for mid to long distances aft of the BBWG, beyond $x = 1.4L_C$.

## 4.3 Effect of an Upstream Wake Generator

The purpose of the experimental study is to quantify the effect of the upstream wake, in this case from the wake generator (BBWG), on a following vehicle. The wake generator was placed on the moving ground between the nozzle and the 25% Formula 1 car, figure 4.24. With the Formula 1 car placed $500mm$ ahead of the rear of the moving belt the greatest possible separation to the wake generator was one car length, $1.0L_C$, when measured from the rearmost overhang of the wake generator to the foremost overhang of the Formula 1 car. A total of five axial separations were tested in divisions of $0.2L_C$, to a minimum separation of $x = 0.2L_C$, figure 4.25, any shorter was considered to be unrepresentative of an overtaking manoeuvre. The wake at the $x = 0.2L_C$ separation is the least accurately recreated of all the axial locations, but is still downstream of any recirculated flows in the wake. While the inter-vehicle positions are given relative to the rear overhang of the wake generator, figure 4.25, the wake generator was moved relative to the tunnel co-ordinate system so that the instrumented vehicle location was stationary in the wind tunnel.

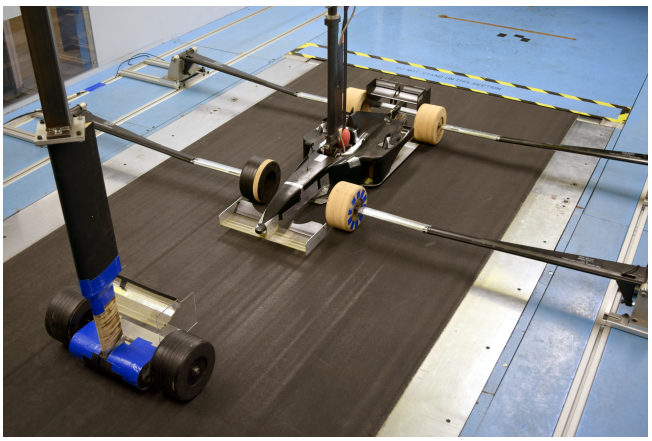

**Figure 4.24:** Experimental setup in Durham University 2m wind tunnel, vehicle at $(x, y) = (0.4L_C, 0.0W_C)$ (BBWG reference).

As well as axial separations a number of lateral offsets were tested, $0.75W_C$ being the greatest offset possible with both of the wake generators wheels on the moving ground. As the wake was presumed to be symmetrical about the centreline, forces were recorded only in the Y+ direction, figure 4.25. The surface pressure tappings were distributed solely on the Y- side of the car so pressures measurements were recorded for both positive and negative lateral offsets.

### 4.3.1 Effect of the Wake Generator, Axially Aligned at Single Vehicle Separation

The most fundamental slipstreaming case to consider is the axially aligned case with a one vehicle separation, $(x, y) = (L_C, 0)$, which is considered to be the closest a pair of vehicles would come on-track in normal conditions (i.e. both drivers are in full control of their respective vehicles) prior to commencement

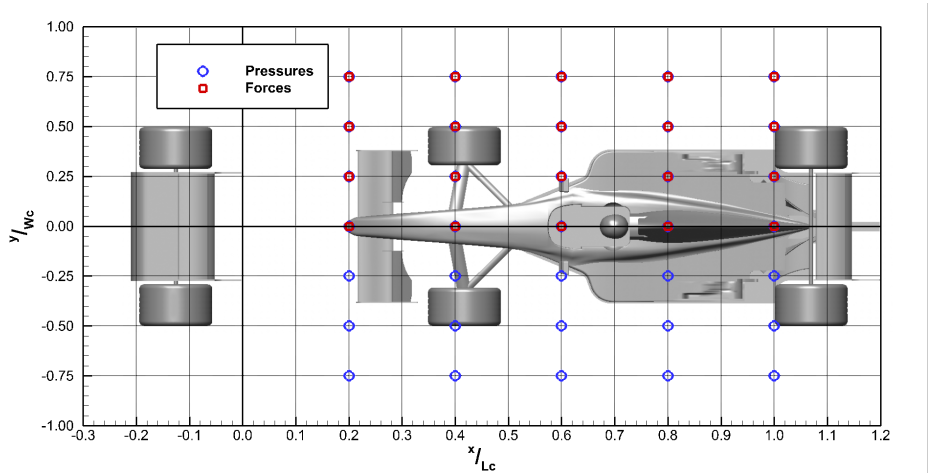


**Figure 4.25:** Experimental setup for wake generator study, vehicle at $(x, y) = (0.2L_C, 0.0W_C)$ (BBWG reference).

of an overtaking manoeuvre.

The upstream wake causes a loss of downforce, $0.426 < C_L < 0.456$, and decreased drag, $-0.157 < C_D < -0.141$, for the following vehicle, figure 4.26. The effect of vehicle posture, at this location relative to the BBWG, is minimal; though downforce seems less affected by the upstream wake when the car is at high pitch angles, conversely the greatest loss of downforce occurs when the car is flat. For each pitch angle, the drag decrease is greater at the higher ground clearance. In this instance the drag loss is smallest at the lowest ground clearance with maximum pitch.

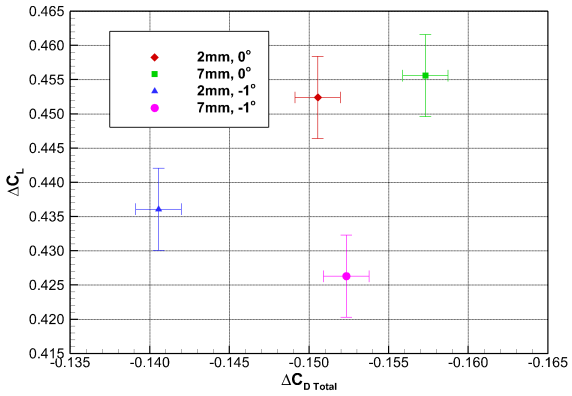


**(a)** Δdrag vs Δdownforce.

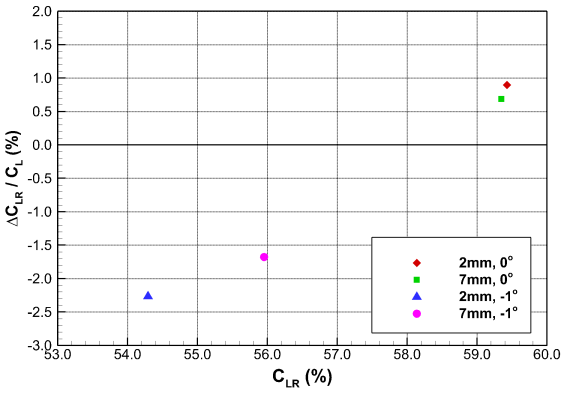


**(b)** Balance (absolute) vs Δbalance.

**Figure 4.26:** Effect of upstream BBWG at $x = 1.0L_C$, $y = 0.0W_C$.

Like the downforce loss, the change of the aerodynamic balance is linked to the vehicle pitch. The balance moves rearwards for flat postures and forwards with nose down pitch. The balance shift is only in the range of $-2.5\% < \dfrac{C_{LR}}{C_L} < 1\%$, which is a smaller shift than seen in previous slipstreaming studies [1, 92], however the separation between vehicles in this study is greater than has been previously achieved.

The front wing pressure distribution experiences a change with the upstream wake (figure 4.27), with only small variation between the four postures tested. The front wing centreline lower surface experiences a

$\Delta C_P \approx 0.6$ which occurs at around $15 - 20\%$ of the chord, approximately the same location that peak suction occurs. On the centreline the upper surface of the wing experiences a reduction of pressure over the leading edge to $x = 0.12c$ of the chord, after which pressure increases, though by less than $\Delta C_P = 0.1$.

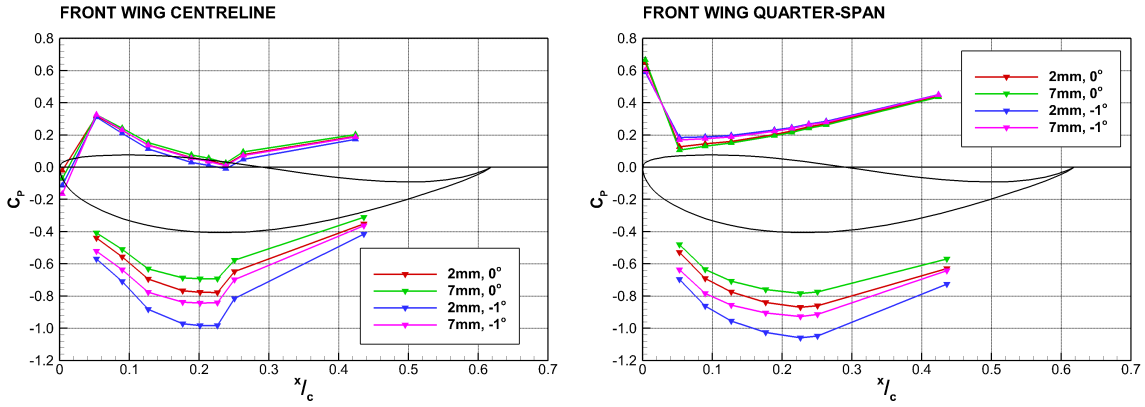


**(a)** Pressure distribution.

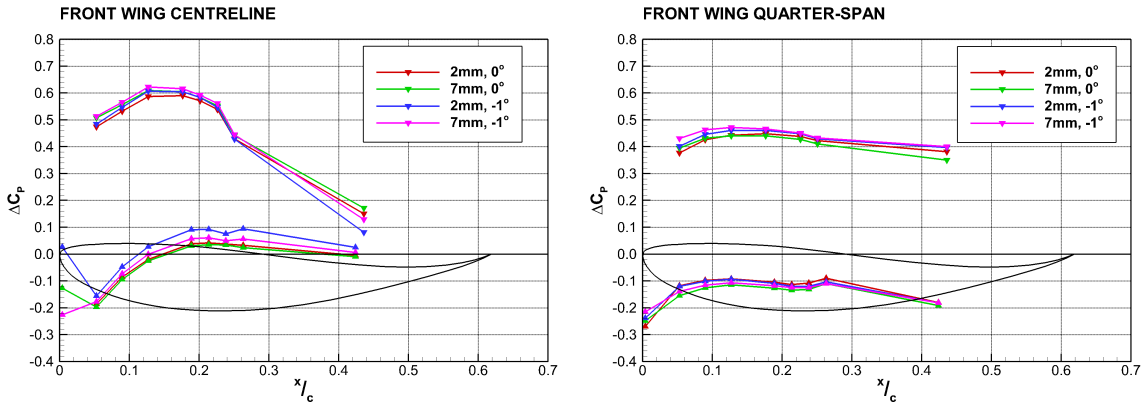


**(b)** Change of pressure compared to isolated vehicle.

**Figure 4.27:** Effect of BBWG at $(x, y) = (L_C, 0)$ on front wing static pPressures (up arrows = upper surface, down arrows = lower surface).

The quarter-span lower surface experiences a pressure increase over the whole instrumented length of the chord, this is because in freestream running the flap affects the pressure towards the trailing edge. The overall suction loss is lower magnitude than the centreline $\Delta C_P < 0.5$, but the flatter profile indicates that the under surface of the flap also loses suction. Like the underside the upper surface loss is more significant at the trailing edge, due again to the flap pressure profile towards the trailing edge. The leading edge pressure does not reduce by much $(-0.2 < \Delta C_P < -0.26)$, considering for all conditions the first tapping is near the stagnation point. The reduction is unlikely to be the result of the static pressure deficit in the wake of the BBWG, which is $C_P < 0.05$ at this separation.

The effect of the wake generator on downforce generated by the front wing mainplane, approximated from the pressure distributions of both the centreline and at quarter-span, is shown in figure 4.28. Downforce generated by the wing is reduced from the baseline for all car postures. The effect of the wake on front wing downforce increases as the ground clearance of the front wing is reduced. Nose-down pitch moves the front wing closer to the ground so that for the $7mm, -1°$ posture, the front wing is at a similar

ground clearance to $2mm, 0°$, and the downforce loss is similar, $\approx 45\%$. While the front wing is lowest for the $2mm, -1°$ posture, and downforce loss is greatest, almost $65\%$ on the centreline. The reduction of downforce is greater on the centreline than at the quarter-span for all postures, by between $5\%$ and $15\%$, which could relate to the concentration of the wake dynamic pressure deficit on the car centreline (figure 4.21).

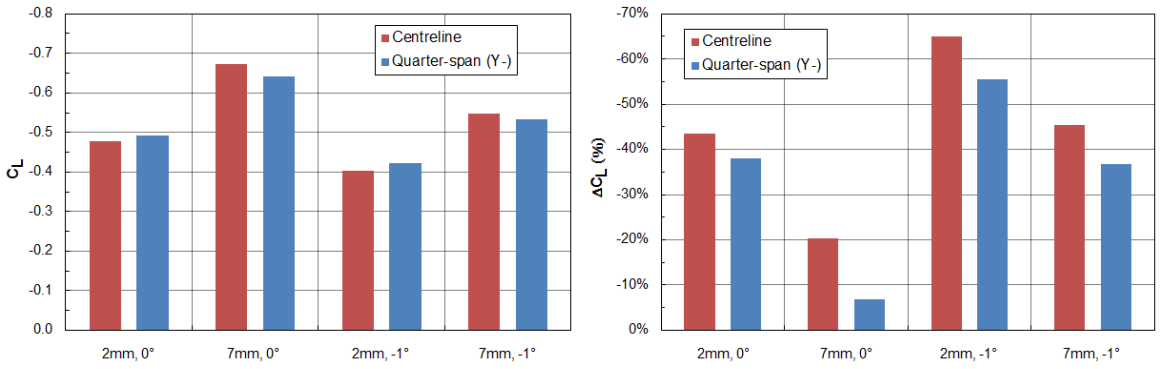


**(a)** Absolute downforce. **(b)** Percentage downforce loss.

**Figure 4.28:** Effect of BBWG at $(x, y) = (L_C, 0)$ on front wing downforce.

Like the front wing, the underfloor pressure distribution is not significantly varied by car posture, at this BBWG separation (figure 4.29). The change in pressure for both ride heights at $\theta = 0°$ is mostly a uniform $\Delta C_P = 0.05$, with local increases of $\Delta C_P = 0.1$ at the leading edge of the floor and $\Delta C_P = 0.15$ just ahead of the diffuser throat. When the car is at $\theta = -1°$ the pressure increase towards the rear of the floor is lower ($\Delta C_P < 0.05$). It could be said that in freestream conditions the $-C_P$ in this area is lower for the nose-down cases than the flat cases, and the percentage difference is similar. The change in pressure just in front of the diffuser kick also peaks at a smaller $\Delta C_P$ with pitch on the car ($\Delta C_P \approx 0.1$) than with no pitch ($\Delta C_P \approx 0.15$).

The integral of the surface pressure in the region of the contours shows an average loss of downforce of $34\%$ for the instrumented area of the underbody, figure 4.30. The greatest downforce losses, at this BBWG separation, occur for the $7mm$ ride height cases at each attitude. Contrarily to the front wing downforce loss, the greatest underbody loss of downforce happens for the $7mm, 0°$ posture, $\Delta C_L = -39\%$. It is more difficult to infer a cause of the loss for the underbody, as the quality of flow to this region is dependant on the front wing and wheel wakes.

### 4.3.2 Effect of the Wake Generator, Axially Aligned with Reducing Inter-Vehicle Separation

The general trend, with reducing the separation to the BBWG, is a further reduction of the drag and downforce with the balance shifting increasingly rearwards, figure 4.31. The maximum decrease in drag

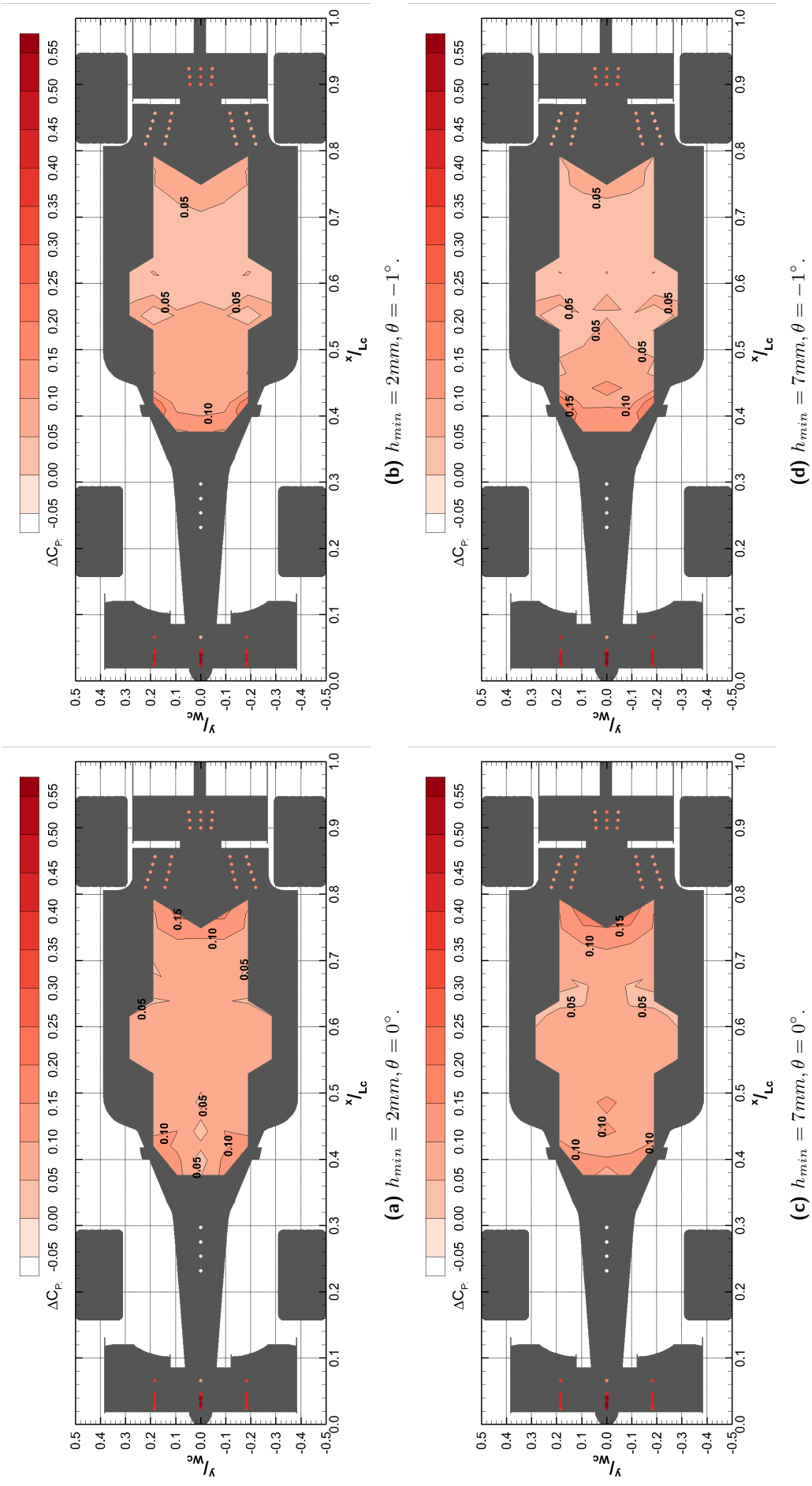


**(a)** $h_{min} = 2mm, \theta = 0°$.

**(b)** $h_{min} = 2mm, \theta = -1°$.

**(c)** $h_{min} = 7mm, \theta = 0°$.

**(d)** $h_{min} = 7mm, \theta = -1°$.

**Figure 4.29:** Contours of $\Delta C_P$ on vehicle underbody with upstream BBWG at $(x, y) = (L_C, 0)$.

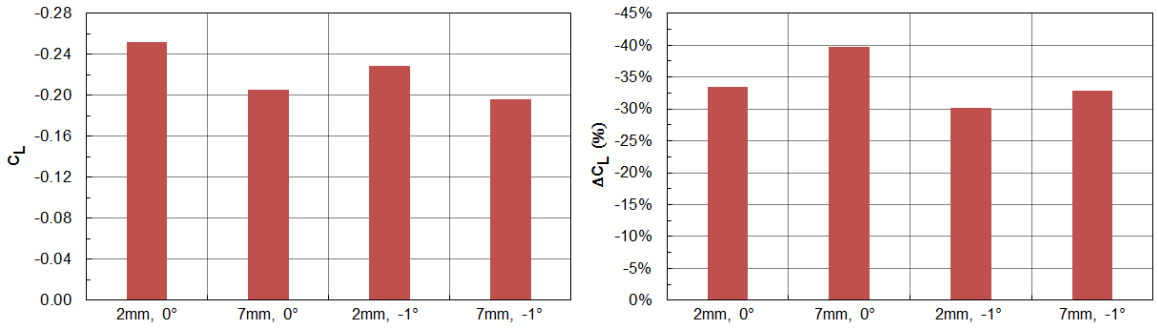


**(a)** Absolute downforce.

**(b)** Percentage downforce loss.

**Figure 4.30:** Effect of BBWG at $(x, y) = (L_C, 0)$ on underfloor downforce.

is found at the minimum separation to the BBWG, $\Delta C_D \approx -30\%$, though the minimum decrease is not found at the maximum separation. Instead the minimum loss of drag ($\Delta C_D \approx -15\%$) is experienced at $x = 0.8L_C$ downstream of the BBWG. There does appear to be a relationship between the decrease of drag and vehicle posture, with the $2mm, -1°$ case experiencing the smallest decrease for all separations and the $7mm, 0°$ case experiencing the greatest decrease, especially at the closer separations. That said the effect of posture on drag reduction is not substantial, only in the range of $\Delta C_D \approx \pm 0.01$ or $\pm 1.3\%$ of the baseline drag.

The change in downforce with BBWG separation is more in line with conventional thinking, with the loss increasing as the separation to the BBWG is reduced from an average of $-38.4\%$ of the undisturbed total at $x = 1.0L_C$ to $-69.9\%$ at $x = 0.2L_C$. Even a $38\%$ loss of downforce as experienced at the greatest separation would result in a significant reduction of cornering performance, and a major effect on lap-time. Posture again appears to affect to the force loss with the $\theta = 0°$ set-ups experiencing the greatest loss of downforce, especially at separations greater than $x = 0.4L_C$. The variance between postures is greater than for drag ($\pm 0.015 < \Delta \bar{C}_L < \pm 0.03$), but still small compared to the total downforce lost. It can be concluded that to potentially compromise the car set-up for the possibility of running in another cars wake would not result in a significant enough improvement to overcome the reduced lap-time.

As previously noted the aerodynamic balance actually moves forwards between $-1.5\% < \dfrac{C_{LR}}{C_L} < -2.5\%$ at $x = 1.0L_C$ for the $\theta = -1°$ car postures. The forwards shift of the balance continues up to $x = 0.6L_C$ for the $\theta = -1°$, low ride height case; $x = 0.7L_C$ for the higher ride height. As well as vehicle pitch the ride height also appears to affect the extent of the rearwards balance shift, with the $h_{min} = 2mm$ cases experiencing less of a balance shift than the $h_{min} = 7mm$ cases for both postures. Like downforce loss the slope of the rearwards balance shift increases with decreasing separation to an average of $\Delta \dfrac{\bar{C}_{LR}}{C_L} = 23\%$, which would cause a significant change in the handling balance to increased understeer. What is surprising is that the balance shift remains under $5\%$ for all postures for separations greater than $0.6L_C$, while a $5\%$ increase of load on the rear axle represents a fairly significant change of balance, it is lower than expected and perhaps represents a limitation of the short BBGW.

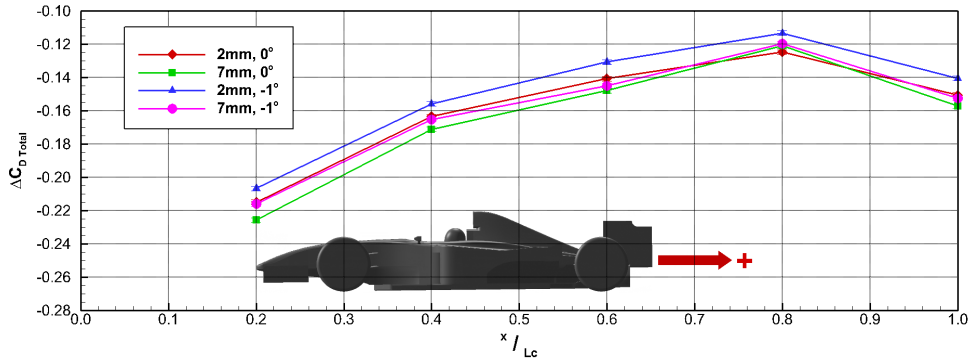


**(a)** Δ drag.

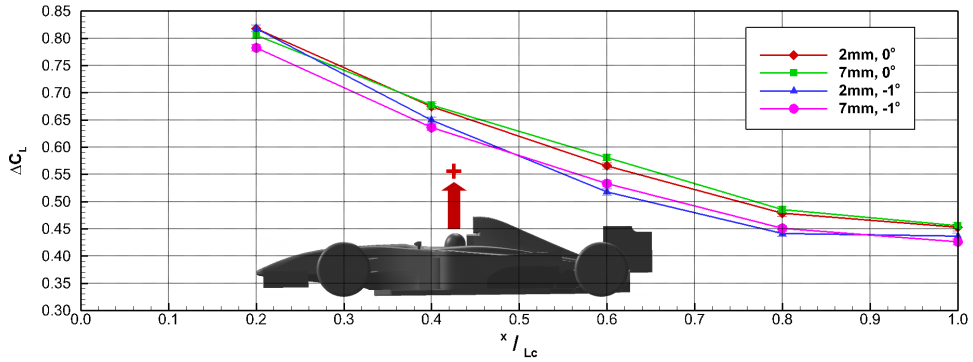


**(b)** Δ lift.

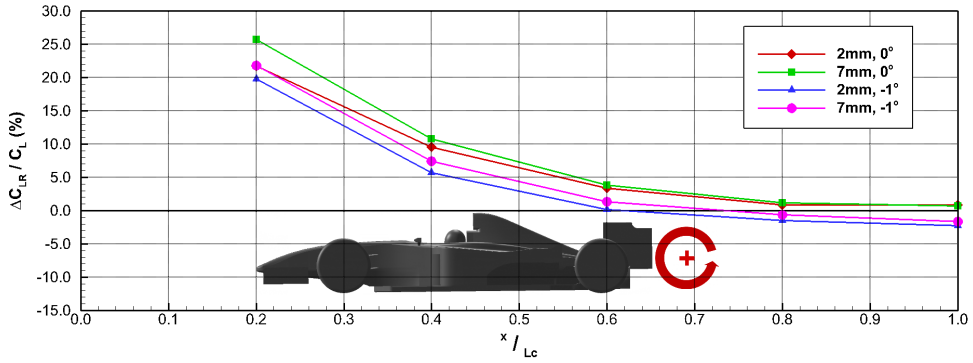


**(c)** Δ aero-balance.

**Figure 4.31:** Effect of axially aligned BBWG on downstream vehicle forces.

The effect of the reducing separation to the BBWG on the front wing pressure distribution of the optimal car posture is shown in figure 4.32. The lower surface pressure at both centre and quarter-spans increases incrementally with the reducing separation. The only exceptions are the front wing centreline between $x = 0.4L_C$ and $x = 0.2L_C$, which is potentially caused by the up-wash in the very near wake driving the lower surface of the wing. The other exception is between $x = L_C$ and $x = 0.8L_C$ on the quarter-span where the greater separation experiences a greater increase of surface pressure, though the difference is less than $\Delta\bar{C}_P = 0.02$. On the lower surface of the centreline the chordwise location of the peak $\Delta C_P$ remains at $x \approx 0.18c$ for all separations, while the quarter-span $\Delta C_P$ moves rearward on the chord as the vehicle separation reduces, from $x \approx 0.18c$ to $x \approx 0.23c$.

The effect of the wake on the front wing downforce for all postures is shown in figure 4.33. The profile of

the centre-span downforce loss is very different to the quarter-span, peaking at between $90\%$ and $100\%$ at the $x = 0.4L_C$ separation for all but the $2mm, 0°$ posture, this must predominantly be the result of the concentration of the velocity deficit and up-wash in the wake on the car centreline. The posture results in a great discrepancy in the downforce loss of around $45\%$ on both the centre and quarter-spans at $x = L_C$, the rest of the axial BBWG separations only experience a $< 20\%$ difference of downforce loss between postures. The profile of the downforce loss at quarter-span is almost linear between $x = 0.8L_C$ and $x = 0.2L_C$, and the wing Z direction force per span actually crosses into lift for all but the $2mm, -1°$ posture, albeit $C_L < 0.03$.

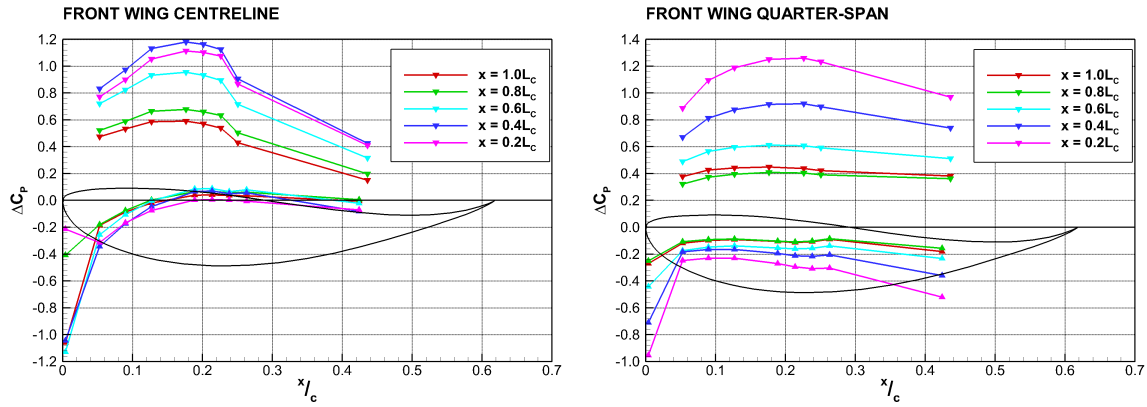


**Figure 4.32:** Front wing pressure distribution with reducing axial separation, $2mm, 0°$ posture.

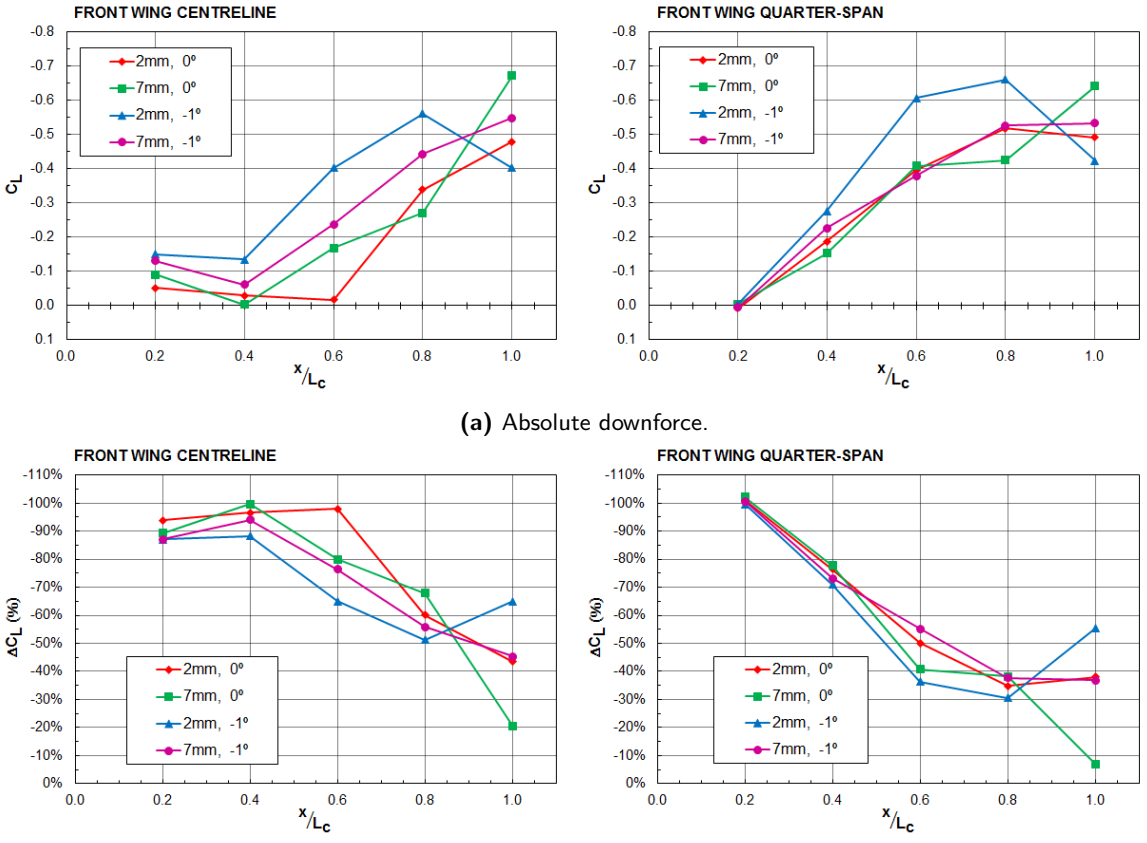


**(a)** Absolute downforce.

**(b)** Percentage downforce loss.

**Figure 4.33:** Effect of axially aligned BBWG, with reducing separation, on downstream vehicle front wing downforce.

The underbody surface pressure distribution is similarly affected to the $(x, y) = (L_C, 0)$ case for all the inter-vehicle separations, figures 4.35 and 4.36, with the magnitude of $\Delta C_P$ increasing with the shorter separation. Like the front wing, regions of high $-C_P$ are more affected than regions of low $-C_P$. Meaning for the $0°$ postures the greatest $\Delta C_P$ happens at the front of the floor and ahead of the diffuser throat, with relatively little change in the mid-floor region. Conversely for the nose-down postures the greatest $\Delta C_P$ occurs at the leading edge of the underfloor, with a smaller change from the mid-floor to the diffuser throat. This must, in part, be the reason that the aero-balance shift is less rearward for the nose-down postures for all separations, figure 4.31c, as the underbody loses more downforce toward the front axle for the nose-down postures.

The absolute downforce generated by the underbody corresponds to the vehicle ride height, figure 4.34a, with the $2mm$ ride height cases generating a greater quantity of downforce than the $7mm$. This is not the behaviour of the car in freestream conditions, where the flat postures both create more downforce from the underfloor than the nose-down postures. The downforce loss is however linked to the vehicle attitude, figure 4.34b, and the the flat postures lose more downforce. The $7mm, 0°$ posture loses the greatest downforce for all postures, with the exception of the $x = 0.8L_C$ separation. The sudden decrease of the underbody downforce loss at this separation could be considered anomalous, however that it occurs for both the $7mm$ ride height cases means it could be the result of sheer in the wake at a height of above the ground plane between $0.008H_C$ and $0.029H_C$ at this downstream separation. The peak underbody downforce loss is significantly lower than the front wing, which experiences almost total force loss for the closest separations, peaking at between $45\%$ and $57\%$ depending on posture. This could be because important features of the underfloor are not represented by pressure tappings, the contour plot only covers $79\%$ of the total undertray area, so the actual underfloor loss could be greater than the results show, however as the total vehicle downforce loss at the shortest separation is $60\%$ (figure 4.31b) and the underfloor must be responsible for some of this downforce.

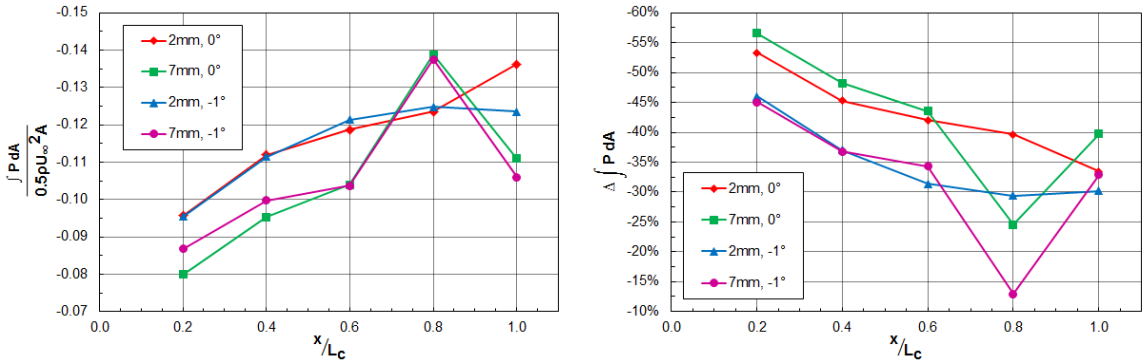


**(a)** Absolute downforce.

**(b)** Percentage downforce loss.

**Figure 4.34:** Effect of axially aligned BBWG, with reducing separation, on downstream vehicle underbody downforce.

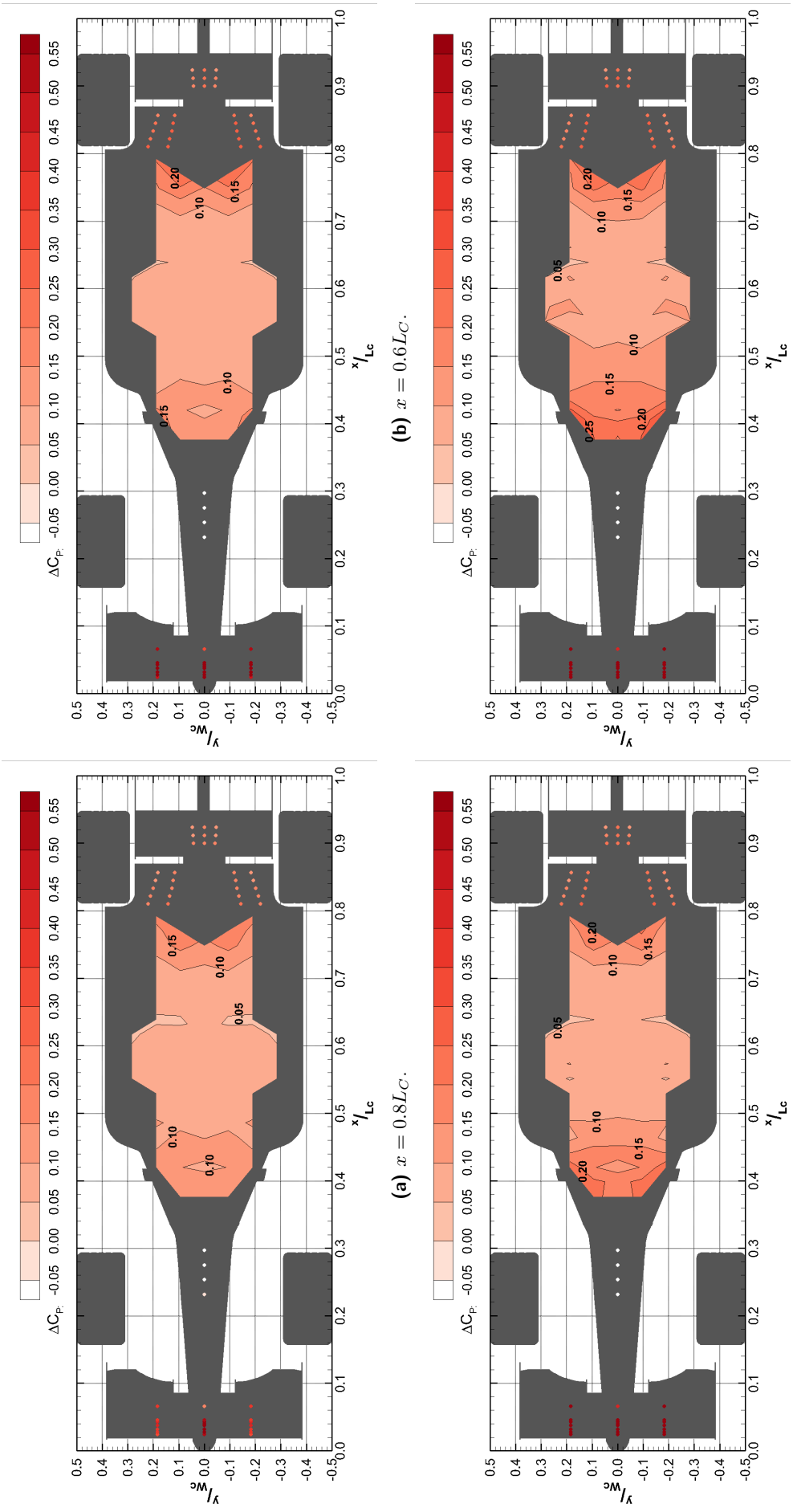


**Figure 4.35:** Effect of reducing axial separation to BBWG on underbody pressure sistribution, $2mm, 0^{\circ}$ posture.

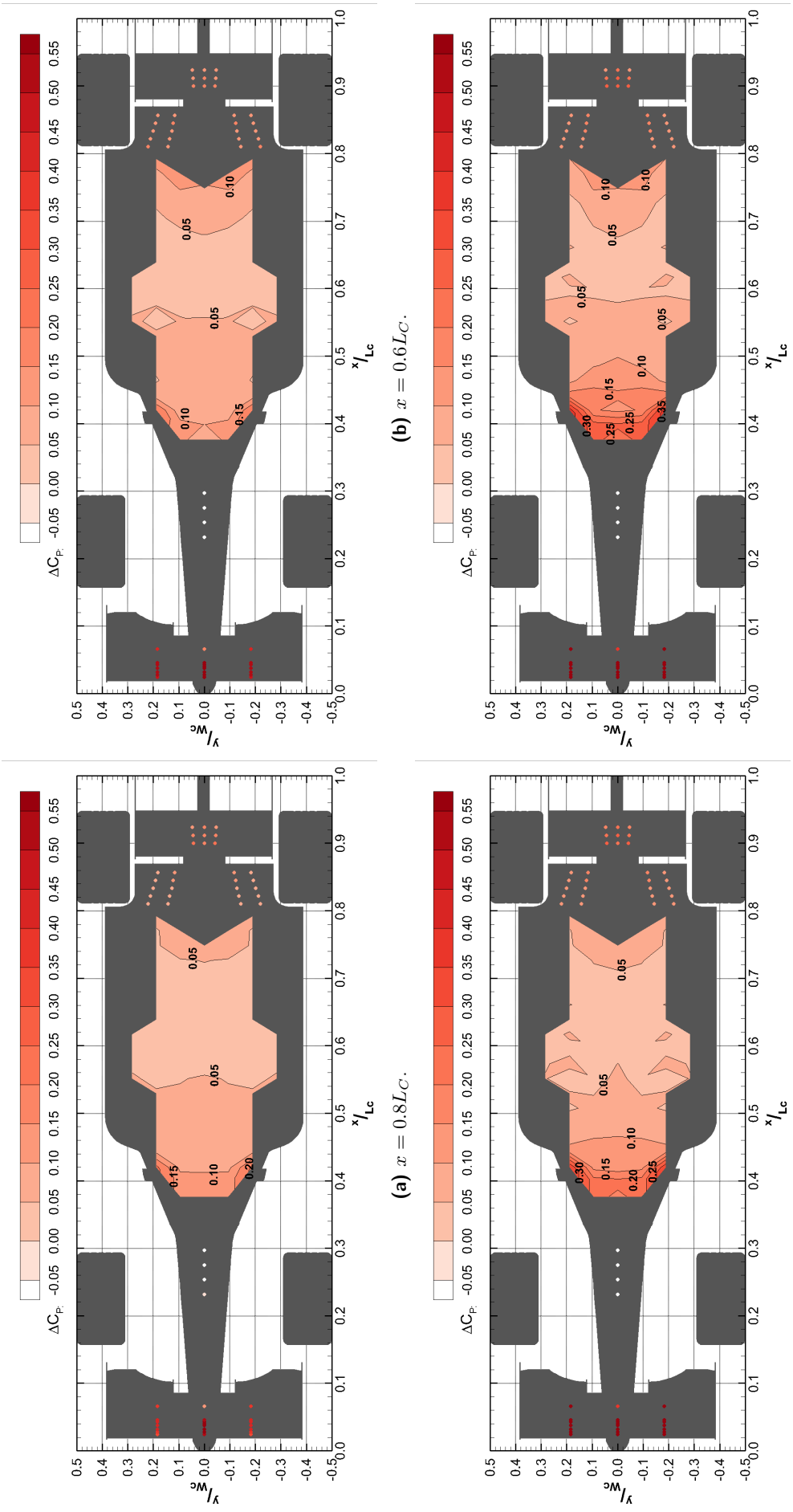


**(a)** $x = 0.8L_C$. **(b)** $x = 0.6L_C$. **(c)** $x = 0.4L_C$. **(d)** $x = 0.2L_C$.

**Figure 4.36:** Effect of reducing axial separation to BBWG on underbody pressure distribution, $2mm, -1^\circ$ posture.

### 4.3.3 Effect of the Wake Generator, Lateral Offsets

It is highly unlikely that in a drafting scenario the second vehicle will follow precisely in the tyre tracks of the lead car; so for each axial separation, forces and pressures were collected for lateral offsets up to $y = \pm 0.75 W_C$ in increments of $0.25 W_C$ (figure 4.25). The $y = 0.75 W_C$ offset was the furthest outboard the wake generator could be placed in the wind tunnel with both wheels still on the moving ground plane, also situating the outboard wheel of the wake generator in the fluid jet. As the wake is symmetrical about the car centreline, especially for the force balance averaging interval, so force measurements were only collected for positive (Y+) offsets. The distribution of pressure tappings over one side of the car meant that surface pressures were collected for both positive and negative offsets.

The effect of the upstream wake generator on the aerodynamic forces of the downstream vehicle are shown using contours of the change of force, figures 4.37, 4.38, and 4.40, with the downstream location given relative to the nose of the following car (figure 4.25). Posture was seen not to affect the change of vehicle forces experienced by the downstream vehicle so the average of the four postures tested is presented, plots for the individual postures can be found in Appendix C.

Aerodynamic drag produced by the following vehicle is reduced for all downstream positions tested, figure 4.37. The effect of the wake is visibly concentrated on the centreline of the wake generator, increasing as the vehicle separation is reduced, peaking at $\Delta C_D \approx -30\%$ at $(x, y) = (0.2 L_C, 0)$. A $30\%$ drag reduction would increase straight line speed by $13\%$, or assuming an average top speed of $U_{max} = 320 kph$ [131], $\Delta U_{max} = 40 kph$. Drag returns to the baseline value more rapidly with a small lateral offset than an equivalent axial offset, if $0.5 W_C = 225 mm$ and $0.2 L_C = 240 mm$ at this scale; from $(0.2 L_C, 0)$ to $(0.4 L_C, 0)$ drag loss decreases by $10\%$, while the lateral offset reduces drag loss by $20\%$.

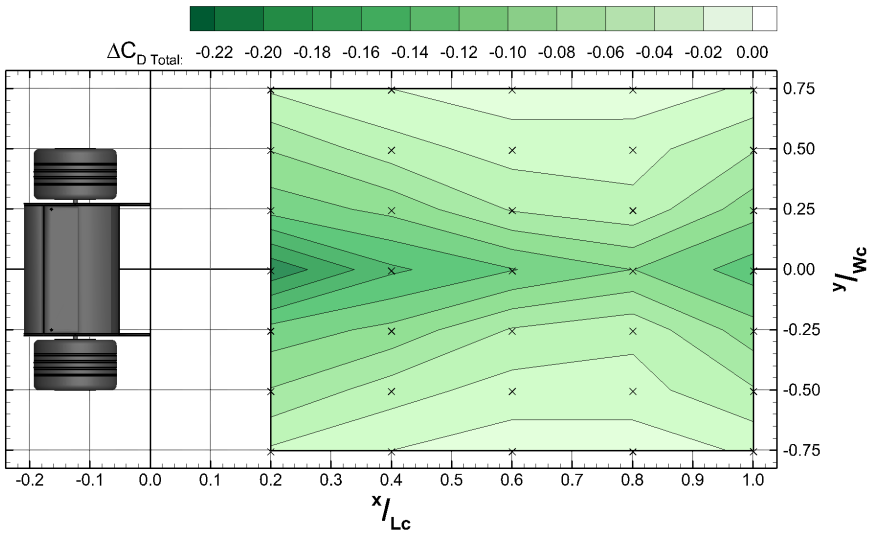


**Figure 4.37:** Effect of upstream wake on drag ($C_D$), averaged for all car postures.

Like drag, downforce loss for the following vehicle is greatest when aligned to the centreline of the wake generator, figure 4.38; however, downforce loss peaks significantly higher than drag loss, $\Delta C_L = -73\%$. As is the case with the reduction of drag, downforce loss is reduced with just a small lateral offset, in this case recovering to the same deficit with a $y = 0.25W_C$ offset as occurs with a $x = L_C$ axial separation. Unlike drag, the downforce recovers to the baseline level with an offset of $y = 0.75W_C$, for all axial separations, meaning that the lift-to-drag ratio (figure 4.39) is greater than the baseline. That drag loss recovers less rapidly with a lateral offset means that for all offsets outboard of $y = 0.5W_C$ the $^L/_D$ is greater than the baseline. While the downforce loss would reduce lateral acceleration in cornering, the lower drag on straights would improve top speed.

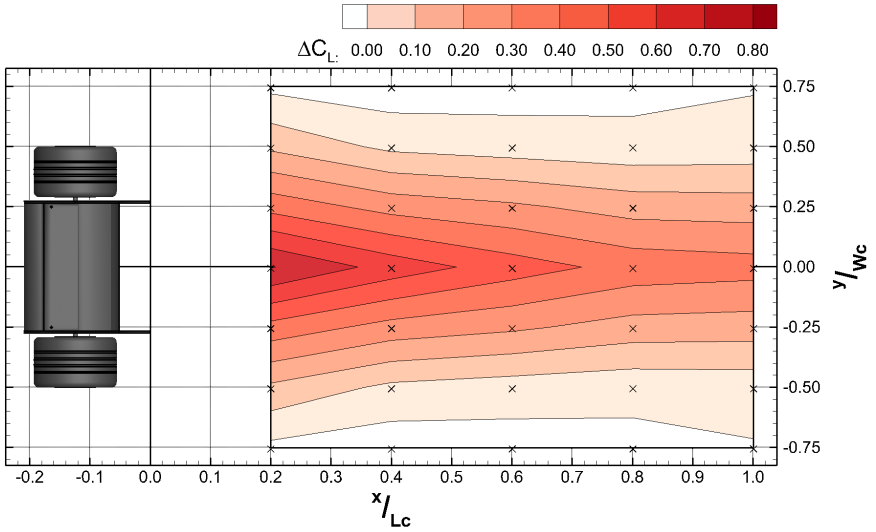


**Figure 4.38:** Effect of upstream wake on downforce ($C_L$), averaged for all car postures.

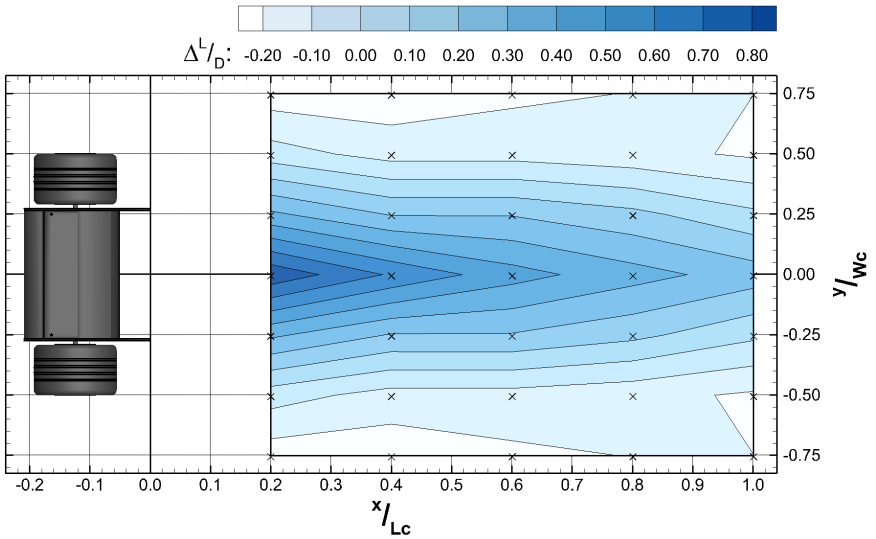


**Figure 4.39:** Effect of upstream wake on lift-to-drag ratio ($^L/_D$), averaged for all car postures.

Not only the downforce loss has an effect on lap-time, the aero-balance (figure 4.40) can affect the handling balance, driver confidence, and ultimately in-corner time. As with the forces, aero-balance is more significantly affected when axially aligned to the wake generator, and for short axial separations.

Interestingly for most positions where $x > 0.8L_C$ and $y > 0.5W_C$ the aero-balance is either unchanged or moves forwards. This is contrary to the established belief that the front axle experiences the greatest downforce loss - certainly for these downstream locations. Closer to the rear of the wake generator the aero-balance does move significantly rearwards, up to $\Delta\frac{C_{LR}}{C_L} = 24\%$ of the wheelbase.

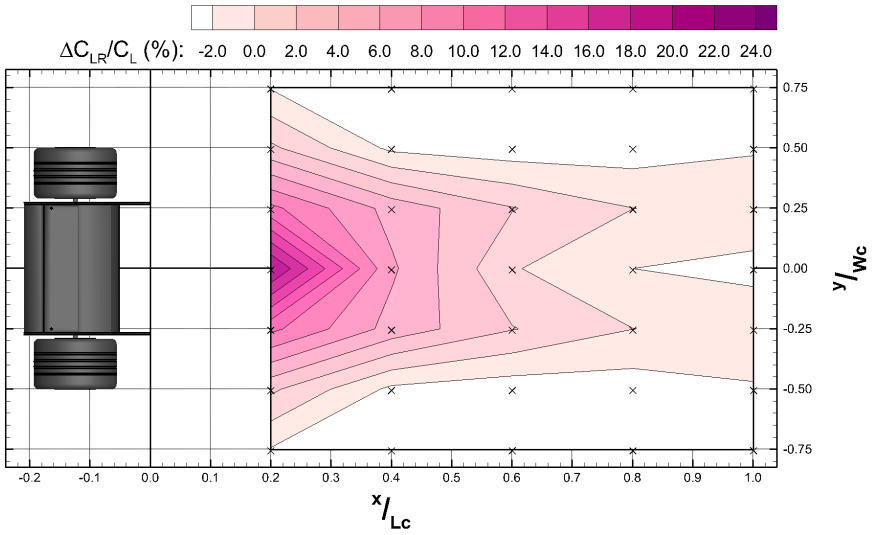


**Figure 4.40:** Effect of upstream wake on aerodynamic balance ($\frac{C_{LR}}{C_L}$), averaged for all car postures.

As with all the force behaviour preceding both the front wing and underbody experience the greatest downforce loss when the car is axially aligned to the wake generator (red lines figure 4.41 and figure 4.44), with the deficit decreasing as the lateral offset increases. The average downforce delta across the span of the front wing is shown in figure 4.41. At the closest separation, when axially aligned, the front wing loses almost $100\%$ of the downforce generated without the upstream wake. This is in-line with the conventional notion that the front wing is responsible for the majority of the downforce loss experienced in the wake [7]. However for the three closest axial separations at $y = 0.75W_C$ the front wing actually gains $\approx 5\%$ downforce relative to the 'clean air' case, possibly due to down-wash in the wake outboard of the rear wheels of the wake generator. The downforce gain could be the cause of the forwards aero-balance shift seen in the outboard positions, however the car aero-balance is forwards of the baseline for most offsets outboard of $y = 0.5W_C$ so there must be secondary cause.

Examination of the front wing downforce distribution for the three instrumented span-wise planes, the front wing centreline with the quarter-span for both the positive (Y+) and negative (Y-) lateral offsets, presented as if the car is travelling in the Y+ direction relative to the wake generator (figure 4.42). Figure 4.43 shows that the individual stations do not deviate from the trend of greater loss with axial alignment, with the exception of the Y- quarter-span at $y = 0.25W_C$; this is the result of the Y- quarter-span sitting behind the centreline of the wake generator (figure 4.42b) and the Y- quarter span at $y = 0.25W_C$ experiences the same sudden increase of downforce between $0.2L_C < x < 0.4L_C$ as the centreline when $y = 0W_C$, which could be due to a sudden change of incidence in the wake very close to the rear of the wake generator.

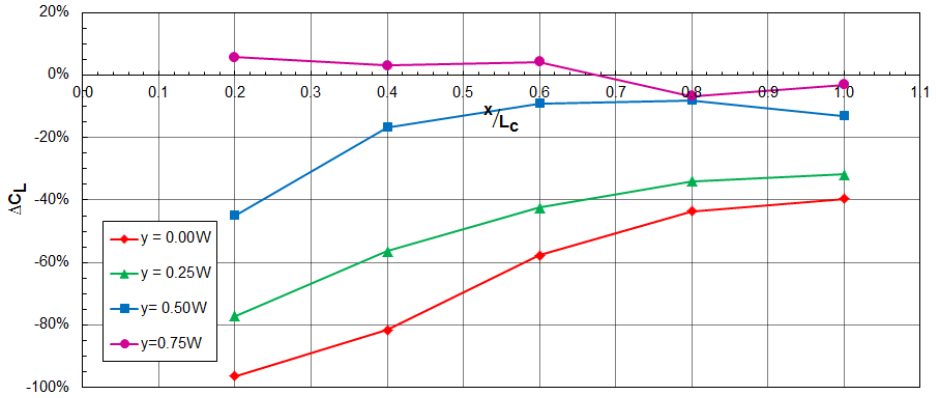


**Figure 4.41:** Effect of upstream wake on span-wise posture averaged front wing downforce, lateral offsets.

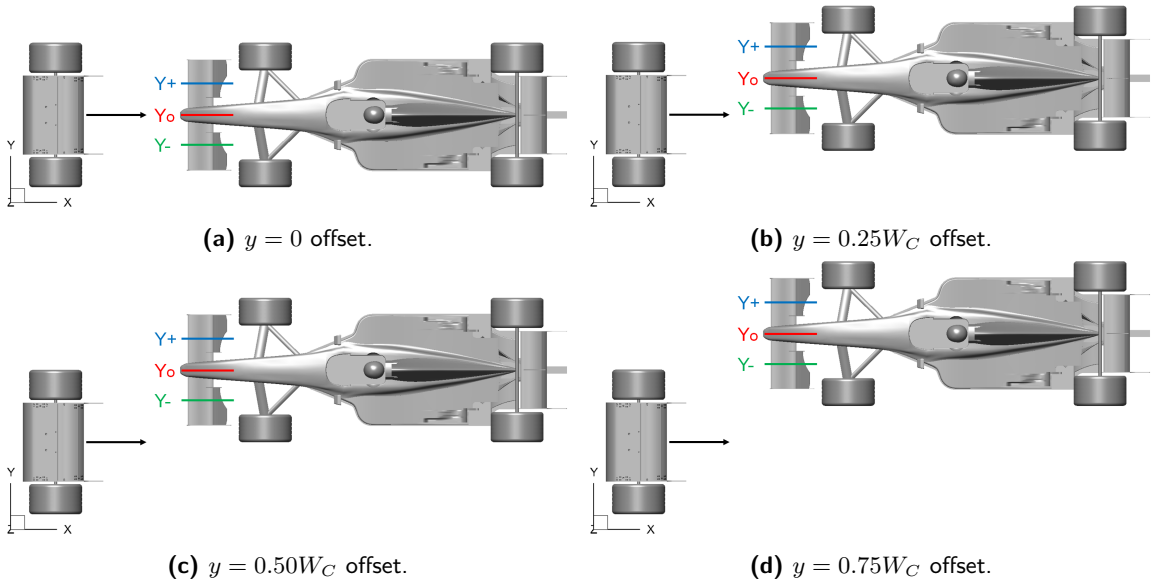


**(a)** $y = 0$ offset.

**(b)** $y = 0.25W_C$ offset.

**(c)** $y = 0.50W_C$ offset.

**(d)** $y = 0.75W_C$ offset.

**Figure 4.42:** Alignment of instrumented front wing and wake generator centreline with lateral offset at $x = 0.2L_C$ ($y = 0$ to $y = 0.75W_C$, left to right).

The downforce gain at $y = 0.75W_C$ is predominately the result of the Y- quarter-span, which increases relative to the freestream for all separations and is $\approx 20\%$ for separations closer than $x = 0.6L_C$. It would be reasonable to infer that the down-wash in the wake outboard of the rear wheels would increase the relative angle-of-attack of the wing, whilst as the velocity in the wake by far this outboard of the centreline is close to freestream, this could increase the downforce. The Y+ quarter-span also experiences an increase of lift at the closest axial separation when $y = 0.75W_C$, this is just outboard of the outboard face of the wheel (figure 4.42) so the wake could be in down-wash. However the front wing centreline, while also outboard of the wake generator, experiences downforce loss for all offsets, as downforce at both quarter-span locations increases there must be an interaction with the front wing flaps.

At the longest separation ($x = L_C$) the underbody integral pressure downforce deficit is at a similar level to the front wing downforce deficit, between $\approx 0\%$ and $-40\%$, with the axial offset increasing from $0 < y < 0.75W_C$. As the axial separation is reduced the loss of downforce does not increase at the same rate as the front wing, this is in line with the conventional theory that the front wing loses the most

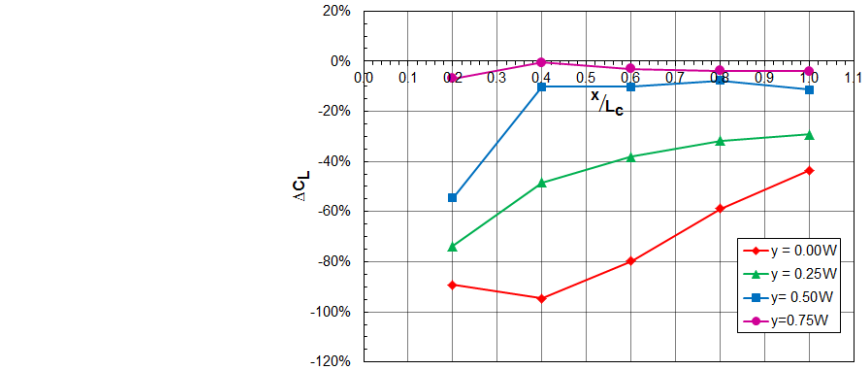


**(a)** Centreline.

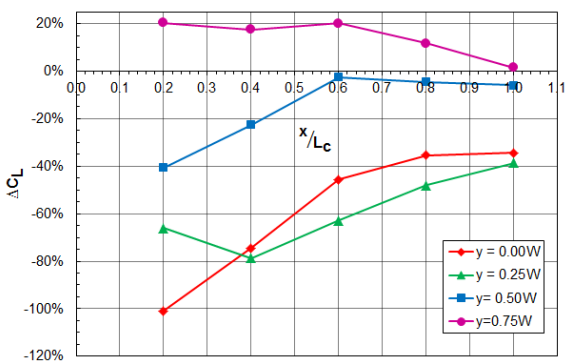


**(b)** Y- quarter-span.

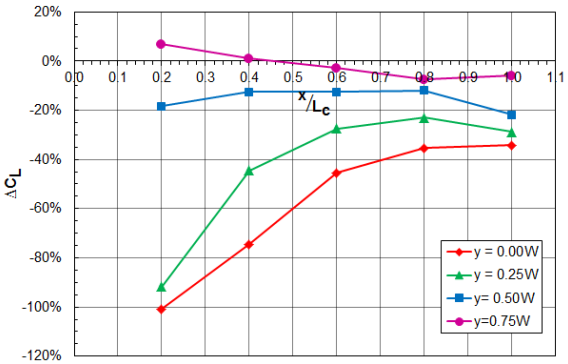


**(c)** Y+ quarter-span.

**Figure 4.43:** Effect of upstream wake on front wing downforce (posture averaged), for vehicle offsets shown in figure 4.42.

performance in the wake. However this appears to only be true for this car at axial separations less than a car length, which is less than would be representative of an on-track slipstreaming manoeuvre.

Like the front wing, for the $y = 0.75W_C$ offset the downforce generated by the underbody increases relative to the baseline. Like the front wing this could be the result of the down-wash in the wake outboard of the rear wheels of the upstream vehicle. Formula 1 cars rely on a series of complex interactions to generate downforce. This is especially true of the underbody where positive circulation, particularly in the region around the driver and the middle of the chassis, is used to create localised down-wash to improving cooling flows, underbody and rear wing performance [18]. It is therefore feasible that the near uniform down-wash outboard of the rear wing vortex could enhance these flows thereby creating more downforce.

For the $y = 0.75W_C$ offset the rate of the increase of underbody downforce slows as the separation reduces between $0.6L_C < x < 0.2L_C$. This could be caused by the front wing generating more downforce than the isolated car in this same range of axial separations. It is known that the front wing will reduce underbody downforce [18] as a result of the wake reducing onset velocity and pressure, and the wake up-wash reducing mass flow to the front of the floor; so it is not unreasonable to suggest the two phenomenon are connected.

Investigating the effect of posture on the integral pressure of the underbody shows that the nose down postures lose less, and in the case of the $y = 0.75L_C$ offset, gain more downforce than the flat postures

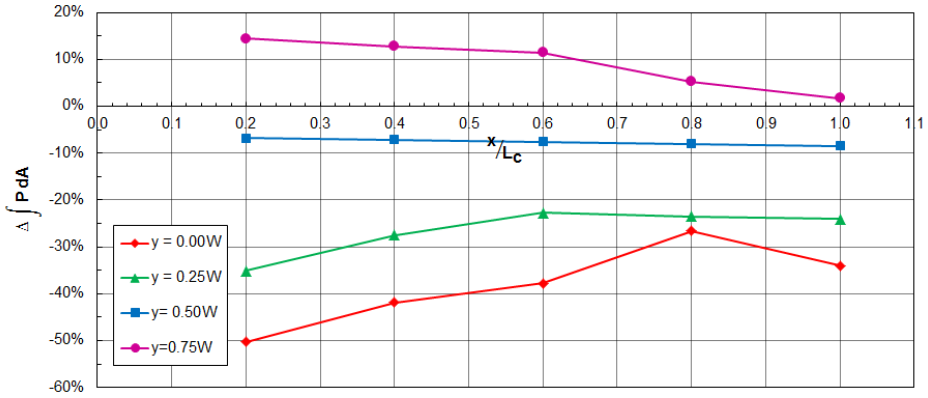


**Figure 4.44:** Effect of upstream wake on vehicle posture averaged underbody integral pressure, lateral offsets.

(figure 4.45); and it has been shown that the nose down postures develop more downforce at the front of the floor than the rear which results in a more forwards aero-balance for the isolated car.

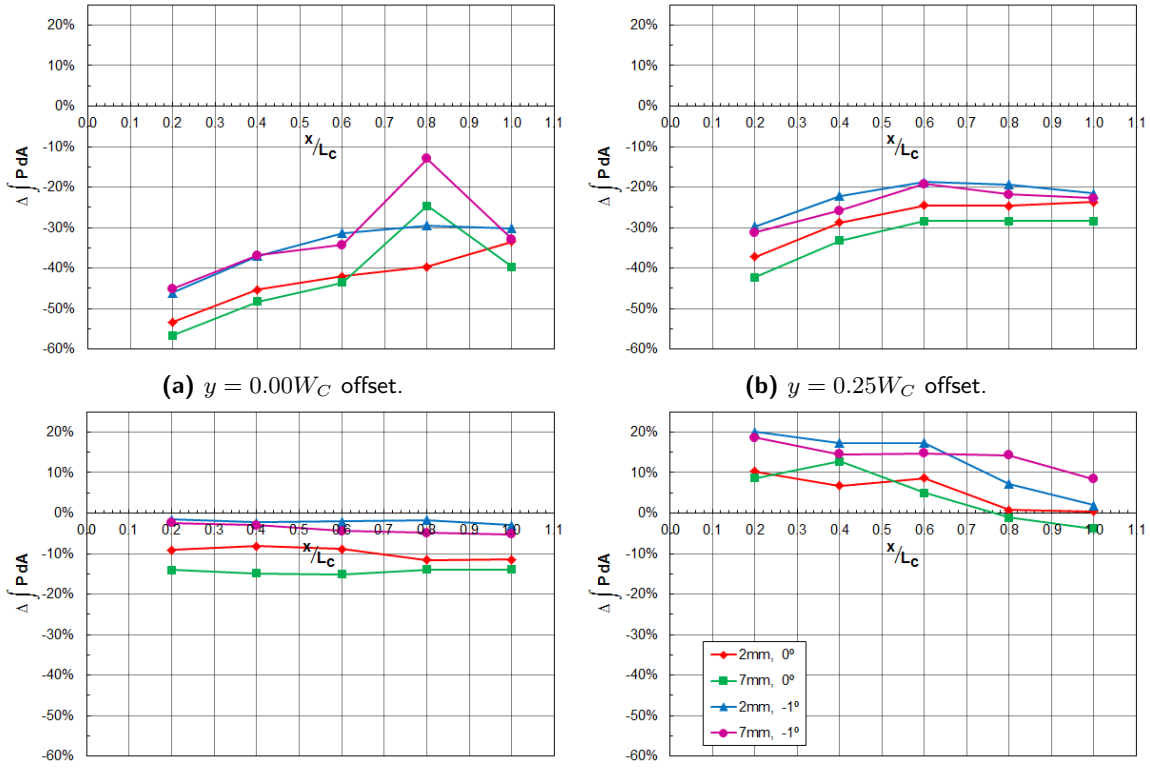


**(a)** $y = 0.00W_C$ offset.

**(b)** $y = 0.25W_C$ offset.

**(c)** $y = 0.50W_C$ offset.

**(d)** $y = 0.75W_C$ offset.

**Figure 4.45:** Effect of upstream wake on underbody integral pressure by lateral offset.

## 4.4 Chapter Summary

The aerodynamic characteristics of the $25\%$ Formula 1 car have been investigated experimentally. The aerodynamic set-up of the car was optimized for isolated running by altering the front wing flap incidence and car posture, i.e. car pitch angle and ride height. Peak downforce is lower than would be anticipated for an open-wheeled race car of this design while drag is also lower, so the lift-to-drag ratio is $\approx 30\%$ of a modern Formula 1 car. In particular the downforce from the integrated pressure on the underbody is lower than would be expected. This could be a result of inefficient design, particularly in the regions of the front splitter and rear diffuser, or the pressure tappings in the underbody do not capture the low pressure ($C_P << -3$) peaks which would be expected under the car.

The wake of the car is dominated by the counter-rotating vortex pair from the rear wing endplates, the relatively short wing span means that the rear wing vortex pair interacts to create a strong centreline up-wash. The vorticity is coupled with a total pressure deficit which extends far beyond the furthest downstream plane measured, $x = 1.75L_C$. Static pressure in the wake is relatively low magnitude, and decays rapidly, so most of the pressure deficit in the wake is dynamic resulting from the axial velocity deficit caused by the relative bluffness of a Formula 1 race-car, particularly the rear wheels and wing.

The bluff bodied wake generator used in this study creates a counter-rotating vortex pair with similar size and rotation to the Formula 1 car, owing to the use of the same wing profiles as the car. However the velocity deficit in the near wake is slightly different, primarily due to the short axial length of the wake generator, which is less than $20\%$ the length of the car. The velocity deficit resulting from the wheel wakes is greater, mostly as the wheels are exposed to the airflow rather than shadowed by the upstream vehicle as in the case of the full car. As the wake continues the velocity deficit is swept to the centreline by the wing vorticity so that by $x > 0.2L_C$ aft of the wake generator the accuracy of the wake is very high.

This is the first experimental program to be completed using an upstream wake generator with a full downstream race-car geometry. The short length of wake generator means that the axial separation achieved is greater than any previously published experimental slipstreaming study [1]. Aerodynamic forces generated by the downstream car are greatly affected by the upstream wake. Drag reduction peaks at $\approx -30\%$ at very short axial separations, and reduces as both the axial and lateral offsets increase, though for all positions tested the aerodynamic drag is reduced from the isolated car. This would mean that for all downstream positions straight line speed would be increased, up to $40^{km}/_{hr}$ based on the measured reduction of drag and the top-speed of a modern Grand Prix car [131]. Downforce loss experienced in the wake is more than double the drag deficit, peaking at $\approx -67\%$ of the isolated car. While downforce loss reduces with axial separation, it disappears by a lateral offset of $y = 0.75W_C$, meaning the lift-to-drag ratio is higher for offsets greater than $y = 0.5W_C$. It could be that training the drivers to drive corners

with an offset to the car ahead would compensate the downforce loss with greater acceleration on corner exit, thus allowing the driver to effect an overtake. However this approach assumes the potential for more than one racing line through corners which, with tyre debris build up and lack of adhesion 'off-line', is at this point not always possible.

Downforce loss at the longest axial separation tested is approximately the same for the underbody and front wing, at all lateral offsets. As the separation is reduced the rate of loss of the front wing is greater than the underbody, and the aerodynamic balance of the car moves rearwards, up to $24\%$. The aero-balance change would increase understeer and making it increasingly difficult for the following driver to corner. However, like downforce loss, the balance shift reduces with lateral offset, even moving forwards at the greatest offsets, caused by an increase of downforce from the front wing and underbody, which would even serve to induce oversteer.

# Chapter 5

# Computational Methodology

## 5.1 EXA PowerFlow

All the cases presented in this thesis were run using the Exa PowerFlow 5.0 commercial software package, in particular the PowerCase pre-processing and PowerVIZ post-processing programs. PowerFlow is a transient solver which utilizes the Lattice-Boltzmann Method (LBM) to model the time-dependant behaviour of fluid-flow around a geometry. Physical and time dependant behaviours are resolved at lattice scale, i.e. as the fluid migrates between cells fluid interactions occur in real time. Turbulence modelling is performed at grid scale using a Very-Large Eddy Simulation (VLES) model for large scale turbulence, coupled with a VLES compatible two equation ($k-\epsilon$) model for smaller scale turbulence (sub-grid scale). Boundary layer growth and separation is approximated using with a near wall model which imposes a dynamic velocity gradient near the surface, simulating boundary layer behaviour.

The cubic lattice generated is split into voxels (3D fluid cells) and surfels, which are surface cells and are generated where the geometry intersects the fluid (figure 5.1) allowing fully-detailed geometries to be easily inserted into the mesh. Lattice refinement is controlled using Variable Resolution (VR) regions, with the lattice length doubling as the VR level increases (i.e. the lattice cube expands by $2^3$), Exa best practice guidelines [132] recommend 8 to 11 VR regions for an external automotive case. More information about the operation and accuracy of PowerFlow can be found in [108, 132, 133, 134, 135].

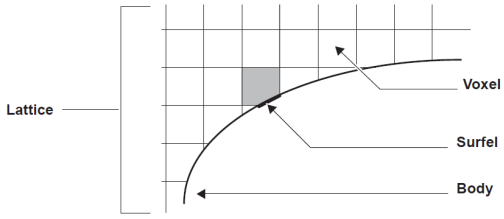


**Figure 5.1:** Definition of 'voxel' and 'surfel' elements in PowerFlow lattice, from EXA PowerFlow user guide [132].

## 5.2 Generic 25% Formula 1 Car

The vehicle used for the CFD study is a copy of the 25% scale model used in the experimental programme. Much of the geometry has been designed and manufactured at Durham University so CAD files for the wheels, underfloor with diffuser, and the front and rear wings exist. The upper bodywork shell of the car was taken from a commercially available 25% scale model so CAD was not available. Using a Baumer Electric OADM 20I4560/S14C laser (class 2) distance sensor, with accuracy of $\pm 0.2mm$ at ranges between 30mm to 130mm, mounted to a 3-axis probe traverse. The upper and side surfaces of the upper shell was scanned using a cartesian aligned grid with minimum resolution of $5mm^2$ and turned into a point cloud, shown in figure 5.2. The point cloud was imported into Solidworks and used to generate the external surface of the vehicle, which was then combined with the existing CAD to create the CFD geometry, figure 5.3.

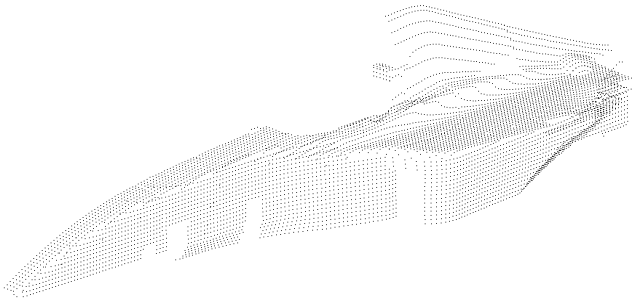

**Figure 5.2:** Point cloud for 25% scale Formula 1 wind tunnel model.

To prevent flow ingress through the cockpit into the car, the cockpit is sealed where in the experimental model the overhead strut exits through the cockpit. The experimental model features mesh inserts in both the sidepod cooling inlet and engine air intake, both of which are approximated using porous media to retard the passage of flow through the openings.

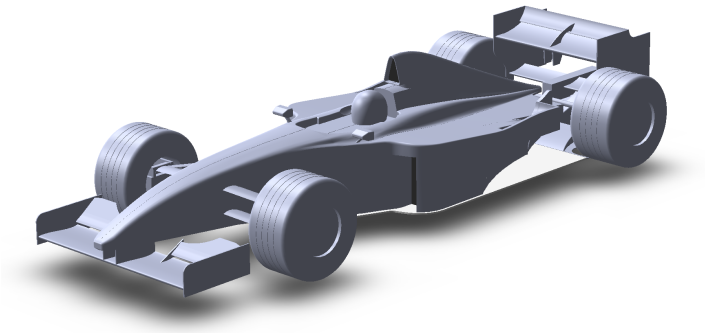

**Figure 5.3:** 25% Formula 1 CFD model.

## 5.3 Setup

For comparison of results to the experimental study all computational cases are run at the same Reynolds number, $Re = 2.05 \times 10^6$ with the rest of the characteristic variables shown in table 5.1 and are matched to the international standard atmospheric (ISA) conditions at sea level, turbulence conditions were set to the PowerFlow defaults. The ground of the simulation volume was set as a velocity matched sliding wall to prevent boundary layer growth. As the simple wheel geometry does not feature spokes rotating walls were used in place of the more computationally expensive sliding mesh. Where a sliding mesh rotates the whole geometry and mesh about a prescribed axis, the rotating wall modifies the boundary condition with a stationary mesh, in this case at $303.1 rads^{-1}$.

**Table 5.1:** Characteristic variables for freestream cases.

| Variable (Unit) | Value |
|---|---|
| Pressure $(Pa)$ | 101325 |
| Velocity $(ms^{-1})$ | 25 |
| Temperature $(^{\circ}C)$ | 15 |
| Density $(kgm^{-3})$ | 1.225 |
| Kinematic Viscosity $(m^2s^{-1})$ | $1.461 \times 10^{-5}$ |
| Turbulence Intensity $(\%)$ | 1 |
| Turbulence Length Scale $(mm)$ | 5 |

The simulations were computed using the Durham University high-performance computer clusters, 'Hamilton', which features $\approx 2000$ Intel Xeon 2.6GHz CPUs split into 122 compute nodes each of 16 cores, with a further 3600 cores of four and six core Intel 2.26GHz and 2.4GHz processors. Depending on the boundary conditions of the case, and the processors used, between 1500 and 3800 CPU hours were required to compute the cases.

The vehicle body forces from the simulations were recorded at $4kHz$ to monitor the time dependant forces, figure 5.4. The large scale start-up transients decayed after $\approx 350ms$ (or after 150,000 timesteps). Time averaged fluid and surface measurement frames were output between $350ms$ and $700ms$ after which the cases were halted, this was deemed a long enough interval to average the time dependant force fluctuations. A further pair of force and measurement files were output at $1kHz$ from $645ms$ to the end of the simulation

to capture the vehicle and wake unsteadiness. Only 55 measurement frames were captured for the $1kHz$ output in order to keep the output file volume low.

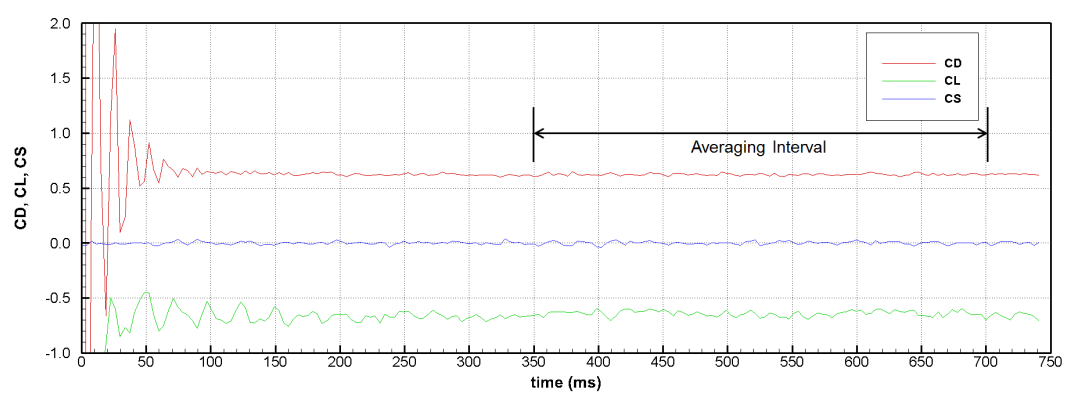


**Figure 5.4:** Plot of vehicle force coefficient over time (sampling at 4kHz) for freestream case.

### 5.3.1 Cases

A number of computational cases are presented in this thesis, all of which feature the vehicle in straight ahead conditions using the freestream boundary conditions as shown in table 5.1. As the model is symmetric about the centreline, in some cases an XZ symmetry plane was used to reduce computational load. The conditions of the wind tunnel experiments were not recreated, instead the CFD was used as a complementary, and arguably more realistic, tool; without the constrains of model blockage and wall effects, moving ground width, and model mounting struts. Where the advantage of the wind tunnel experiments are the capability to test a large range of vehicle conditions and wake generator positions for a comparatively low time cost. Wind tunnel validation studies have been performed in PowerFlow with accuracy of within 0.002 on $C_D$ [133].

In addition to the isolated vehicle case, a number of slipstreaming cases were simulated and compared to the baseline to determine the effect of an upstream vehicle. Where in the wind tunnel the length of the working section, in particular the rolling road, are limiting factors in the separation between a pair of vehicles, no such obstacle exists in the computational environment. However other restrictions do exist in CFD; in particular altering the mesh and domain to add a second vehicle can affect force measurements, limiting the confidence of a parametric study.

What CFD instead allows is the ability to impose a set of non-uniform boundary conditions on the inlet. This allows the original mesh and domain to be maintained, allowing direct comparison between cases. This approach also has the advantage of being able to directly manipulate the onset wake to determine the most significant wake features causing the downstream vehicle performance loss, be it total pressure deficit, vorticity, or up-wash.

The cases presented fall into three categories:

1. **Undisturbed**. Baseline case, against which all cases are compared. Velocity and static pressure are uniform at the inlet. Run both with and without a symmetry plane.

2. **Two Vehicle**. A pair of identical vehicles are included in the domain. Cases were run both with and without a symmetry plane. These cases are primarily used to validate the effect of the imposed wake on the following vehicle from the wind tunnel study, but can also be used to show the effect of the following vehicle on the lead vehicle.

3. **Imposed Wake**. The wake from both the baseline and lead vehicle in the two vehicle cases was sampled and imposed on the inlet, creating a non-uniform pressure and velocity field. Cases were run both with and without a symmetry plane and using time averaged and unsteady sampled inlets. Cases are also presented where the inlet variables are adjusted to test the effect of the different salient wake features from the 'upstream' vehicle on a car immersed in the wake.

It was decided for that the 'following' cases a separation equal to one vehicle length would be the closest two cars would get to one another on track, during slipstreaming before an overtaking manoeuvre and assuming the following driver had not missed their braking point. It is assumed that the closest separation would also result in the greatest downforce and drag loses, so as the worst reasonable case for a following vehicle the majority of testing was performed with a $1L_C$ separation and the vehicles axially aligned. Simulations were also performed with a longer separation of $2L_C$ and with a $0.5W_C$ lateral offset to determine how proximity affects the following vehicle.

To impose the wake on the inlet a static pressure with velocity boundary condition was used. This allowed to a non-uniform static pressure, as well as the cartesian aligned components of velocity to be input. Pressure and velocity were sampled and then input using a uniform $10 \times 10mm$ grid with 400,000 spatial data points. PowerFlow then uses trilinear interpolation where the sample grid resolution is bigger than the imposed inlet plane voxel resolution, to determine pressures and velocities at voxel scale. The outlet was set as a uniform static pressure with free flow direction, this is one drawback of PowerFlow as it would be preferable to use an 'outflow' boundary condition, which is available in other commercial solvers. The outflow boundary condition does not define pressure or velocity on the outlet, meaning that any residual pressure or velocity deficit in the wake at the outlet is not forced to the boundary condition, so the domain and mesh can be smaller. However, the outlet was simply placed sufficiently far from the rear of the car that pressure has returned to freestream.

### 5.3.2 Domain & Mesh

In order to create a simulated $1L_C$ offset with an imposed wake the domain length upstream of the car had to be significantly shortened form a 'best practice' case, figure 5.5, where the upstream dimension is in excess of four car lengths. To prevent any reversed flow on the inlet the wake was sampled far enough downstream that the wake had closed, $0.25L_C$. This means that to achieve a $1L_C$ separation the inlet is only $0.75L_C$ upstream of the car. This shortening of the domain was shown to decrease drag by $\Delta C_D = -0.082$ and decrease downforce by $\Delta C_L = 0.10$ with a 1% forwards shift of the centre of pressure. While shortening the inlet does affect the results, the error is systematic. As the effect of the upstream wake is of more interest than the actual lift and drag values of this car this domain was deemed acceptable.

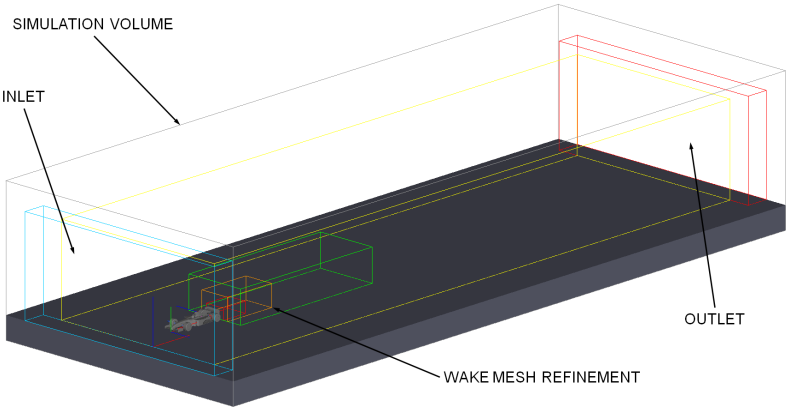


**Figure 5.5:** Isometric view of baseline CFD domain.

To remove wall effects the inlet was dimensioned for a blockage of $< 1\%$, or $10.7m^2$ with an aspect ratio approximately $2:1$. The simulation volume extends $10L_C$ downstream of the vehicle, making the total domain $11.75L_C$ in length.

The minimum mesh resolution in the highest VR region was set to include 800 voxels over the characteristic length of the car, in other words a minimum lattice size of $1.5mm$. The structured mesh generated contains over $16 \times 10^6$ voxels and over $1.7 \times 10^6$ surfels split between 10 VR regions. The mesh is weighted to the near wall region around the body with 88% of the voxels and 97% of the surfels in the finest VR scale. Mesh density is also increased downstream of the car to capture important flow features in the wake, and upstream of the car to improve accuracy of the onset wake.

The total mesh fidelity of $16 \times 10^6$ cells may be coarse for a motorsports study, where meshes exceeding $50 \times 10^6$ cells are commonplace [22], however, in motorsports CFD is used in the development of vehicles where configuration changes can be small and absolute accuracy is essential in order to correlate to wind tunnel and track data [136]. Validation of PowerFlow with a 25% model scale wind tunnel study have been performed by Cyr, Ih & Park [133]; with half the minimum lattice size of this study the authors produced

results within 0.0014 on $C_D$ of wind tunnel measurements. Arguably in the study of this generic Grand Prix vehicle determination of absolute forces is secondary to the determination of the large differences resulting from the upstream vehicle wake.

In order to compare the lead vehicle to the baseline the upstream dimension of the two vehicle domain was matched to the baseline case. The second vehicle was added downstream, with the total domain elongated to accommodate the second vehicle with domain length of $10L_C$ behind. The same near wake mesh refinement was used for the second vehicle as the lead vehicle, though differences occur when the higher density VR mesh of the trailing vehicle intersects the lead vehicle wake refinement.

# Chapter 6

# Effects on a Following Vehicle (Computational)

This chapter details the effect of an upstream wake on the aerodynamic performance of the $25\%$ scale Formula 1 car using CFD. The upstream wake is created by three means. (1) A second, identical, Formula 1 model situated upstream at a number of locations. (2) The same bluff bodied wake generator as was used in the experimental study (Chapter 4) and (3) by imposing a sampled wake on the inlet of the test domain. The method of imposing a sampled wake on the inlet is unique for a race-car drafting study, and allows the flow field of the wake to be modified as is performed in the cases presented in Chapter 9. This chapter focuses on quantifying the effect of the unmodified wake as produced by the $25\%$ Formula 1 car.

## 6.1 Undisturbed Case

As with the experimental study, the undisturbed flow condition is used as the baseline for all further experiments. So that there is direct comparison between the experimental and CFD studies the car set-up is matched to the optimal set-up found experimentally with the model using a 'wheels on' configuration (not presented in Chapter 4), shown in figure 6.1. Coincidentally it was found that all the criteria for an 'optimal' set-up, namely peak downforce, peak lift to drag ratio, and an aerodynamic centre of pressure at around 60% of the car wheelbase, occurred at the same car condition. This set-up corresponds to a $-0.6^{\circ}$ pitch (nose-down) with a nominal (non-dimensional) ground clearance of $h_{min} = 0.02H_C$ (4.83mm model scale, 19mm full scale) measured relative to the reference plane.

Using a 'wheels-on' approach experimentally means that while wheel lifts are not measured by the balance wheel drag is, so for comparison to the experimental data table 6.1 shows the sprung body lift and total body

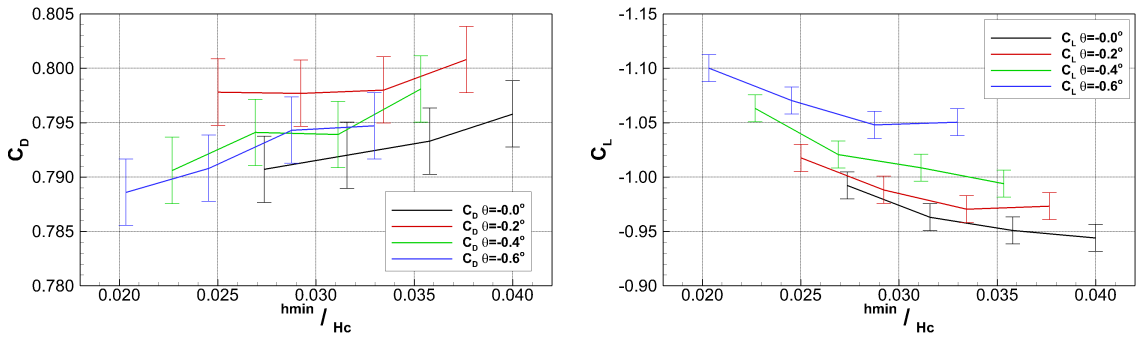


**(a)** Drag. **(b)** Downforce.

**Figure 6.1:** Aerodynamic forces from 'wheels-on' experimental study.

drag for the CFD baseline cases. For both half car and full car cases the total downforce is underestimated, when compared to the wind tunnel, though the difference is almost halved without the symmetry plane in the simulation. Conversely drag is overestimated for both CFD baseline cases while the disparity is significantly lower with a symmetry plane than without. Like lift, the lift to drag ratio is closer to the experimental data for the case without a symmetry plane, the location of the centre of pressure is also closer to the experimental study with a $< 2\%$ difference.

**Table 6.1:** Comparison of sprung lift and total drag coefficients for experimental and CFD baseline cases.

| | $C_D$ | $\Delta(\%)$ | $C_L$ | $\Delta(\%)$ | $\frac{C_{LR}}{C_L}$ | $\Delta(\%)$ | $\frac{L}{D}$ | $\Delta(\%)$ |
|---|---|---|---|---|---|---|---|---|
| Experimental | 0.789 | - | -1.100 | - | 61.62 | - | -1.395 | - |
| Computational (Half Car) | 0.799 | ↑ 1.27 | -0.788 | ↓ 28.4 | 55.20 | ↓ 10.4 | -0.986 | ↓ 29.3 |
| Computational (Full Car) | 0.918 | ↑ 16.4 | -0.938 | ↓ 14.7 | 60.52 | ↓ 1.79 | -1.022 | ↓ 26.7 |

### 6.1.1 Vehicle Force Behaviour

Total vehicle downforce is lower with the vertical wheel loads included, table 6.2, indicating that the wheels are, as would be expected, generating lift. The aerodynamic centre of pressure for the car is also more rearward ($\approx 8\%$) both with and without the X-Z aligned symmetry plane. Component force coefficients, figure 6.2, show that both front and rear wheels generate lift, with front wheels generating $C_L = 0.09$ more than the rears. Rear wheel drag is also lower than the front wheels by $C_D = -0.03$; as the rear wheels operate in the large wake resulting from the exposed front wheels. Combined, the wheels contribute $33.5\%$ of the total vehicle drag with the front wheels being the single largest contributor of drag, $C_D = 0.16$, also making up $35\%$ of the total vehicle frontal area, and the rear wheels and rear wing joined as the second highest contributor to drag, $C_D = 0.14$.

**Table 6.2:** Comparison of total force coefficients for baseline cases.

| | $C_D$ | $C_L$ | $C_{LF}$ | $C_{LR}$ | $\frac{C_{LR}}{C_L}$ | $\frac{L}{D}$ |
|---|---|---|---|---|---|---|
| Full Car (Baseline) | 0.918 | -0.796 | -0.253 | -0.544 | 68.3 | -0.868 |
| Half Car | 0.799 | -0.646 | -0.235 | -0.412 | 63.7 | -0.809 |

Of the downforce generating components the front wing in ground effect generates the most downforce, followed closely by the rear wing ($\Delta C_L = 0.0068$), each contributing $\approx 42\%$ of the total downforce. However the front wing efficiency ($^L/_D = -7.50$) is significantly higher than the rear wing ($^L/_D = -2.42$). While the combined upper body and underfloor only generates 22% of the vehicle downforce the underfloor is the most efficient component of the car with $^L/_D = -14.2$. The underfloor by itself creates downforce approximately equal to the whole vehicle while the upper body generates lift, though the net result remains a downforce. The combined body and underfloor drag is shared relatively evenly with a 54% contribution from the upper body.

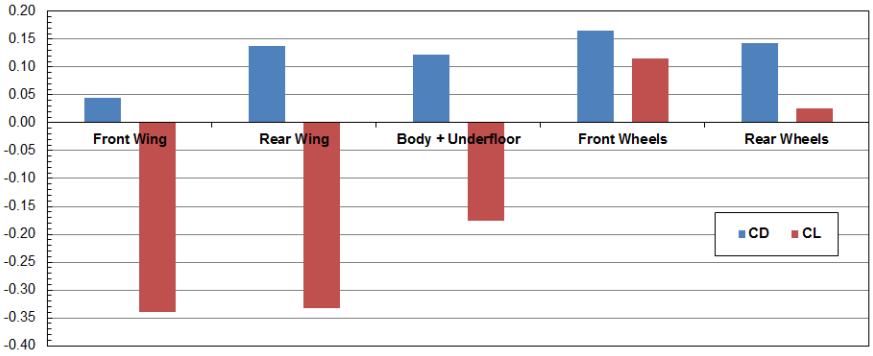


**Figure 6.2:** Time averaged vehicle component force coefficients for baseline case.

### 6.1.2 Surface Pressures

The front wing chordwise surface pressures for the centreline and quarter-span are shown in figure 6.3. The front wing suction surface shows a pressure peak of $C_P \approx -1.1$ on the centreline at around 20% of the chord, with the pressure increasing towards the wing tips, figure 6.4. Like the vehicle forces, both the front wing centreline and quarter-span suction surface pressure curves are lower in magnitude than the experimental study. The quarter-span pressure surface shows good agreement between the experimental and CFD, however the worst correlation is the centreline pressure surface with up to $\Delta C_P = 0.3$ toward the mainplane mid-chord. The centreline pressure surface is situated under the nose and in the narrow gap between the front wing mounting pylons, any imperfection in manufacture could result in very different flow conditions in this region. At quarter-span the flap suction pressure distribution features a flattening toward the rear indicative of separation.

The highest magnitude suction peak occurs at the leading edge of the underfloor, at the minimum ground clearance, where $C_P = -1.5$. Pressure recovers over the length of the floor before another low pressure spike at the throat of the diffuser, the magnitude of which is lower than would be expected for such a vehicle, $C_P > -1.0$. There are two other low pressure peaks at the front of the floor under the sidepod inlets, between the splitter and these points a counter-rotating pair of vortices form. The vortices rotate with an in-wash toward the car centreline and serve to increase flow ingress to the underfloor, increasing

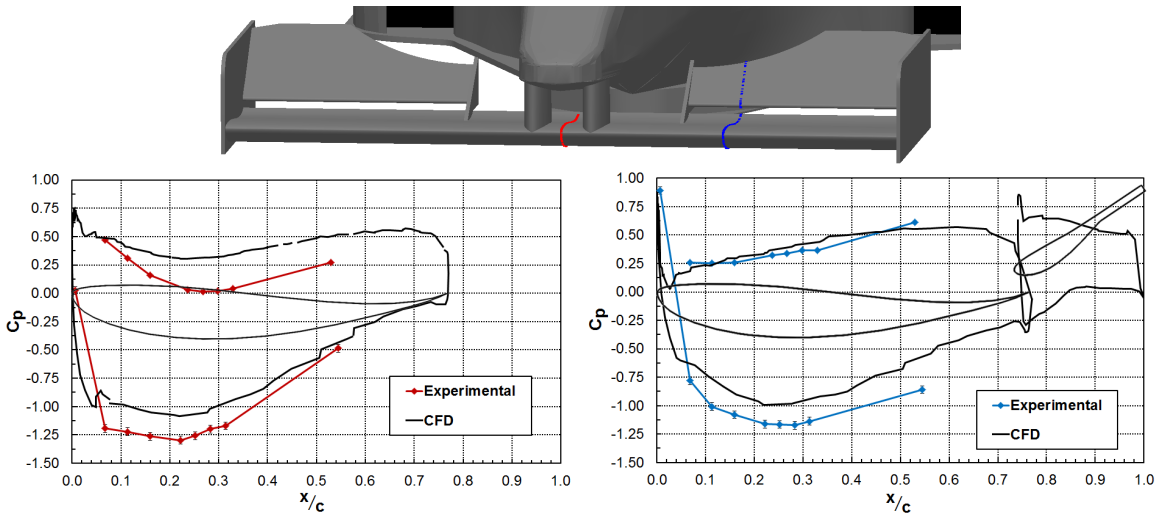


**(a)** Centreline. **(b)** Quarter-span.

**Figure 6.3:** Front wing static pressure distribution.

the underfloor pressure and reducing downforce. The rear wing mainplane features a peak of $C_P = -1.4$ near the leading edge and a relatively uniform static pressure distribution across its span, though with a lower magnitude $C_P$ on the centreline due to a combination of the wake from the air intake and the rear wing supports which connect to the suction surface.

There are two regions of negative pressure on the leading edge of the sidepods, responsible for some of the lift experienced by the upper body. In the recent past Formula 1 teams have adopted a number of turning vanes and vortex generators to minimize separation along the top of the sidepod. Were the purpose of this research the optimization of this Formula 1 car, this is an area where some improvements could be made.

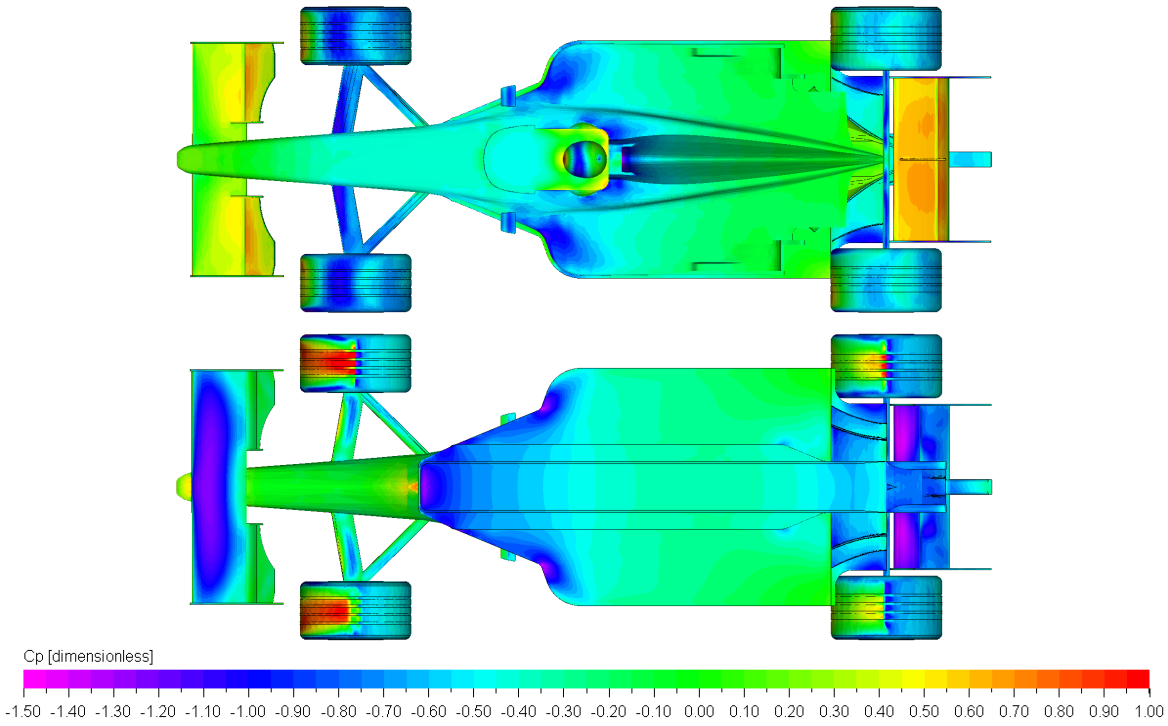


**Figure 6.4:** Baseline underfloor surface pressure distribution.

### 6.1.3 Vehicle Wake

#### 6.1.3.1 Flow Around the Vehicle

The front wing of the car creates a three vortex system per side, with co-rotating pairs formed at the endplates and a single vortex at the inner junction of the flap, as per Jasinski [40]. Due to the wing span the wing tips are situated directly upstream of the front tyres. Front wheel drag could be reduced by changing the incident airflow by angling the endplates in such a way that the flow is diverted either inside or outside the front wheels, albeit at the expense of front wing span and therefore ultimate downforce. The upper endplate vortex moves inboard as it continues downstream and merges with the lower front wheel vortex and front suspension wake. The main front wing vortices do not get a chance to develop as they immediately impact the front wheels.

The front wheel wakes are dominated by a large region of reversed axial velocity, with reversed flows extending $\approx 0.75d$ behind the rearmost point of the tyre. The majority of the reversed flows are found near the ground where the vortices in the inverted T $(\perp)$ shape wake are found. The external front wheel vortex occasionally sheds, figure 6.5(b), increasing the axial velocity deficit in the base wake. The reversed flows behind the rear wheels do not extend as far downstream as the fronts, as is reflected by the reduced drag, only extending $< 0.62d$ behind the rearmost face of the tyre. The shape is also different to the front tyre wake, with the majority of the velocity deficit at and above axle height.

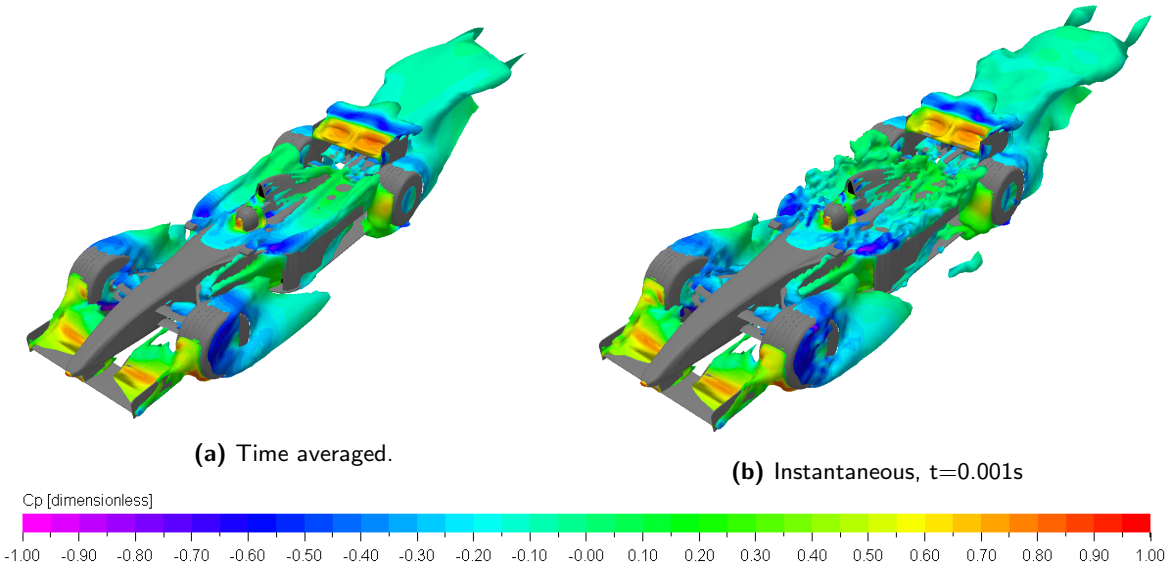


**(a)** Time averaged.

**(b)** Instantaneous, t=0.001s

**Figure 6.5:** 3-D isosurface plots of $u_X = 0.4U_\infty$ coloured by static pressure.

There is a region of reversed flow behind the rear wing, both the flap and mainplane, extending up to a chord length $(c_{RW})$ downstream of the wing. The separated region extends $\pm 0.2b_{RW}$ either side of the centreline, behind the wing support pillars. Finally, the central diffuser channel is stalled, with asymmetric regions of zero velocity from each half of the diffuser.

#### 6.1.3.2 Flow Downstream of the Vehicle

At the base of the vehicle the wake is seen to commence with the roll-up of the rear wing vortices, figure 6.6, low static pressure ($C_P = -0.38$) is seen in the vortex cores with high magnitude secondary flows ($u_{YZ} = 0.44U_\infty$) around the rear wing endplates. The roll-up is also seen in the axial velocity deficit contour plot (figure 6.6(c)) around the upper edge of the endplates. Axial velocity over much of the base of the car is $u_X < 0.5U_\infty$; the axial velocity plot also show that reversed flows, $< -0.2U_\infty$, are present in the wake behind the rear wing and rear wheels at this downstream plane.

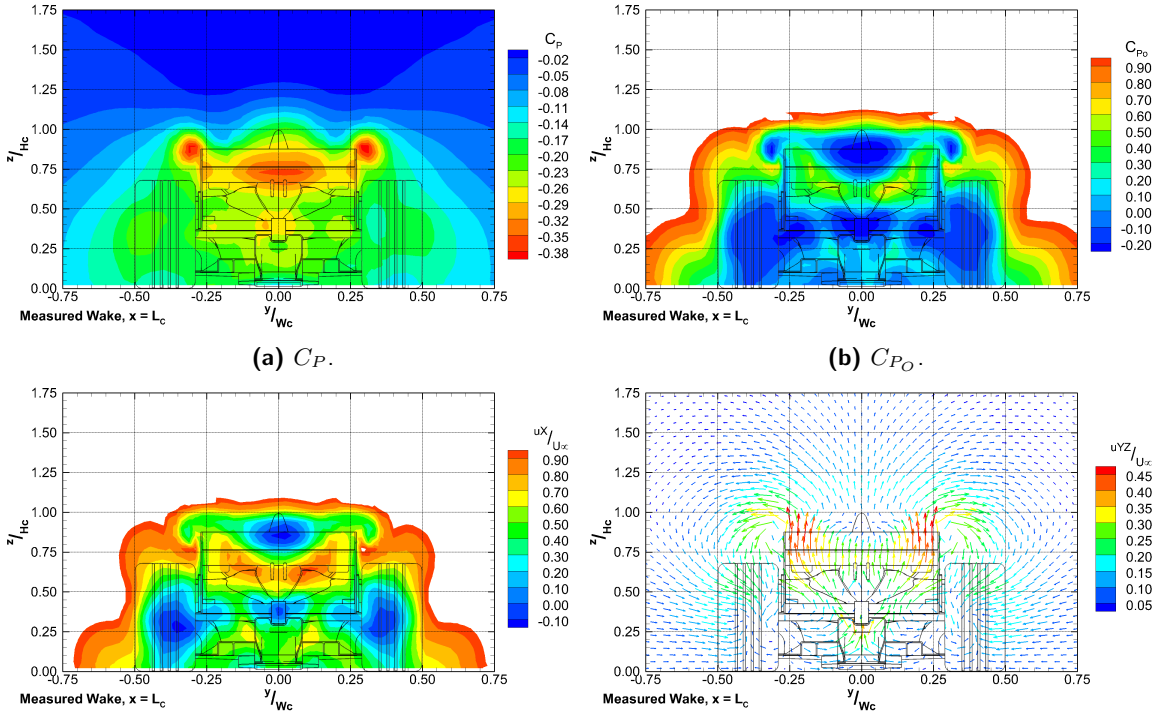


**(a)** $C_P$. **(b)** $C_{P_O}$. **(c)** $u_X$. **(d)** $u_{YZ}$ vectors.

**Figure 6.6:** Time averaged wake contours at $x = 1.00L_C$.

By a quarter car-length ($1.25L_C$) downstream of the car, figure 6.7, all regions of reversed flow in the wake have closed. The static pressure in the vortex cores are significantly reduced in magnitude $C_P = -0.15$ and have migrated inboard of the rear wing endplates and under the mainplane. The secondary flows in the wake have become dominant by this downstream plane, with a large pair of vortices with strong cross-flow at approximately axle height. The vortices are eccentrically shaped at this point and are the result of the merging of the main wing-tip vortices and a lower pair of vortices seen in figure 6.6(d) behind the 'beam' element wing. The axial velocity deficit has become more homogeneous over the base of the car with the greatest deficit taking the form of an X with magnitude $u_X = 0.20U_\infty$. At this downstream plane there is a slight asymmetry in the axial and total pressure deficits, possibly resulting from the stalled rear wing and diffuser.

As the wake propagates downstream to $1.5L_C$ the vortices have become more circular, figure 6.8(d), with

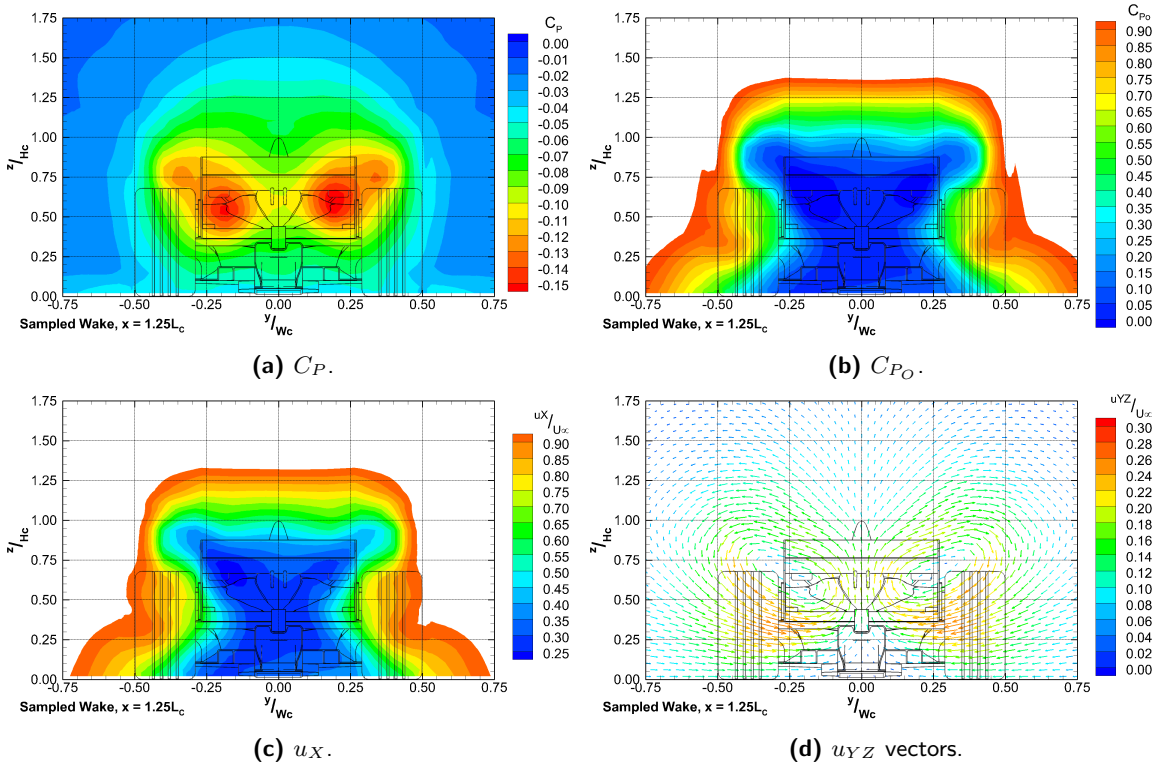


**(a)** $C_P$. **(b)** $C_{P_O}$. **(c)** $u_X$. **(d)** $u_{YZ}$ vectors.

**Figure 6.7:** Time averaged wake contours at $x = 1.25L_C$.

a strong centreline upwash. The upwash has moved the vortex cores upward, though the magnitude has decreased further to $C_P = -0.13$. At this location downstream the majority of the axial velocity deficit is located at rear wing height with a column on the centreline connecting the main deficit to the ground, forming the familiar mushroom shaped profile. The asymmetry in the axial velocity and total pressure deficits in the wake is still present at this downstream plane with a slightly greater deficit on the y- side of the centreline. By a car length downstream the vortices have become even more dominant with the centre of rotation driven higher by the upwash to above the rear wing, by moving further from the ground the vortices are less constrained so become almost uniformly circular. The elongation of the vortices is reflected in the more circular shape of the velocity and total pressure deficits, with the majority of the deficit above axle height.

In summary, the wake of this generic Formula 1 car is characterised by low static pressure, axial velocity and total pressure deficits, combined with a pair of counter-rotating vortices. The wake is complex at the base of the base of the car but by a quarter car length downstream becomes more homogeneous as the secondary flows from the rear wing become dominant. The static pressure loss is localised to the cores of the counter-rotating vortices, is of low magnitude, and decays from the wake relatively quickly. It could be argued that the static pressure is sufficiently low magnitude and localised in such a way that the effect on a trailing vehicle is minimal. More than a quarter car length downstream there is a strong cross-flow in the wake at wheel axle height, though as the vortices are influenced by the strong centreline up-wash the cross-flow reduces as the vortices become less constrained by the ground. At very close following

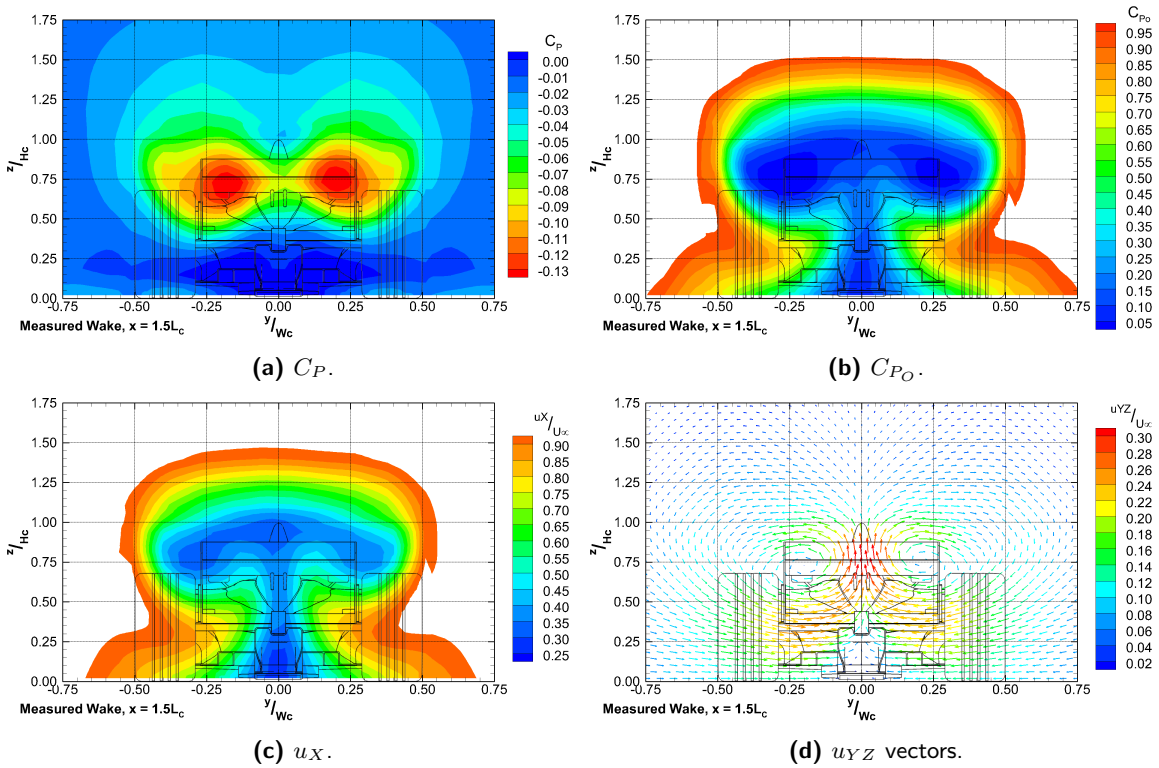


**(a)** $C_P$. **(b)** $C_{P_O}$.

**(c)** $u_X$. **(d)** $u_{YZ}$ vectors.

**Figure 6.8:** Time averaged wake contours at $x = 1.50L_C$.

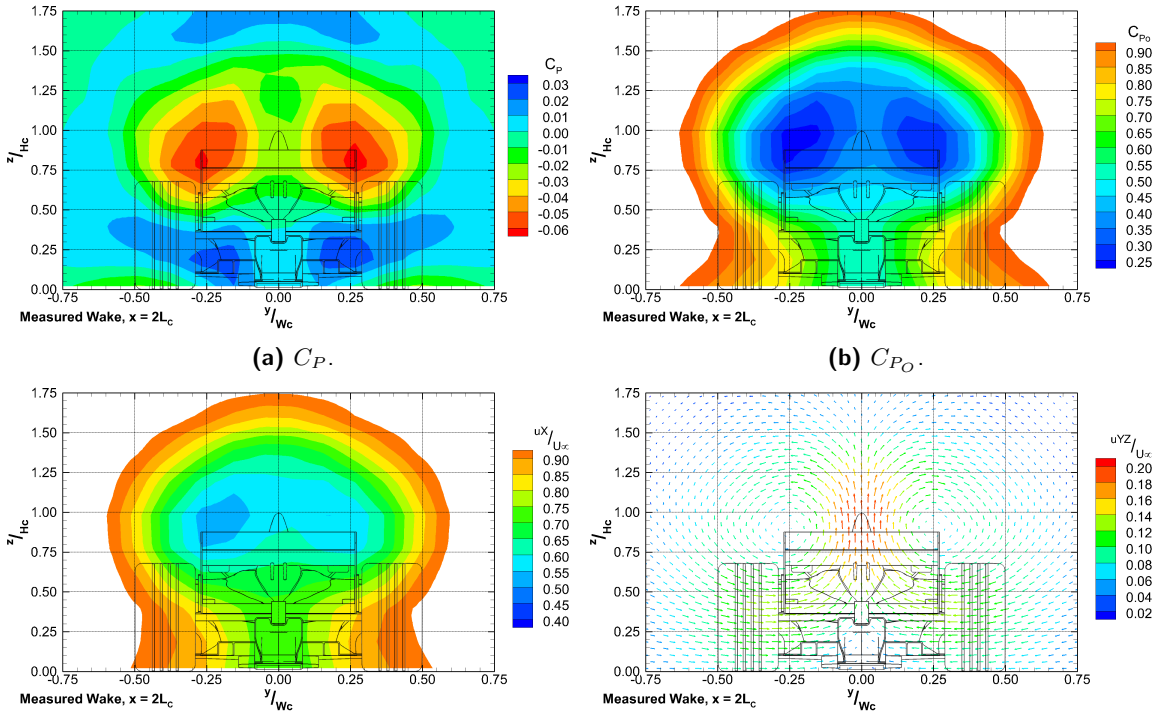


**(a)** $C_P$. **(b)** $C_{P_O}$.

**(c)** $u_X$. **(d)** $u_{YZ}$ vectors.

**Figure 6.9:** Time averaged wake contours at $x = 2.00L_C$.

distances the strong cross-flow from the vortices would have a substantial impact on the front wing of the trailing vehicle, beyond a half car separation the influence of cross-flow diminishes, although the up-wash at front wing height becomes more dominant. As well as the vortices the axial velocity and total pressure

deficits are pushed further from the ground with the up-wash and by a car length downstream and are mainly localised at rear wing height. It can therefore be concluded that the secondary flows, especially the up-wash component, are the key constituent features of the wake. If the up-wash could be increased, such that the majority wake moves over the trailing car then the impact of an upstream vehicle could be reduced.

## 6.2 Two Vehicles in the Domain

A pair of identical vehicles were placed in the CFD domain in order to determine the effect of the wake from a generic race car on a trailing vehicle. The upstream vehicle was placed in the same position relative to the inlet as the undisturbed vehicle, allowing for direct comparison between the two. The downstream vehicle was placed at a number of positions to compare to the experimental study and the imposed wake case.

### 6.2.1 Axially Aligned with a One Vehicle Separation

#### 6.2.1.1 Upstream 25% F1 Car

Initially the second vehicle was inserted such that it was aligned axially and one car length behind the lead vehicle. The one car length separation was selected as the closest realistic on-track following distance before affecting an overtake and thus the separation where the greatest loss occurs. The effect on both vehicles is shown in table 6.3, as expected, the greatest losses are experienced by the following vehicle however the lead vehicle also experiences some force loss due to the interaction with the trailing car. The lead car experiences a small decrease of drag, a phenomenon which is noted in literature [89], there is also a similar magnitude ($\delta C_L = 0.014$) loss of downforce. More significantly, the lead vehicle aero-balance ($\frac{C_{LR}}{C_L}$) moves rearward, with an $11\%$ increase in load on the rear axle. This would serve to increase understeer for the lead car, though not to the same extent as for the following vehicle

**Table 6.3:** Comparison of force coefficients from axially aligned case with one vehicle separation study to baseline.

| | $C_D$ | $\Delta(\%)$ | $C_L$ | $\Delta(\%)$ | $\frac{C_{LR}}{C_L}(\%)$ | $\Delta(\%)$ | $\frac{L}{D}$ | $\Delta(\%)$ |
|---|---|---|---|---|---|---|---|---|
| BL[a] | 0.918 | - | -0.796 | - | 68.3 | - | -0.868 | - |
| TVL[L,0][b] | 0.902 | $\downarrow$ 1.74 | -0.782 | $\downarrow$ 1.80 | 79.1 | $\uparrow$ 10.8 | -0.867 | $\downarrow$ 0.06 |
| TVF[L,0][c] | 0.741 | $\downarrow$ 19.2 | -0.323 | $\downarrow$ 59.4 | 106 | $\uparrow$ 37.4 | -0.436 | $\downarrow$ 49.7 |

[a] BL = Baseline case
[b] TVL[L,0] = Two vehicle case, lead vehicle with one vehicle length separation and no offset
[c] TVF[L,0] = Two vehicle case, following vehicle with one vehicle length separation and no offset

The downstream vehicle experiences a $37\%$ rearwards shift of the aero-balance, to aft of the rear axle, meaning that the front axle experiences no aerodynamic downforce, and is even generating lift. Coupled with the rearwards $\frac{C_{LR}}{C_L}$ shift is a significant reduction in the overall downforce of the following car compared to both the lead ($57\%$) and undisturbed vehicles ($59\%$). The trailing vehicle also experiences reduced drag of $\approx 20\%$ of the baseline vehicle, which would increase top speed by $\sim 8\%$.

Vehicle component forces (figure 6.10) show very little difference between the undisturbed and leading

vehicles, with the front wing drag and downforce only $1\%$ lower than the freestream case. The rear wing, unsurprisingly as the closest geometry to the following vehicle, sees the biggest variation between cases with $4\%$ lower drag and $5\%$ less downforce.

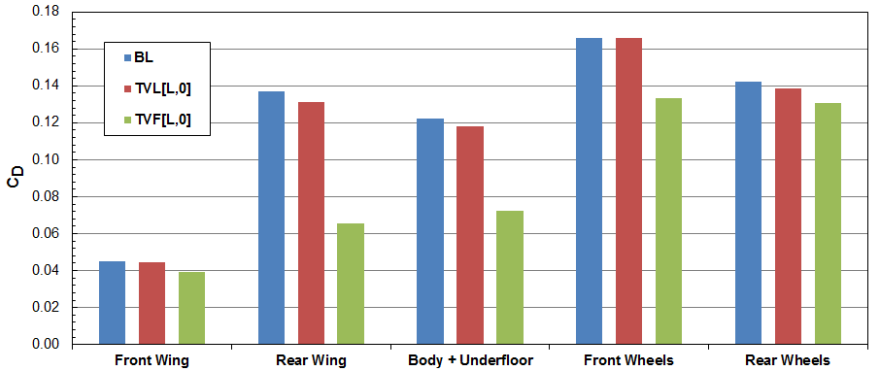


**(a)** Drag.

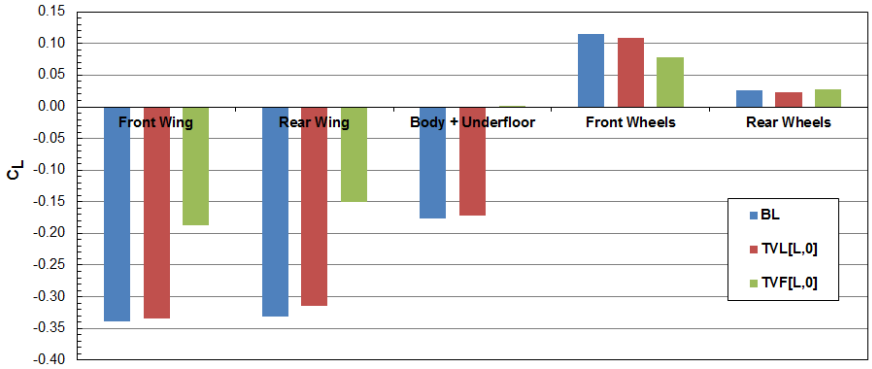


**(b)** Downforce.

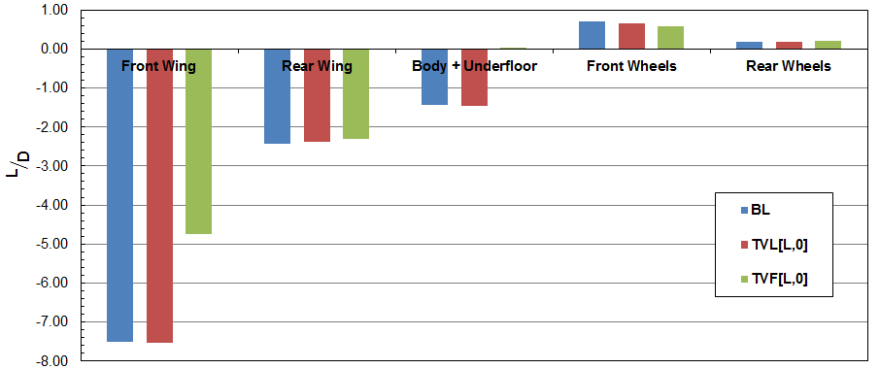


**(c)** Lift-to-drag.

**Figure 6.10:** Component forces for axially aligned case with one vehicle separation.

As seen in table 6.3 the following vehicle experiences a much greater loss than the lead vehicle and the individual components are no different (figure 6.10). As predicted in literature the front wing efficiency ($^L/_D$) is significantly reduced by the upstream vehicle wake, figure 6.10c. However, the front wing does not lose the most downforce relative to the undisturbed vehicle, $\Delta C_L = +0.15$. This is a surprise as it is expected that as the first geometry to contact the wake, where the velocity and pressure deficits and vorticity is strongest, the front wing would lose the most performance; this coupled with the considerable aft-ward displacement of the aero-balance has lead to the seemingly incorrect conclusion. As a matter of

fact both the rear wing and body lose the most downforce, $\Delta C_L = +0.18$, though the rear wing efficiency remains almost unchanged from the freestream. That the rear wing drag and lift are shed at almost the same rate seems to be the result of the axial velocity deficit from the wake of the upstream vehicle, which is predominantly localised at rear wing height. More surprisingly, considering the assertion that ground effect is less affected by an upstream wake, the combined upper and under-body loses all downforce, actually generating a small net lift, albeit only $C_L = 0.0005$. In the undisturbed condition the upper-body generates a large amount of lift, resulting in a net body downforce equal to only $22\%$ of the total downforce generated by the under-body. In the wake the upper-body lift is reduced by only $25\%$ while the underfloor experiences a $42\%$ reduction of downforce. It is clear that the components in ground-effect (front wing and underfloor) are more significantly affected by the upstream wake than components out of ground-effect, such as the rear wing or bodywork.

The surface pressure plot for the following vehicle, figure 6.11(b), shows a significantly different static pressure distribution on the front wing underside than the undisturbed vehicle (figure 6.4). Where in the undisturbed case the mainplane features a low static pressure region extending across most of the span, there is instead a pair of low pressure regions localised upstream of the flaps. The $\Delta C_P$ surface plot shows that most of the mainplane sees an increase of $\Delta C_P = 0.35$ across the majority of the wing span and chord, with a peak loss of $\Delta C_P = 0.8$ concentrated on the centreline. The upper surface of the front wing sees a reduction of static pressure over much of the surface of both mainplane and flaps in excess of $\Delta C_P = -0.35$.

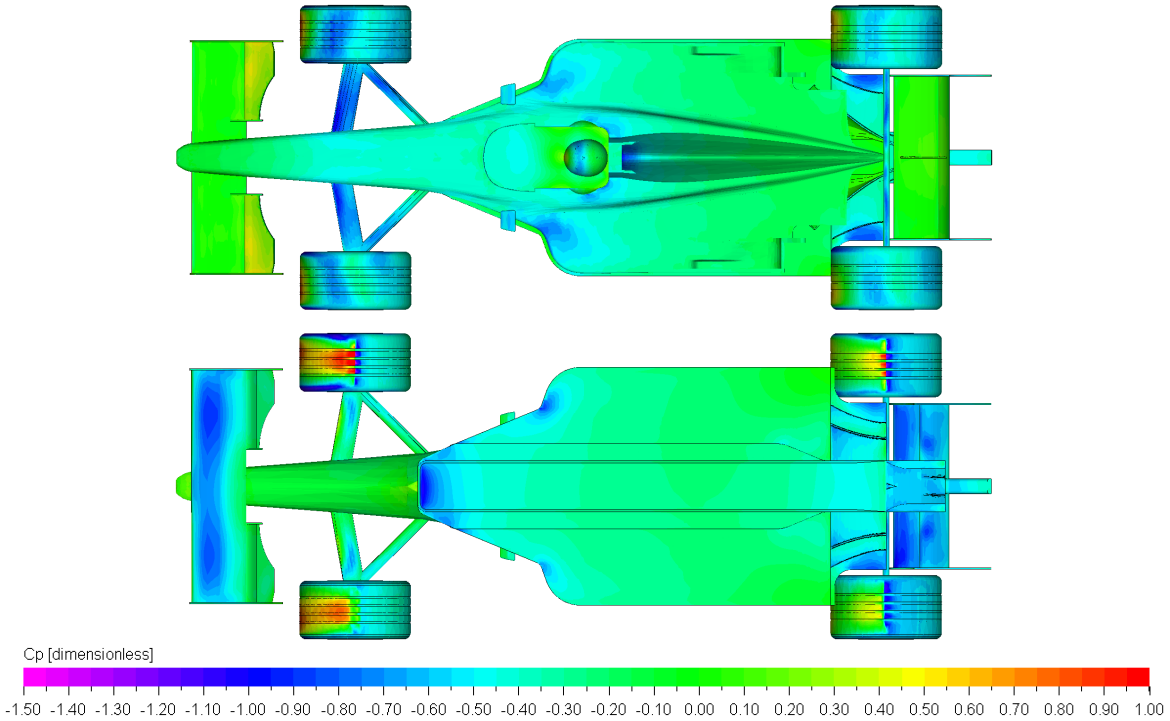


**(a)** $C_P$.

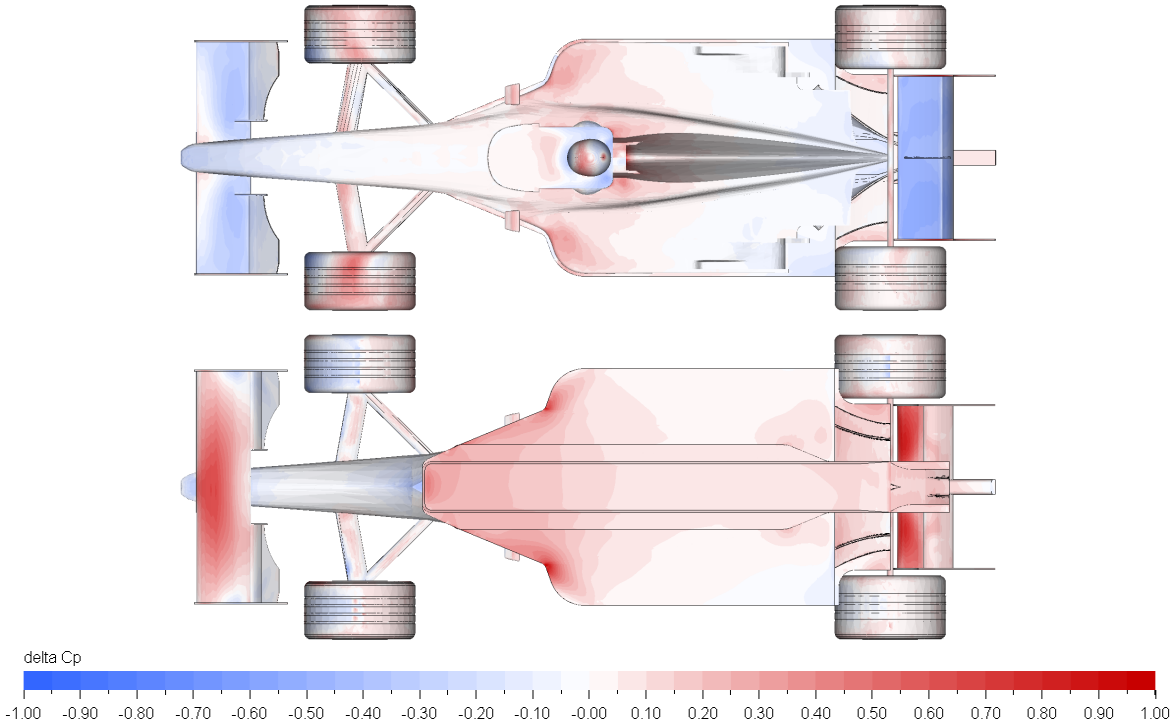


**(b)** $\Delta C_P$ to baseline case.

**Figure 6.11:** Downstream vehicle surface pressure distributions.

#### 6.2.1.2 Upstream BBWG

In order to compare the effect of the wake in CFD to experimental results, the upstream bluff body was simulated at the same representative separation as the full vehicle, i.e. one vehicle length downstream, also corresponding to the greatest axially aligned separation achieved during wind tunnel testing.

Using CFD allows the aerodynamic forces of the bluff bodied wake generator to be measured, table 6.4. The exposed wheels generate more aerodynamic drag than the baseline car, presumably as the wake generator has no front wing partially shadowing the wheels; aerodynamic lift generated by the front wheel is approximately matched to the baseline car, $C_L \approx 0.13$. While total downforce of the wake generator is relatively low, compared to the $25\%$ Formula 1 car, the peak loading on the lower surface of the wing is almost double that of the F1 car's rear wing, $C_P \approx -3$, figure 6.12. The increased suction will be the result of a combination of the the onset flow, which has not passed over any upstream geometries, so is closer to freestream, and the contraction caused by the upper deck of the bluff body.

**Table 6.4:** Bluff bodied wake generator force coefficients, based on reference area of $1.5m^2$ (full scale).

| | $C_D$ | $C_L$ | $\frac{L}{D}$ |
|---|---|---|---|
| Body + Wing | 0.328 | -0.276 | -0.843 |
| Wheels | 0.246 | 0.134 | 0.545 |
| Total | 0.574 | -0.142 | -0.247 |

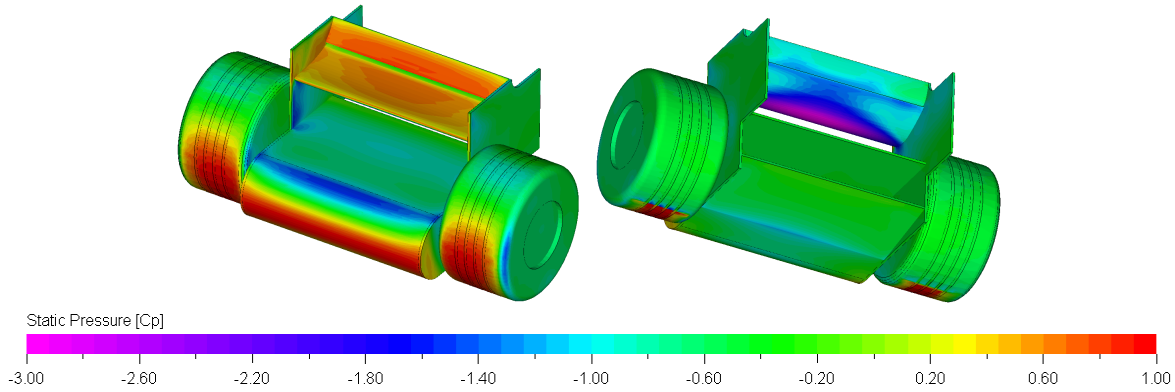


**Figure 6.12:** BBWG surface pressure distribution.

The effects of the bluff bodied wake generator on the downstream vehicle forces are shown in table 6.5. It should be noted while the freestream (wheels-off) forces in the wind tunnel are greater than the forces (wheels-on) recorded in CFD, the percentage change of total force due to the wake generator is similar, within $2.5\%$ of the experimental case for drag and $6.5\%$ for downforce. The effect of the upstream wake on total vehicle drag is less significant with the upstream wake generator than the full upstream vehicle, which is not a surprise considering the lower levels of velocity deficit in the wake of the BBWG (figure 4.15).

**Table 6.5:** Comparison of force coefficients from following vehicle and bluff bodied wake generator (both CFD and experimental), delta to baseline case.

| | $C_D$ | $\Delta(\%)$ | $C_L$ | $\Delta(\%)$ | $\frac{C_{LR}}{C_L}(\%)$ | $\Delta(\%)$ | $\frac{L}{D}$ | $\Delta(\%)$ |
|---|---|---|---|---|---|---|---|---|
| TVF[L,0][a] | 0.741 | ↓ 19.2 | -0.323 | ↓ 59.4 | 106 | ↑ 37.4 | -0.436 | ↓ 49.7 |
| BBWG | 0.757 | ↓ 17.5 | -0.448 | ↓ 43.8 | 96.9 | ↑ 28.5 | -0.592 | ↓ 31.8 |
| Experimental | 0.610 | ↓ 19.8 | -0.752 | ↓ 37.5 | 59.4 | ↑ 0.90 | -1.23 | ↓ 22.2 |

[a] TVF[L,0] = Two vehicle case, following vehicle with one vehicle length separation and no offset

The effect of the wake generator on the total vehicle downforce is also lower for the upstream BBWG,

$\approx 16\%$ lower than the downforce loss experienced behind a full vehicle as simulated in CFD. The lesser downforce loss is coupled with a reduced shift of the aerodynamic balance ($\Delta C_{LR} \approx 9\%$); which, while a relatively significant balance shift, would not significantly impact car handling as the majority (all but $3\%$) of the total downforce is still acting at the rear axle. Investigation of the component forces shows that the downstream vehicle experiences a similar change of drag, within $C_D = \pm 0.01$ for all components, with the exception of the rear wing which is $C_D \approx 0.02$ closer to the baseline value. The change of component downforce is also similar when compared to the full upstream vehicle, within $C_L = \pm 0.01$. Like drag, the rear wing experiences a reduced loss of performance of $\delta C_L \approx -0.06$, the combined upper and underbody also loses less downforce with the upstream wake generator $\delta C_L \approx -0.04$ compared to a full upstream vehicle.

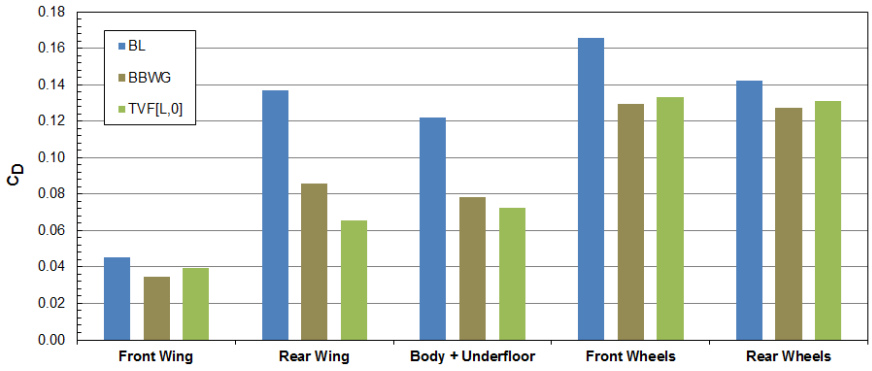


**(a)** Drag.

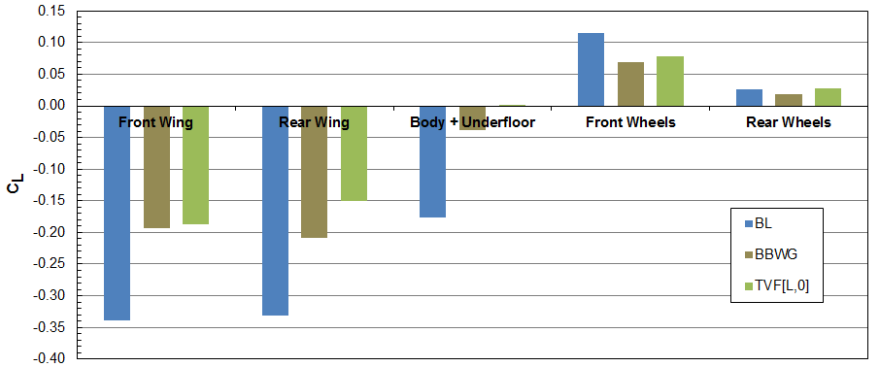


**(b)** Downforce.

**Figure 6.13:** Component force coefficients (based on car frontal area) for upstream bluff body and full vehicle with a one vehicle separation.

Comparing the surface pressure distributions of the downstream vehicles, where $\Delta C_P$ (the absolute pressure distributions can be found in Appendix E) is the surface pressure of the BBWG case subtracted from the two vehicle following case, shows very little difference between the effect of the upstream wake generator and car, figure 6.14. The resulting contour is very flat, with much of the car's aerodynamic surfaces within $\Delta C_P \approx \pm 0.1$. As the component forces suggest, the greatest difference between the cases is seen on the rear wing, with the upper surface pressure almost uniformly greater by $\Delta C_P \approx 0.2$, while the lower surface pressure is $\Delta C_P < -0.3$ lower with the upstream wake generator. There is a slight asymmetry in the $\Delta C_P$ on both the lower surface of the front wing and underbody, which can be attributed to a lack

of asymmetry in the wake of the wake generator. As previously discussed the rear wing and diffuser of the car in isolation both feature separated regions, leading to asymmetry in the wake of the car. The wing of the wake generator, without any bodywork upstream, is subject to a very different onset flow to the rear wing of the car, slightly changing the wake characteristics.

While the effect of the upstream wake generator is not identical to the full vehicle, there are sufficient similarities between the two cases to indicate that the use of the wake generator in the wind tunnel will produce similar results to a full vehicle.

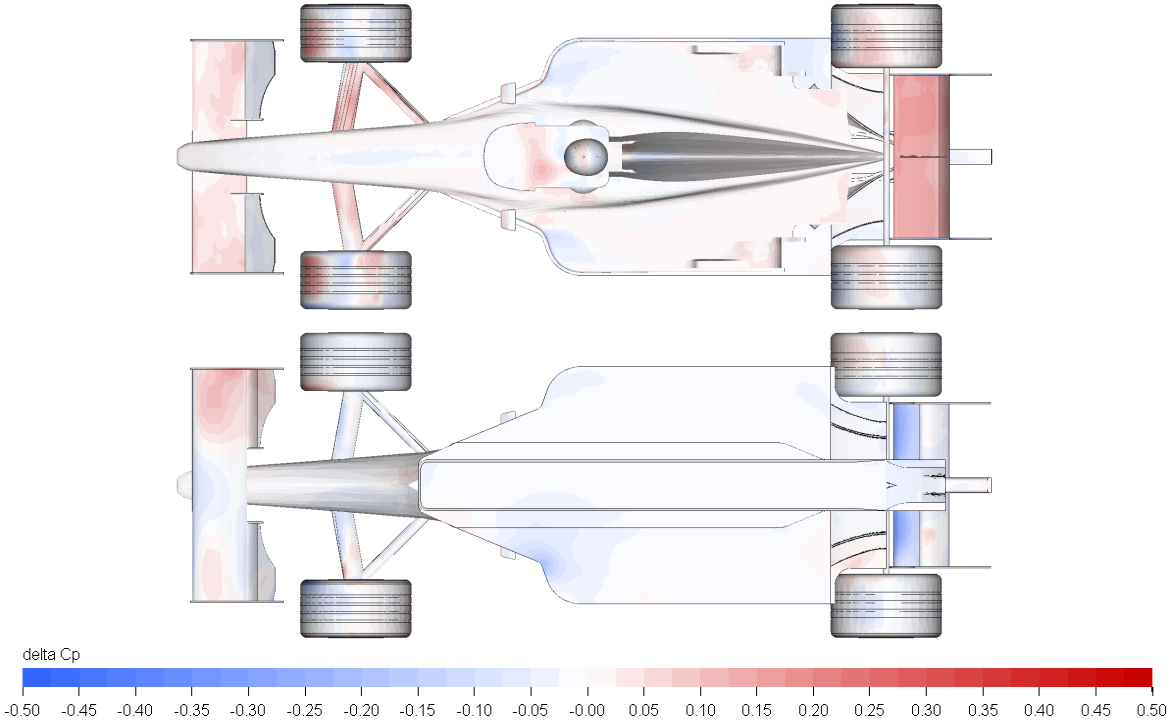


**Figure 6.14:** Downstream vehicle surface $\Delta C_P$, comparing effect of upstream bluff bodied wake generator to full vehicle.

### 6.2.2 One Vehicle Separation with a Half Car Lateral Offset

Rather than repeat all the wind tunnel cases, at high computational cost, the only other case tested both experimentally and computationally was the $x = L_C$ separation with a $y = 0.5W_C$ lateral offset. In the wind tunnel, downforce is seen to recover with an offset to the freestream value more quickly than drag, and this trend is also seen in CFD, table 6.6. At the same axial spacing, the effect of the upstream wake on vehicle drag is seen to drop from $19\%$ to $7\%$, while downforce increases by $57\%$ to just $2\%$ lower than an isolated vehicle. This increases the $^{L}/_{D}$ ratio of the car from freestream, with higher top speed from the reduced drag, with less of an impact on lateral acceleration than when axially aligned at the same separation. Like the experimental case, the aero-balance experiences a forwards shift at this relative septation to the lead vehicle.

**Table 6.6:** Comparison of force coefficients from two vehicle case with one vehicle separation and a $0.5W$ lateral offset study to baseline.

| | $C_D$ | $\Delta(\%)$ | $C_L$ | $\Delta(\%)$ | $\frac{C_{LR}}{C_L}(\%)$ | $\Delta(\%)$ | $\frac{L}{D}$ | $\Delta(\%)$ |
|---|---|---|---|---|---|---|---|---|
| TVF[L,0] | 0.741 | ↓ 19.2 | -0.323 | ↓ 59.4 | 106 | ↑ 37.4 | -0.436 | ↓ 49.7 |
| TVF[L,0.5W][a] | 0.852 | ↓ 7.19 | -0.779 | ↓ 2.14 | 65.5 | ↓ 2.78 | -0.915 | ↑ 5.43 |
| Experimental[b] | 0.686 | ↓ 11.4 | -1.12 | ↓ 3.47 | 57.6 | ↓ 0.20 | -1.625 | ↑ 7.08 |

[a]TVF[L,0.5W] = Two vehicle case, following vehicle at a one vehicle length separation with a $0.5W_C$ offset
[b]Posture averaged data of axial separation with half car offset, compared to experimental posture averaged baseline

The upstream vehicle's influence on the component forces of the downstream vehicle is also reduced from the axially aligned case, figure 6.15. Aerodynamic drag generated by both the rear wing and body increases from the axially aligned case to within $8\%$ of the baseline case, however the effect of the upstream vehicle on the front wing is unchanged from the axially aligned case. Drag generated by the front wheels decreases relative to the axially aligned case, primarily as a result of the X-Y+ wheel which generates $45\%$ less drag than the baseline, which can be seen in figure 6.17 to be the result of the reduction of static pressure on the front face of the tyre. Downforce generated by all the downforce producing surfaces also recovers to the baseline with the offset, for the front and rear wings this is to within $8\%$ while the body is within $12\%$ of the baseline downforce.

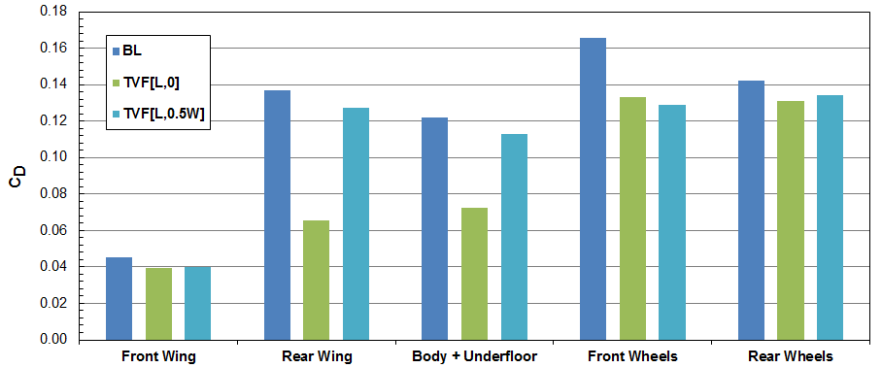


**(a)** Drag.

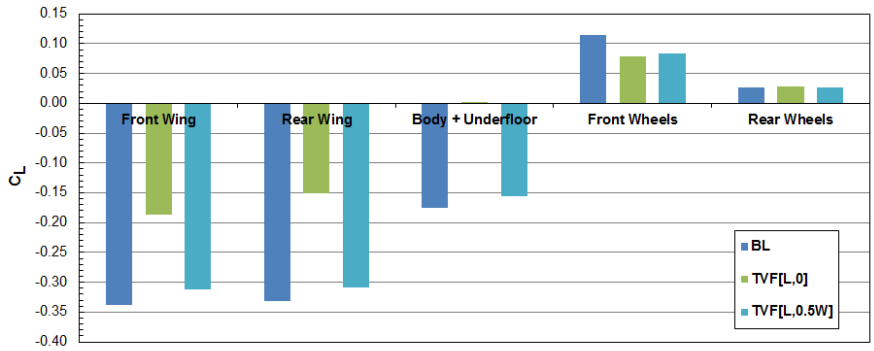


**(b)** Downforce.

**Figure 6.15:** Component force coefficients (based on car frontal area) for $x = L_C$ axial sepration cases, both axially aligned and with a $y = 0.5W_C$ offset.

The effect of the upstream vehicle wake on the surface pressure distribution, compared to the baseline vehicle, is shown in figure 6.16; the plots of absolute surface pressure can be found in Appendix E.

Unsurprisingly, much of the effect on the car is concentrated on the Y+ side (i.e. that which is directly downstream of the upstream vehicle), especially the front Y+ wheel and the front and rear wings. The peak $\Delta C_P$ on the body and wings is also significantly lower than experienced by the axially aligned car (figure 6.11) peaking at $C_P \approx \pm 0.3$. Interestingly the effect of the upstream wake on the underbody is relatively symmetric, though $\Delta C_P$ is very small, with peaks of less than $0.15$ limited to the front of the floor and diffuser throat, and $\Delta C_P \approx 0$ over the rest of the underfloor.

Comparing the surface pressure distribution to the axially aligned case, figure 6.17, static pressure on the underside of the front and rear wings is lower by $-0.5 < \Delta C_P < -0.8$, which would explain why the downforce of these elements almost doubles with the introduction of a half car offset, figure 6.15.

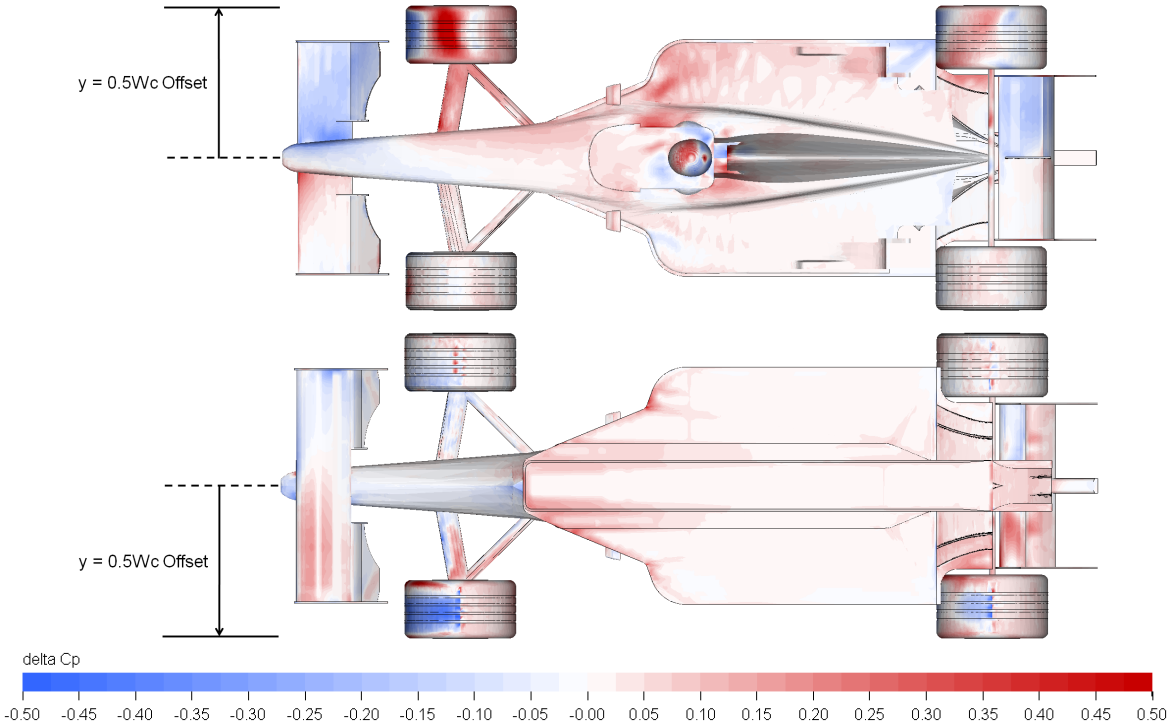


**Figure 6.16:** Downstream vehicle surface $\Delta C_P$, comparing effect of following vehicle at $x = 1L_C$ separation with $y = 0.5W_C$ offset to baseline case.

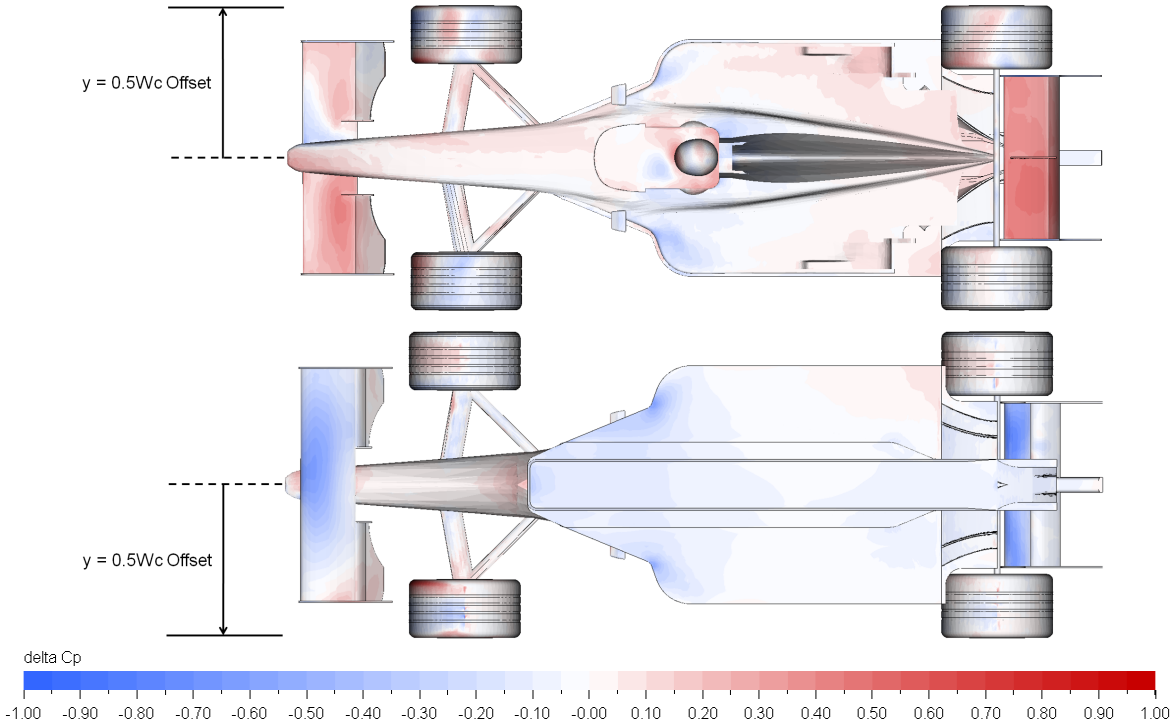


**Figure 6.17:** Downstream vehicle surface $\Delta C_P$, comparing effect of following vehicle at $x = 1L_C$ separation with $y = 0.5W_C$ offset to axially aligned case with a $x = L_C$ sepration.

### 6.2.3 Axially Aligned with a Two Vehicle Separation

What could not be achieved in the wind tunnel, owing to restrictions in the working section length (in particular the moving ground plane), was axial separations greater than on car length. While no such restrictions exist in CFD; increasing the domain length to accommodate a second vehicle, using the mesh refinement regions and minimum voxel scale around the lead vehicle almost doubles the lattice count from 16 million to 31 million cells, and will increase computational cost. It was decided that while simulating further vehicle separations would inform the effect of the wake on this car, it does not improve the understanding of which feature in the wake is actually responsible for the aerodynamic effect.

With twice the axial separation to the upstream vehicle, aerodynamic drag increases by $5\%$, table 6.7, which is $15\%$ lower than the baseline drag; downforce also increases, by over $20\%$, though is still $39\%$ lower than the baseline which would still have a significant impact on cornering performance. The trend of aerodynamic drag and downforce recovering to their baseline values less rapidly with increasing axial separation than occurs with a small lateral offset, even at very short following distances (table 6.15), is the same as was seen in the experimental study (figures 4.37 and 4.38). The aerodynamic balance shift is less severe at this offset to the leading car, only $7.5\%$, which is a similar magnitude of aero-balance shift seen with a $\alpha = 12°$ detuning of the front flap, figure 4.1c.

As would be expected, component forces for much of the car are closer to the baseline with the increased

**Table 6.7:** Comparison of force coefficients from axially aligned case with two vehicle separation study to baseline.

| | $C_D$ | $\Delta(\%)$ | $C_L$ | $\Delta(\%)$ | $\frac{C_{LR}}{C_L}(\%)$ | $\Delta(\%)$ | $\frac{L}{D}$ | $\Delta(\%)$ |
|---|---|---|---|---|---|---|---|---|
| TVF[L,0] | 0.741 | ↓ 19.2 | -0.323 | ↓ 59.4 | 106 | ↑ 37.4 | -0.436 | ↓ 49.7 |
| TVF[2L,0][a] | 0.784 | ↓ 14.6 | -0.486 | ↓ 38.9 | 75.8 | ↑ 7.50 | -0.620 | ↓ 28.5 |

[a]TVF[2L,0] = Two vehicle case, following vehicle with two vehicle length separation and no offset

inter-vehicle separation, figure 6.18, the exception being the forces generate by the rear wheels. Like the $x = L_C$ case, of the downforce generating surfaces the front wing is the least affected by the upstream wake, $\Delta C_D = -0.006$ and $\Delta C_L = 0.1$. While the body and rear wing downforce decrease by $\Delta C_L = 0.115$ and $\Delta C_L = 0.125$ respectively; the rear wing lift-to-drag ratio remains unchanged, as with the $x = L_C$ case, as it's drag reduces at the same rate as downforce.

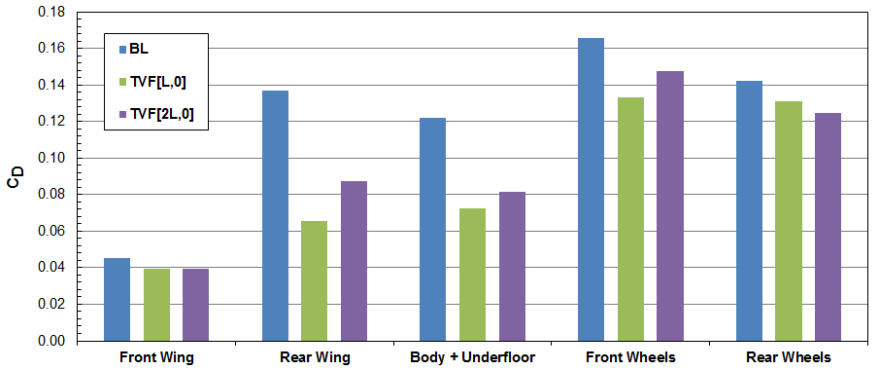


**(a)** Drag.

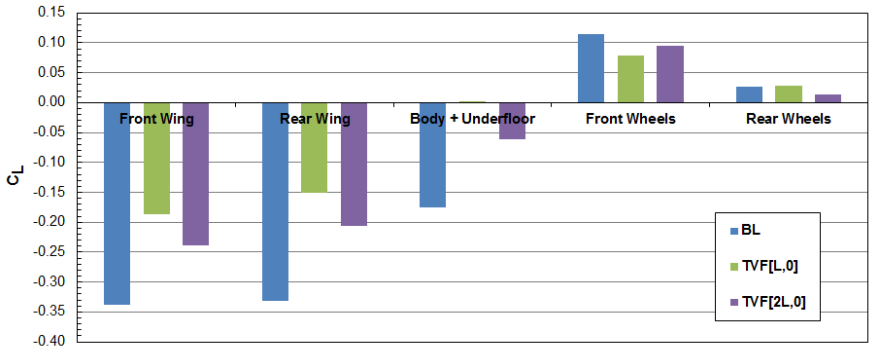


**(b)** Downforce.

**Figure 6.18:** Component force coefficients (based on car frontal area) for axially aligned cases.

The surface $\Delta C_P$ distribution (figure 6.19) shows that the upstream wake affects the same regions of the car as the $x = L_C$ separation case (figure 6.11b), though magnitude of the change of pressure is smaller. The front wing lower surface pressure increases by $\Delta C_P = 0.2$ across the majority of the mainplane span and chord, with a peak $\Delta C_P < 0.4$ on the wing centreline. The front of the underbody and diffuser throat also experiences an increase of pressure from the baseline, with peaks of $\Delta C_P = 0.8$ at the front edges under the sidepods. As with the $x = L_C$ case pressure increases ($0.1 < \Delta C_P < 0.15$) at the leading edges of the sidepods, which would reduce upper bodywork lift. Like the $x = L_C$ case the rear wing is

subjected to the greatest $\Delta C_P$ over the largest area, the lower surface increasing $0.25 < \Delta C_P < 0.65$ over much of the chord across the whole span, and the upper surface pressure decreasing almost uniformly by $\Delta C_P = -0.4$.

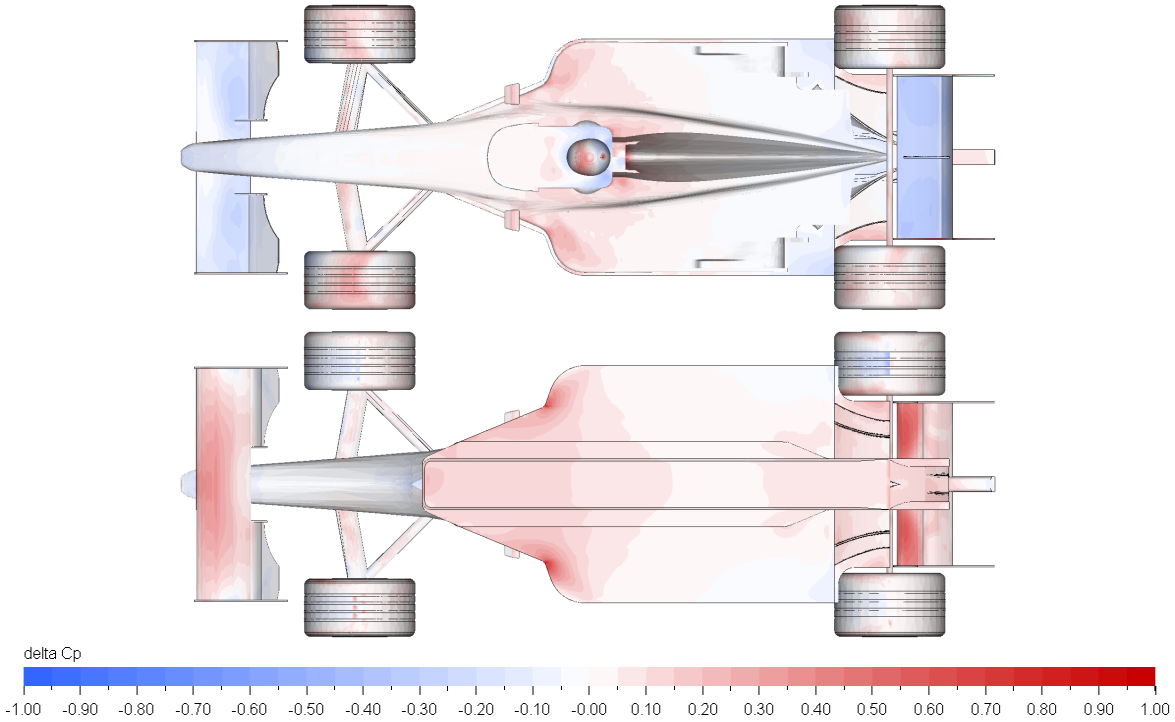


**Figure 6.19:** Surface pressure distribution for following vehicle, with a $2L_C$ separation and no lateral offset compared to baseline case.

## 6.3 Imposing the Wake on the Inlet Plane

While inserting a second vehicle in the domain, upstream of the test vehicle allows the effect of the upstream wake on a downstream vehicle to be measured, this thesis also proposes to determine which constituent elements of the wake most significantly affects the downstream vehicle. To achieve this the wake must be modified and the effect of the new wake recorded. Using a two vehicle approach, alterations to the onset flow field can only be achieved by modifying the upstream vehicle, thereby changing its wake. It would be difficult to achieve precise changes to a single flow field parameter, while optimizing a geometry to produce the desired wake would be an inefficient use of time and resources. Therefore a new method was proposed, whereby the wake's flow field is created using the inlet boundary conditions, figure 6.20. In this section the robustness of the method is tested, by matching the onset conditions to the wake of the car.

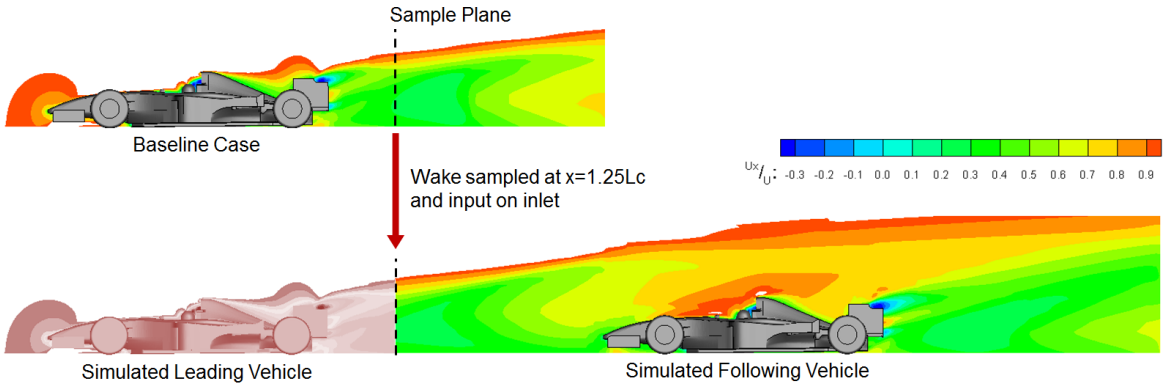


**Figure 6.20:** Method of simulating an upstream vehicle by sampling the wake and imposing it on the inlet of a simulation, shown by centreline contours of axial velocity, wake sampled at $x = 1.25L_C$ behind baseline case.

This method also has the unintended advantage that it is not specifically prohibited by the FIA Formula 1 sporting regulations (Appendix 8: Aerodynamic Testing Restrictions [79]), which stipulate the use of a single vehicle at any time during wind tunnel and CFD testing.

### 6.3.1 Recreating the 25% Formula 1 Wake

To impose the wake on the inlet plane first the wake must be sampled. It was desired that no reversed flow be present on the inlet plane; while flow reversal only exists in the very near wake of the car, $x < 0.12L_C$, the wake in this region is relatively unstructured. So to assure the correct wake development the sample plane was selected at $x = 0.25L_C$, which also made certain that the wake had fully closed. As mentioned in the CFD methodology, to impose the wake with a simulated $x = L_C$ separation to the lead vehicle required the inlet to be placed closer to the car than best practice would dictate, just $x = 0.75L_C$ from the nose of the car. While this does affect the measured forces in freestream, the difference is small, less the $\pm 0.1$ on both $C_D$ and $C_L$, and is systematic affecting all CFD cases. As the effect of the wake is

desired, rather than the accurate force measurements required for vehicle development, this was deemed an acceptable compromise.

Data for static and total pressure, and the three components of velocity were sampled using a structured grid measuring $10mm \times 10mm$ (figure 6.21) or $99,575$ total points, each with x, y, z co-ordinates and $C_P$, $u_X$, $u_Y$, and $u_Z$ measurements. The subsequent table was loaded into PowerFLOW and used to define the boundary conditions of the inlet via the equation editor.

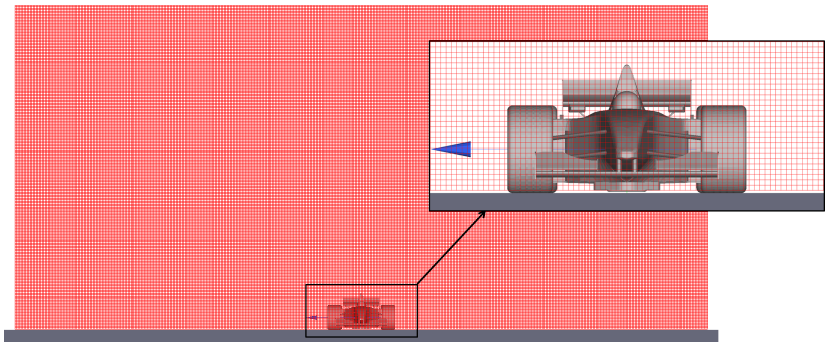

**Figure 6.21:** Imposed wake inlet grid, resolution $10mm^2$.

In order to impose the wake onto the inlet plane a suitable set of boundary conditions had to be selected. The inlet and outlet pairings which are recommended by PowerFLOW are shown in table 6.8; as can be seen none of the reccommended inlet conditions will recreate more than two of the wake variables. However, by pairing a static pressure with velocity inlet plane with a static pressure outlet all the wake variables can be imposed, with total pressure deficit recreated by the sum of static and dynamic pressures. While it is not ideal to constrain the static pressure on both the inlet and outlet it is an acceptable practice within PowerFLOW, and does allow the key parameters of the wake to be recreated, figure 6.23. "Simulations that use static pressure boundary conditions for both the inlet and the outlet are also acceptable, but are recommended only when none of the other boundary condition pairings can be used." [132]

**Table 6.8:** PowerFLOW recommended inlet and outlet boundary conditions pairings.

| Inlet | Outlet | $P$ | $P_o$ | $u_X$ | $u_{Y,Z}$ |
|---|---|---|---|---|---|
| Total Pressure | Static Pressure | × | ✓ | × | × |
| Velocity | Static Pressure | × | × | ✓ | ✓ |
| Static Pressure | Velocity | ✓ | × | × | × |
| Static Pressure | Mass Flow | ✓ | × | × | × |
| Static Pressure & Velocity | Static Pressure | ✓ | ✓$(\Sigma(P+q))$ | ✓ | ✓ |

Comparisons of the sampled wake and inlet wake variables are shown in figure 6.23, velocity fields ($u_X$ and $u_{Y,Z}$) are well recreated on the inlet plane, though some subtle differences are present. The main visual difference is that the imposed wake appears less smooth than the sample plane, this is due to the grid used to sample and impose the wake, with any interpolation occurring at voxel scale.

Of the imposed variables static pressure is the least well recreated, both in shape and the value, with the low pressure regions associated with the rear wing tip vortices noticeably more outboard. Interestingly, by just a

few millimetres downstream ($x < 0.05L_C$) of the inlet the static pressure field is much more representative of the wake, figure 6.22, with the low pressure regions shifted inboard to their correct positions.

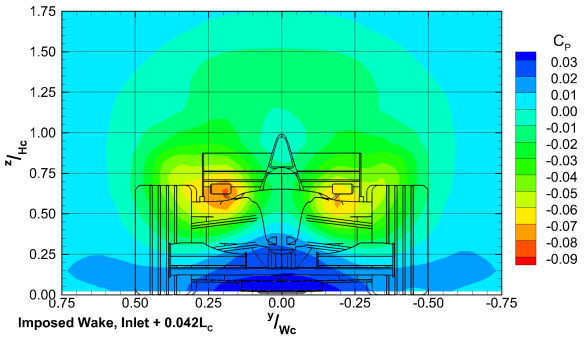


**Figure 6.22:** Contours of static pressure 50mm downstream of imposed wake case inlet.

Using a static pressure inlet with the x, y, and z aligned velocities created by directional vectors more accurately represented the static pressure deficit on the inlet, however, the axial velocity deficit (and consequently total pressure) and secondary flows were less accurately reproduced. As the static pressure deficit is relatively close to uniformity it was decided that it was more important to create the velocity deficit with greater accuracy.

As the imposed wake develops to a simulated $x = 0.5L_C$ distance downstream of the inlet, figure 6.24, the four key wake parameters remain well matched to the wake of the baseline case. The velocity deficit is marginally lower, $\delta u_X < 0.05U_\infty$, owing to the loss of resolution from the inlet plane grid, this also affects the total pressure deficit, $\delta C_{Po} < 0.05$, however the shape of both is well matched to the real wake. The static pressure deficit above $z = 0.5H_C$ is also more representative of the real wake, with the main difference being the region of greater than atmospheric pressure ($C_P > 0.06$) below $z = 0.5H_C$, in front the the 'trailing' vehicle front wing. This is evidence of a combining of the pressure field ahead of the stagnation points on the nose and front wing of the vehicle, which is not present in the baseline case, and the wake profile.

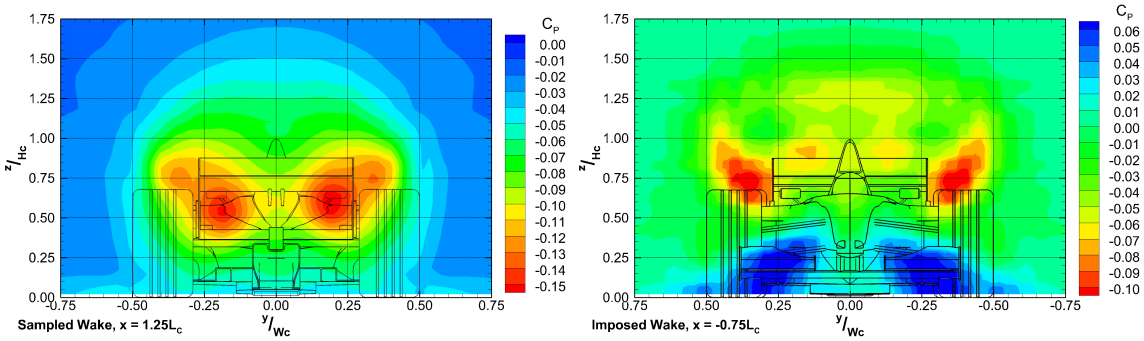


**(a)** Static pressure deficit.

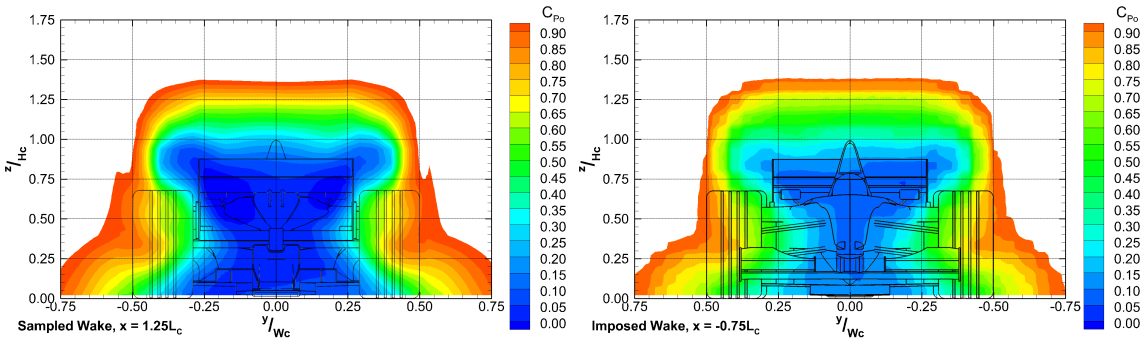


**(b)** Total pressure deficit.

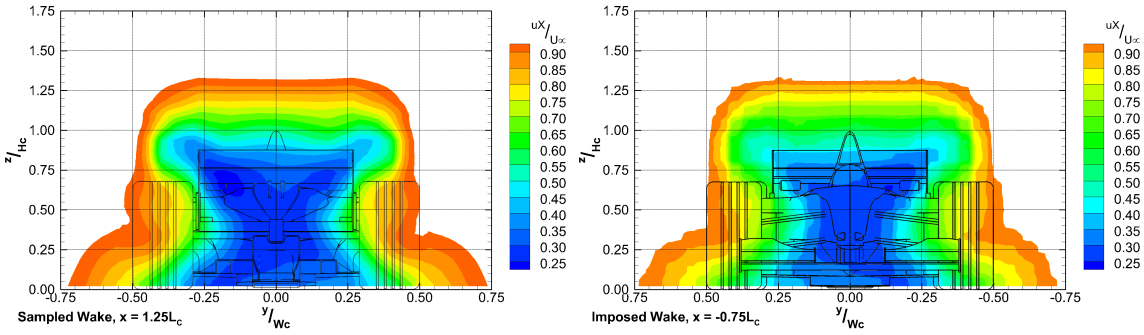


**(c)** Axial velocity deficit.

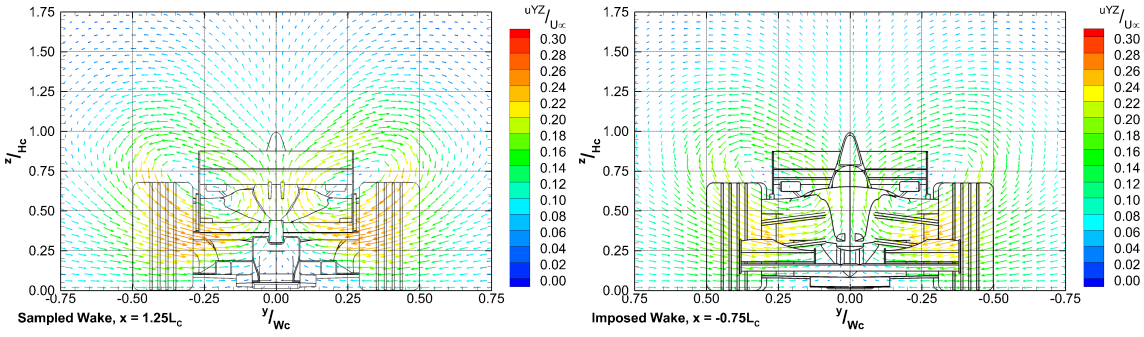


**(d)** Secondary flow vectors.

**Figure 6.23:** Comparison of sampled wake (at $x = 1.25L_C$) to imposed wake case inlet boundary conditions (at $x = -0.75L_C$).

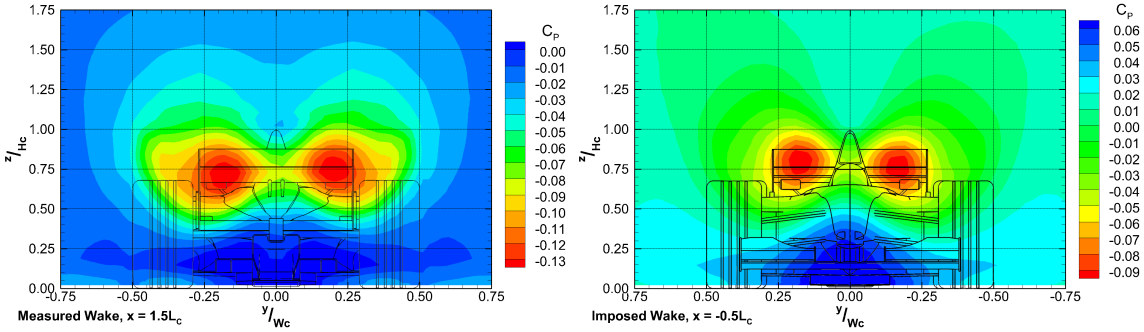


**(a)** Static pressure deficit.

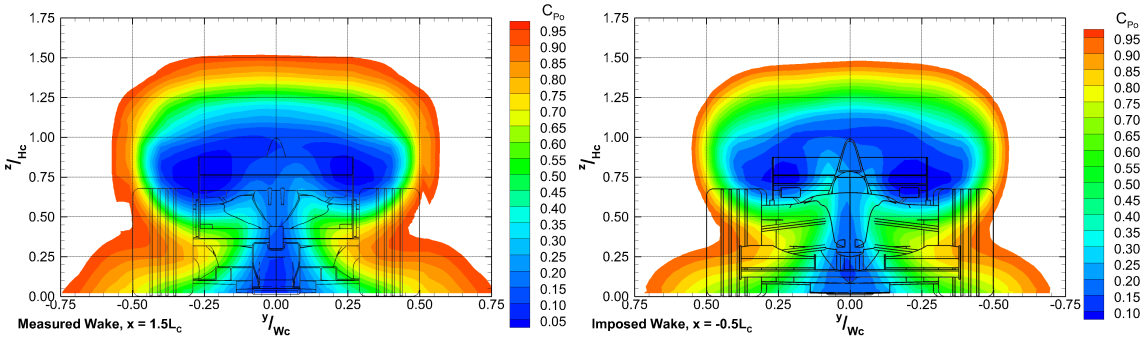


**(b)** Total pressure deficit.

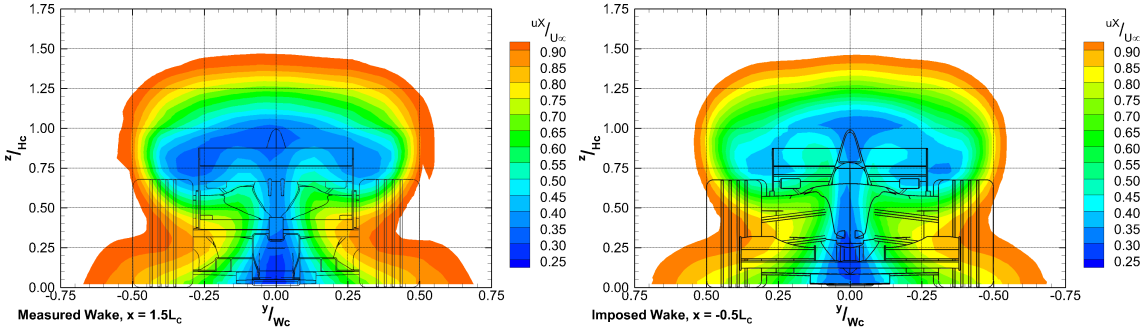


**(c)** Axial velocity deficit.

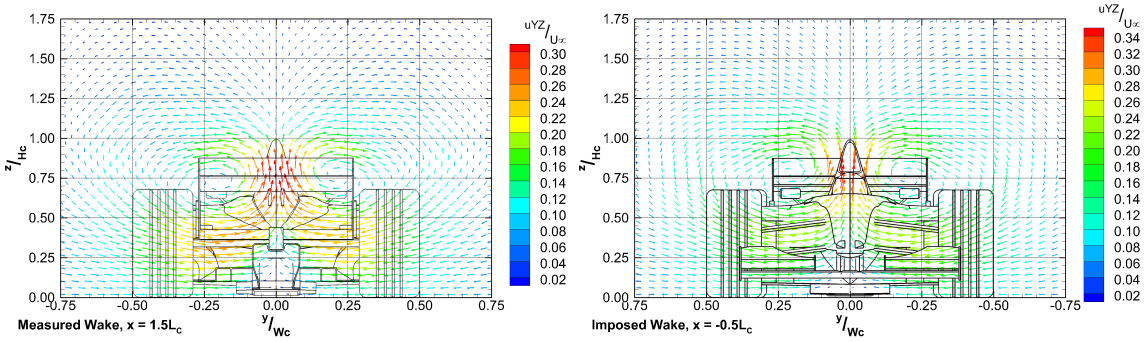


**(d)** Secondary flow vectors.

**Figure 6.24:** Comparison of baseline case wake (at $x = 1.50L_C$) to imposed inlet case wake development (at $x = -0.50L_C$).

### 6.3.2 Effect of Imposed Wake

Two imposed wake cases were simulated, in the first the wake was sampled from the baseline case at the $x = 1.25L_C$ plane and imposed on the inlet, figure 6.20. The second case imposes the wake as sampled between the lead and trailing vehicles in the axially aligned case with an $x = L_C$ separation case. As the downstream vehicle has been shown to affect forces generated by the upstream vehicle, it could also affect the wake at the sample plane. The effect of both of the imposed wakes is shown in table 6.9. The imposed wake has a similar effect on the downstream vehicle as an upstream vehicle, total drag and downforce are reduced and the centre of pressure moves rearwards, although the exact magnitude of the effect is different. This is especially true for downforce, $\Delta C_L$ is $7\%$ greater, and aero-balance, which moves $\Delta\frac{C_{LR}}{C_L}(\%) = 22\%$ more rearward, while $\Delta C_D$ is lower than the upstream vehicle it is within $1\%$.

The effect of the inlet wake as sampled between the two vehicles is greater on both drag ($\Delta C_D = 2.6\%$) and downforce ($\Delta C_L = 1\%$) than the baseline case sampled inlet, though the centre of pressure shift is $2\%$ less rearward. The aero-balance shift in both these cases places the centre of pressure of the car significantly behind the rear axle line. Examination of the component lift forces, figure 6.25, shows that wheel lift is greater for the imposed cases than for the two vehicle case, especially the front wheels which are $C_L = 0.03$ greater, or $22\%$ closer to the baseline lift. Ignoring wheel forces, the sprung component $\frac{C_{LR}}{C_L}(\%)$ still moves more significantly rearward than the two vehicle case, but only by $4.3\%$ rather than $22\%$.

**Table 6.9:** Comparison of baseline, following vehicle and imposed inlet wake cases.

| | $C_D$ | $\Delta(\%)$ | $C_L$ | $\Delta(\%)$ | $\frac{C_{LR}}{C_L}(\%)$ | $\Delta(\%)$ | $\frac{L}{D}$ | $\Delta(\%)$ |
|---|---|---|---|---|---|---|---|---|
| TVF[L,0][a] | 0.741 | $\downarrow 19.2$ | -0.323 | $\downarrow 59.4$ | 106 | $\uparrow 37.4$ | -0.436 | $\downarrow 49.7$ |
| IW[b] | 0.750 | $\downarrow 18.3$ | -0.265 | $\downarrow 66.7$ | 128 | $\uparrow 59.3$ | -0.354 | $\downarrow 59.2$ |
| IWTV[c] | 0.726 | $\downarrow 20.9$ | -0.257 | $\downarrow 67.7$ | 126 | $\uparrow 57.3$ | -0.354 | $\downarrow 59.1$ |

[a] TVF[L,0] = Two Vehicle Case, following at a separation of 1 car length with no lateral offset
[b] IW = Imposed wake, sampled from BL case
[c] IWTV = Imposed wake, sampled from between the cars in the two vehicle case

The component force breakdown (figure 6.25) also shows that the effect of the imposed wakes on the downstream car is very similar to the effect of an upstream vehicle; with the exception of the wheel forces as previously mentioned. As with the full vehicle forces, the effect of the baseline case sampled inlet is closer than the two vehicle sampled case to the upstream vehicle case for the majority of the car surfaces. With the exception of the wheels, the greatest difference between the three cases on component drag is $C_D \approx 0.004$, which occurs for the rear wing; while body and front wing measurements are within $C_D = 0.002$.

As is the case with the full upstream vehicle, the front wing downforce loss is lower ($0.164 < \Delta C_L < 0.170$) than both the rear wing ($0.186 < \Delta C_L < 0.197$) and body ($0.164 < \Delta C_L < 0.173$). The body downforce

loss is less severe for both imposed inlet cases, while the upstream vehicle causes a total loss of body downforce, some downforce remains for the imposed cases. While the variation in downforce between the cases is greater than drag, it is still less than $C_L = 0.018$, again the exception to this is the wheels. Front and rear wheel lift for the two vehicle sampled case is lower than the baseline sampled case, which could explain why the balance shift is slightly less severe, though only by $\Delta\frac{C_{LR}}{C_L}(\%) = -2\%$.

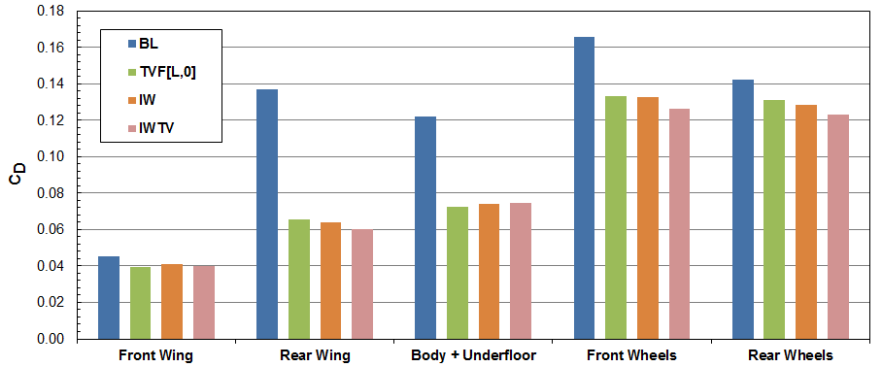


**(a)** Drag.

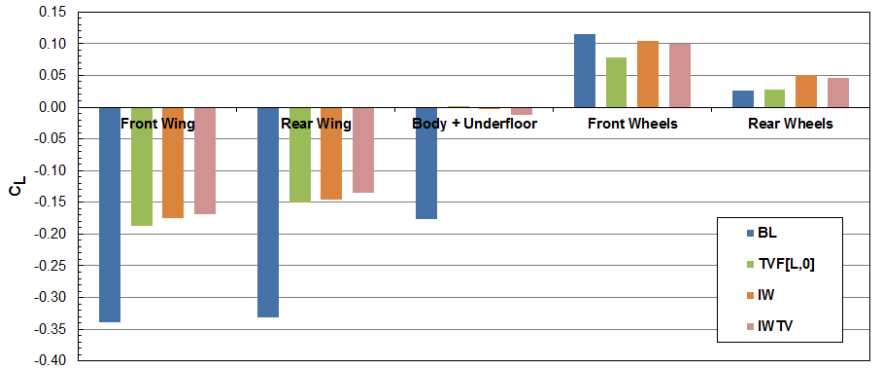


**(b)** Downforce.

**Figure 6.25:** Component forces for imposed wake cases with simulated one vehicle separation.

Contour plots of the change of surface pressure ($\Delta C_P$) are shown in figure 6.26, as can be seen there is very little difference between the baseline and inter-vehicle sampled imposed wake cases. As is the case with an upstream vehicle, low pressure regions on the lower surfaces of the front wing, rear wing, and underfloor experience an increase of pressure. While high pressure regions such as the upper surface of the front and rear wings experience a reduction of pressure. The magnitude and locations of the static pressure change with the inlet imposed wakes is very similar to the full vehicle wake, which is perhaps not unexpected after examination of the individual surface forces.

While imposing the wake on the inlet does produce a similar result to an upstream vehicle, there are subtle differences between the effect of the imposed and vehicle wakes, primarily in the wake's effect on total downforce generated and the associated change of aerodynamic balance. Investigations of vehicle component forces (figure 6.25) and surface pressures (figure 6.26) do not indicate any significant differences between the effects of the wakes on the car. However, visualizing the flow up to and over the downstream car does indicate a difference in the diffusion of the wake, figure 6.27, whereby the wake vortices from

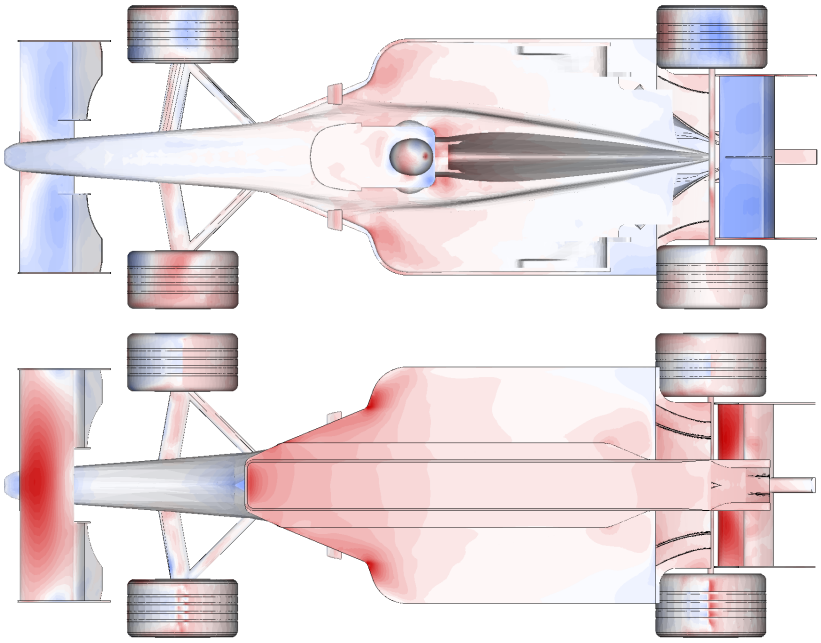

**(a)** Baseline case sampled.

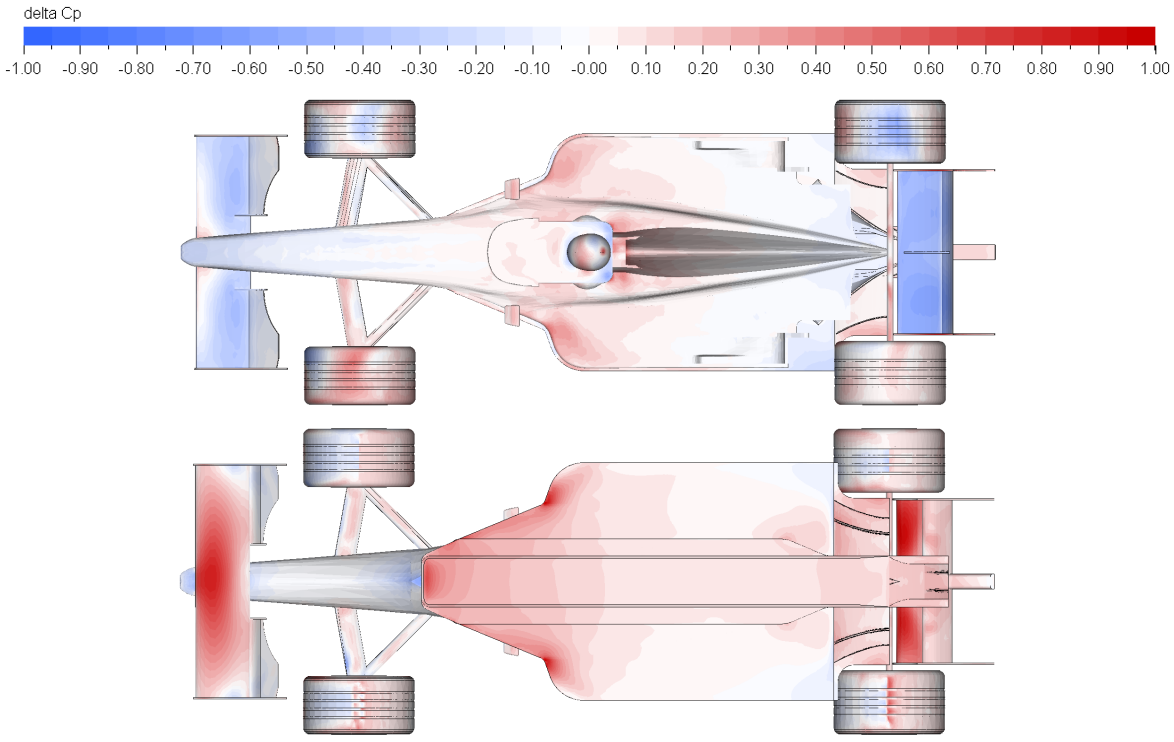


**(b)** Two vehicle case sampled.

**Figure 6.26:** Effect of imposed wakes on vehicle surface pressure distribution ($\Delta C_P$).

the imposed wake car are less diffuse over the downstream car. The key difference between the imposed wake and the upstream vehicle is the simulation of wake unsteadiness, which occurs in the wake of the car (figures 6.28, 6.29 & 6.30) so is naturally simulated with an upstream vehicle, but is averaged out of the results file. The imposed wake, however, is generated from the long time averaged data set, figure 6.23, with instantaneous fluctuations of the vortex structures (figure 6.28. The instantaneous wake also has local and mean variations in the axial velocity deficit, figure 6.29, meaning that the time averaged dynamic

pressure deficit, and subsequently the total pressure deficit, is not equal to the average of the time varying dynamic pressure deficits,

$$0.5\,\rho\,\bar{u_X}^2 \neq \frac{1}{n}\sum_{t=0}^{n} 0.5\,\rho\,u_X(t)^2. \tag{6.1}$$

i.e. if $u_X(t)$ fluctuates between $9ms^{-1}$ and $11ms^{-1}$ then the mean velocity is $\bar{u_X} = 10ms^{-1}$; so $(\bar{u_X})^2 = 100m^2s^{-2}$, however, the average of instantaneous velocities squared is $\overline{u_X(t)^2} = 101m^2s^{-2}$.

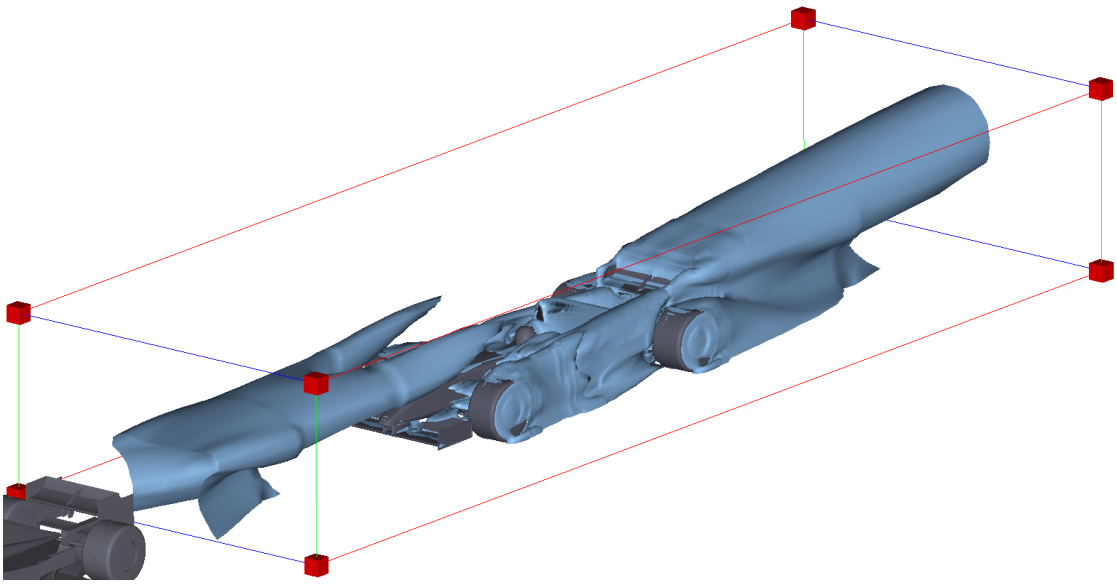

**(a)** Upstream vehicle wake case.

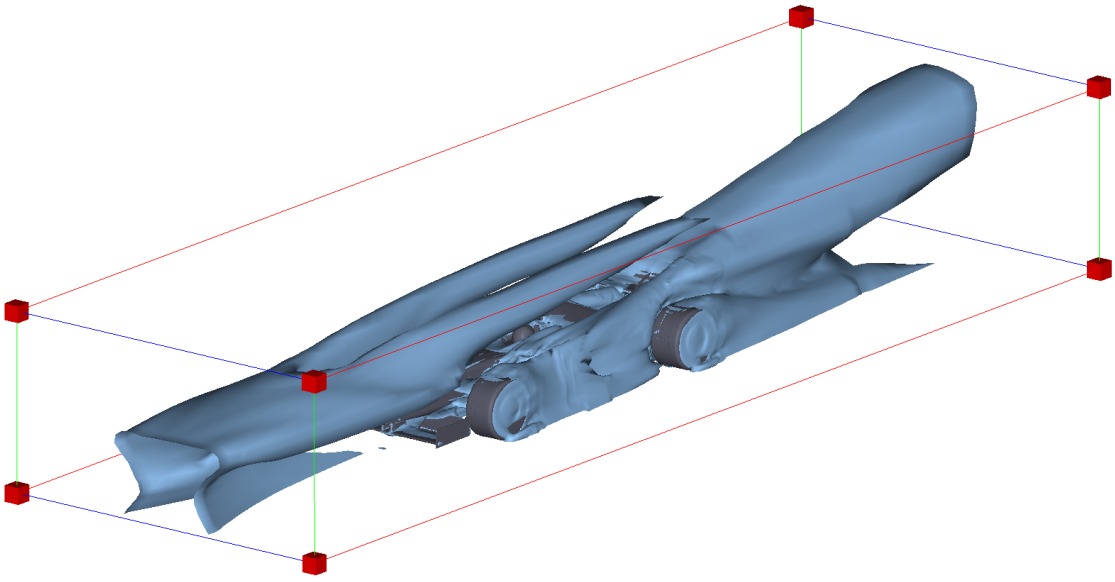

**(b)** Imposed wake case.

**Figure 6.27:** 3-D isosurface of $C_{P_O} = 0.25$ showing the difference between real and imposed wakes over downstream car.

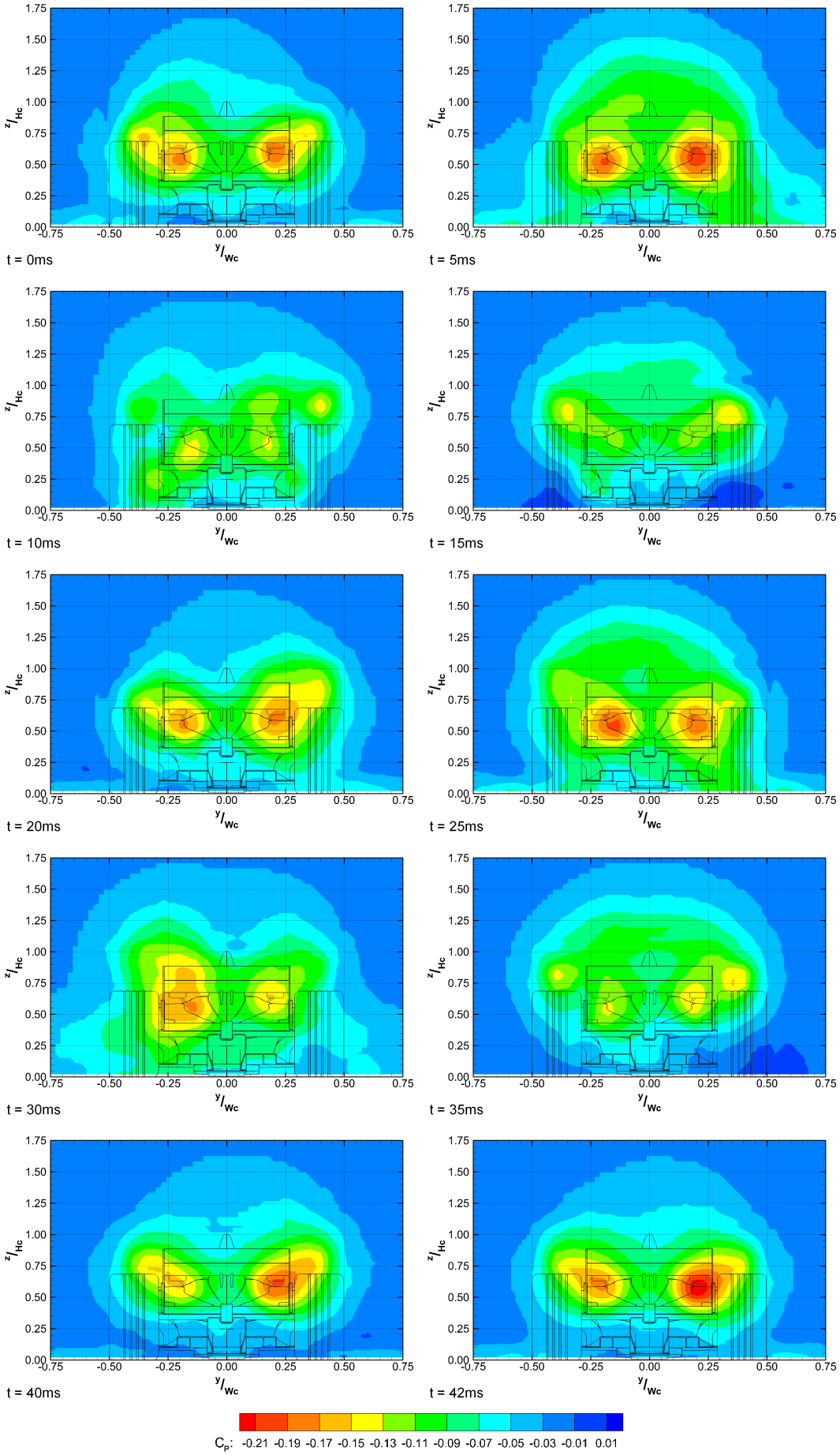


**Figure 6.28:** Instantaneous contours of static pressure deficit at $x = 1.25L_C$, $T = 1kHz = 1ms$.

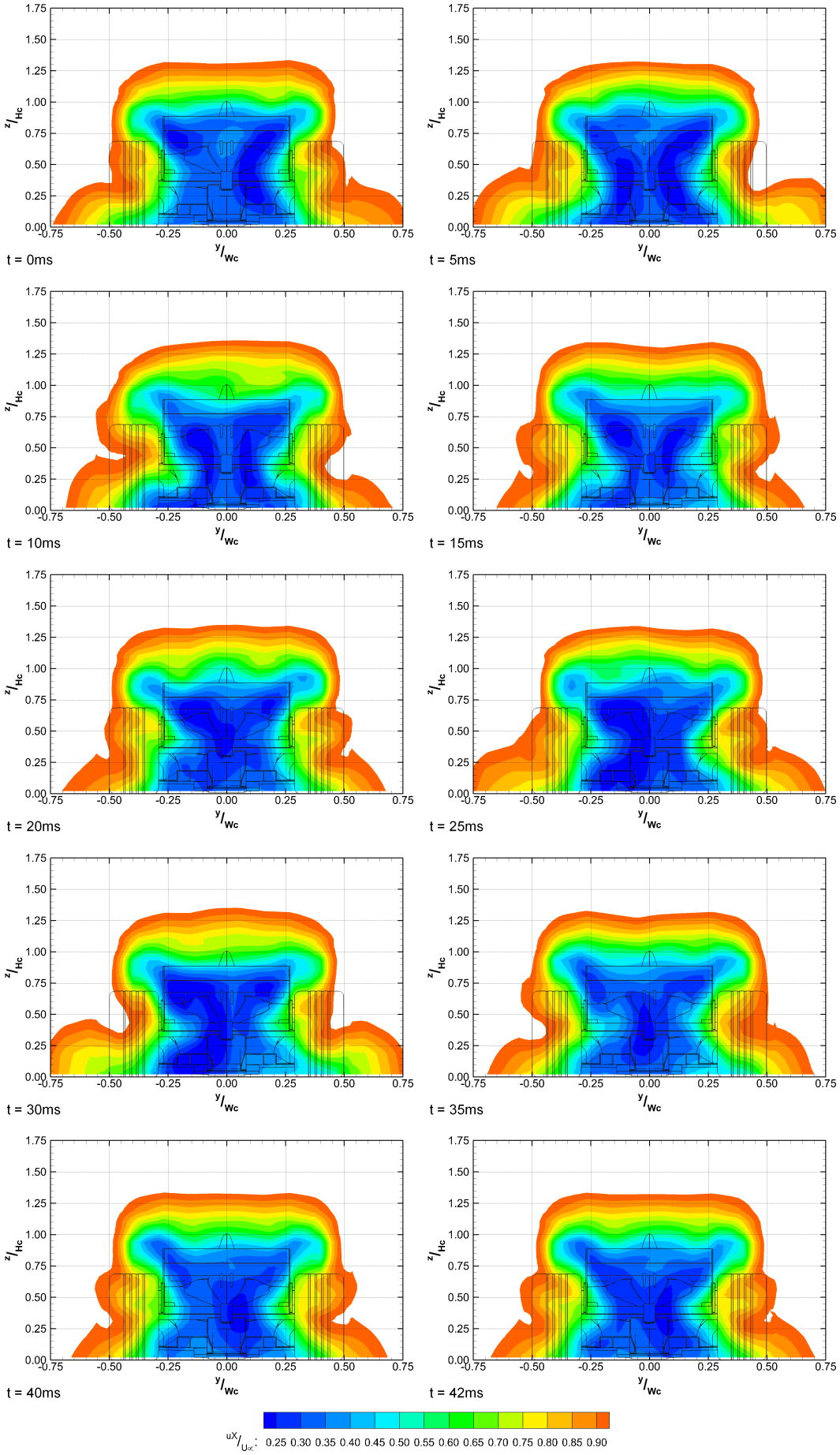


**Figure 6.29:** Instantaneous contours of axial velocity deficit at $x = 1.25L_C$, $T = 1kHz = 1ms$.

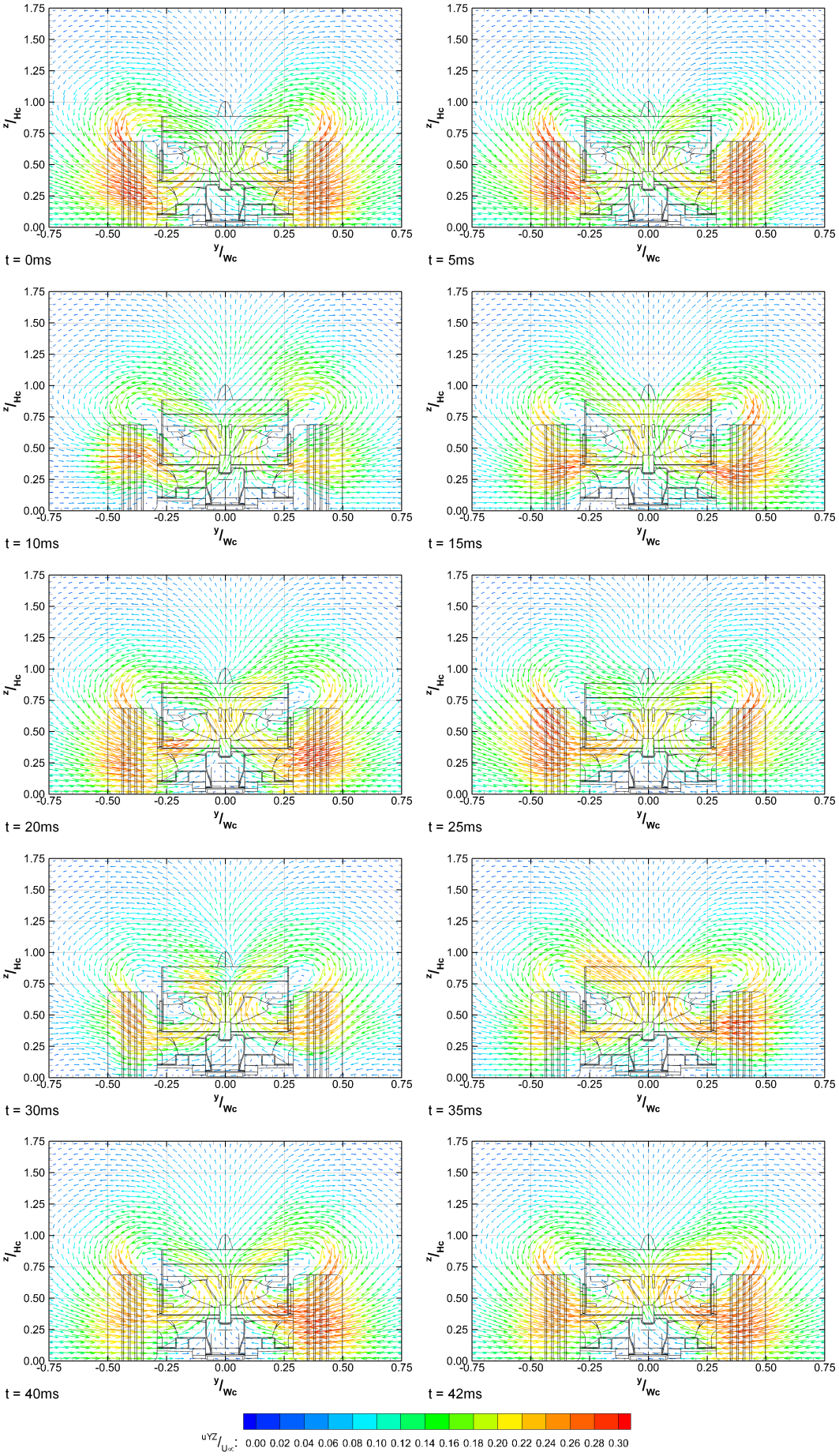


**Figure 6.30:** Instantaneous contours of secondary flows at $x = 1.25L_C$, $T = 1kHz = 1ms$.

### 6.3.3 Effect of Wake Unsteadiness in the Imposed Wake

In order to simulate the unsteadiness of the wake using the inlet boundary condition a time variable was required in the inlet table. It would be impractical to create an instantaneous representation of the wake, instead a series of shorter time averaged frames is required. The period of time averaging is a compromise, as it should be short enough that variations in the onset flow are captured, however, each inlet time frame also increases the volume of data in the inlet table (for each inlet time frame there is a y and z spatial co-ordinate, a temporal co-ordinate, a $C_P$, $u_X$, $u_Y$, and a $u_Z$ value), increasing the computational effort required to read the table and begin the simulation. It is therefore desirable for the period of the time-frame to be longer, but also not so long as to create a series of discontinuities from the imposed inlet parameters. The compromise therefore was to capture the wake using a series of relatively high fidelity time averaged frames ($1kHz$) for a short period ($50ms$) and loop the non-uniform inlet boundary conditions throughout the simulation. For this process it is desired that the average of the input frames be symmetric, or at least no less symmetric than the long time average.

The effect of the periodic imposed wake on the downstream vehicle is much closer to the effect of an upstream vehicle than the steady state inlet case, table 6.10; within $0.5\%$ on $\Delta C_D$ and $\Delta C_L$. The shift of aero-balance is also closer to the upstream car ($\Delta\frac{C_{LR}}{C_L}(\%) = -19\%$), though is less severe than the upstream vehicle. Like the steady state imposed wake cases examination of the individual component (figure 6.31) forces shows a difference of the wheel lift forces, subtracting the unsprung geometries the aero-balance shift is $\frac{C_{LR}}{C_L}(\%) = -5.5\%$ forward of the two vehicle case.

**Table 6.10:** Comparison of steady state and unsteady periodic imposed inlet wake cases.

| | $C_D$ | $\Delta(\%)$ | $C_L$ | $\Delta(\%)$ | $\frac{C_{LR}}{C_L}(\%)$ | $\Delta(\%)$ | $\frac{L}{D}$ | $\Delta(\%)$ |
|---|---|---|---|---|---|---|---|---|
| TVF[L,0][a] | 0.741 | $\downarrow 19.2$ | -0.323 | $\downarrow 59.4$ | 106 | $\uparrow 37.4$ | -0.436 | $\downarrow 49.7$ |
| IW[b] | 0.750 | $\downarrow 18.3$ | -0.265 | $\downarrow 66.7$ | 128 | $\uparrow 59.3$ | -0.364 | $\downarrow 59.2$ |
| IWP[c] | 0.747 | $\downarrow 18.7$ | -0.327 | $\downarrow 59.0$ | 86.3 | $\uparrow 18.0$ | -0.437 | $\downarrow 49.6$ |

[a] TVF[L,0] = Two vehicle case, axially aligned with a one vehicle separation, forces on the following vehicle
[b] IW = Imposed wake with a steady state inlet, sampled from baseline case
[c] IWP = Imposed wake with periodic inlet, sampled from baseline case

Component drag is similar to the steady state imposed wake and upstream vehicle cases, within $C_D = 0.01$ for the front wing, rear wing, and body, while the front and rear wheels are within $C_D = 0.04$. While the change of vehicle drag with the steady state inlet was satisfactory, the change of lift was less accurate, it is here the periodic inlet conditions more precisely match the upstream vehicle case, especially the wheel lifts which are within $C_L = 0.012$. Front and rear wing downforce losses are also more closely matched to the upstream vehicle, at $\delta C_L = 0.009$ and $\delta C_L = 0.001$ to the following case respectively. The greatest difference between the imposed wake and upstream vehicle is the body, which generates lift in this case, albeit $C_L = 0.017$, whereas the body generates no lift with the upstream vehicle.

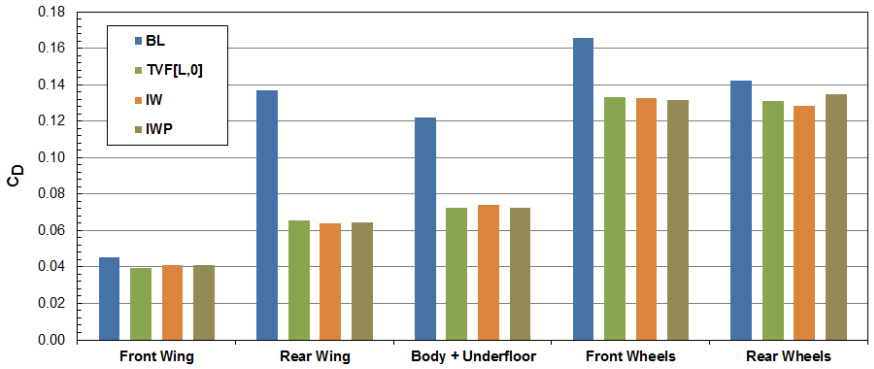


**(a)** Drag.

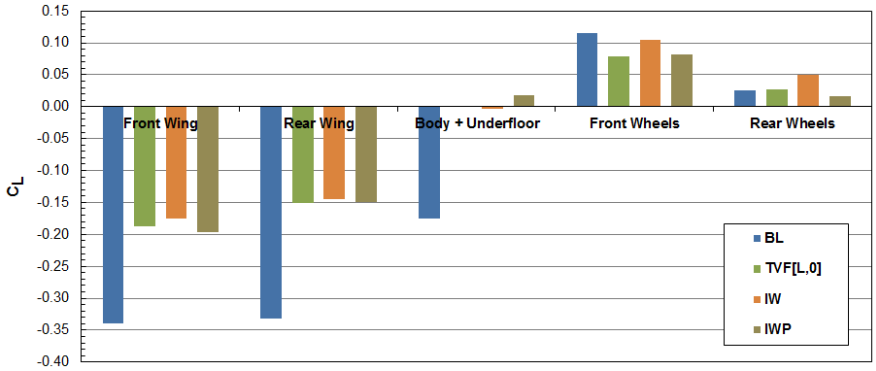


**(b)** Downforce.

**Figure 6.31:** Component forces for periodic imposed wake case with simulated one vehicle separation, compared to baseline case.

As with the other imposed wake cases, the periodic inlet wake has a similar effect on the surface pressures, figure 6.32. The effect of the wake is slightly less asymmetric though, as can particularly be seen in the $\Delta C_P$ of the tops of the wheels and the front edge of the underbody. As the surface forces suggest the magnitude of $\Delta C_P$ in the important areas is similar to the case with an actual upstream vehicle, and it is not immediately obvious where the difference in the body downforce occurs the increase of static pressure on the front edges of the sidepods peaks at $\Delta C_P \approx 0.05$ lower than the two vehicle case.

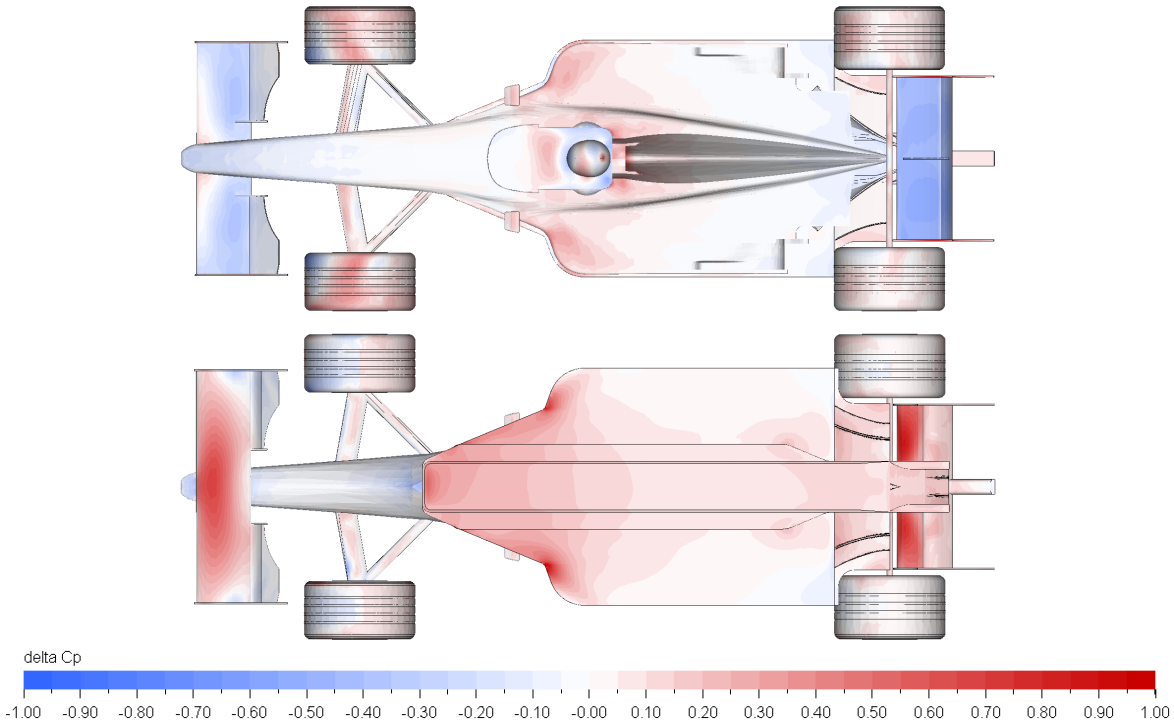


**Figure 6.32:** Effect of periodic imposed wake case on vehicle surface pressure distribution ($\Delta C_P$).

## 6.4 Chapter Summary

The aerodynamic characteristics of the same $25\%$ Formula 1 car as was used in the experimental study have been investigated using CFD. Simulations were performed at a single vehicle posture, which was found to produce the greatest downforce during a wheels-on experimental study. The CFD simulations were seen to over predict aerodynamic drag while under predicting aerodynamic downforce, however, aero-balance was found to be similar with $\approx 60\%$ of downforce acting on the rear axle. As with the experimental study overall downforce is lower than would be expected for a vehicle of this design, indicating a fundamental inadequacy of the geometry. Though this is not unprecedented for a Formula 1 geometry created in an outside of an F1 team [4] as the resource dedicated to developing the car is not on the scale of a Formula 1 team.

The effect of an upstream vehicle at a number of upstream positions has been tested, both with an identical upstream model and the bluff bodied wake generator. As expected total aerodynamic drag ($\Delta C_D = -19\%$) and downforce ($\Delta C_L = -59\%$) are reduced with the upstream vehicle at $x = L_C$, while the aero-balance shifts rearwards ($\Delta \dfrac{C_{LR}}{C_L}(\%) = 37\%$). What is unexpected is that the front wings appears to lose the least quantity of downforce, $\Delta C_L = 0.15$, while the rear wing and body lose the most downforce, $\Delta C_L \approx 0.18$. This is contrary to popular opinion which suggests that the underbody is least affected by an upstream wake. As the effect on the front wing is smaller than the rear, it must be that the aero-balance shift is the responsibility of the combined upper and underbody not, as previously suggested, the front wing.

Like the experimental study a small lateral offset ($y = 0.5W_C$) has been shown to reduce the loss of downforce experienced by the downstream vehicle, more so than increasing the axial spacing between the cars. Even with half of the car shadowed by the upstream vehicle, downforce returns to within $98\%$ of the baseline level. While it is not in the purview of the aerodynamicist it appears that modifying racing circuits such that multiple lines could be driven in corners could help to mitigate much of the aerodynamic effect of an upstream car's wake.

While total force changes with the upstream wake generator are lower than the upstream car, the trends are similar enough to give confidence in the experimental results, especially when considering the length of the wake generator. The greatest difference between the upstream wake generator and vehicle is the downforce loss experienced by the rear wing, which is lower with the upstream wake generator by $\Delta C_L = -0.058$.

A new method of simulating an upstream vehicle by using the inlet boundary conditions to impose the wake parameters has been detailed and the results documented. The wake was imposed using both a single sample, created from a long time-averaged output, and a series of shorter averaged frames looping throughout the simulation. The effect of the imposed wakes is shown to be similar to the effect of an upstream vehicle at the same effective vehicle separation, both in the reduction of total vehicle and individual surface forces, and the change to the vehicle surface pressure distribution. Sampling the wake from a single vehicle case, or between a pair of vehicles had no effect on the accuracy of the method.

Simulating the unsteadiness in the wake resulted in a better match to the upstream vehicle case, especially the downforce reduction of the following car; downforce of the trailing car is $\sim 8\%$ higher using a series of short time averaged frames on the inlet than it is using the steady state inlet. It would be imprudent to suggest from this that removing fluctuations from the mean velocity (i.e. turbulence intensity) in the wake is more harmful to the trailing vehicle. Though the time averaged velocity deficit does not generate the same time averaged dynamic pressure deficit as an average of instantaneous dynamic pressure deficits. Simulating the transient velocity field on the inlet also means that the momentum deficit in the wake of the effective upstream vehicle is different; so it could be that fluctuations of the velocity deficit in the wake of the upstream vehicle are ultimately beneficial to allow a Formula 1, or similar race-car, car to follow another.

# Chapter 7

# Altering the Onset Wake

In this chapter the effect of modifying the onset flow conditions, both the aerodynamic impact on a downstream vehicle and the propagation of the wake, is tested. Using the methodology of imposing the wake on the inlet described in Chapter 6 the upstream wake parameters are altered to test sensitivity to the salient wake features, primarily the secondary flows and axial velocity deficit. The source and effect of the secondary flows in the wake are then further decomposed and recreated using a simplified vortex model with uniform up-wash.

## 7.1 Effect of Removing Wake Parameters

The advantage of imposing the wake of the Formula 1 car on the inlet of a CFD case is the ability to change the wake without the requirement of designing a different set of aerodynamic surfaces, which would result in a long parametric study. The easiest change to perform is to remove flow features from the upstream wake. Wake conditions were imposed in the same method described in Chapter 6, but with subsequent cases leaving out the axial velocity deficit (i.e. $u_X = U_\infty$) and secondary flows ($u_Y = u_Z = 0$) from the inlet. Simplistically, axial velocity deficit in the onset wake would be associated with the upstream vehicle drag, while secondary flows are the attributed to the upstream vehicle's downforce. While it is not reasonable to suggest a Formula 1 car could be designed without either of these parameters being present in the wake, especially considering the high lift and high drag nature of the cars, it is a quick way to isolate the contribution of the wake variables to the downstream vehicle performance loss. To reduce computational cost, for these unrealistic cases, simulations were performed with a centreline symmetry plane and without the unsteady effects described at the end of Chapter 6.

Vehicle forces with the modified wakes are shown in table 7.1. Removing the axial velocity deficit from

the wake reduces the effect of the wake on vehicle force by $\Delta C_D = -3.5\%$ and $\Delta C_L = -9\%$, compared to an upstream vehicle. While removing the secondary flows has the opposite effect, a surprising result considering the dominance of the rear wing vortex pair in the wake, significantly increasing the force loss experienced by $\Delta C_D = 28\%$ and $\Delta C_L = 23\%$. The aero-balance shift is less extreme for both the $u_X = U_\infty$ and $u_{Y,Z} = 0$ cases than the real wake, as change in load is greater for the rear axle than the front. In the $u_X = U_\infty$ case the load is relatively evenly distributed between both axles as $\Delta C_{LF} < 0.04$.

**Table 7.1:** Effect of removing the axial velocity deficit and secondary flows from the wake of a 25% Formula 1 car on the downstream vehicle (cases with centreline symmetry plane).

| | $C_D$ | $\Delta$ | $C_L$ | $\Delta$ | $C_{LF}$ | $\Delta$ | $C_{LR}$ | $\Delta$ |
|---|---|---|---|---|---|---|---|---|
| Isolated | 0.799 | - | -0.646 | - | -0.235 | - | -0.412 | - |
| Upstream Vehicle | 0.691 | -0.108 | -0.348 | +0.298 | -0.001 | +0.234 | -0.340 | +0.071 |
| No $u_X$ Deficit | 0.720 | -0.079 | -0.407 | +0.239 | -0.199 | +0.035 | -0.208 | +0.204 |
| No $u_{Y,Z}$ | 0.468 | -0.331 | -0.198 | +0.448 | -0.047 | +0.187 | -0.151 | +0.261 |

Component forces for the wake variable removed cases are shown in figure 7.1. In the $u_X = U_\infty$ case most of the individual component forces lie somewhere between the baseline and upstream vehicle, the exception being the front wing, which generates more drag ($\delta C_D = 0.012$) and downforce ($-\delta C_L = 0.017$) than the isolated vehicle. Of the downforce generating surfaces the combined body loses the most downforce in the $u_X = U_\infty$ case ($\delta C_L = 0.156$) followed by the rear wing ($\delta C_L = 0.116$) coupled with the increase of front wing downforce this would explain the quantity of downforce acting on the front axle. While the underbody loses the most downforce the level of loss is lower than is the case with an upstream vehicle.

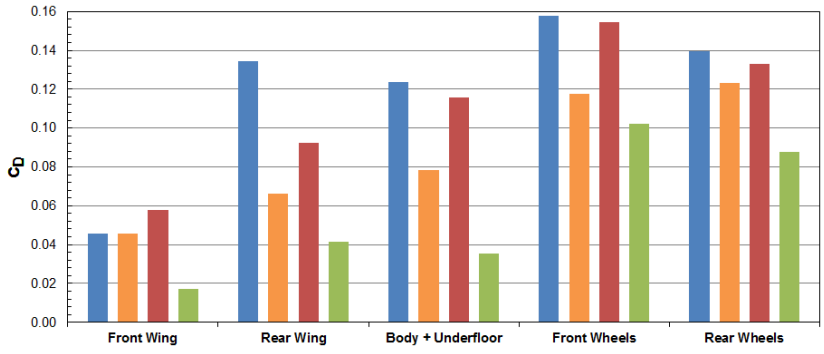


**(a)** Drag.

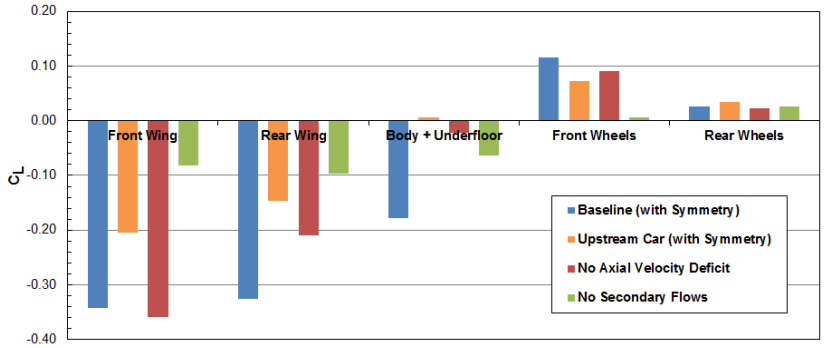


**(b)** Downforce.

**Figure 7.1:** Component forces comparing imposed wakes with removed parameters to freestream and upstream vehicle cases (cases with Ccentreline symmetry plane).

The downstream vehicle in the $u_{Y,Z} = 0$ case experiences a significantly greater loss of both drag and downforce for all components, compared to the upstream vehicle case; with the exception of the body, which loses less downforce than even the $u_X = U_\infty$ wake case ($\delta C_L = 0.114$), though this could be connected to the front wing wake rather than a direct response to the onset flow conditions. The greatest difference between the $u_{Y,Z} = 0$ and upstream vehicle cases is the front wheel lift, which is $C_L \approx 0$.

The effect of altering the imposed wake inlet parameters on the onset flow is shown in figures 7.2, 7.3 and 7.4. Removing the axial velocity deficit from the inlet appears to reduce the decay of the wake vortices, as streamwise vorticity ($\Omega_X$) from the upstream vehicle remains present up to the rear of the downstream car, figure 7.2. This is also seen in the difference between the wake of the real upstream vehicle and steady state imposed wake inlet conditions (figure 6.27), and could result from time averaged inlet conditions being imposed in this case.

Removing secondary flows from the inlet affects the propagation and decay of the wake, figure 7.3, resulting in a tube of low velocity forming between the inlet and front of the downstream car (figures 7.3b and 7.4c). In the case of the real vehicle wake (figures 7.3a and 7.4a) the region of low velocity in the wake is swept inboard and upwards by the secondary flows in the wake, until the axial velocity deficit in concentrated in the vortex cores at rear wing height of the trailing vehicle, i.e. the mushroom shaped wake. What this shows is that while the secondary flows appear to have a detrimental effect on the downstream vehicle forces, as is evident from the $u_X = U_\infty$ case vehicle forces (table 7.1), they are also important in diverting the wake deficits away from the sensitive areas of the downstream vehicle.

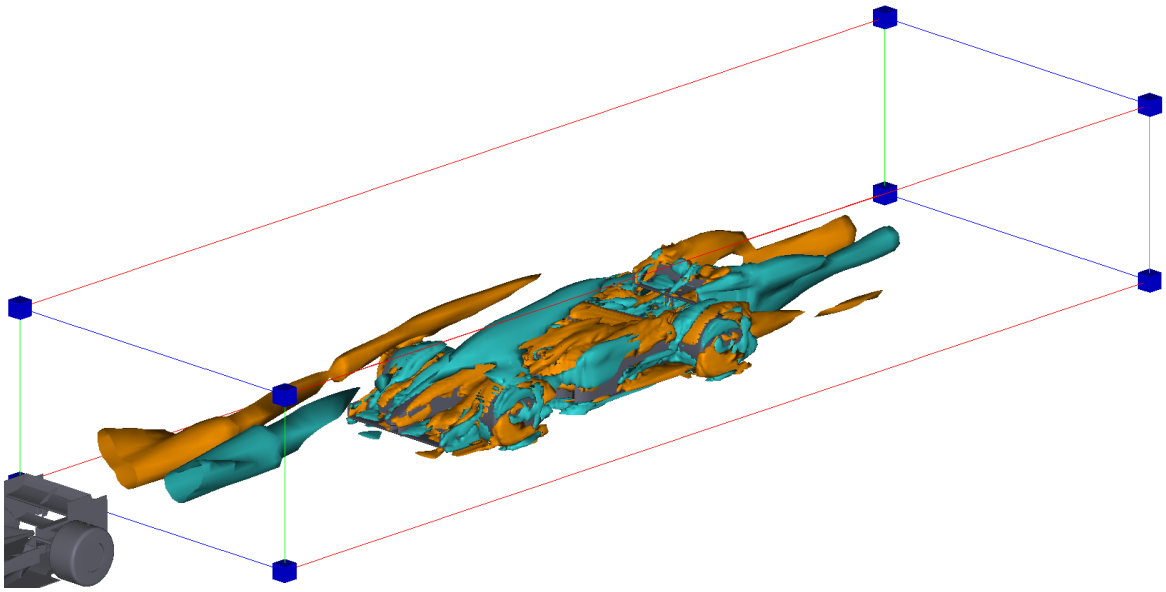

**(a)** Upstream vehicle case.

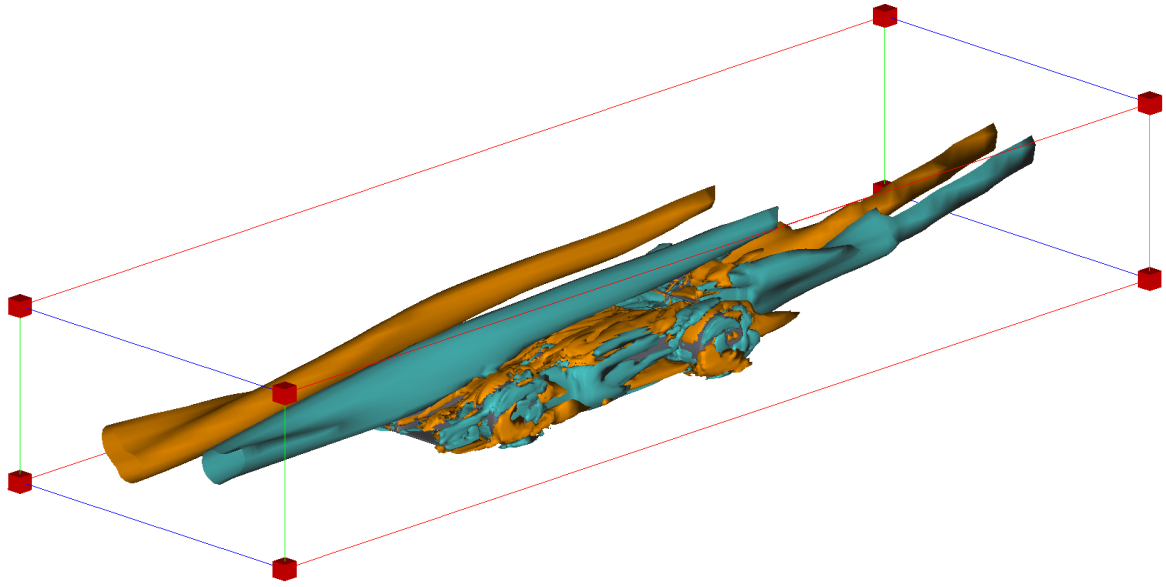

**(b)** Wake $u_X = U_\infty$ case.

**Figure 7.2:** 3-D isosurfaces of $\Omega_X = \pm 100$ ($+100$ = blue, $-100$ = orange) between inlet plane ($x = -0.75L_C$) and $x = 2L_C$, comparing imposed wake with axial velocity deficit removed to upstream vehicle wake.

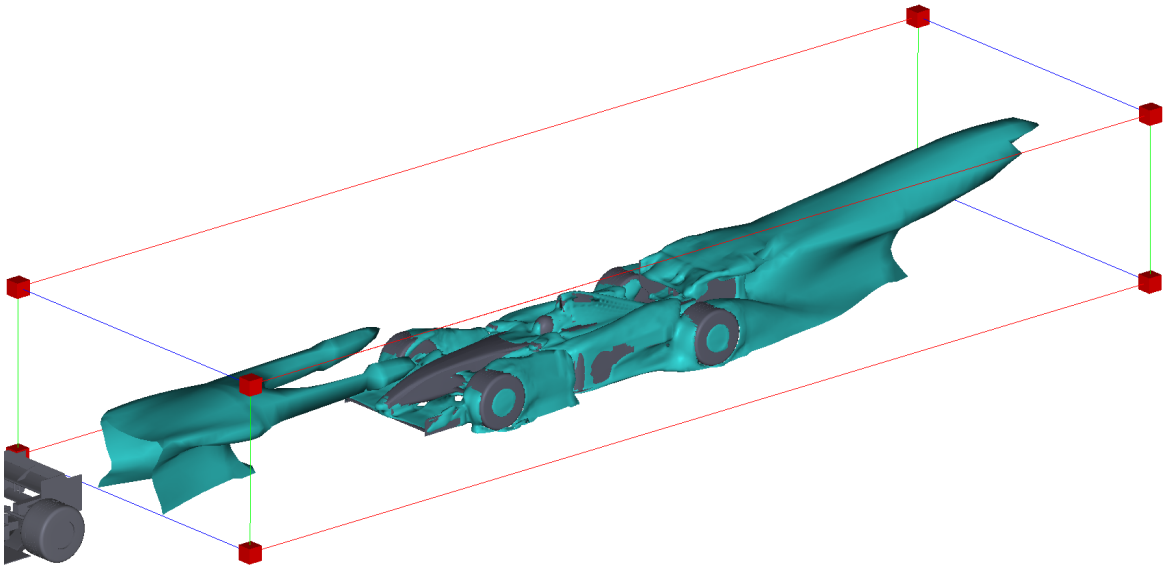

**(a)** Upstream vehicle case.

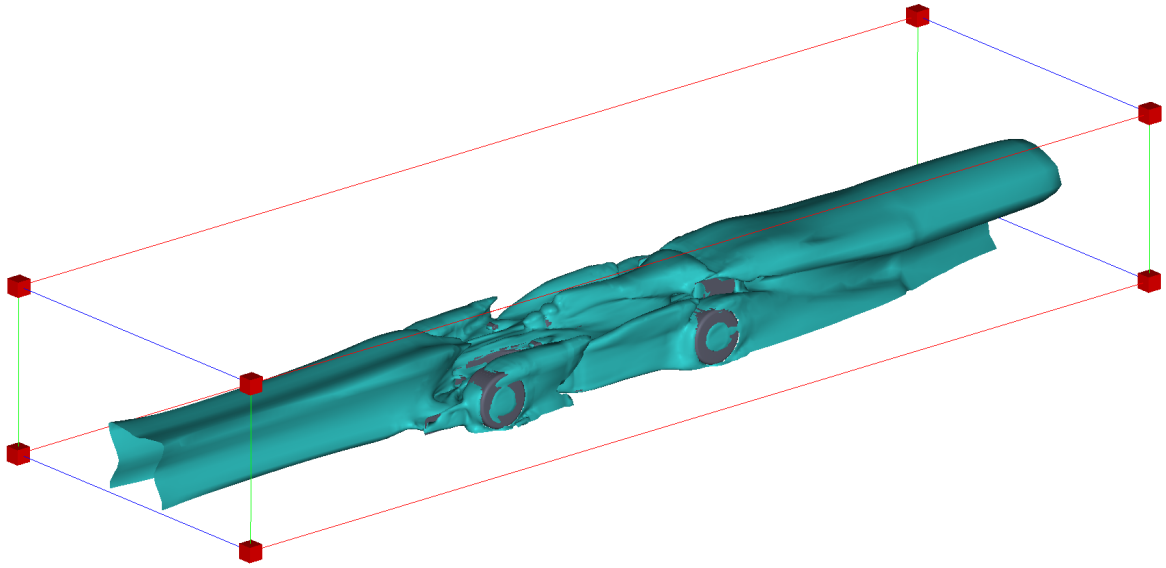

**(b)** Wake $u_{Y,Z} = 0$ case.

**Figure 7.3:** 3D isosurfaces of $u_X = 0.4U_\infty$ between inlet plane ($x = -0.75L_C$) and $x = 2L_C$, comparing impsoed wake with cecondary flows removed to upstream vehicle wake.

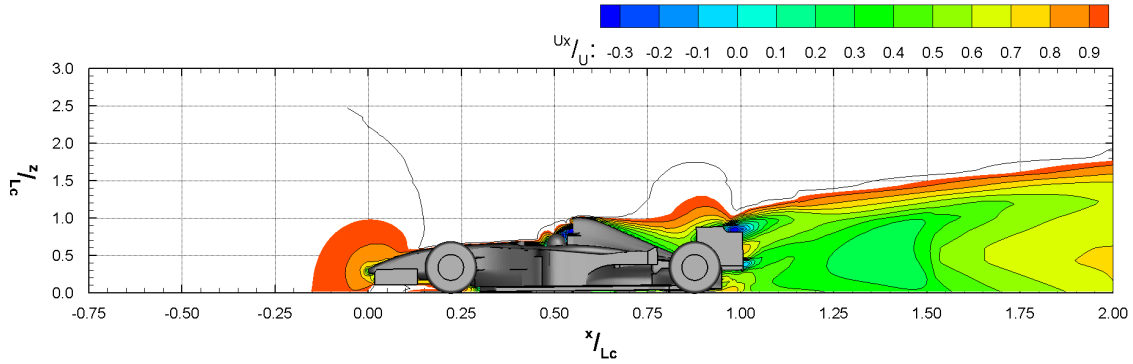


**(a)** Isolated.

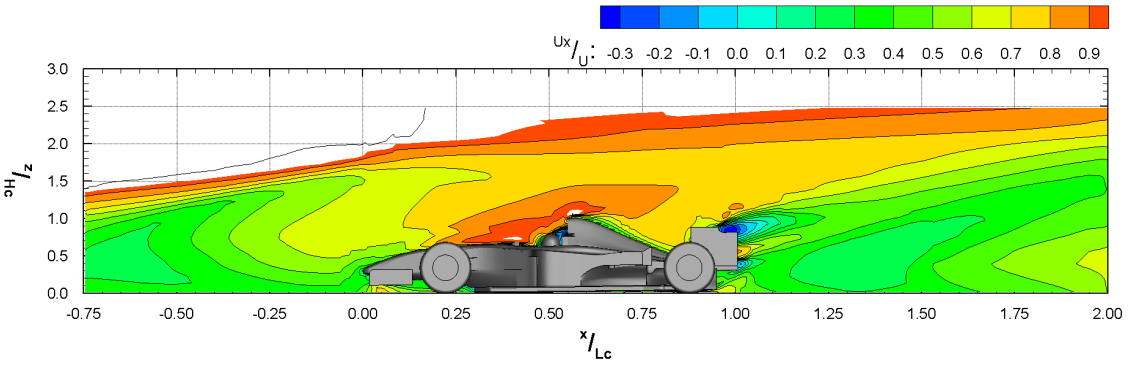


**(b)** Full imposed wake.

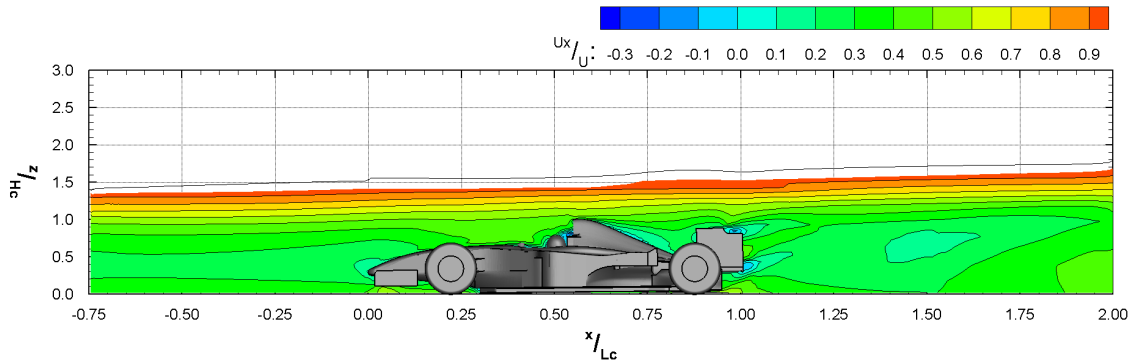


**(c)** No secondary flows

**Figure 7.4:** Wake centreline contours of axial velocity deficit.

## 7.2 Modification of the Secondary Flow Field

It has often been asserted that increasing the ground-effect (underbody) contribution to downforce, thereby reducing the proportion of total downforce generated by the rear wing, would result in a vehicle less influenced by the presence of an upstream vehicle, though the author found no published data in support of this claim. This does present an interesting question, namely the extent to which the respective underbody and rear wing contributions to the downforce of a Formula 1 car affects the propagation of the wake and the effect on a following vehicle.

The simplest wake variables to manipulate in isolation are the secondary flows ($u_{Y,Z} = \sqrt{{u_Y}^2 + {u_Z}^2}$), as peak secondary flows are low compared to the axial velocity deficit, peaking at $< 0.3U_\infty$ and $<< 0.2U_\infty$ over the majority of the base of the car at the sampled downstream plane ($x = 1.25L_C$). So the effect of changing $u_{Y,Z}$ on dynamic pressure, and thus the total pressure deficit in the wake is negligible. The majority of secondary flows found in the wake of a Formula 1 car, especially at this downstream plane, are the responsibility of the dominant rear wing counter-rotating vortex pair, so it is not unreasonable to infer that the magnitude of $u_{Y,Z}$ in the wake is proportional to the magnitude of rear wing downforce. So it can be said that increasing the rear wing downforce of the car would result in increased secondary flows, and conversely reduced secondary flows would result from a reduced level of rear wing downforce. The inlet secondary flow field was therefore uniformly multiplied to achieve a $\pm 5\%$ and $\pm 10\%$ change of $u_{Y,Z}$ in the onset flow. As these inlet conditions have the potential to be realistically created with an upstream race-car, unlike the $u_X = U_\infty$ and $u_{Y,Z} = 0$ cases presented above, the periodic inlet conditions were used (Section 6.3.3).

As with the baseline recreated inlet wake case, where $u_{Y,Z} = 100\%$, both drag and downforce decrease relative to the isolated case and $C_{LR} > C_{LF}$ for all the modified $u_{Y,Z}$ flow field cases, table 7.2. The performance loss is not linearly correlated to the magnitude of secondary flow variation though, especially downforce on the front axle, which is greater than zero for all $u_{Y,Z}$ variations. The effect on the rear axle is lower than the baseline wake effect for all variations, with the increased $u_{Y,Z}$ experiencing a smaller $\Delta C_{LR}$.

**Table 7.2:** Comparison of variable secondary flows imposed wake cases.

| | $C_D$ | $\Delta$ | $C_L$ | $\Delta$ | $C_{LF}$ | $\Delta$ | $C_{LR}$ | $\Delta$ |
|---|---|---|---|---|---|---|---|---|
| Isolated | 0.918 | - | -0.769 | - | -0.253 | - | -0.544 | - |
| 90% $u_{Y,Z}$ | 0.747 | -0.171 | -0.314 | +0.482 | +0.036 | +0.289 | -0.349 | +0.195 |
| 95% $u_{Y,Z}$ | 0.742 | -0.176 | -0.304 | +0.492 | +0.035 | +0.288 | -0.339 | +0.205 |
| 100% (IWP) | 0.747 | -0.171 | -0.327 | +0.469 | -0.045 | +0.208 | -0.282 | +0.262 |
| 105% $u_{Y,Z}$ | 0.753 | -0.165 | -0.335 | +0.461 | +0.031 | +0.284 | -0.366 | +0.178 |
| 110% $u_{Y,Z}$ | 0.755 | -0.163 | -0.345 | +0.451 | +0.031 | +0.284 | -0.376 | +0.168 |

When the magnitude of secondary flow intensity is reduced (figure 7.5), both drag and downforce losses

increase compared to the baseline wake. Conversely force losses reduce when secondary flows in the wake are increased. The effect of multiplying the inlet secondary flow field on the downstream vehicle drag is minimal, $\Delta C_D = +0.01$ as $u_{Y,Z}$ is increased to $110\%$ of the real wake; while $\Delta C_D = -0.005$ at $u_{Y,Z}$ is reduced to $95\%$ (figure 7.5). The change of downforce is slightly more pronounced than the change of drag, though is still smaller than $\Delta C_L \pm 0.02$ compared to the the unaltered wake. Both drag and downforce losses are greatest when $u_{YZ}$ is reduced by $5\%$, and smallest when $u_{YZ}$ is increased to $110\%$.

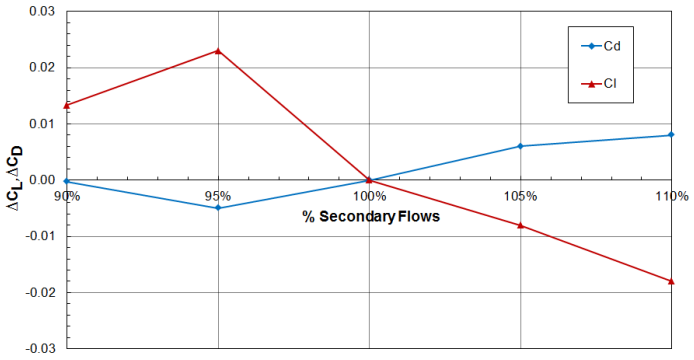


**Figure 7.5:** Change of vehicle force coefficients due to secondary flow variation, compared to $u_{YZ} = 100\%$ case.

The effect of reducing and increasing the secondary flow field on component drag is monotonic for the rear wing and the combined underbody drag force, figure 7.6, however, the front wing remains linear for all secondary flow variations. This could be because front wing downforce increases with increased $u_{Y,Z}$ intensity, and the opposite with reduced secondary flows. The increased $u_{Y,Z}$ has the same effect on rear wing downforce, though body downforce is less influenced, probably as a result of the front wing downforce increasing.

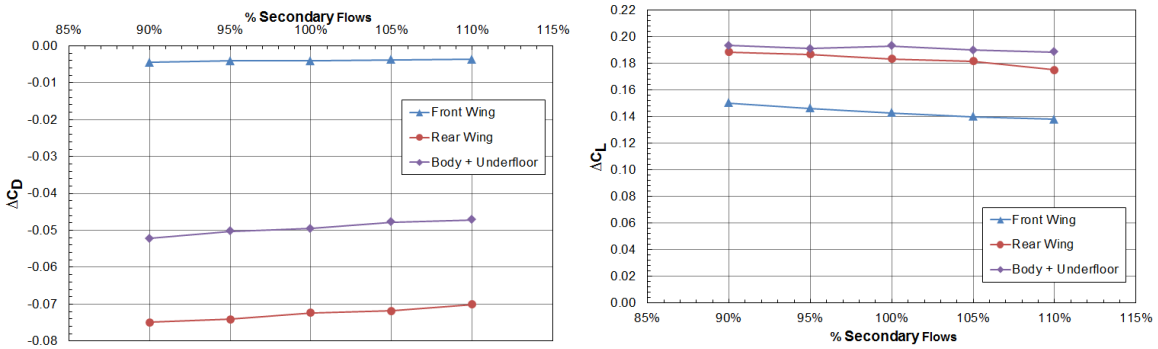


**(a)** Drag loss. **(b)** Downforce loss.

**Figure 7.6:** Effect of secondary flow variation on downforce generating surface force loss.

The effect of altering the inlet secondary flow field on the wake centreline 2D profiles of up-wash and axial velocity deficit are shown in figures 7.7 to 7.10. On the inlet (figure 7.7a) the up-wash increases and decreases with the scaling factor of the secondary flows. Wake up-wash peaks at $z \approx 0.6H_C$ for all the cases with the difference in peak up-wash between minimum to maximum secondary flow intensity only $\delta u_Z = \pm 0.02 U_\infty$. As desired, the axial velocity on the inlet plane remains unaffected by the modification to the imposed secondary flows (figure 7.7b).

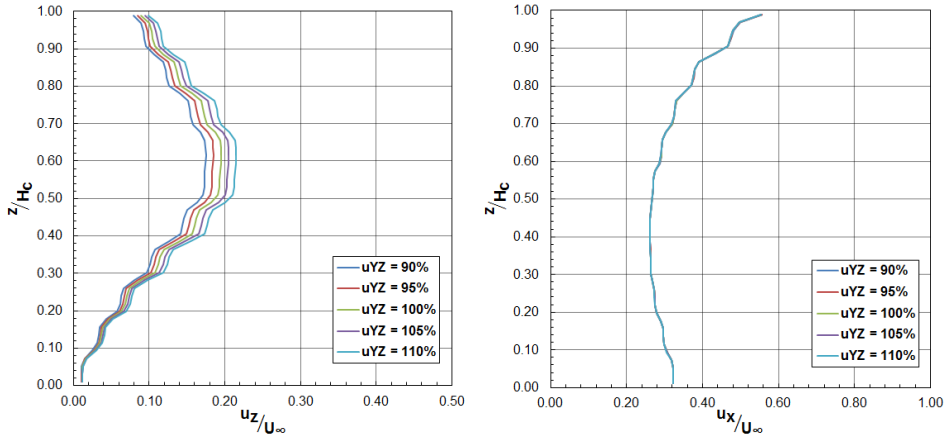


**(a)** Wake up-wash. **(b)** Axial velocity.

**Figure 7.7:** Non-dimensional car centreline 2-D wake profiles at $x = -0.75L_C$ (inlet plane).

As the wake progresses to $x = -0.5L_C$ upstream of the car (figure 7.8), the difference in the wake up-wash profiles from minimum to maximum secondary flow intensity becomes more pronounced, and the difference in peak up-wash doubles to $\delta u_Z = \pm 0.04 U_\infty$. As with the wake profile on the inlet plane, the height of peak up-wash above the ground plane for all cases remains consistent with the unaffected ($u_{Y,Z} = 100\%$) wake case, $z = 0.72H_C$. By $x = -0.25L_C$ upstream of the car the difference in peak up-wash returns to $\delta u_Z = \pm 0.2 U_\infty$, at $z \approx 0.92H_C$ for all cases. It is not clear why up-wash increases between the inlet ($x = -0.75L_C$) and $x = -0.5L_C$ planes, considering the flow field on the inlet is uniformly multiplied; possibly as the axial velocity at this plane is low, $u_X < 0.4$ at $x = -0.5L_C$, the velocity of wake up-wash can increase.

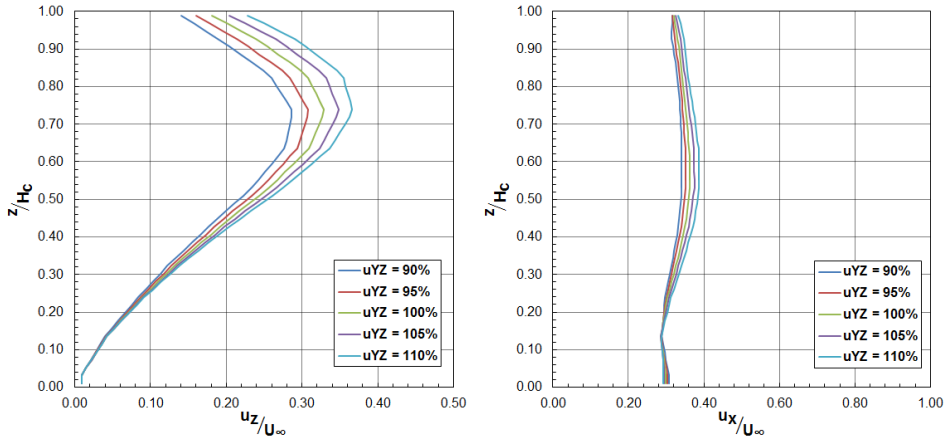


**(a)** Wake up-wash. **(b)** Axial velocity.

**Figure 7.8:** Non-dimensional car centreline 2-D wake profiles at $x = -0.50L_C$.

While the axial velocity on the inlet is unaffected by the modified secondary flow field, downstream of the inlet the wake velocity increases as the secondary flows are increased from $90\%$ of the the real wake to $110\%$. At $x = -0.5L_C$ the difference is only noticeable above $z = 0.2H_C$, peaking at $\delta u_X = \pm 0.02$ at $z = 0.55H_C$. By $x = -0.25L_C$ ahead of the car the difference in the velocity deficit is relatively uniform from the ground plane to the maximum height of the car, albeit $\delta u_X < 0.03 U_\infty$.

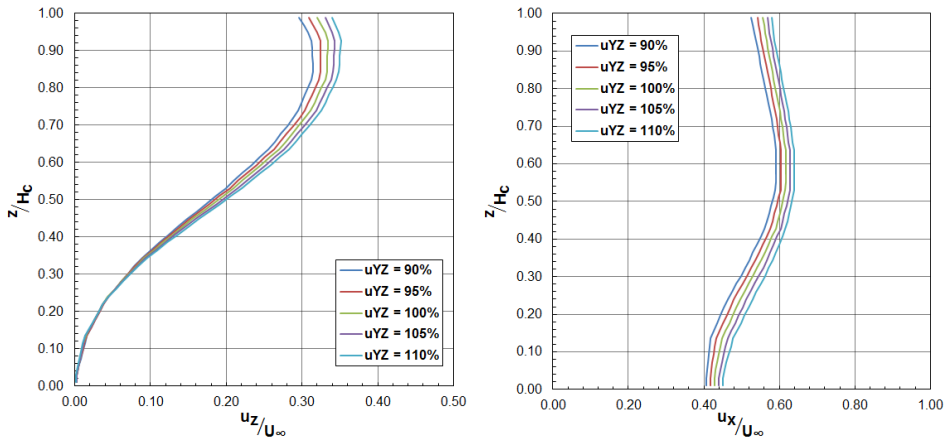


**(a)** Wake up-wash. **(b)** Axial velocity.

**Figure 7.9:** Non-dimensional car centreline 2-D wake profiles at $x = -0.25L_C$.

At the nose of the car (figure 7.10) the wake profiles take an appreciably different form to the preceding wake, in particular under $z = 0.4H_C$, figure 7.10. The wake up-wash profile captures the diverging flow around the nose cone, up-wash increases above, while there is down-wash under the nose towards the front wing. The 2-dimensional profile of axial velocity shows evidence of the stagnation point of the nose at $z = 0.3H_S$. What is particularly striking is the axial velocity under $z = 0.2H_C$, which is incrementally faster ($\delta u_X = \pm 0.03U_\infty$) with increasing secondary flow intensity. This is the height which provides airflow to the front wing and subsequently the underbody, and must, at least in part, be responsible for the increased forces experienced by these elements (figure 7.6) as $u_{Y,Z}$ is increased.

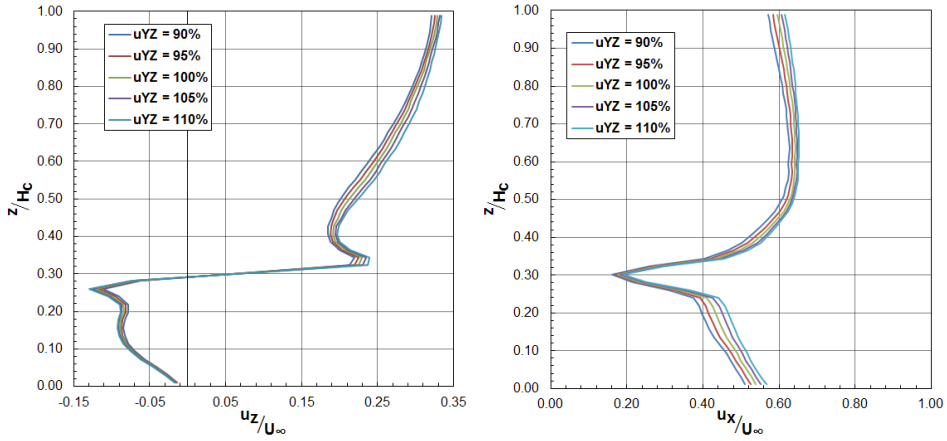


**(a)** Wake up-wash. **(b)** Axial velocity.

**Figure 7.10:** Non-dimensional car centreline 2-D wake profiles at $x = 0$ (downstream vehicle nose).

It has been shown that altering the secondary flow field in the wake of a Formula 1 car has an effect on the aerodynamic forces generated by a downstream vehicle. Uniformly increasing the secondary flows in the wake by up to $10\%$ reduces the effect of the wake on the downstream vehicle's aerodynamic surfaces, while reducing the secondary flow intensity ($-10\%$) has the opposite effect. While the centreline up-wash in the wake does increase in magnitude as inlet secondary flow intensity is increased, the angle of the wake does not change as would perhaps be expected. What is further evident is that as the inlet secondary flow field

is increased, the velocity deficit on the centreline of the wake is reduced, thereby reducing the dynamic pressure deficit in the wake. It is not just the velocity deficit on the wake centreline which is affected, as the isosurfaces of $u_X = 0.4U_\infty$ (figure 7.11) show, but also the decay and diffusion of the velocity deficit in the whole wake.

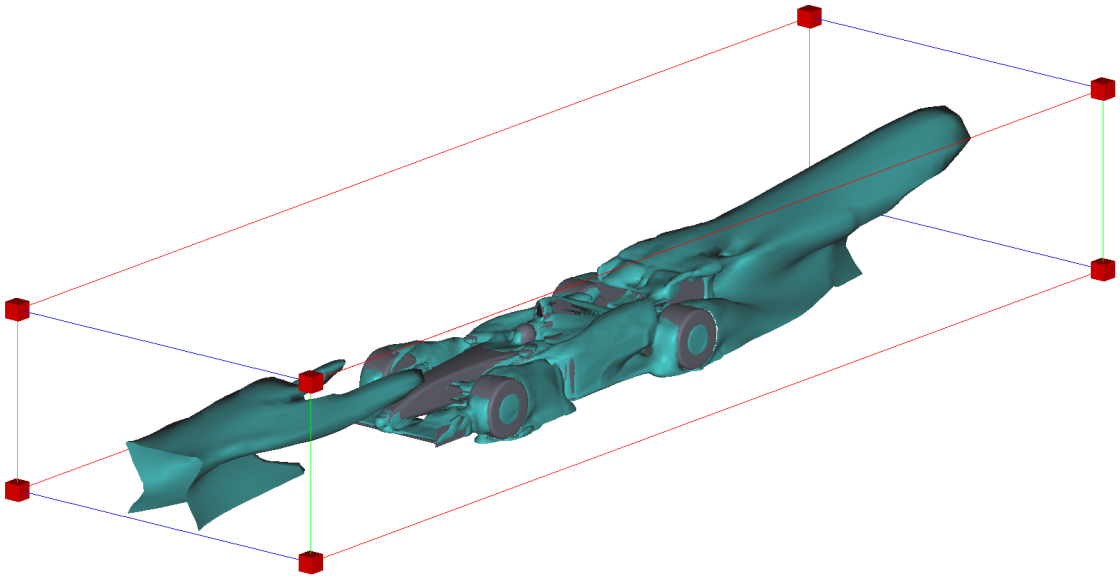

**(a)** $u_{Y,Z} = 90\%$ case.

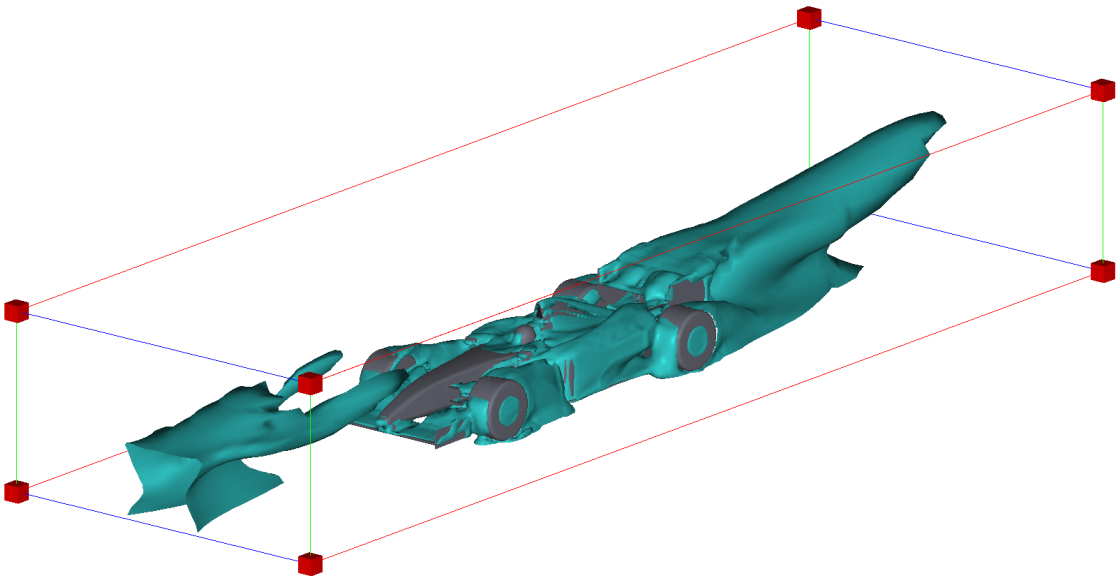

**(b)** $u_{Y,Z} = 110\%$ case.

**Figure 7.11:** Isosurfaces of $u_X = 0.4U_\infty$ between inlet plane ($x = -0.75L_C$) and $x = 2L_C$, comparing adjusted secondary flows cases

## 7.3 Characterizing the Wake

The previous section has shown that the effect of increasing the magnitude of secondary flows in the wake is to reduce the downforce loss experienced by the following vehicle, compared to the unmodified wake. The method used to increase the secondary flows was relatively unsophisticated, uniformly increasing or decreasing the whole flow field, without taking into account how the individual means of downforce generation will affect the wake. Theoretically the secondary flows, particularly the up-wash in the wake, will be the result of the non-ground-effect surfaces, i.e. the rear wing, however this assumes that the underbody is acting purely in ground-effect, in reality there are localized regions of up-wash and down-wash at the rear of the car sources other than the rear wing.

### 7.3.1 Analysis of the Formula 1 Wake Using the Wake Momentum Integral Equations

Standard CFD force measurements are determined by the integral of surface static pressure and local shear stress over the wetted area of the body, Giles & Cummings [137]. The resultant forces are then determined from the sum of the individual surface mesh cell normals, before being decomposed and expressed as Cartesian aligned forces, i.e. drag, lift and side force. This is generally adequate for the development cycle of Formula 1 cars, as the primary interest is maximizing vehicle downforce within the constraints of a given set of technical regulations, rather than the effect the means of downforce has on the wake.

The wake momentum integration method [138, 139, 140, 137, 141, 142, 143] instead allows the forces acting upon the car to be determined from the effect on the surrounding fluid, by calculating the change of static pressure and momentum within a given control volume,

$$F = \int_0^A \Delta P \, dA + \int_0^{\dot{m}} \Delta u \, d\dot{m}, \tag{7.1}$$

where,

$$\dot{m} = \int_0^A \rho u \, dA, \tag{7.2}$$

so,

$$F = \int_0^A \Delta P \, dA + \int_0^A (\Delta u) \rho u \, dA. \tag{7.3}$$

The shape and size of the control volume may be arbitrary, though to avoid introducing error should be sufficiently sized as to enclose all features of the wake [140]. Given the structured mesh generated by

PowerFLOW a rectilinear integration volume is the easiest to implement, figure 7.12, where planes C and D are 2-dimensional slices bisecting the fluid perpendicularly to the vehicle centreline. B is a streamline from A to C which is assumed to be at freestream velocity and pressure, and A is on the inlet plane so matches the freestream velocity and pressure. Like surface force measurements, error can be introduced by the mesh scale in the wake. As mentioned in the Computational Methodology there is mesh refinement in the wake, but even so the cubic lattice growth means that aft of $x = 2L_C$ the mesh lattice length is greater than $16\times$ the minimum voxel scale implemented adjacent to surface of the car.

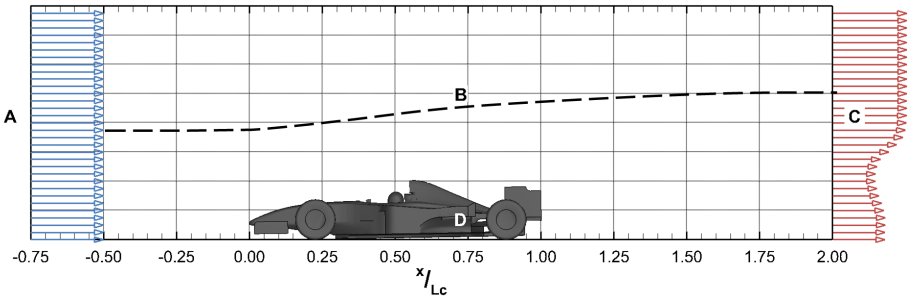


**Figure 7.12:** Centreline slice of wake integral boundary, inlet and outlet vectors of axial velocity.

Drag and downforce are calculated by the difference between out flow and freestream conditions; where drag is calculated between plane A and C,

$$D = F_X = \iint_0^C (P_\infty - P)\, dydz + \iint_0^C (U_\infty - u_X)\rho u_X\, dydz. \tag{7.4}$$

Downforce due to pressure is calculated between plane D and B and due to flow incidence (up-wash) is measured between A and C,

$$L = F_Z = \iint_0^D (P - P_\infty)\, dxdy - \iint_0^C (\cancelto{0}{u_{Z\infty}} - u_Z)\rho u_X\, dydz, \tag{7.5}$$

so,

$$F_Z = \iint_0^D (P - P_\infty)\, dxdy + \iint_0^C u_Z \rho u_X\, dydz. \tag{7.6}$$

The main advantage of implementing the wake momentum continuum equations is in the decomposition the sources of measured forces, especially with regards to downforce generated by ground-effect and out of ground-effect. Where surfaces such as the front wing and underbody are undoubtedly operating in ground-effect, they also generate flows associated with non-idealized ground-effect downforce generation, i.e. tip vorticity and wake up-wash. Therefore while it is possible to estimate the contribution to downforce from ground-effect from the car surface pressure integrals, it is not possible to give an definitive measurement. Using the integrated pressure term of the momentum equation the force reacted by the ground can be calculated, while the vertical momentum term can be attributed to the out of ground-effect downforce.

The size of the integration control volume is important as it has been shown to affect the accuracy of forces calculated by the wake integral approach [140], with the greatest discrepancy in the determination of Z-axis normal forces. Figure 7.13 shows how both the area of the transverse exit plane and the downstream location of plane C (figure 7.12) have an effect on measured drag and downforce. If the YZ-aligned measurement plane is equal to a rectangle the same size as the base of the car (i.e. $y = W_C$, $z = H_C$) the wake is not fully enclosed, so both the wake calculated drag and downforce would be erroneous. The smallest YZ plane which encloses the wake at C is equal to $(y, z) = (1.5W_C, 2H_C)$ or an area of $3.5A_{ref}$.

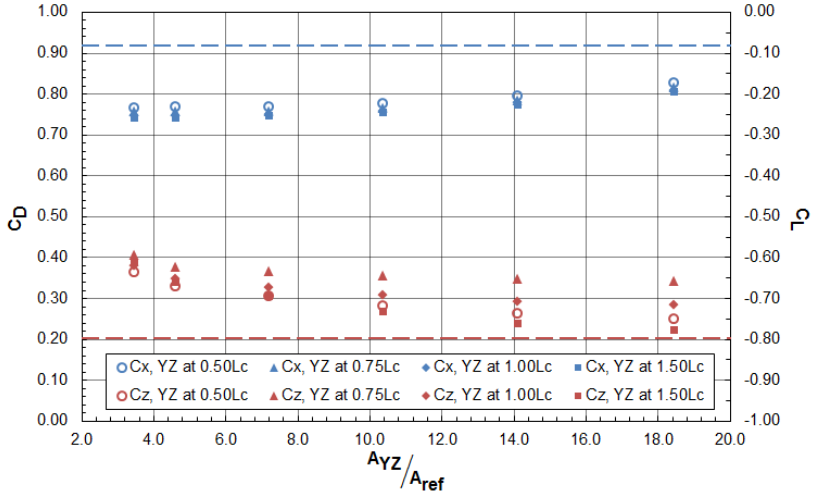


**Figure 7.13:** Effect of momentum integral measurement plane area (plane C) on drag and downforce coefficients calculated by momentum integral approach between inlet and YZ plane, measured from the rear of the car [dashed lines = forces calculated by standard surface integral.]

What is surprising, considering the rear wing generates $< 42\%$ of the total car downforce and the presence of the wake centreline up-wash, is that the average vertical velocity ($u_Z$) on plane C is a net downwash - i.e. the vertical momentum of the wake is that of a lifting body. Examination of the area integrated pressure term of $F_Z$ shows that the ground plane reacts in excess of the total vehicle downforce as calculated by the momentum integrals (figure 7.14). It is surprising that the ground plane reacts more than the sum total of downforce, to this end the rear wing must also be considered to be subject to the increased vertical force and reduced wake up-wash associated with the "ground-effect".

### 7.3.2 Decomposing the Wake

As it appears to be impossible to separate the wake from from ground-effect and the out of ground-effect sources, instead the wake will be considered as that from the rear wing and that from the body, where the body is the sum of upper and under body surface forces. The ratio of rear wing-to-body downforce of the $25\%$ Formula 1 car is $L_{RearWing} = 1.83L_{Body}$, which is greater than would be anticipated for a modern Formula 1 car; where the ratio of rear wing-to-body downforce is closer to $L_{RearWing} = 0.5L_{Body}$ [144]. The lower than anticipated body downforce being due to in part to an unoptimized underbody geometry

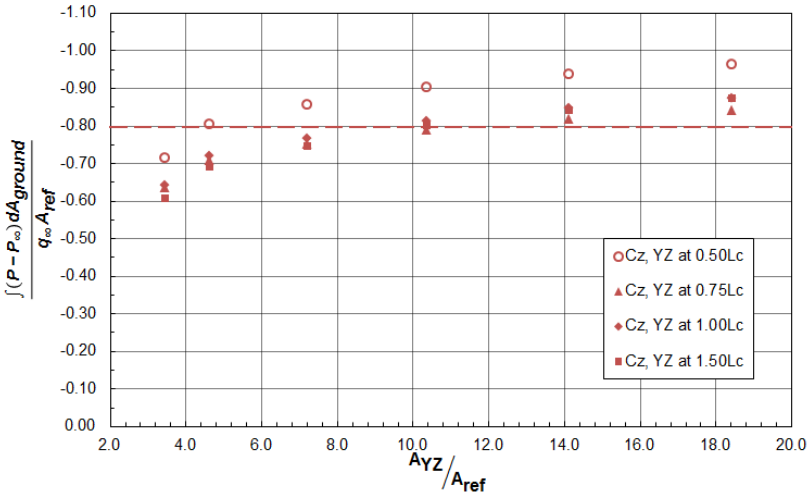


**Figure 7.14:** Downforce reacted by ground plane from wake intergral method.

coupled with regions of low pressure (lift) on the upper body of the car, reducing the total aerodynamic downforce of the body. Lift on the upper body is important for producing overall downforce of the car, especially in enhancing rear diffuser performance; as Ogawa et al explain [18], down-wash in the middle of the car (in particular under the chassis towards the front of the sidepods) helps to create a sealing effect for the mid to rear of the under-floor thereby increasing underbody suction. Arguably on the $25\%$ F1 car the aerodynamic lift on the upper body is in the wrong regions of the car to enhance the underfloor downforce, but positive circulation towards the middle of the car is expected on a modern Formula 1 car.

In order to quantify the wake up-wash from both the rear wing and body a simple three parameter design of experiments method was implemented, equation 7.7, where downforce generated by the rear wing and underbody were individually altered and the effect on wake up-wash measured. The slopes of the change of up-wash with the change of downforce for the rear wing and body are then expressed by the coefficients $C_1$ and $C_2$,

$$\Delta u_Z = C_1(\delta L_{RearWing}) + C_2(\delta L_{Body}), \tag{7.7}$$

where

$$C_1 = \frac{\partial u_Z}{\partial L_{RearWing}}, \tag{7.8}$$

and

$$C_2 = \frac{\partial u_Z}{\partial L_{Body}}. \tag{7.9}$$

To increase the rear wing downforce the angle of attack was increased by $\alpha = 3°$, by pivoting the upper 2-elements of the wing about the flap trailing edge, maintaining the maximum height above the ground plane. Assuming the rear wing operates in the linear region of the ideal lift curve slope, $a_\infty = 2\pi$, an anticipated $\Delta C_{LRearWing} \approx -0.194$ or $\Delta C_L = -0.045$ based on car frontal area. The underbody downforce was reduced by doubling the car's ride height, though the minimum ground clearance remains

low, $h_{min} \approx 0.013H_C$. This reduces the venturi effect in the contraction between the car and ground plane, increasing the static pressure and reducing the suction under the floor. For the increased ride height case the rear wing was returned to the baseline angle. For the purposes of comparison, average up-wash the wake was measured using a plane measuring $(y, z) = (1.5L_C, 1.5W_C)$ set behind the rear of the car at $x = 1.25L_C$.

The results of the design of experiments method are shown in figure 7.15, serendipitously for both the increased rear wing incidence and increased car ride height the rear wing downforce increases by the same amount, $\Delta C_{LRearWing} = -0.016$ (based on car frontal area). In the case of the increased rear wing incidence the reason for the gain is evident, though the change in downforce is less than predicted by the ideal lift slope. However, with increased ride height this could be assumed to be due to the wing moving further from the ground and the negative influence of the rear wheels. With the increased wing angle the body downforce actually increases, $\Delta C_{LBody} = -0.015$. That the increase in body downforce is a greater percentage ($\delta C_L = 8.5\%$) of the baseline force than the rear wing ($\delta C_L = 5\%$), serves to further highlight the interconnectedness of the aerodynamic surfaces, especially around the rear of the car, whereby the reduced pressure at the base of the car from the rear wing downforce increase in turn increases underbody suction and downforce.

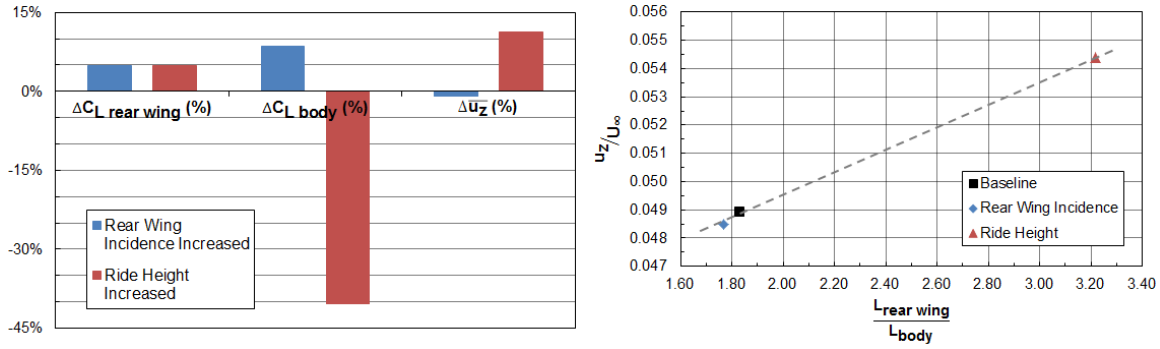


**(a)** Downforce and wake up-wash percentage change. **(b)** Downforce ratio vs non-dimensional up-wash.

**Figure 7.15:** Results of design of experiements method.

While the expectation based on the increased wing angle would be an increase of the wake up-wash, due to the increase of body downforce, the result of the increased wing incidence is to decrease the mean wake up-wash by $1\%$. Increasing the ride height has the expected effect on the body downforce, $\Delta C_{LBody} = -40\%$, which in turn results in a significant increase of the average wake up-wash ($^{uz}/_{U_\infty} = 11\%$). Plotting wake up-wash against the ratio of downforce generated by the rear wing compared to the body (figure 7.15b) shows a very clear trend of increasing the rear wing downforce ratio resulting in increased wake up-wash, even though wake averaged up-wash remains below $5.5\%$ of freestream velocity ($U_\infty$).

Solving equation 7.7 for the increased wing and reduced body downforce cases allows the coefficients $C_1$ and $C_2$ to be calculated. The change of up-wash with rear wing downforce ($C_1$) is positive, while

increasing the body downforce has the effect of inducing a down-wash in the wake, albeit not quite the same magnitude as the rear wing up-wash.

$$C_1 = 0.00308\, U_\infty N^{-1}$$

$$C_2 = -0.00192\, U_\infty N^{-1}$$

In this section it has been shown that the effect of increasing the rear wing downforce level does not necessarily result in an increase of wake up-wash as might be expected, while surprisingly the effect of the the car body, despite generating downforce, is to reduce the up-wash in the wake. It is not so simple to increase rear wing downforce independently of the underbody as complex interactions at the rear of the car means that rear wing downforce can disproportionately increase underbody downforce. The ratio of rear wing to body downforce is shown to be important, with more wake up-wash occurring when a greater proportion of downforce is generated by the rear wing than the car body.

## 7.4 Simplified Wake Model

### 7.4.1 Recreating the Wake of a Formula 1 car Using a Simplified Vortex Model

As well as wake up-wash the other downforce effect on the wake is the wing tip vortex pair of the rear wing. Due to the relatively high downforce to low aspect ratio of a Formula 1 rear wing, $\lambda = 2.86$, the induced drag of the wing forms a large portion of the rear wing drag, $({}^{C_{Di}}/_{C_D})_{RearWing} > 43\%$ for span efficiency factors lower than $e = 0.9$. So in order to investigate the effect of the rear wing downforce level on the wake and thus a downstream vehicle, the wing tip vorticity needs to be recreated, but in a controllable manner. To do this a simplified vortex model was used, with the circulation, centre of rotation, core diameter, and angular velocity matched to the real wake.

The vortex models selected for analysis were the Rankine [145, 146, 23] and Lamb-Oseen [147, 23] models. The Rankine vortex (equation 7.10) is a simple model, which assumes the behaviour of a forced vortex up to the core radius ($R_o$), surrounded by a free vortex,

$$u_\Theta = \begin{cases} \Omega r, & \text{if } r \leq R_o \\ \dfrac{\Omega {R_o}^2}{r}, & \text{if } r > R_o \end{cases}, \tag{7.10}$$

where $u_\Theta$ is the tangential velocity ($\sqrt{{u_Y}^2 + {u_Z}^2}$), $\Omega$ is the vorticity, $r$ is the radius from the vortex centre of rotation, and $R_o$ is the vortex core radius. The forced vortex behaves as if a solid body were rotating in the core, avoiding a singularity at the centre of rotation, which could lead to numerical error when it comes to generating the inlet for CFD simulation. The Rankine vortex can also be expressed in terms of total circulation of the vortex ($\Gamma_o$) [23],

$$u_\Theta = \begin{cases} \dfrac{\Gamma_o}{2\pi {R_o}^2}\, r, & \text{if } r \leq R_o \\ \dfrac{\Gamma_o}{2\pi r}, & \text{if } r > R_o \end{cases}. \tag{7.11}$$

The Lamb-Oseen vortex model is a single equation model, described as "a self-similar solution of the NavierStokes equation". It is a time dependant function, with the vortex radius ($R_o$) increasing with time by $R_o(t)^2 = R_o(0)^2 + 4\nu t$. As the inlet requires a consistent vortex, the time constraint, and therefore the vortex radius, is constant,

$$u_\Theta = \frac{\Gamma_o}{2\pi r}\left(1 - e^{\frac{-r^2}{R_o(t)^2}}\right). \tag{7.12}$$

In order to accurately recreate the tip vorticity, the tangential velocity in the wake was sampled at $x = 1.25L_C$. The wake was sampled by averaging the tangential velocity circumferentially, using a series of circular boundaries radiating from the centre of rotation of the rear wing vortex, at $(y, z) = (0.36W_C, 0.78H_C)$, to the car centreline (figure 7.16). The measured average tangential velocity against vortex radius is shown in figure 7.17 (red line). Tangential velocity in the wake peaks at a radius of $r = 0.18b_{RearWing}$, which was taken as $R_o$. There is a second peak on the sampled wake which occurs at $r \approx 0.4b_{RearWing}$, which is the result of the peak secondary flows near the ground (which can be seen behind the wheels in figure 7.16) where the vortex rotation is constrained by the ground plane.

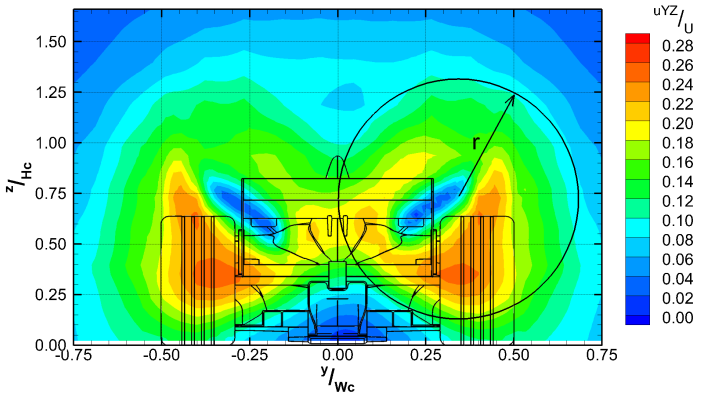


**Figure 7.16:** Annular sampling of wake tangential velocity, circumferential averaging from vortex centre.

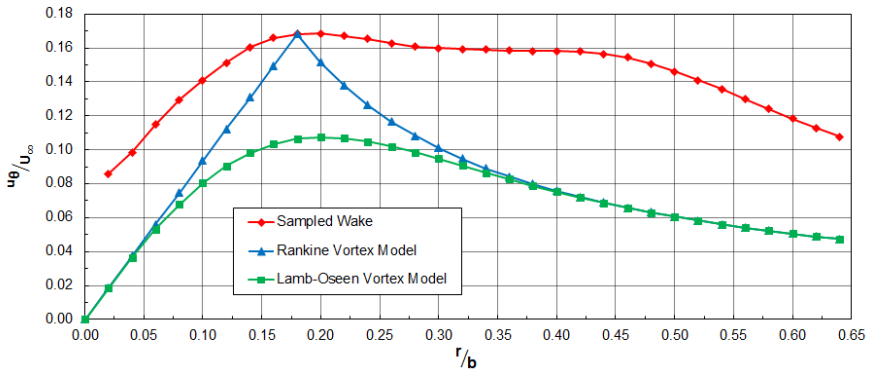


**Figure 7.17:** Comparison of circumferentially averaged tangential velocity from wake with idealized vortex models.

Using Stokes theorem (equation 7.13) to calculate the vortex circulation shows that for the sampled wake, circulation continues to grow even after the peak tangential velocity is reached, peaking at $r = 0.52b$ figure 7.18. For the purpose of the generating the wake with the vortex models, the circulation at the same radius at which peak tangential velocity occurs ($R_o = 0.18b$) was used to define the vortex circulation ($\Gamma_o$).

$$-\Gamma = \int_0^{2\pi} u_\Theta r \, d\theta \tag{7.13}$$

Comparison of the tangential velocity and circulation created by the Rankine (Green) and Lamb-Oseen

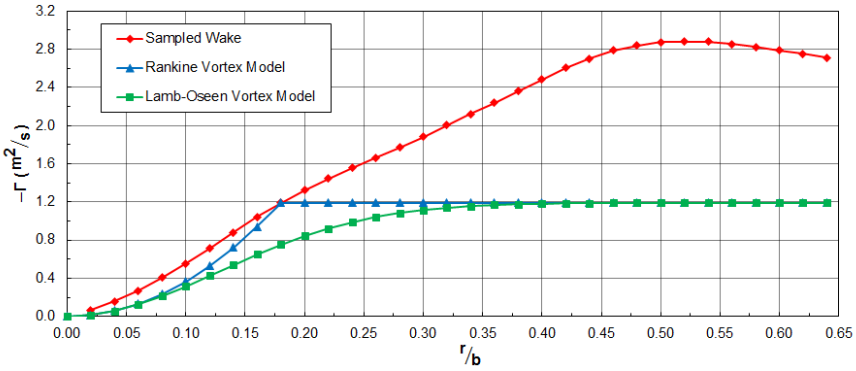


**Figure 7.18:** Comparison of circulation of sampled wake with Rankine and Lamb-Oseen vortex models.

(Blue) vortex models, and the real wake (Red) is shown in figures 7.17 and 7.18. For both vortex models the same vortex core radius ($R_o$) and vortex circulation ($\Gamma_o$) were used. While the Lamb-Oseen vortex model does more accurately recreate the shape of the real wake vortex than the Rankine model, the absolute peak tangential velocity ($u_\Theta$) is not so well matched. The profile of the vortex circulation is also more realistic than the Rankine model, though peak circulation asymptotes to $\Gamma_o$ rather than continuing to increase. The transition between the forced and free vortex behaviours of the 2-equation Rankine vortex model means there is a sharp discontinuity between the forced to free vortex models at $R_o$, which does not resemble the measured wake, however, the absolute peak tangential velocity is the quantity that is matched to the measured wake. The Rankine model also reaches $\Gamma_o$ at $R_o$, though is constant for $r > R_o$.

Using the actual circulation of the rear wing with the Lamb-Oseen vortex model would result in closer agreement to the real wake, though the peak tangential velocity remains below the peak from the sampled wake and the gradient of $u_\Theta$ from the centre of rotation to $R_o$ would be too steep. Even using an arbitrary constant for $\Gamma_o$, to match peak tangential velocity at $R_o$, still would not result in a perfect recreation of the wake profile. It must be remembered that the vortices in the wake of the Formula 1 car are not ideal, instead they are a combination of vorticity, up-wash, and down-wash from multiple sources on the car. The vortex core is also not perfectly cylindrical, and is rather eccentrically shaped in the near wake as the upper and lower rear wing co-rotating vortices merge with the wheel wakes. The purpose of this section is not to perfectly recreate the wake vortex but to simplify the wake so that it is possible to test the effect of altering wake vorticity on a following vehicle.

### 7.4.2 Construction of a Simplified Wake Model

To construct the simplified wake model the secondary flows from the simplified vortex models (figure 7.19) were combined with a uniform up-wash and a region of axial velocity deficit. The velocity deficit was imposed as a rectangular region of uniformly low velocity on the inlet of an empty domain case (figure 7.20); the magnitude of the velocity deficit was matched to the average axial velocity in the wake of the car

on the sample plane (figure 7.21). The area of the imposed velocity deficit corresponds to the approximate height and width of the wake velocity deficit on the sample plane ($(y, z) = (\pm 0.375 W_C, H_C)$). The average up-wash generated solely by the vortex models in the region of the imposed velocity deficit was calculated, and a uniform up-wash was added so that the average up-wash in this region matched the real wake. As the wake is simplified, and symmetric about the car centreline, a Z-axis aligned symmetry plane was used for all the following simplified wake cases.

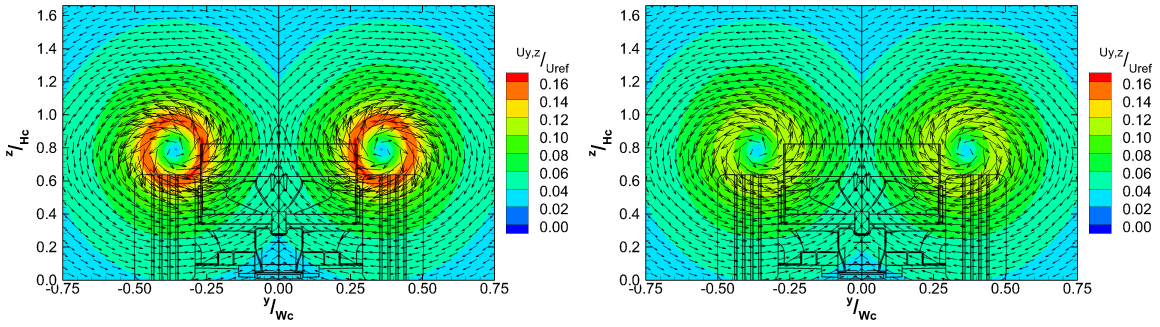


**(a)** Rankine. **(b)** Lamb-Oseen.

**Figure 7.19:** Imposed inlet secondary flow field from Rankine and Lamb-Oseen vortex models.

Despite being considerably simplified, the combination of the counter-rotating vortices and wake velocity deficit means that by just $x = 1.5L_C$ ($x = 0.25L_C$ from the inlet) the wake starts to take on the familiar 'mushroom' shape, figure 7.20, which is synonymous with the wake of high downforce cars. Whereby the axial velocity deficit in the wake is swept inboard to the car centreline and upwards to surround the vortex cores.

The development of the downstream YZ plane averaged axial velocity and up-wash from the simplified vortex models compared to the real wake are shown in figure 7.21. On the inlet, when averaged in the area of the rectangle in which the uniform velocity deficit and up-wash are imposed, both axial velocity and up-wash match the real wake. While the wake, aft of the inlet, does take the correct mushroom shape, the average velocities in the simplified vortex model and real wakes diverge slightly. For both the real and simplified wakes, the decay of the axial velocity deficit follows a $y \approx f(x^{1/2})$ trend, from $u_X \approx 0.4U_\infty$ at $x = 1.25L_C$ to $u_X \approx 0.85U_\infty$ at $x = 3L_C$. For both the simplified vortex model wakes the axial velocity is lower than the real wake by $u_X < 0.05U_\infty$. The difference in the wake averaged up-wash is slightly greater, figure 7.21b, especially at $x = 1.75L_C$ where up-wash in the simplified wakes is $\approx 50\%$ lower than the real wake, albeit the difference being only $2.5\%$ of $U_\infty$.

While there is ultimately little difference between the Rankine and Lamb-Oseen vortex models on the wake propagation, going forward the rest of this chapter uses the wake from the Rankine model as circulation (figure 7.18) and tangential velocity (figure 7.17) were matched to the real wake at the radius of the vortex core ($R_o$).

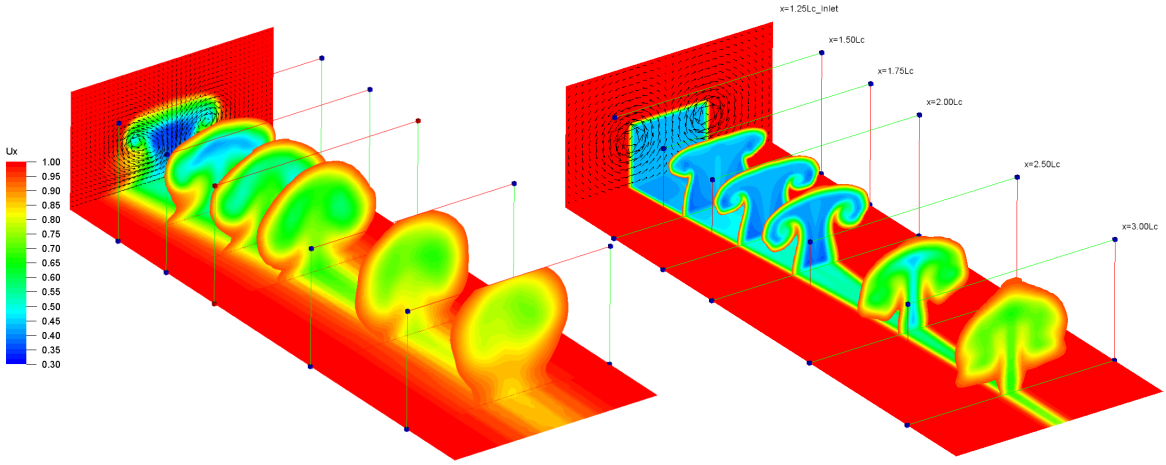


**Figure 7.20:** PowerFLOW wake $2W_C \times 2H_C$ slices of axial velocity, comparing real wake (left) to Rankine vortex model wake (right).

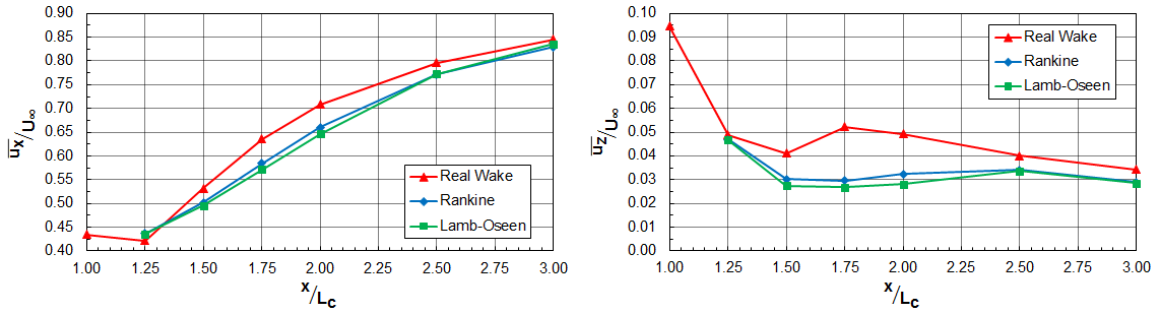


**(a)** Axial velocity deficit.

**(b)** Wake up-wash.

**Figure 7.21:** Comparison of Rankine and Lamb-Oseen vortex model wakes with $25\%$ Formula 1 sampled wake, averaged over velocity deficit imposed area $[(y, z) = (\pm 0.375W_C, H_C)]$.

### 7.4.3 Effect of Altering the Rear Wing to Body Downforce Ratio on the Wake Propagation (Empty Tunnel)

To determine the effect of the rear wing-to-body downforce ratio on wake propagation, the wake's vortex strength and level of up-wash must be altered. It is desired that the total downforce of the theoretical simulated upstream vehicle remain consistent with the $25\%$ F1 model, so any increase of rear-wing downforce must be matched by an equal reduction of the body downforce, and vice versa. It is also desired that the drag of the theoretical upstream vehicle remain constant, so the region of velocity deficit was left unaltered, such that the wake momentum deficit remains constant.

By using equation 7.7 the change in wake up-wash for a given rear wing-body downforce ratio can be calculated. To match the vortex to the desired rear wing downforce level, the circulation of the wake vortex ($\Gamma_o$) must be altered. Using the absolute rear wing downforce of the scale model the change of the vortex circulation can be calculated using,

$$\Delta\Gamma_o = \frac{\Delta L}{\rho U_\infty b}. \tag{7.14}$$

The effect of altering the rear wing downforce by $\pm 10\%$ and $\pm 50\%$ on the downforce ratio of the simulated upstream vehicle and therefore the change of vortex circulation and average wake up-wash are shown in table 7.3. Changing the downforce ratio of the simulated upstream car would result from altering the geometry of the car, especially the $\pm 50\%$ cases. While total downforce of the simulated vehicle remains as low as the $25\%$ model, reducing the simulated rear wing downforce from the baseline level by $50\%$ results in a similar rear wing to body downforce ratio to a modern, well developed, Formula 1 car. Increasing the downforce of the rear wing by $50\%$ results in the rear wing generating $> 50\times$ the downforce of the body; this is due to the baseline body force, as the sum of under and upper body forces, being close to $C_L = 0$.

**Table 7.3:** Effect of altering rear wing downforce level on wake vortex circulation and up-wash.

| Rear Wing Downforce | $-50\%$ | $-10\%$ | $+10\%$ | $+50\%$ |
|---|---|---|---|---|
| $C_{L\,RearWing}$ | -0.166 | -0.299 | -0.365 | -0.498 |
| $C_{L\,Body}$ | -0.342 | -0.209 | -0.143 | -0.010 |
| $L_{RearWing} : L_{Body}$ | 0.486 | 1.43 | 2.56 | 50.6 |
| $\Delta\Gamma_o$ $(m^2 s^{-1})$ | 0.778 | 0.156 | -0.156 | -0.778 |
| $\Delta\frac{u_Z}{U_\infty}$ | -0.0298 | -0.00596 | 0.00596 | 0.0298 |

The effect of altering the rear wing to body downforce ratio on wake propagation is shown in figure 7.22, of interest is how the changes affect the flow onset to a downstream vehicle, so the wake was integrated from transverse (YZ) wake planes over a box measuring $W_C \times H_C$. The mass flow weighted wake up-wash, figure 7.22a, is a measure of the vertical momentum of the fluid at the point of the downstream car. In order to attain a non-dimensional term the non-dimensional up-wash $\left(\frac{u_Z}{U_\infty}\right)$ is integrated. Where,

$$\frac{1}{\dot{m}} \int_0^{\dot{m}} \frac{u_Z}{U_\infty}\, d\dot{m} \;=\; \frac{1}{\rho\, U_\infty\, A} \int_0^{A} \frac{u_Z}{U_\infty}\, \rho\, u_X\, dA. \tag{7.15}$$

The mass flow weighted up-wash increases downstream of the inlet, despite the mean wake up-wash reaching a plateau downstream of the inlet (figure 7.21b), which is due to the transit of mass flow into the integration region.

The effect of altering the downforce ratio on the axial component of the wake, figure 7.22b, is shown by the ratio of the integral of dynamic pressure deficit and freestream dynamic pressure. Where,

$$\frac{1}{q_\infty\, A} \int_0^{A} q_X\, dA \;=\; \frac{1}{0.5\,\rho\, {U_\infty}^2\, A} \int_0^{A} 0.5\,\rho\, {u_X}^2\, dA \;=\; \frac{{u_X}^2}{{U_\infty}^2}. \tag{7.16}$$

Modifying the rear wing to body downforce ratio by $\pm 10\%$ does not have a significant impact on either wake up-wash or dynamic pressure deficit, following the same trends as the baseline RWDF level case. Increasing the RWDF by $10\%$ increases both the up-wash and dynamic pressure in the wake, while conversely reducing the RWDF by $10\%$ reduces the vertical momentum and dynamic pressure. Increasing the RWDF level by

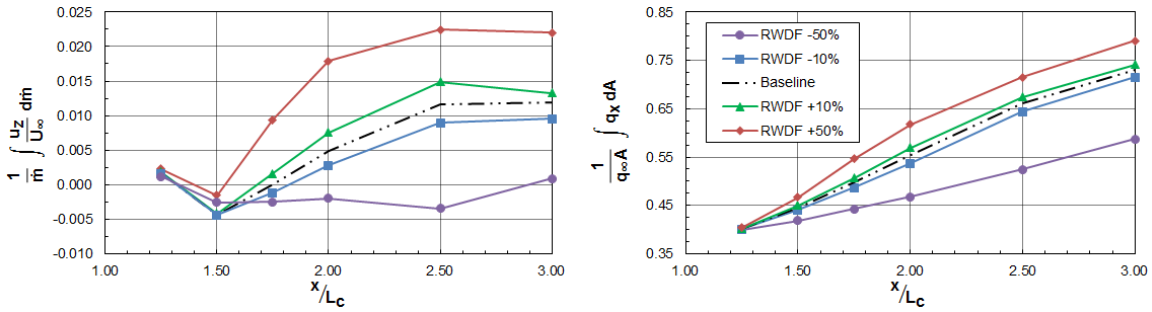


**(a)** Mass flow weighted wake up-wash.

**(b)** Dynamic pressure deficit to freestream dynamic pressure fraction.

**Figure 7.22:** Wake integrals resulting from altering rear wing to body downforce ratio on flow onset to downstream vehicle (integration area $= W_C \times H_C$).

$50\%$ also follows the same trend as the baseline, with a larger offset than the $10\%$ increase case, significantly increasing the up-wash, while the dynamic pressure fraction increases by $< 10\%$ at $x = 3L_C$. The most pronounced effect on the wake propagation is when the RWDF was reduced by $50\%$ reducing the dynamic pressure by $< 20\%$ at $x = 3L_C$. The mass flow weighted up-wash is also negative for most downstream planes, despite being a net up-wash, meaning there is not the same quantity of mass flow entering the integral region as in the other cases.

As well as the difference in average wake dynamic pressure and up-wash values, the effect of altering rear wing downforce level on the shape of the wake is obvious, figure 7.23. While the wake takes the 'mushroom' form, even for the RWDF -50% case, the location of the vortex cores and the width of the 'mushroom stem' are both influenced by the wake vortex circulation strength. When the rear wing downforce level is reduced by $50\%$ the wake is visibly lower and thicker than the RWDF+50% case wake. The compaction of the 'mushroom stem' should alter the effect the wake has, especially on a downstream vehicle front wing, limiting the dynamic pressure deficit to the mid-span region.

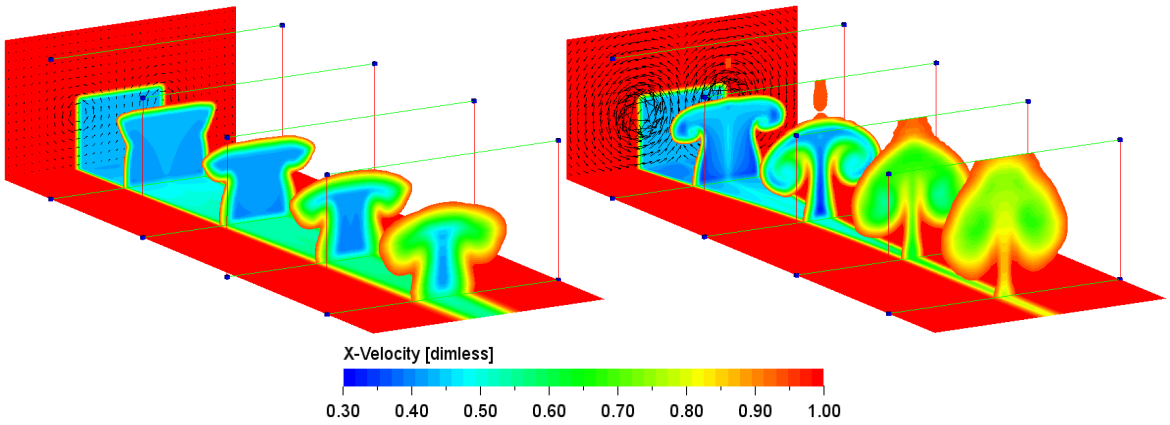


**Figure 7.23:** Effect of altering vortex circulation strength and wake up-wash on wake propagation, RWDF -50% (left) RWDF +50% (right), 2-D slices of axial velocity deficit measuring $2W_C \times 2H_C$.

## 7.5 Effect of Simplified Wake on a Downstream Vehicle

### 7.5.1 Baseline Rear Wing Downforce Level

The final consideration is the effect the simplified wake has on a downstream vehicle, the results from which are shown in table 7.4. The wake used the Rankine vortex model to generate vorticity, with a region of velocity deficit to match the mass averaged wake (drag) of the isolated vehicle. As with the other wake cases, the effect is to reduce aerodynamic drag and downforce. The effect of the simplified wake is almost identical to the imposed wake on the change of total vehicle downforce, table 7.4, the range of $\Delta C_L$ is within $0.05$, with $\Delta C_{LF}$ and $\Delta C_{LR}$ within $0.006$ and $0.05$ respectively. The magnitude of the change of total vehicle drag force is almost double that of the imposed wake, which is the most similar onset flow condition to the simplified wake case based on the real car wake.

**Table 7.4:** Comparison of effects of upstream vehicle and imposed simplified wake model on a downstream vehicle.

| | $C_D$ | $\Delta$ | $C_L$ | $\Delta$ | $C_{LF}$ | $\Delta$ | $C_{LR}$ | $\Delta$ |
|---|---|---|---|---|---|---|---|---|
| Imposed Wake[a] | 0.750 | -0.168 | -0.265 | +0.531 | +0.073 | +0.326 | -0.338 | +0.206 |
| Simplified Wake[b] | 0.460 | -0.339 | -0.070 | +0.576 | +0.085 | +0.320 | -0.155 | +0.257 |

[a]No symmetry: delta to isolated vehicle case
[b]Symmetry plane: delta to isolated vehicle with symmetry plane case

A breakdown of component forces (figure 7.24) indicates where some of the differences to the real wake occur. The effect of the simplified wake on aerodynamic drag of the downforce generating elements (i.e. the front and rear wings, and body) is similar for all three cases, within $\Delta C_D = 0.01$. The key difference between the real and simplified wake is on the wheels, where aerodynamic drag force increases from the baseline on the both front and rear wheels, $\Delta C_D = 0.010$ and $\Delta C_D = 0.003$.

The difference between onset flow conditions on $\Delta C_L$ is greater than $\Delta C_D$, albeit still within a range of $\Delta C_L < \pm 0.05$. The greatest difference on downforce generating elements is on the front wing and underbody; the front wing losing more downforce with the simplified wake, by $\Delta C_L \approx +0.04$ than the imposed wake, while the underbody loses less downforce by $\Delta C_L \approx -0.045$. These differences could be sympathetic, as it is known that the generation of front wing downforce will negatively impact downforce generated by the underbody. The effect of the wake on the rear wing is similar to both the upstream and imposed real wakes. Like drag, the greatest difference between the cars is the wheels, which experience an increase of lift relative to the baseline conditions, $\Delta C_L \approx 0.025$ on the fronts and $\Delta C_L \approx 0.05$ for the rear.

The effect of the simplified wake on the surface pressure distribution of the 25% Formula 1 car are shown in figure 7.25. As the forces would suggest, the change of surface pressure is very similar over much of the

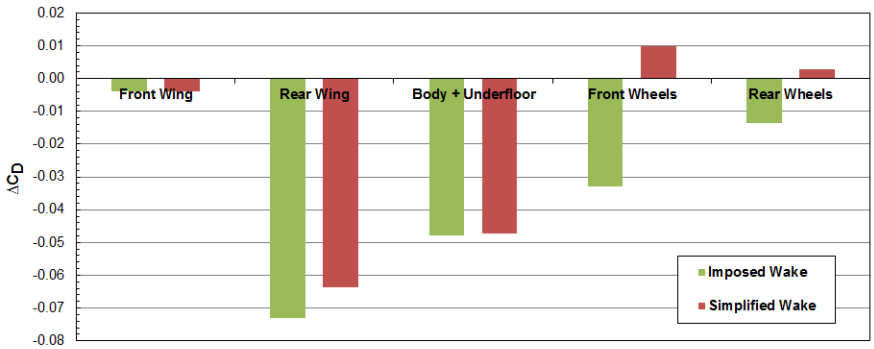


**(a)** Drag.


**(b)** Downforce.

**Figure 7.24:** Change of component force coefficients (based on car reference area) comparing simplified and imposed wake cases to isolated vehicle.

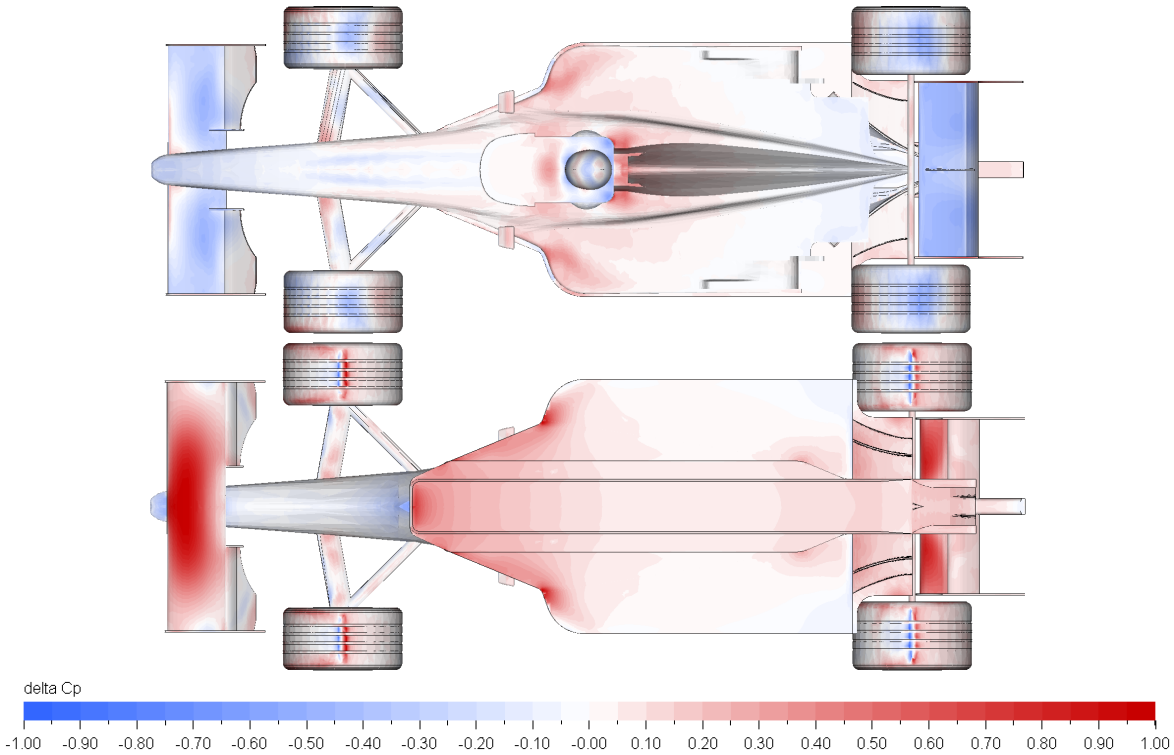


**Figure 7.25:** Effect of simplified wake model on vehicle surface pressure distribution, compared to isolated case.

car to the upstream vehicle and imposed wakes from the real car, figures 6.11 and 6.26. Suction reduces significantly on the underside of the front wing centreline, if slightly more so than with the real wake, the

leading edge of the underbody and sidepods, rear diffuser throat, and the rear wing. While on the upper surfaces of the front and rear wings static pressure reduces. This gives a level of confidence in the accuracy of the simplified wake, that while absolute forces and the relative coefficient changes are not reproduced precisely, the trends and locations of force and surface pressure losses are similar to the real wake.

### 7.5.2 Altering Rear Wing Downforce Level

The effect of altering the simplified wake effective rear wing downforce level on a downstream vehicle was tested. It should be noted that changing the contribution to downforce from the rear wing by as much as $\pm 50\%$ would result from a drastic alteration of the aerodynamic surfaces of the car, and so it is difficult to do anything but infer the effect the wake would have on the downstream vehicle; assuming such a vehicle would be constructed of front and rear wings and flat underbody with upswept rear diffuser (not Venturi tunnels). As with the cases where the real wake secondary flow field was adjusted, the change of rear wing downforce level does not have a monotonic effect on drag and downforce generated by the downstream vehicle, figure 7.26.

Interestingly for all the modified rear wing downforce cases, the change of aerodynamic drag is lower than the baseline wake case, where the wake vortex circulation ($\Gamma_o$) is matched to the real wake. When rear wing downforce level is increased, the reduction of drag experienced by the car reduces, and vice versa when rear wing downforce level is reduced. For the exaggerated cases RWDF-50% case experiences almost twice the loss of drag as the RWDF+50% case; this is the expected result, and follows the same trend as the modified secondary flow field of the real wake, if slightly exaggerated. Surprisingly, modifying the wake does not seem to impact total vehicle downforce loss significantly, $\Delta C_L$ is within $0.02$, though the effect on front downforce ($C_{LF}$) reduces as wake circulation is increased.

**Table 7.5:** Effect of modifying wake vortex circulation strength and up-wash on a downstream vehicle.

| | $C_D$ | $\Delta$ | $C_L$ | $\Delta$ | $C_{LF}$ | $\Delta$ | $C_{LR}$ | $\Delta$ |
|---|---|---|---|---|---|---|---|---|
| RWDF -50% | 0.466 | -0.333 | -0.060 | +0.586 | +0.097 | +0.331 | -0.156 | +0.255 |
| RWDF -10% | 0.520 | -0.279 | -0.078 | +0.568 | +0.084 | +0.318 | -0.162 | +0.249 |
| Baseline RWDF | 0.460 | -0.339 | -0.070 | +0.576 | +0.085 | +0.320 | -0.155 | +0.257 |
| RWDF +10% | 0.516 | -0.283 | -0.059 | +0.587 | +0.088 | +0.323 | -0.147 | +0.264 |
| RWDF +50% | 0.635 | -0.164 | -0.059 | +0.587 | +0.065 | +0.300 | -0.124 | +0.287 |

Comparing the component force coefficients to the baseline rear wing downforce case (figure 7.26), further exemplifies the non-monotonic effect of increasing or decreasing wake secondary flow and up-wash. Altering the wake rear wing downforce by $\pm 10\%$, has very little impact on component drag and $\Delta C_D < 0.005$ with the front wing and body slightly less affected by a $10\%$ increase, and the rear wing slightly less affected by the $10\%$ reduction. Like the drag loss altering rear wing downforce by $\pm 10\%$ does not significantly affect the $\Delta C_L$ on any components. The front wing experiences a slightly greater downforce loss for the RWDF-10% case, while rear wing and underbody lose more downforce when the wake vortex circulation is

increased by $10\%$.

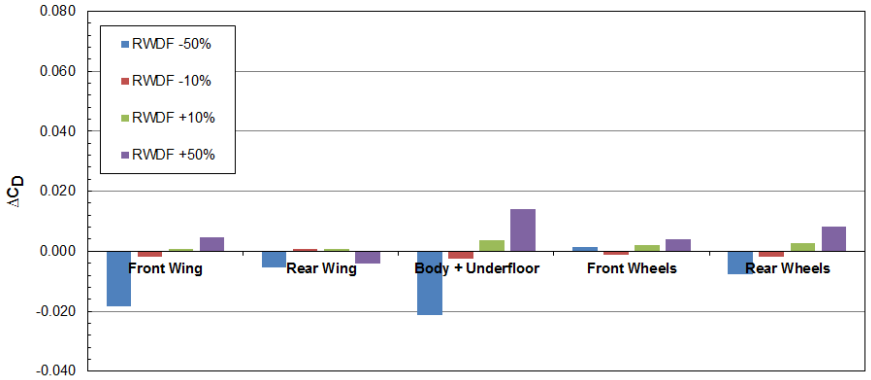


**(a)** Drag.

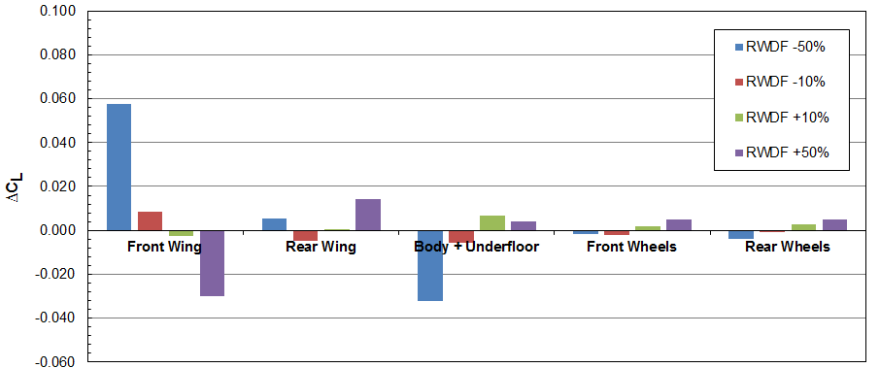


**(b)** Downforce.

**Figure 7.26:** Change of component force coefficients compared to baseline RWDF wake case (based on car reference area) for increased and reduced rear wing to body downforce ratio.

A $50\%$ reduction of simulated rear wing downforce the wake has a more significant effect on front wing and body drag than the $10\%$ alterations, albeit still small, $\Delta C_D > -0.02$. Increasing the vorticity and up-wash for a $50\%$ increase of rear wing force reduced the drag deficit for the front wing and body, even serving to increase front wing drag $\Delta C_D = +0.001$ from the isolated case. The effect of the wake on rear wing drag is similar reduction for both the RWDF-50% and RWDF+50% cases, $\Delta C_D = 0.004$. It should be noted that for the case where the vehicle ride height was increased to reduce underbody downforce (figure 7.15) rear wing drag ($\delta C_D = 0.02$) and downforce increased ($\delta C_L = -0.006$), so the greater drag deficit on the rear for the RWDF+50% case could well be the result of added interactions between components rather than necessarily a direct result of the wake. $\Delta C_D = 0.004$.

The RWDF-50% case also has the greatest impact on front wing downforce, $\Delta C_L \approx 0.06$ higher than the simplified wake case. As with $\Delta C_D$ the underbody downforce deficit is opposite the front wing. Downforce increases relative to the simplified wake, which as previously discussed could be due to a reduced front wing wake rather than directly resulting from the upstream wake. The front wing downforce deficit is reduced for the RWDF+50% case compared to the simplified wake, $\Delta C_L \approx -0.03$, and subsequently the underbody downforce deficit increases, $\Delta C_L = 0.005$. The effect of the RWDF+50% case is to increase

loss of downforce experienced by the rear wing, which seems to be the opposite effect to that which would be expected. However, while the increased wake up-wash and vorticity reduces velocity deficit in the wake near the ground helps the front wing, figure 7.23, it does increase the magnitude of the wake towards the rear wing of the downstream vehicle.

Surface pressure contours of the $\pm 50\%$ cases (figure 7.27) show the increased surface pressure on the lower surface and reduced pressure on the upper surface of the front wing for the RWDF-50% case, over a greater span-wise portion of the wing than the $+50\%$ case, which confirms the findings from the force coefficients.

The underbody experiences a greater $\Delta C_P$ on both the front edge and rear diffuser for the RWDF-50% wake case. This seems contrary to the change seen in the body force coefficients, however, the force coefficient is given for combined body and underbody. It can be seen that regions of suction ($-C_P$) on the tops of the side-pods also increase in the $-50\%$ case, so the combined force is actually higher than the $+50\%$ case. On a more developed vehicle downforce generated by the underbody should by far exceed the lift generated by the upper body. So it would be expected that the effect of $\Delta C_P$ on the underbody would reduce total downforce by more than is seen for this vehicle. A vehicle with $50\%$ less rear wing downforce would also have a different underbody geometry, either from a longer diffuser, or lower ground clearance therefore generating larger suction peaks.

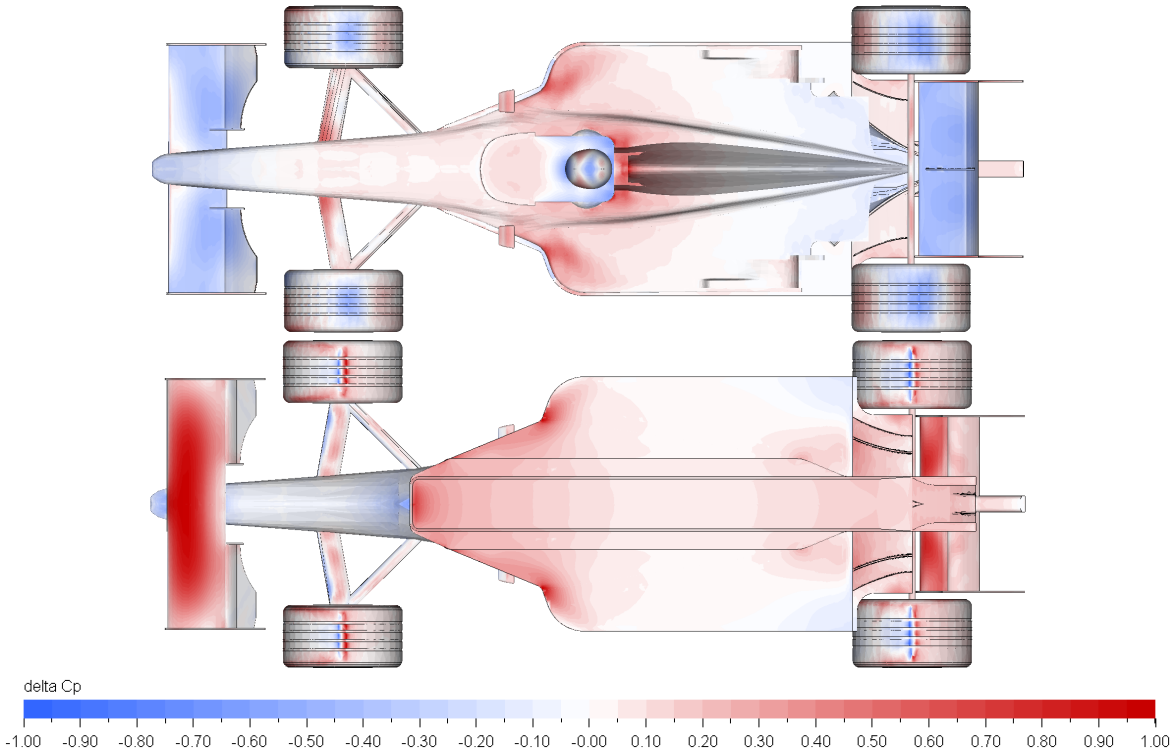


**(a)** RWDF-50%.

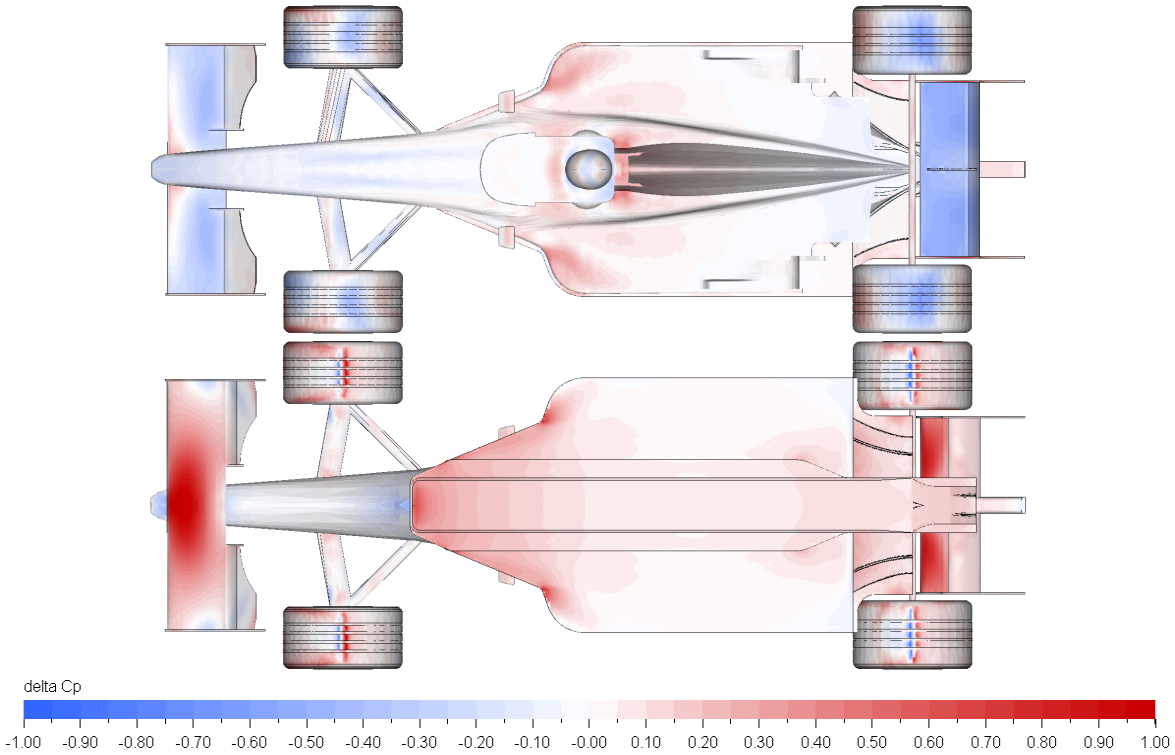


**(b)** RWDF+50%.

**Figure 7.27:** Effect of altering wake vortex circulation strength and up-wash on downstream vehicle surface pressures, compared to isolated vehicle.

## 7.6 Chapter Summary

In this chapter the effect of modifying the wake of a Formula 1 car, both on the propagation of the wake itself and on a downstream vehicle, has been investigated and discussed. Using the same method of imposing the wake, as described in Chapter 6, allows the onset flow field to be modified by changing the inlet boundary conditions, at $x = -0.75L_C$ upstream of the following vehicle.

Initial tests removed key variables from the onset wake, namely the axial velocity deficit and secondary flows. Removing the axial velocity deficit from the wake reduced the loss of aerodynamic drag and downforce experienced by the downstream vehicle, relative to an upstream vehicle, by $3.5\%$ and $9\%$ respectively. The dynamic pressure deficit resulting from the axial velocity deficit is a large part of the total pressure deficit in the wake of this Formula 1 car, so removing $u_X$ from the inlet has a greater effect on the generated wake than desired. Removing the secondary flows from the inlet is a more isolated change, as arguably the only other variable affected is the static pressure deficit in the trailing vortex cores, which is both small and characterized by the inlet boundary conditions. Removing the secondary flows from the inlet had a considerable effect on the propagation of the wake, resulting in a low velocity tube which saturated the downstream vehicle, and increasing drag and downforce losses by $28\%$ and $23\%$ respectively. From this it is clear that while the secondary flows must have a negative effect on the trailing vehicle, up to $\Delta C_D = 0.08$ and $\Delta C_L = 0.24$, they are also beneficial for wake decay and for diverting the axial velocity deficit over the downstream car.

As the effect of manipulating the secondary flow field on the other inlet wake parameters is minimal, $u_{Y,Z}$ was therefore scaled between $90\% < u_{Y,Z} < 110\%$ to test the sensitivity of the downstream vehicle to secondary flow intensity. While scaling of the inlet variables has the obvious effect on the secondary flows in the wake, what is interesting is the increase of axial velocity ($\Delta u_X < 0.03U_\infty$) onset to the downstream vehicle when secondary flows are increased. This is especially pronounced by the nose of the downstream car, where the increased velocity reduces the effect of the wake on the front wing and underbody. The effect of the wake on the rear wing of the downstream vehicle is also reduced with increasing secondary flows, and this can be seen to be the result of a more rapid rate of decay in the wake.

To determine how downforce generated by the rear wing and underbody affect up-wash in the wake, the wake momentum continuum equations were applied in the flow field around the car. While it is well known that a wing operating in ground effect is subject to reduced wake up-wash compared to a wing in freestream, the surprising result is that the average vertical velocity measured in the wake of the car is down-wash. Further investigation showed that up-wash in the wake is increased when the proportion of car downforce generated by the rear wing is increased, and that down-wash is induced as the downforce of the body is increased.

While uniformly multiplying the secondary flow field does indicate a relationship between increased $u_{Y,Z}$ reducing the drag and downforce loss for the following vehicle, it does not take into account the source of the wake vortices or how the relative levels of downforce affects the circulation of those vortices. The secondary flows in the wake of a Formula 1 car are primarily the result of the rear wing tip counter-rotating vortex pair, but are also the result of weaker vortex structures from the underbody, front and rear wheels, which merge with the dominant wing-tip pair. Arguably these weaker vortex structures will change little when rear wing downforce is changed, so scaling the whole secondary flow field does not represent a change of the rear wing downforce.

Finally the wake was recreated using a simplified vortex model coupled with a region of uniform velocity deficit and wake up-wash. The simplified wake produced the same mushroom shaped wake downstream of the inlet, as the wake velocity deficit is influenced by the trailing vortex pair. While the momentum deficit and up-wash on the inlet plane are matched to the real wake, the propagation of the simplified wake is different, especially between $0.5L_C < x < 1.5L_C$ behind the inlet, where up-wash and axial velocity are lower than the real wake; resulting in a greater effect on drag and downforce generated by the downstream vehicle at $x = L_C$. Despite the differences to the real wake, the vortex models allowed direct manipulation of the circulation of the rear wing tip vortices. Changing the vortex circulation, consistent with an increase of rear wing downforce, and increasing wake up-wash, consistent with reducing the body downforce such that total downforce was unaffected, reduced the average axial velocity deficit in the wake $\Delta u_X > -7\%$. While reducing vortex strength and up-wash, consistent with increasing the body downforce, increased the velocity deficit $u_X < 14\%$.

# Chapter 8

# Collective Analysis and Discussion

This chapter presents short review and discussion of the results found in chapters 4, 6, and 7. Where experimental results (wind tunnel and CFD) have been discussed individually, this chapter brings together various strands from results in previous chapters to present a coherent theory for the cause of aerodynamic performance loss when operating in the wake of an upstream vehicle.

## 8.1 Comparison of Wind Tunnel and CFD Results

As was highlighted at the beginning of the CFD results, Chapter 6, the forces generated by the car by experimental and computation methods are slightly different, despite the Reynolds number being matched, $Re = 2.05 \times 10^6$. Each method was used in experiments considering the relative strengths and weaknesses; the wind tunnel allows a large data set to be collected relatively quickly, though the model requires mounting by support struts, which are shown to affect total accuracy of force measurements. The CFD does not require model support nor is the size of the domain constrained, so blockage ratios significantly smaller than the wind tunnel can be run. There are also no constraints for rolling road belt width and length and the whole ground plane can be set to match freestream velocity. CFD can be computationally expensive, with relatively high time costs per simulation. Accuracy is also dependant on mesh quality and resolution, which can further increase computational cost. The following section seeks to examine and explain where the similarities and differences between CFD and the wind tunnel occur.

### 8.1.1 Isolated Vehicle

Vehicle force coefficients for the experimental and computational cases are shown in table 8.1, comparisons for vehicle downforce are given for the sprung component of the car, as wheel forces are not measured by the internal balance; repeatability of forces measured by the balance are within $\pm 0.06$ on $C_L$ and $\pm 0.02$ on $C_D$.

In CFD total drag is $\Delta C_D = 0.15$ higher than the measured drag from the wind tunnel, however, comparing the wheel and body (the sum of wings, upper and underbody) drag forces shows these individual sources to be smaller than in the wind tunnel, by $\Delta C_D \approx -0.08$ each. A large part of the difference on total drag can be attributed to the drag force and downstream wake effect of the front suspension members, which were not present in the wind tunnel.

Downforce generated by the car body appears more significantly different than drag, the CFD producing $0.30$ on $C_L$ less than the wind tunnel, though the percentage difference is in fact similar to the wheel and body drag, between $20\%$ and $25\%$ lower than the peak experimental downforce coefficient. Most of the difference in downforce occurs at the rear axle, $\Delta C_{LR} = 0.22$, rather than at the front, $\Delta C_{LF} = 0.085$. Despite this the aerodynamic centre of pressure (excluding wheels and suspension) is only $\approx 5\%$ further forwards in the computational case.

**Table 8.1:** Comparison of isolated vehicle force coefficients (based on reference area of $1.5m^2$ full scale).

| | $C_{D\ total}$ | $C_{D\ body}$ | $C_{D\ wheels}$ | $C_{L\ body}$ | $C_{LF\ body}$ | $C_{LR\ body}$ | $C_{L\ wheels}$ |
|---|---|---|---|---|---|---|---|
| Experimental | 0.765 | 0.384 | 0.380[a] | -1.14 | -0.485 | -0.656 | N/A |
| Computational | 0.918 | 0.304 | 0.308[b] | -0.847 | -0.402 | -0.444 | +0.128[c] |

[a] Front: $C_{D\ wheels} = 0.193$, Rear: $C_{D\ wheels} = 0.187$
[b] Front: $C_{D\ wheels} = 0.166$, Rear: $C_{D\ wheels} = 0.142$
[c] Front: $C_{L\ wheels} = +0.115$, Rear: $C_{L\ wheels} = +0.026$

Comparison of the total pressure deficit in the wakes (figure 8.1) gives an indication of where some of the differences in the measured forces between the two methodologies may occur. It is necessary to support the model in the wind tunnel, and both the overhead strut and wheel sting wakes can still be seen in the wake downstream of the car. Behind the rear wheels the wake is wider in the CFD case, especially outboard of the outside face of the rear wheel and under $z \approx 0.25H_C$. Possibly as the wheel wakes are disrupted by the stings.

The experimental wake is visibly more diffuse than the CFD, extending further in the vertical direction with a slightly reduced pressure deficit over much of the base. The exception to the lower total pressure deficit wake is in the region of the rear wing tip vortex, which is more obvious when $x < 1.25L_C$ behind the car. The streamwise vorticity ($\Omega_X$), figure 8.2a, at $x = 1.25L_C$ shows that the tip vortex from the main wing is more defined in the experimental case ($\Delta\Omega_X = 0.006$), which results in a greater magnitude secondary

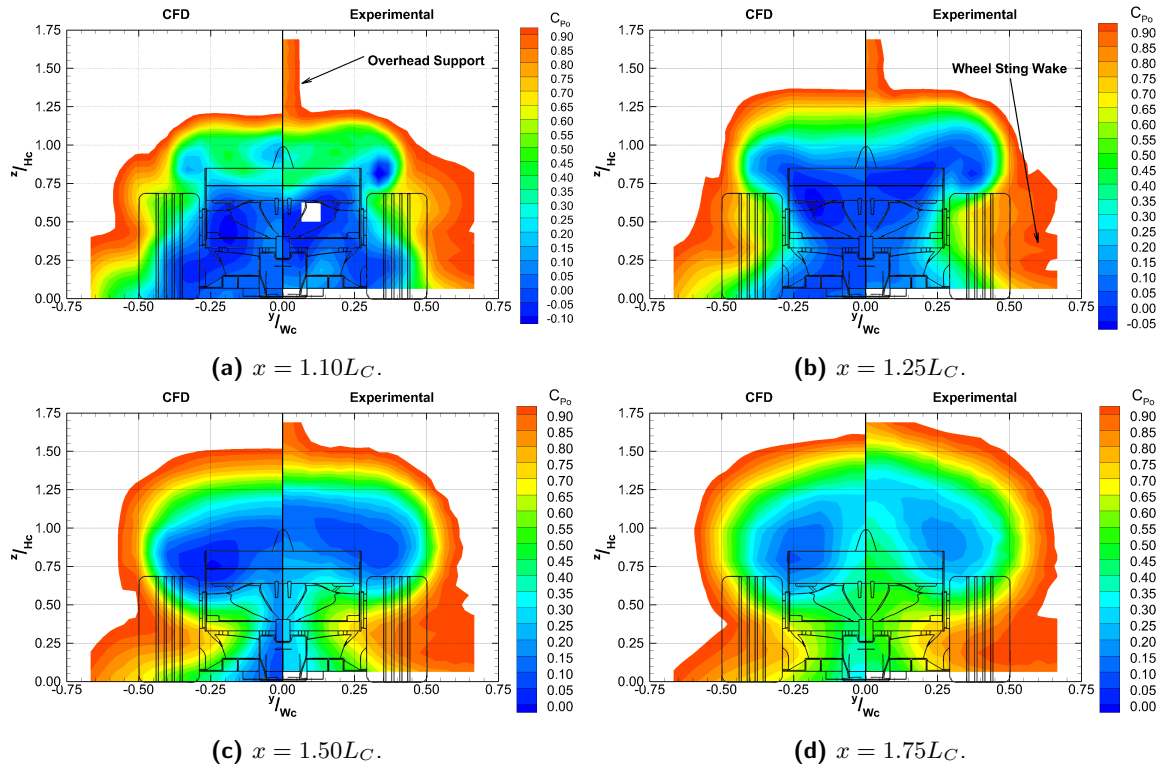


**(a)** $x = 1.10L_C$. **(b)** $x = 1.25L_C$.

**(c)** $x = 1.50L_C$. **(d)** $x = 1.75L_C$.

**Figure 8.1:** Comparison of $C_{Po}$ contours in the wake of the 25% Formula 1 car from CFD and wind tunnel experiments.

flow circulating the more structured upper wing tip vortex core figure 8.2b, driving the wake inboard and upwards with greater expedience, perhaps explaining in part why the wheel wakes are less defined.

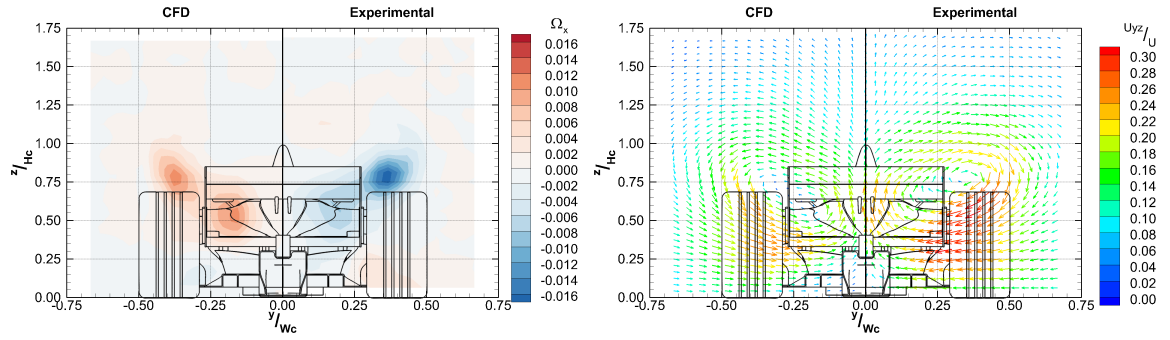


**(a)** Streamwise vorticity. **(b)** Secondary flows.

**Figure 8.2:** YZ plane at $x = 1.25L_C$ comparing computational and experimental wake vortex.

Force measurements show the greatest difference on $C_L$ is in the magnitude of downforce acting upon the rear axle. The stronger vorticity in the wake of the rear wing in the experimental case would seem to indicate a greater level of rear wing downforce, as induced drag is proportional to ${C_L}^2$. The difference in wing tip vortex could result from mesh scale in the near wake, the turbulence modelling native to PowerFLOW ($k - \varepsilon$ coupled with VLES), or even the assumed boundary layer transition on the wing surface from the PowerFLOW wall model [132]. The lower wing element in the CFD case produces a slightly stronger vortex than the experimental case, creating a slightly more eccentric secondary flow field. The lower wing vortex could be influenced by the 'cooling' flow egress through the body, which could be less obstructed in CFD

without the pressure tubing which is present in the wind tunnel.

### 8.1.2 Vehicle in Wake

As well as the difference in the isolated vehicle forces, there are some noticeable differences in the effect of the wake on the downstream vehicle, particularly on the aerodynamic balance. As previously mentioned some of this difference could result from the addition of measured wheel lift forces in the CFD, which are not measured empirically. As wheel forces are measured in CFD it made sense to present the effect of the wake on the whole car in Chapter 6, however for the purposes of comparison the effect of the wake on wheel lift is ignored. Table 8.2 shows the effect of the different upstream wakes on the downstream vehicle body forces, i.e. excluding wheel and suspension forces, though this cannot account for the effect the suspension wakes have on more downstream components.

**Table 8.2:** Comparison of upstream wake effect on drag and downforce coefficients (based on reference area of $1.5m^2$ full scale) of vehicle body with a $x = 1.0L_C$ separation, compared to isolated vehicle.

| | $C_D$ | $\Delta$ | $C_L$ | $\Delta$ | $C_{LF}$ | $\Delta$ | $C_{LR}$ | $\Delta$ |
|---|---|---|---|---|---|---|---|---|
| Experimental - BBWG | 0.278 | -0.096 | -0.712 | +0.438 | -0.304 | +0.183 | -0.407 | +0.261 |
| CFD - Upstream Vehicle | 0.177 | -0.127 | -0.337 | +0.509 | -0.145 | +0.258 | -0.193 | +0.252 |
| CFD - BBWG | 0.199 | -0.105 | -0.439 | +0.407 | -0.158 | +0.244 | -0.281 | +0.163 |
| CFD - Imposed Wake | 0.178 | -0.126 | -0.327 | +0.519 | -0.158 | +0.244 | -0.169 | +0.275 |

As with the isolated vehicle, measured force coefficients are lower for the computational cases than the experimental, by $28\%$ to $36\%$ on $C_D$ and $38\%$ to $54\%$ on $C_L$ depending on the CFD case. The effect of the upstream wake is also greater in the CFD cases than in the wind tunnel, possibly as the CFD vehicle wake is slightly less diffuse than the experimental vehicle wake (figure 8.1), which is itself less diffuse than the experimental wake generator wake. The exception to this is the change of downforce in the CFD with upstream bluff body wake generator case, which is $\Delta C_L = 0.1$ lower than the upstream vehicle. Most of this difference occurs in the change of downforce acting on the rear axle ($\Delta C_L = 0.09$). For all cases the aerodynamic balance remains biased towards the rear of the car, i.e. $-C_{LR} > -C_{LF}$ by between $0.01 < \Delta C_L < 0.12$. The effect on the aero-balance is not the same for all cases though, with the upstream vehicle and upstream bluff body CFD cases experiencing a greater loss of downforce on the front axle, i.e. the aero-balance moves rearward (table 8.3), while the aero-balance shift is forwards for both experimental and imposed wake cases.

**Table 8.3:** Effect of upstream wake with an $x = 1.0L_C$ separation on body aero-balance ($\frac{C_{LR}}{C_L}(\%)$), compared to isolated vehicle.

| | $\frac{C_{LR}}{C_L}(\%)$ | $\Delta$ |
|---|---|---|
| Experimental -BBWG | 57% | Forwards 0.9% |
| CFD - Upstream Vehicle | 57% | Rearwards 4.9% |
| CFD - BBWG | 64% | Rearwards 11.6% |
| CFD - Imposed Wake | 52% | Forwards 0.7% |

While examining the effect of the various upstream wake conditions from the CFD without wheel and suspension forces does indicate a better correlation to the experimental results, the effect of the wake is still greater in the computational domain. This could be related to the lower magnitude tip vortex emanating from the rear wing endplates in CFD, figure 8.2, which results in lower magnitude secondary flows, meaning the wake is less diffuse with greater axial velocity and stagnation pressure deficits at front wing height for the trailing car.

## 8.2 The Effects of Wake Axial Velocity Deficit and Up-Wash on a Downstream Vehicle

The effect of an upstream wake has been quantified for numerous vehicle spacings, using both CFD and wind tunnel methodologies, and is shown to be a reduction of drag and most importantly downforce. The effect of different wake features have also been investigated by removing or varying their magnitude in CFD simulations. In this section the effect of wake up-wash and velocity deficit in the wake on the downstream vehicle are quantified and discussed.

As the most forward geometry on the car, the front wing is easiest to consider in isolation, as subsequent surfaces are affected by the wake from the front wing. A first principals analytical approach is adopted to identify which, if any, of the key features in the wake is most responsible for the downforce loss experienced by the trailing vehicle.

### 8.2.1 Theoretical Effect of Changing Wing Incidence

Up-wash in the wake of the upstream vehicle will serve to reduce the effective incidence of the front wing on the downstream vehicle, figure 8.3. Calculating the effect of up-wash on the effective wing incidence is simply a task of determining the angle of the up-wash velocity vector $\left(\frac{u_Z}{u_X}\right)$ immediately upstream of the front wing (figure 8.3b). For this analysis wake data from the wind tunnel is used so that the results can be compared to the measured effect on front wing downforce, from the integral of front wing pressures collected with the upstream wake generator.

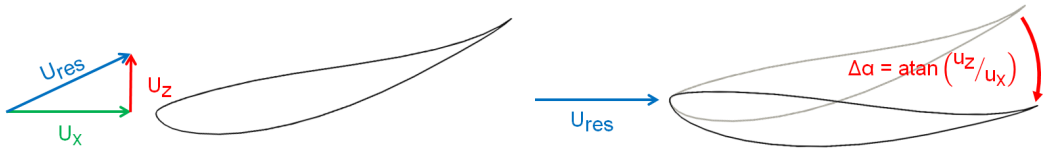


**(a)** Wake velocity vectors. **(b)** Effective incidence.

**Figure 8.3:** Effective change of incidence resulting from wake up-wash.

As the pressure tappings are only present up to $0.7c$ on the front wing mainplane, and not on the flaps, the effect of wake up-wash on downforce produced on the front wing centreline, where the flaps are not present, is easiest to infer. The wake up-wash vector was measured from the centreline wake plane (figure 4.15b) using a series of 1D slices the same height as the front wing. While the up-wash across the front wing span was measured using 2D boxes the height and width of the front wing, imposed on the wake YZ planes (figure 4.21). While taking measurements of the isolated wake ignores the effect of the front wing and nose on the wake, again the purpose is not to determine exact $\Delta C_L$ values, but to approximate the

comparative effects of up-wash and velocity deficit.

The change of incidence due to the up-wash on the wake centreline increases as the vehicle separation is reduced (figure 8.4) from $\approx 3°$ at $x = L_C$ up to $\approx 20°$ as at $x = 0.4L_C$ (depending on vehicle posture). Using the non-dimensional wake up-wash ($\Delta\alpha = ATAN\frac{u_Z}{U_\infty}$), to isolate the effect of up-wash from the axial velocity component of wake incidence, halves the peak change of incidence due to the wake centreline, peaking at $\sim 9°$ at $x = 0.4L_C$. In reality the axial velocity deficit in the wake increases the angle of the wake incidence, especially near the rear of the upstream car, where velocity deficit is greatest. From this it is clear is that the effect of wake up-wash would become a smaller part of the total downforce loss if the axial velocity in the upstream wake is increased, so going forward the effect of wake up-wash is considered independently of axial velocity deficit.

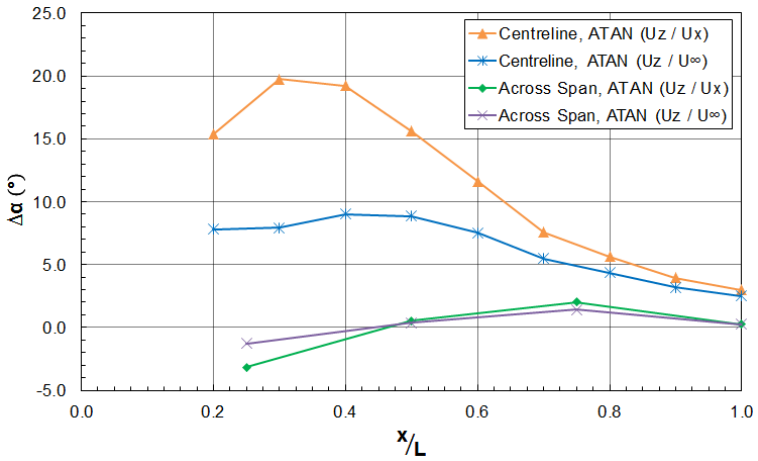


**Figure 8.4:** Effective change of wing incidence due to wake up-wash.

The effect of up-wash is not constant across the front wing span, figure 8.5. While a strong wake up-wash is present on the car centreline, and would have the effect of reducing the effective incidence; towards the front wing tips $\Delta\alpha$ is both in the opposite direction and of greater magnitude than the centreline up-wash. Averaged across the whole span, the effect of up-wash on incidence is significantly lower, figure 8.4, and is even a net up-wash below $x \approx 0.45L_C$.

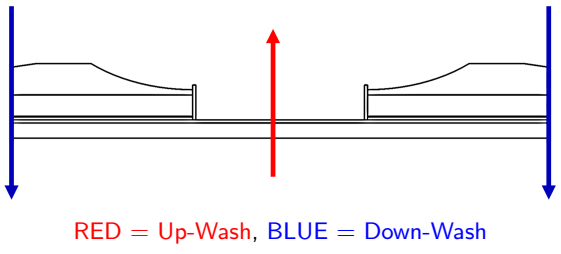


**Figure 8.5:** Approximate change of effective incidence across front wing span (axially aligned).

For the purpose of this analysis the change of downforce from the change of incidence (in radians) will be

approximated from the lift slope ($a$) of a thin aerofoil with elliptical lift profile,

$$\Delta C_L = a\,(\Delta\alpha), \tag{8.1}$$

where,

$$a = \frac{a_\infty}{1 + \frac{a_\infty}{\pi\lambda}}, \tag{8.2}$$

and $a_\infty$ is the infinite lift slope which is assumed to be $2\pi$. For this analysis the wing is also assumed to be operating in the linear region of the lift to incidence slope ($\alpha = 0°$ relative to the car reference plane).

As would be expected the effect of the centreline wake up-wash is to reduce front wing downforce (figure 8.6). The centreline force loss due to incidence roughly follows the measured trend of the front wing, reducing as the separation is reduced to $x = 0.4L_C$ before plateauing. Peak downforce loss is $-0.7$ on $-C_L$, or $\sim 65\%$ of the measured loss. Across the span, the effect of the vertical component of velocity in the wake is very small, reducing downforce up to $x \approx 0.45L_C$, closer than which downforce is increased, albeit only by $-C_L = 0.1$.

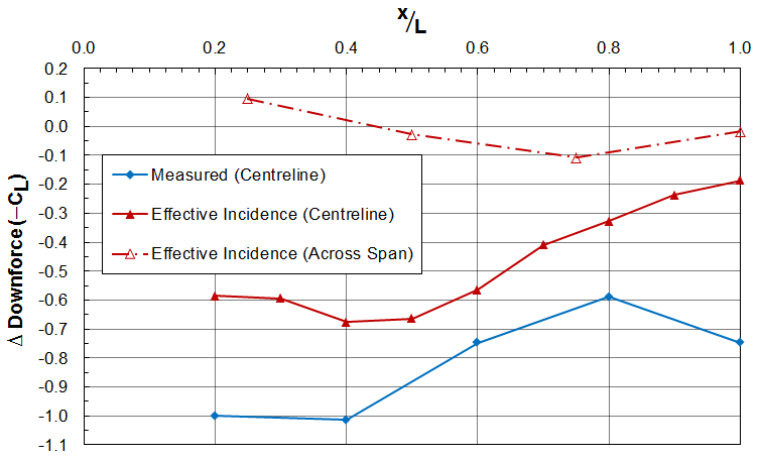


**Figure 8.6:** Comparison of measured $\Delta C_L$ (posture $= 2mm, -1°$) in wake and effect of wake up-wash on front wing $C_L$.

While wake up-wash will have the effect of reducing downforce generated by the front wing of the downstream vehicle, it is not the only cause of force loss and will predominantly be concentrated on the centreline of the upstream vehicle. The outboard extremes of the wing are subject to down-wash, increasing the effective incidence and therefore theoretically generating greater downforce. This analysis does not take into account the effect of cross-flow ($u_Y$) in the wake, which as it is strongest at front wing height, and would serve to reduce the efficiency of the wing either side of the upstream wake centreline.

### 8.2.2 Theoretical Effect of Wake Axial Velocity Deficit

The effect of the upstream wake is to reduce the magnitude of loading on both the upper and lower wing surfaces, figure 8.7, even at the stagnation point where $C_P << 1$. While reducing wing incidence would be expected to "detune" the wing by reducing loading, pressure at the stagnation point would remain $C_P = 1$, even if shifted around the chord. There must therefore be a different mechanism of loss besides wake up-wash. The other wake variable whose effect it should be possible to quantitatively estimate is the axial velocity deficit.

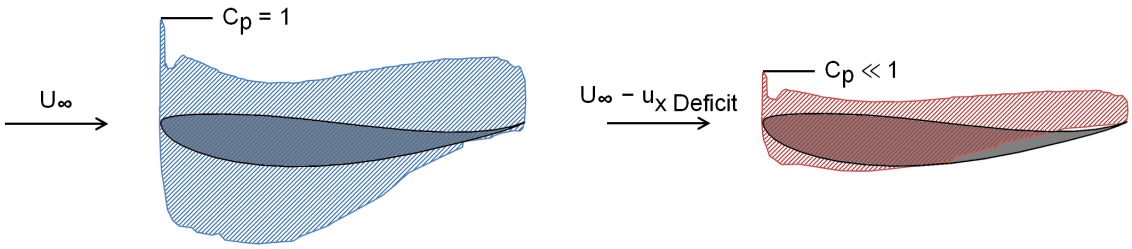


**(a)** Isolated car. **(b)** Upstream vehicle.

**Figure 8.7:** Effect of upstream vehicle wake ($x = L_C$) on front wing centreline mainplane pressure distribution, from CFD.

As the section downforce coefficient can be calculated by

$$C_L = \frac{1}{c}\int_0^{x=c} (C_P)dx,$$

the effect on front wing downforce from the reduced surface pressure due to the wake is dramatic. ${}^{C_L}/_{C_{Lo}} = 65\%$ (where $C_{Lo}$ is the baseline downforce level) on the centreline at $x = L_C$, reducing to just ${}^{C_L}/_{C_{Lo}} = 3\%$ at $x = 0.4L_C$. Assuming the wake axial velocity deficit affects the chord-wise pressure distribution of the wing uniformly. If the static pressure coefficient is

$$C_P = 1 - \left(\frac{u}{U_\infty}\right)^2,$$

then the change in pressure, and therefore downforce, experienced by the front wing mainplane, resulting from the velocity deficit in the wake, can be approximated by

$$C_P{}' = 1 - \left(\frac{u}{U_\infty - u_{X\ Deficit}}\right)^2, \tag{8.3}$$

where $u$ is the velocity at any given point on the wing.

Like the estimated wake up-wash effect on wing downforce (figure 8.6), the wake centreline axial velocity deficit effect on the front wing mainplane follows the same trend as the measured $\Delta - C_L$ with reducing axial separation, figure 8.8. The effect of axial velocity deficit is much closer to the measured effect,

$0.1 < \Delta - C_L < 0.2$. While only an estimate of relative effects of axial velocity and up-wash it is easy to see that the wake velocity deficit plays a larger role in the force loss experienced by the front wing in ground effect of a Formula 1 car, peaking at $\sim 90\%$ of the measured $\Delta C_L$. Unlike the effective incidence, averaging the axial velocity deficit across the wing's span does not significantly alter the theoretical effect of the velocity deficit, remaining within $-C_L \sim 0.3$ of the centreline effect.

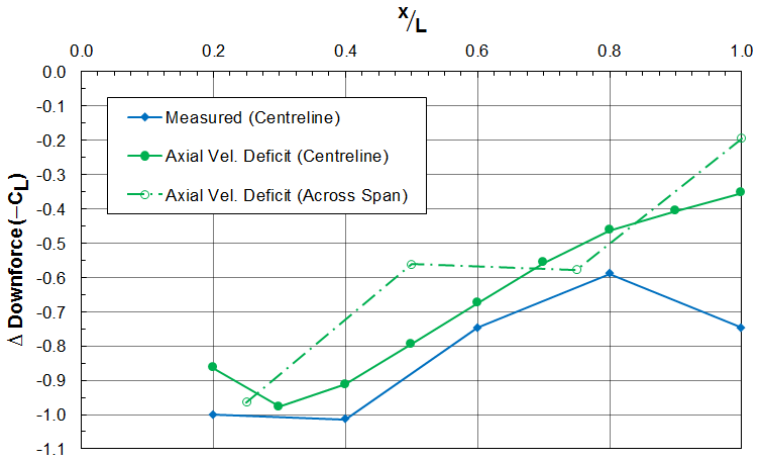


**Figure 8.8:** Comparison of measured $\Delta C_L$ (posture $= 2mm, -1°$) in wake and effect of axial velocity deficit on front wing $C_L$.

### 8.2.3 Theoretical Effect of Wake on Surface Pressure Distribution

In the preceding text the effect of relative incidence and velocity deficit in the upstream wake is considered with regard to the effect it has on the force generated by the front wing. The different features in the wake will have contrasting effects on the wings pressure distribution, where the the total change in pressure is a function of the effects of static ($P$) and dynamic ($q$) pressure deficits, and wing incidence ($\alpha$),

$$\Delta C_P = fn(\delta P, \delta q, \delta \alpha). \tag{8.4}$$

It has previously been noted (figure 8.7) that the pressure at the stagnation point is reduced. Static pressure deficit would result in a translation of the pressure distribution on the $C_P$-axis, figure 8.9 (red line); which will reduce pressure at the stagnation point, though downforce generated by the wing will be unaffected as the integrated region remains constant. Dynamic pressure deficit (blue line, figure 8.9) will compress the pressure distribution towards $C_P = 0$, reducing the stagnation pressure, while also reducing loading on the suction surface. The effect of up-wash is harder to quantify; though the effective reduction of incidence of the wing should reduce peak loading on the suction surface.

As the effect of the wake is to squeeze the pressure distribution of the wing, thereby reducing downforce, the effect of dynamic pressure deficit in the wake was investigated. The velocity deficit in the wake was measured on the centreline and at quarter span, at front wing height and one car length behind the car; by

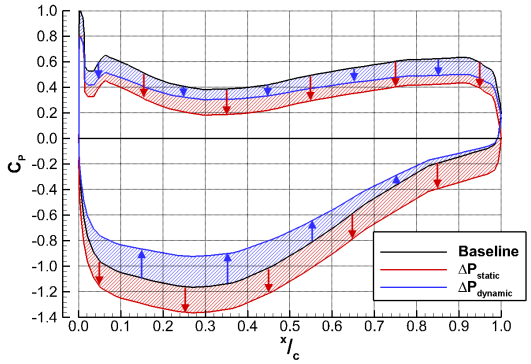


**Figure 8.9:** Theoretical effect of static (red) and dynamic (blue) pressure deficits on front wing pressure distribution resulting in identical stagnation pressure deficit.

measuring the wake of the isolated car the effect the downstream vehicle has on the onset flow is ignored. However, on the centreline pressure distribution, figure 8.10a, the measured stagnation point pressure drops by $\approx 50\%$, which is consistent with the effect of dynamic pressure deficit. The upper surface of the front wing is also well matched between the measured and the theoretical effect of dynamic pressure deficit. The lower surface, scaled by dynamic pressure deficit, remains at a slightly lower pressure over the chord than the measured distribution; it is assumed that this is due to the effective reduction of incidence due to wake up-wash, which is strongest on the wake centreline. Integrating the pressure over the chord the measured effect of the wake on the front wing downforce is $\Delta C_L = +0.67$; the reduction of downforce due to dynamic pressure scaling is $\Delta C_L = +0.61$, so the effect of up-wash must be $\Delta C_L = +0.06$, or $\sim 10\%$ of the of the dynamic pressure effect.

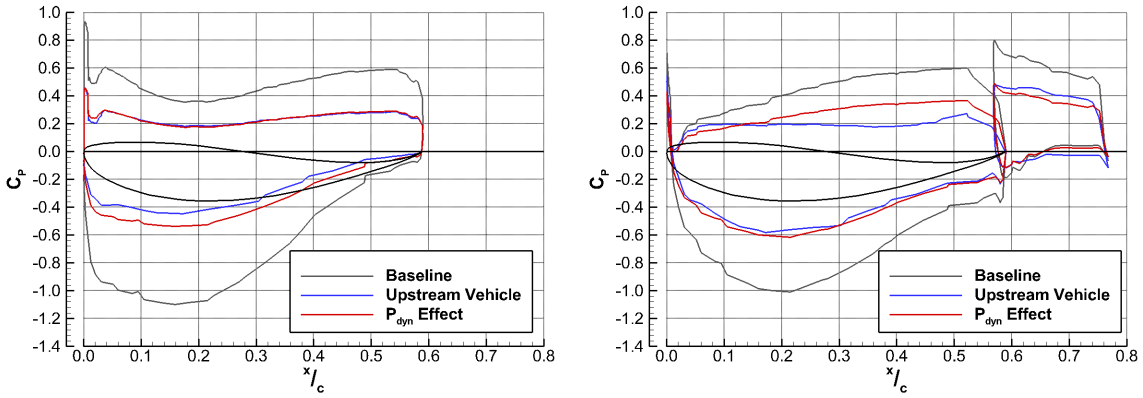


**(a)** Front wing centreline. **(b)** Front wing quarter-span.

**Figure 8.10:** Comparison of measured pressure distribution at one car length separation and effect of dynamic pressure deficit scaling on front wing pressure from CFD.

At the quarter-span, figure 8.10b, the onset dynamic pressure is higher, as the velocity deficit is concentrated on the centreline, so the stagnation point is only $33\%$ lower than the isolated distribution. The lower surfaces (both mainplane and flap) are very similar between scaled and measured pressure distributions; if the difference on the lower surface on the centreline is due to wake up-wash it is reasonable to infer that the similarity at quarter-span is that up-wash away from the wake centreline is negligible, or even

down-wash (figure 8.5). Where the centreline and quarter-span lower surface pressure distributions with an upstream wake are the same shape, the upper surface of the quarter-span is not, leading to a disparity in the measured and dynamic pressure deficit scaled pressure distributions, between $0.2c < x < 0.6c$.

Applying dynamic pressure scaling to the whole surface of the car, figure 8.11, shows the extent to which dynamic pressure affects the downstream vehicle. Scaling is based on the growth of dynamic pressure across the car in the y-direction, from the centreline, at wheel axle height,

$$\frac{q}{q_\infty} = 1.939\,|y| + 0.515. \tag{8.5}$$

This linear growth is only representative of the "stem" region of the "mushroom" shaped wake, so the effect of dynamic pressure scaling on the rear wing surface pressure is smaller than the actual wake. Of the geometry under the "mushroom cap" portion of the wake, the front wing, and underbody with rear diffuser, dynamic pressure scaling produces a $\Delta C_P$ which is notably close to the measured effect of the wake.

It is clear from the front wing and surface pressure distributions that the scaling effect due to dynamic pressure deficit is the primary cause of downforce loss experienced by the following vehicle.

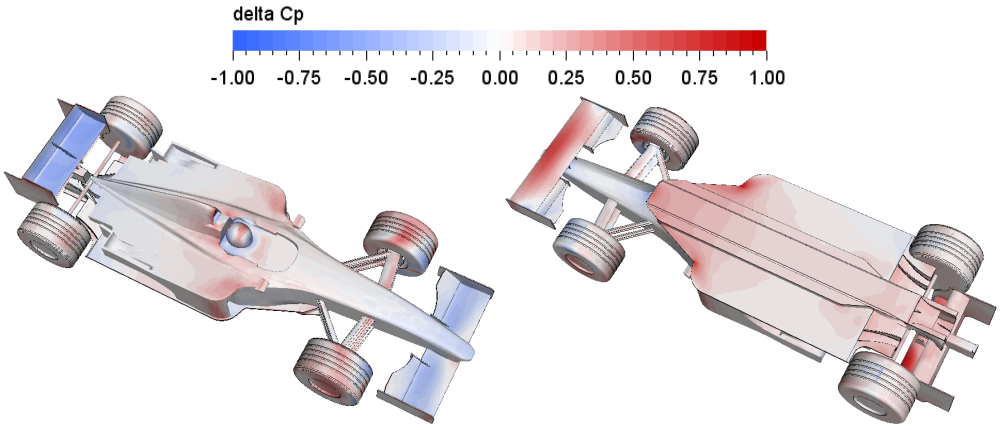


**(a)** Upstream vehicle wake.

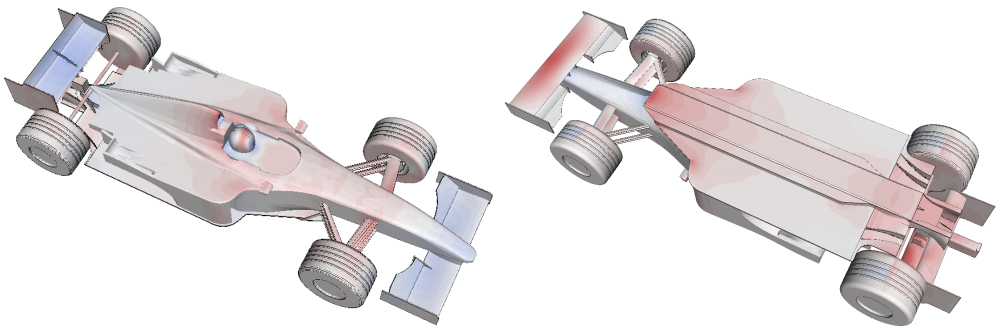

**(b)** Dynamic pressure deficit scaled.

**Figure 8.11:** Surface $\Delta C_P$, compared to isolated vehicle.

## 8.3 Front Wing Vortex System

Arguably the primary function of a Formula 1 car front wing is to generate downforce, a modern F1 front wing generates between $25-30\%$ of the vehicle's total downforce [12, 11] ($40\%$ for this $25\%$ F1 model). The front wing's wake also affects the downstream surfaces of the car, so the secondary function of the front wing is to set up a series of desirable flow structures to minimize it's negative effect. The most important interaction is with the front wheels, whose wakes will naturally pass under the body reducing dynamic pressure under the car [18] and consequently rear end downforce.

On a modern Formula 1 car the regulations regarding front wing span place the tips of the wing somewhere in front of the front tyres [58]. Pre-2009 the wing endplate was closer to the inboard face of the front wheels so a strong and stable tip vortex (figure 8.12) was desired to merge with the vortex shed from the lower inboard face of the tyre [18, 23], maintaining the position of the vortex as it travelled downstream and preventing the low dynamic pressure tyre wake from passing under the floor.

RED $=$ Positive $\Omega_X$, BLUE $=$ Negative $\Omega_X$

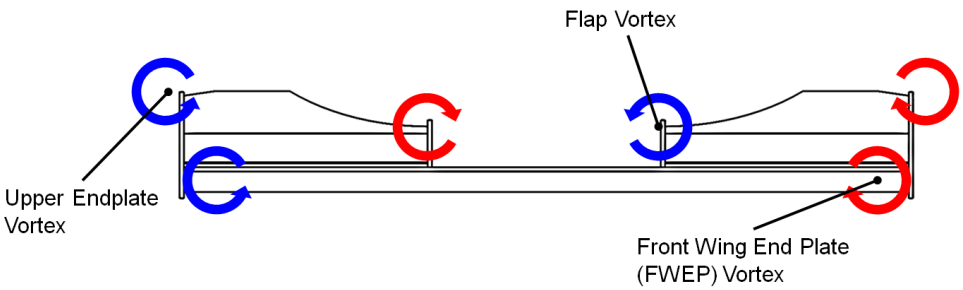


**Figure 8.12:** Freestream front wing vortex system.

Post-2009 the endplates of the front wing are closer to the outboard face of the tyres, while the centre $500mm$ span is defined as a neutral section. The unloaded central section resulting in a sharp discontinuty in the pressure distribution and a strong vortex being shed from the inboard edge of the flaps. As the wing tip vortex interacts with the outboard vortex shed from the tyre [3], instead the inboard vortex (the same approximate location as the flap vortex in figure 8.12) is used in conjunction with barge-boards and turning vanes to divert the inner tyre vortex away from the underbody. The front wing loss resulting from the upstream wake is not just limited to downforce loss, but disruption of the vortex system, which will have a knock-on effect as the modified front wing wake travels down the car.

Due to the simple nature of the front wing on the generic $25\%$ Formula 1 car, especially in the region of the endplates, the vortex structures are not as well defined as might be desired to aid downforce for the rest of the car, figures 8.13a and 8.14a, though are clearly present in the wake of the front wing; namely (1) the main wing tip (FWEP) vortex, (2) a co-rotating to the FWEP, upper endplate vortex, and (3) the inner flap vortex.

The effect of an axially aligned upstream vehicle, at $x = L_C$, on the wake of the front wing is shown in figure 8.13b, the wake of the front wing is noticeably lower energy than the baseline case, especially near the centreline for the reasons previously discussed. The flap vortex, despite being close to the wake centreline, remains intact, though with a slightly lower magnitude of stream-wise vorticity (figure 8.14b), this will be due to the reduction of peak static pressure on upper and lower surfaces. The main endplate vortex also remains and is as strong or even stronger than the baseline case, despite the onset wake. However, the upper endplate vortex completely disappears, resulting to a higher pressure on the front face of the tyre. The upper endplate vortex is the result of high static pressure on the top surface of the flaps moving to the lower pressure on the outer face of the endplate. As the upstream wake reduces static pressure on the upper surface of the flaps (figure 6.11b) but not on the outer face of the endplate (which is $C_P \approx 0$ in baseline conditions) the pressure difference could be equalized such that the vortex does not form. It could also be that the upper endplate vortex is disrupted by the cross-flow ($u_Y$) from the wake, which is strongest acting towards the wake centreline at front wing height, possibly why the FWEP vortex remains strong despite reduced pressure under the wing.

When the cars are offset by $y = 0.5W_C$ the disruption to the front wing wake becomes more complex, figures 8.13c and 8.14c. As the $Y+$ side of the wing is away from the wake centreline, the main and flap vortices are as strong as the freestream case, however the upper endplate vortex is slightly weakened. This lends some credence to the explanation that wake cross-flow also plays a part in disrupting the formation of this vortex, while the FWEP vortex could be shielded by the endplates. On the $Y-$ side of the wing, the flap vortex is strengthened, despite being closer to the wake centreline than the aligned case. The strength of the FWEP and upper endplate vortices are significantly reduced, primarily due to the proximity to the wake centreline, and the associated loss of loading on the wing.

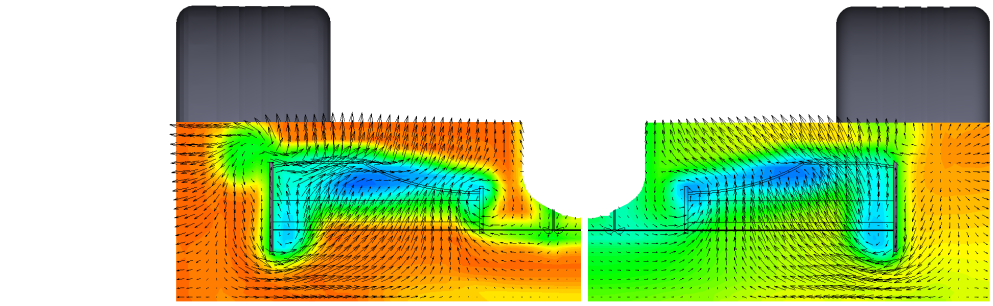

**(a)** Isolated car. **(b)** Upstream vehicle at $x = L_C, y = 0$.

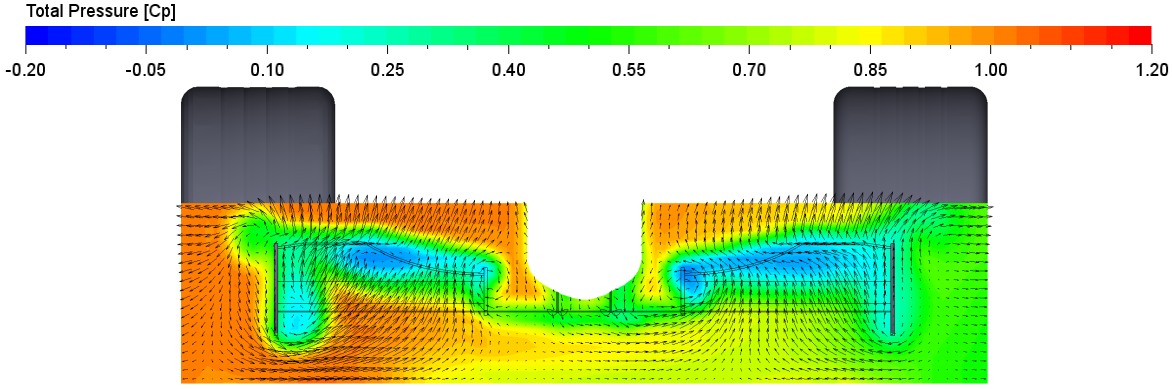


**(c)** Upstream vehicle at $x = L_C, y = 0.5W_C$.

**Figure 8.13:** Effect of upstream Vehicle on total pressure ($C_{Po}$) in front wing wake ($YZ$ plane at rear face of wing endplates).

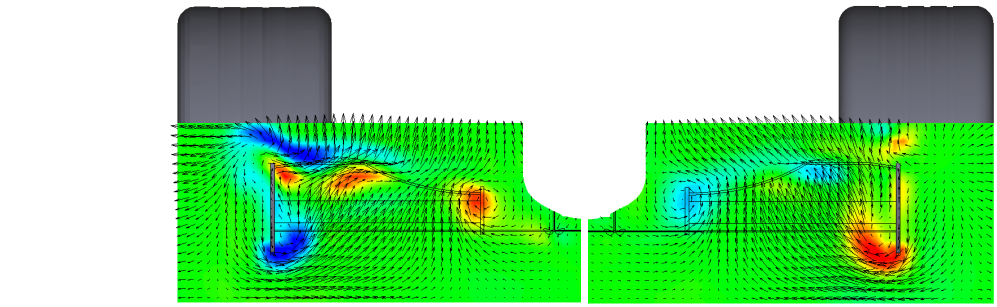

**(a)** Isolated car. **(b)** Upstream vehicle at $x = L_C, y = 0$.

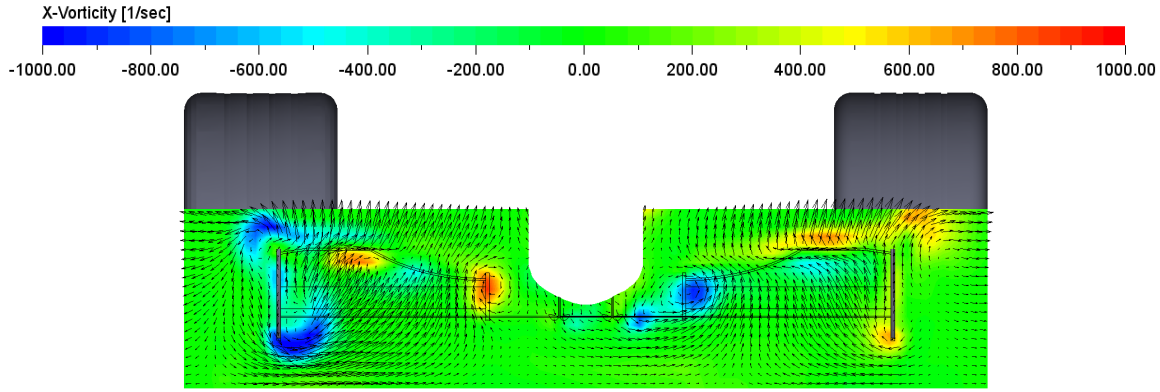


**(c)** Upstream vehicle at $x = L_C, y = 0.5W_C$.

**Figure 8.14:** Effect of upstream vehicle on streamwise vorticity ($\Omega_X$) front wing wake ($YZ$ plane at rear face of wing endplates).

# Chapter 9

# Concluding Remarks

At the beginning of this thesis two key objectives were set out:

1. To measure the effect of the wake of an upstream vehicle on a following vehicle.
2. To characterize the key features in the wake responsible for force loss and thereby propose aerodynamic regulations with reduced downforce loss with an upstream vehicle wake.

Using a combination of experimental and CFD methodologies these objectives have been met, with the key findings of this research presented below.

## 9.1 Measured Effect of an Upstream Vehicle

### 9.1.1 Isolated Vehicle Set-up

The aerodynamic forces and surface static pressure distribution of a generic 25% scale Formula 1 car, featuring front and rear wings and a flat underbody with upswept rear diffuser, have been measured experimentally and computationally over a wide range of vehicle ride heights and incidences. Peak aerodynamic forces were lower than would be anticipated for a vehicle of this design, eg: $C_{L\,max} = -1.2$ and $C_{D\,max} = 0.77$, this is partly due to the model scale; tests were performed at a Reynolds number of $2.05 \times 10^6$, which is an order of magnitude lower than a full scale car travelling at a representative velocity, $U_\infty = 216kph = 135mph$. The generic nature of the model means that aerodynamic loading of aerofoil and underbody elements is not as developed as a contemporary Formula 1 car, which given time and resource could be improved. Despite the low total force, the car is well balanced, with $\approx 60\%$ to $65\%$ of the total downforce acting on the rear axle.

### 9.1.2 Vehicle Wake

The wake of the 25% Formula 1 car is dominated by the rear wing counter-rotating vortex pair, which due to the relatively low aspect ratio of the wing, interact to create a strong centreline up-wash. The vortex pair is coupled with a large region of stagnation pressure deficit, with local peaks below $C_{Po} = -0.15$ at $x < 0.1L_C$ downstream of the car. $C_{Po}$ in the wake, at $x = 0.1L_C$ behind the car, is less than 0.5 over much of the projected area of the car and extends above the rear wing as the wake grows downstream, to $z = 1.5H_C$ by $x = 0.75L_C$ behind the car. Static pressure deficit in the wake is relatively low magnitude, and confined to the rear wing vortex cores so the majority of the total pressure deficit is dynamic from the axial velocity deficit. As the wake progresses downstream the velocity deficit in the wake is swept to the car centreline near the ground by the rear wing vortex pair, which is constrained by the ground plane. Higher in the wake, the velocity deficit circulates the vortex cores, forming a 'mushroom' shaped wake.

### 9.1.3 Alternative Means of Generating Upstream Vehicle Wake

The effect of an upstream vehicle wake was measured using a number of different methods at multiple inter-vehicle separations:

1. A short axial length bluff bodied wake generator, placed upstream of the instrumented vehicle both in the wind tunnel and in CFD. Tests were conducted for axial separations between $0.2L_C < x < 1.0L_C$ and lateral offsets up to $y = 0.75W_C$, also at $(x, y) = (L_C, 0)$ in CFD.
2. The effect of the wake of an identical upstream 25% Formula 1 car was measured. This method produces the most accurate representation of an upstream vehicle wake, though can only be performed in CFD without compromising model scale. The effect of the upstream vehicle was tested for axial offsets of $x = L_C$ and $x = 2L_C$, and for a lateral offset of $x = 0.5LW_C$ at $x = L_C$.
3. The wake of the 25% Formula 1 car was recreated using the inlet boundary conditions of CFD cases. This method was only performed to simulate a $x = L_C$ separation, but showed good correlation to the full vehicle study.

Bluff bodied wake generators have been used previously to recreate the wake of a Formula 1 car, with varying accuracy. The wake generator used in this study measures just $0.2L_C$ in length, allowing axial separations up to $x = L_C$ to be achieved in a conventional length wind tunnel working section, greater than previously published. Despite the shortened length the wake generator recreates the wake with relatively high accuracy, reproducing the rear wing counter-rotating vorticity and localized regions of stagnation pressure deficit, most of which results from a dynamic pressure deficit. The wake is most accurate beyond $x = 0.2L_C$ downstream of the wake generator, with the very near wake dominated by the exposed wheel

wakes. While the wheels are rotated by the moving ground plane, they are not shadowed by upstream geometries, as is the case on the full vehicle rear wheels, resulting in a larger wheel wake.

Another method of simulating an upstream vehicle wake was defined by using the inlet boundary conditions to impose the wake parameters has been detailed. The imposed wake was created by sampling the wake behind the vehicle using a uniform $10 \times 10mm$ grid of up to $100,000$ points, each with a y, z coordinate, x, y & z aligned velocity vectors, static pressure, and in some cases a time co-ordinate. The wake was sampled at $x = 0.25L_C$ behind the vehicle to ensure any reversed regions had closed, while also allowing the wake to be more structured. The vehicle was placed $x = 0.75L_C$ behind the inlet to create a $x = L_C$ simulated vehicle separation. The downstream progression of the imposed wake was very similar to the real vehicle wake, despite some differences on the inlet plane caused by the grid resolution exceeding voxel resolution.

### 9.1.4 Effect of Upstream Wake

#### 9.1.4.1 Axially Aligned

The effect of the upstream vehicle is to reduce forces generated by the vehicle, up to $0.8\,(67\%)$ on $-C_L$ and $0.22\,(29\%)$ on $C_D$ at very close axial separations ($x = 0.2L_C$). The force loss experienced by the downstream vehicle reduces as the axial spacing between the vehicles is increased, $\Delta C_L \approx +0.45$ and $\Delta C_D \approx -0.16$ at $x = L_C$, but is not linearly correlated to the axial separation with the rate of downforce and drag losses increasing as the separation is reduced. There is good agreement in the change of force measured from the wake generator in the wind tunnel and a full upstream vehicle in CFD.

The upstream wake affects peak loading on both high and low pressure regions on the wings and body, in particular the low pressure regions on the lower surfaces of the front (particularly on the centreline) and rear wings, the front of the underbody, and the rear diffuser. Interestingly the effect of the wake on downforce appears to be smaller on the front wing ($\delta C_L = +0.15$) than either the rear wing or body ($\delta C_L = +0.18$) at $x = L_C$, despite the car's aerodynamic balance shifting towards the rear axle by up to $\frac{C_{LR}}{C_L} = 37\%$, mainly due to the front region of the floor losing more downforce than the rear diffuser.

#### 9.1.4.2 Lateral Offsets

The introduction of even a small lateral offset allowed vehicle forces to recover more swiftly than an equivalent increase of the axial separation, especially downforce which is equal to the isolated case for all downstream separations tested at $y = 0.75W_C$. The greater rate of recovery on downforce than drag means that outboard of $y = 0.5W_C$ the lift-to-drag ratio of the car is improved from the baseline.

The greatest effect of the upstream wake on vehicle surface pressure is aligned to the upstream wake centreline, which is particularly noticeable on the front wing. Where the pressure increase on the suction surface of the front wing centreline is greater than towards the tips in the axially aligned cases, the peak loss moves across the span with the lateral offset. The most outboard set of pressure tappings on the front wing in the experiments, at $y = 0.75W_C$, even generates more downforce in the wake than the baseline case.

The recovery of downforce for the trailing vehicle with only a small lateral offset indicates that following and overtaking could be made easier if drivers could corner with an offset to the car ahead. At this time on most Grand Prix circuits drivers will only use a single narrow line, known as the 'racing line', which is the fastest route through a corner. The build up of rubber in the track surface from numerous cars repeatedly driving on the racing line, increases adhesion making the racing line ever faster through the course of a Grand Prix weekend. Build up of tyre and car debris off the racing line, known as 'marbles', increase the lap-time deficit when driving 'off-line'. Admittedly such analysis of tyre and circuit behaviours are external to the purview of the aerodynamicist.

#### 9.1.4.3 Sampled Wake

The method of imposing the wake on the inlet of CFD cases showed good correlation to the upstream vehicle case at the same axial offset, both on total force reduction of the vehicle, and the change of the surface pressure distribution. Wake unsteadiness was shown to be important as downforce loss was greater when using the wake as sampled from the same time averaged output frame used for force measurements. Using a series of shorter time frames, which were looped throughout the simulation to capture wake unsteadiness, improved correlation to an upstream vehicle wake. It would be difficult to infer from the results presented in this thesis that reducing wake unsteadiness would be detrimental to the following vehicle, though this could prove an interesting avenue for further exploration.

## 9.2 Key Wake Features Responsible for Force Loss

### 9.2.1 Key Wake Features

The method of imposing the wake on the inlet plane of CFD cases allowed the wake variables to be adjusted without the necessity to modify the upstream vehicle surfaces. Initial tests independently removed axial velocity deficit and secondary flows from the wake. Removing the axial velocity deficit from the wake resulted in a small reduction of the drag and downforce losses experienced by the downstream car. When the secondary flow field was removed from the wake, the reductions of $C_D$ and $C_L$ increase relative to the

baseline wake. This is because the secondary flows have a considerable impact on the propagation of the wake, by diverting the low velocity regions of the wake to the wake centreline, then upwards to surround the rear wing tip vortex cores.

The secondary flow field proved to be the easiest to manipulate in isolation and so was scaled by $\pm 10\%$ to test sensitivity. While changing the secondary flow field did not have a monotonic effect on total vehicle force, there was a trend of increasing downforce loss with reduced secondary flow intensity, and conversely reduced downforce loss with increasing secondary flows. Interestingly increasing secondary flows also reduced the axial velocity deficit in the wake, especially on the centreline, indicating that the secondary flow intensity also has a beneficial effect on wake decay.

To determine how downforce generated by the rear wing and underbody affect up-wash in the wake, the wake momentum equations were applied in the flow field around the car. The surprising result is that the average vertical velocity in the wake is a net down-wash, especially when considering the centreline up-wash. The integrated pressure on the ground plane is also as great as, if not greater than, total downforce. Using a design of experiments approach to respectively alter the proportion of vehicle downforce generated by the rear wing and underbody showed that wake up-wash can be increased by increasing the fraction of car downforce generated by the rear wing. Likewise net wake up-wash is reduced when the underbody downforce fraction was increased.

### 9.2.2 Wake Variable Effect on Car Forces

The effect of wake up-wash and axial velocity deficit were considered using a theoretical approach. The front wing is the easiest to infer the effect of the wake, as subsequent geometries will be affected by the modified front wing wake. While the centreline wake up-wash has the effect of reducing effective incidence and downforce from the front wing, more of the front wing span is subjected to wake down-wash (increased incidence), especially with lateral offsets to the upstream vehicle. The effect of wake up-wash on effective incidence is also diminished when the wake axial velocity deficit is reduced or removed.

The key variable in the wake appears to be the axial velocity/dynamic pressure deficit, which scales the vehicle surface pressures by the reduction of stagnation pressure (total head), effectively detuning the downforce generating surfaces. On the front wing, dynamic pressure deficit accounts for up to 90% of the measured loss in the wake. Unlike wake up-wash, axial velocity deficit affects the entire span of the front wing, though the effect is still concentrated on the wake centreline. Reducing the wake axial velocity deficit at car height should therefore be the primary objective of new regulations.This has been seen to be possible by increasing secondary flow intensity by increasing rear wing downforce and reducing underbody downforce, while reducing baseline vehicle body and rear wheel drag would also be beneficial.

# Chapter 10

# Recommendations and Future Work

## 10.1 Proposal For a set of Aerodynamic Regulations

The following section presents a proposal for a set of new regulations, based on the findings of this research, with the aim of minimizing the effect of an upstream vehicle wake.

### 10.1.1 Key Conclusion from this Research

The key conclusion to be taken from this research is the importance of wake up-wash, especially from the rear wing, in reducing the impact of the wake on the forces generated by a downstream vehicle. Increasing wake up-wash, using CFD to alter the level of secondary flow, reduced the axial velocity and stagnation pressure deficits at the height of the downstream vehicle's front wing. Reducing the underbody downforce level, by increasing the vehicle ride height, also resulted in increased wake up-wash. Underbody downforce can be reduced by increasing vehicle ride height, reducing the floor's planform area, or the size of the rear diffuser. The experimental study in this thesis has also shown that the underbody is less susceptible to downforce loss in the wake when the car posture is nose down, i.e. the rear ride height is greater, though the underbody produces slightly less total downforce in this condition. While the underbody is a relatively efficient source of downforce compared to the rear wing, it does appear to negatively affect the downstream vehicle.

In order to minimize the effect of the upstream wake on a following vehicle the key changes to the vehicle geometry should be:

1. To increase wake up-wash through a reduction of underbody downforce, and corresponding increase of rear wing downforce.

2. To maintain downforce levels and aerodynamic balance, such that they are consistent with a contemporary Formula 1 car.
3. Allow greater freedom for upper body elements, especially around the rear wheels, to reduce the impact of the rear wheel wakes at front wing height for the downstream vehicle.

These proposals assume that the means of downforce on the vehicle will remain the same, namely a front wing in ground effect, an underbody with upswept diffuser, and a rear wing.

### 10.1.2 Proposed Aerodynamic Regulations

In order to achieve the targets set out above, a definition for the preliminary shape of the vehicle surfaces are set out.

**Vehicle Force Targets**

- Downforce, $-C_L \geq 4$ (Depending on circuit)
- Lift-to-Drag, $-{}^{L}/_{D} >> 4.5$
- Aero-balance, $60\% < \dfrac{C_{LR}}{C_L} < 70\%$ (Depending on vehicle weight distribution)
- Underbody Downforce, $C_L \approx 25\%$ of Total
- Rear Wing Downforce, $C_L \approx 50\%$ of Total

**Chassis**

The current Le Mans Prototype (LMP1 and LMP2) regulations [148] imposed a limit on the length of the vehicle; this is useful as a means of controlling the quantity of downforce generated by the underbody. The current Formula 1 regulations define an overhang, forward of the front axle of between $950mm$ to $1200mm$, with a rear overhang (aft of the rear axle) of $600mm$ to accommodate the rear impact structure. If vehicle length were limited to $4750mm$ then the wheelbase length, and therefore underbody length, becomes bounded, in this case between $2950mm$ and $3200mm$.

Since 1998 Formula 1 cars have had a total track of $1800mm$, experiments (Appendix F) adjusting the vehicle track to $2000mm$ have shown that increasing the total vehicle width both increases vehicle drag and the width of the velocity deficit close to the ground in the very near wake, which is has an important effect on downforce generated by the downstream vehicle front wing and underbody. However, moving the wheels away from the rear wing endplates increases wake vorticity and secondary flow intensity, expediting the decay of the velocity deficit downstream of the car.

It has been shown by that the rear wheel wakes significantly affect the downstream vehicle front wing and underbody, it is therefore desired that the bodywork regulations allow greater freedom, especially around the rear wheels. The optimal solution would include fenders around the rear wheels to close the wake more

efficiently, though this would go against the open-wheel tradition of Formula 1.

**Front Wing**

In 2009 the 'neutral' section was added to the centre of the front wing to mitigate front wing performance loss with an upstream wake. This study has shown that while the centreline of the front wing experiences the greatest $\Delta C_P$ when the cars are axially aligned, this shifts across the wing span with the centreline of the upstream vehicle. The neutral centre section is therefore causing a greater reduction of front wing downforce with a lateral offset, as only half the wing is capable of generating downforce.

One possible consideration would be the addition of a common front wing mainplane to replace the neutral section. A common rear wing mainplane is used in the recent Indycar regulations [149] as a means of limiting downforce. As it is desired that the front wing only produce $25\%$ of the total car downforce, generating a sufficient pressure loading is not problematic, but maintaining peak pressures with an upstream vehicle wake is. It could be that some aerofoil families lose less downforce with an upstream wake, which further and focussed testing could show.

The final proposal for the front wing is that the ground clearance be reduced to move it into a region of higher velocity flow. This is combined with the concept for the underbody, where increased ground clearance injects a region of higher velocity airflow in the vicinity of the ground plane.

**Rear Wing**

The rear wing wake has been shown to be important in diverting the wake of the car over a following vehicle, and reducing the wake velocity deficit. For this vehicle concept the rear wing is arguably the most important downforce generating surface, contributing at least half the total vehicle downforce. Rear wing downforce can be increased from current levels by increasing span, chord, or a combination of both. Increasing the wing span would have the added benefit of increasing aspect ratio, which would reduce induced drag, while increasing wake up-wash across the span; although the vortex interactions would be reduced. One potential solution would be to allow multiple slotted flaps on the rear wing, the flaps could be deployed from braking to acceleration zones in corners to increase downforce and wake up-wash, allowing the cars to follow. The flaps could then be retracted on straights to reduce induced drag, reducing wake up-wash and increasing the slipstream effect. This is similar to the DRS (Drag Reduction System) currently employed in Formula 1, though instead of being used as an overtaking aid would be deployable throughout the race weekend.

To decouple the rear wing from the underbody (and remove it from ground interactions) the height above the ground should be set as high as is reasonable, however, it is also desired that the wing interact with the car base and underbody wakes in order to divert it vertically.

**Underbody & Rear Diffuser**

Since the beginning of the 1995 season the underbody of Formula 1 cars have been split between a pair of parallel planes, the reference and step planes. The step in the floor is used to ensure that the majority of the floor remain at a moderate ride height ($h_{min} \geq 50mm$) to prevent the abrupt downforce loss experienced at very low ground clearances. The step plane creates a relatively bluff blockage under the car, contributing significantly to the centreline stagnation pressure deficit, especially near the ground. It is therefore desired that the step be removed, and a different means of controlling minimum ride height be sought.

Underbody downforce is a function of $\bar{C_P}$ and plan form area, so an alternative means of controlling the underbody downforce is to limit the permissible underbody area. It is assumed that an area of $3m^2$ is a reasonable limit for underfloor projected area, with a nominal ride height of $60mm$ measured between the ground plane and the reference plane, though testing is required to find definitive measurements.

Changing the downforce distribution of the car such that the rear wing generates twice the downforce of the floor would result in a significantly more rearward centre-of-pressure if the underbody design remained in it's current configuration. To balance the car, so that the rear axle carried $\approx 60\%$ of the total downforce, the diffuser kick needs to be moved forwards so that the underfloor centre-of-pressure is just aft of the centre of the wheelbase (figure 10.1, assuming a wheelbase of $3200mm$). The alternative is to prescribe a more rearwards centre-of-gravity, the FIA currently specify that $\approx 45\%$ of mass act on the front axle.

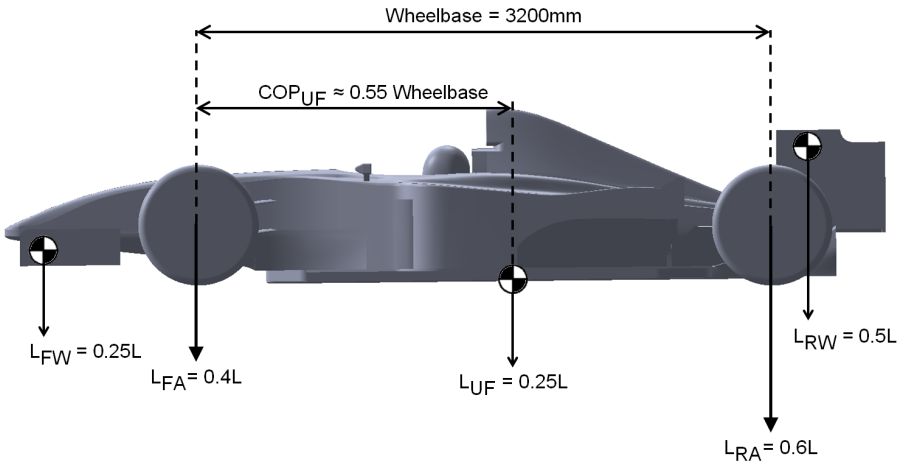


**Figure 10.1:** Target downforce values and approximate position of underfloor centre-of-pressure.

In the preceding text the underbody has been shown to be primarily responsible for the aero-balance shift experienced by the downstream vehicle. This is because the front suction peak experiences a greater loss of loading than the suction peak at the diffuser throat. Altering the underbody so that only a single suction peak occurs, using a wing shaped underbody, could mitigate the balance loss associated with following another vehicle. Care would have to be taken to not generate excessive downforce, which limiting ride height, floor area, and the floor profile should prevent.

### Other

The tyres and wheels of a Formula 1 car contribute a large portion of the total vehicle drag. The rear tyre wakes in particular have been shown to have an impact on the following vehicle, especially the downforce generated by the front wing, so it would not be recommended that tyre width or diameter be increased from the current sizes, especially if they remain uncovered.

As well as aerodynamic drag generated by the exposed wheels another large and arguably unnecessary source of aerodynamic drag on a Formula 1 car is from the open cockpit. Leaving the driver's head exposed, much like keeping the wheels uncovered, is predominantly down to tradition. While not essential, gains could be made in aerodynamic efficiency by covering the cockpit with a canopy, figure 10.2.

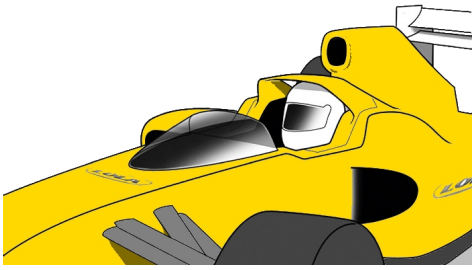

**Figure 10.2:** Lola motorsports 2011 F1 canopy concept drawing, from Racecar Engineering [150].

Finally cooling, while not investigated in this thesis, is known to be detrimental to a following vehicle, where the cooling flow and exhaust gases from the upstream car causes the following car to overheat. Teams tend to run with a cooling package optimized for isolated running, to minimize drag, building in a redundancy with variable area cooling inlets on brake ducts and sidepods could allow vehicles to follow closely for longer before overheating occurs, while maintaining low drag in isolated conditions.

## 10.2 Suggestions for Further Work

From the conclusions presented in Chapter 9 the following suggestions for further research are proposed:

1. Design a vehicle based on the proposed aerodynamic regulations.
   (a) Develop the vehicle to attain representative levels of downforce with a suitable lift-to-drag ratio.
   (b) Investigate the wake of the vehicle - is it as desired? i.e. A low axial velocity deficit at the height of the car, coupled with a suitable wake up-wash to divert wake vertically.
   (c) Investigate the effect of wake on a downstream vehicle using 1 or all the methodologies presented above. Does the vehicle have a significantly reduced impact on a following vehicle?
2. Further investigate the effect of wake unsteadiness on a downstream vehicle.
3. Using the non-uniform inlet conditions investigate the effect of upstream wakes on different wings in ground-effect, i.e. different ground clearances, chord lengths, cambers, and incidences.
4. Perform a lap-time simulation taking into account downforce and drag affect of the upstream vehicle wake. Can performance loss in the wake be reduced by altering the driven line?
   If yes:
   (a) Perform investigation of tyre wear behaviour to reduce off-line debris.
   (b) Investigate other means of reducing the adhesion deficit off the racing line. e.g. a high grip painted surface or reduce the 'rubbering-in' effect on the racing line by using harder tyres.

# References


[1] R Dominy. The influence of slipstreaming on the performance of a Grand Prix racing car. *Proceedings of the Institution of Mechanical Engineers, Part D: Journal of Automobile Engineering*, 204(1):35–40, 1990.

[2] Fédération Internationale de l'Automobile. *2009 FIA Formula 1 Technical Regulations*, 2009.

[3] T Larsson. Formula one aerodynamics - BMW Sauber F1.09: Fundamentally different. In *4th European Automotive Simulation Conference, Munich, Germany*, pages 9–20, July 2009.

[4] M Watts and S Watkins. Aerodynamic structure and development of Formula 1 racing car wakes. *SAE International Journal of Passenger Cars - Mechanical Systems*, 7(3):1096–1105, 2014.

[5] M Soso. Wings in ground effect. Masters thesis, University of Illinois, 2002.

[6] A Straker. The influence of slipstreaming on racing car wing performance. Masters thesis, Durham University, 2007.

[7] M Wilson, R Dominy, and A Straker. The aerodynamic characteristics of a race car wing operating in a wake. *SAE International Journal of Passenger Cars - Mechanical Systems*, 1(1):552–559, 2009.

[8] W McClintock. The aerodynamic influence of slipstreaming on a Formula One race car. Masters thesis, Durham University, 2007.

[9] M Soso and P Wilson. The influence of an upstream diffuser on a downstream wing in ground effect. *Proceedings of the Institution of Mechanical Engineers, Part D: Journal of Automobile Engineering*, 222(4):551–563, 2008.

[10] J Katz. Aerodynamics of race cars. *Annual Review of Fluid Mechanics*, 38:27–63, 2006.

[11] X Zhang, W Toet, and J Zerihan. Ground effect aerodynamics of race cars. *Applied Mechanics Reviews*, 59(1):33–49, 2006.

[12] B Agathangelou and M Gascoyne. Aerodynamic design considerations of a Formula 1 racing car. *SAE Technical Paper*, (980399):1–8, 1998.

[13] W Toet. A devious way to disguise what is really important? `https://www.linkedin.com/pulse/devious-way-disguise-what-really-important-willem-toet?trk=mp-reader-card`, 2015. [Online; accessed 11/12/2015].

[14] M Nakagawa, S Kallweit, F Michaux, and T Hojo. Typical velocity fields and vortical structures around a Formula One car, based on experimental investigations using particle image velocimetry. *SAE International Journal of Passenger Cars - Mechanical Systems*, 9(2016-01-1611), 2016.

[15] J Katz. *Race car aerodynamics: designing for speed*. Robert Bentley, 2nd edition, 1995. ISBN: 0837601428.

[16] P Wright. Ferrari Formula 1: under the skin of the championship-winning F1–2000. *Warrendale, PA: Society of Automotive Engineers*, 2004. ISBN: 0768013410.

[17] W Toet. Keynote speech. IMechE International Vehicle Aerodynamics Conference, Loughbrough, October 2014.

[18] A Ogawa, S Mashio, D Nakamura, Y Masumitsu, M Minagawa, and Y Nakai. Aerodynamics analysis of formula one vehicles. *Development Methodologies for Formula One Aerodynamics, Honda R&D Technical Review 2009, F1 Special (The Third Era Activities)*, pages 152–161, 2009.

[19] England and Wales Court of Appeal. Force India Formula One Team LIMITED v Aerolab SRL. *Reports of Patent, Design and Trade Mark Cases*, 130(12):947–984, 2013.

[20] H Gerhardt, C Kramer, E Zakowski, and H Barth. The aerodynamic optimization of the zakspeed formula 1 racing car. *Journal of Wind Engineering and Industrial Aerodynamics*, 22(2):291–297, 1986.

[21] T Larsson, T Sato, and B Ullbrand. Supercomputing in F1–unlocking the power of CFD. In *2nd European Automotive CFD Conference, Frankfurt, Germany*, pages 29–30, 2005.

[22] A Ogawa, S Yano, S Mashio, T Takiguchi, S Nakamura, and M Shingai. Development methodologies for formula one aerodynamics. *Development Methodologies for Formula One Aerodynamics, Honda R&D Technical Review 2009, F1 Special (The Third Era Activities)*, pages 142–151, 2009.

[23] J Pegrum. *Experimental Study of the Vortex System Generated by a Formula 1 Front Wing*. Doctoral thesis, Imperial College London (University of London), 2006.

[24] M van den Berg. *Aerodynamic interaction of an inverted wing with a rotating wheel*. Doctoral thesis, University of Southampton, 2007.

[25] Fédération Internationale de l'Automobile. *2006 FIA Formula 1 Technical Regulations*, 2005.

[26] Fédération Internationale de l'Automobile. *2014 FIA Formula 1 Technical Regulations*, 2014.

[27] CD-Adapco. http://www.cd-adapco.com/cfdImage. [Online; accessed 5/5/2015].

[28] E Benzing. *Ali/Wings: Their Design and Application to Racing Cars*. Giorgio Nada Editore s.r.l, 2nd edition, 2012. ISBN: 978-88-7911-539-1.

[29] F1Technical. F1 rules and stats 1960-1969. http://www.f1technical.net/articles/24/. [Online; accessed 27/10/2015].

[30] R Aiguabella. Formula one rear wing optimization. Masters thesis, Mondragón Unibertsitatea, 2011.

[31] E Cui and X Zhang. Ground effect aerodynamics. In *Encyclopedia of Aerospace Engineering*, volume 1, chapter 18, pages 245–256. John Wiley & Sons, Ltd, 2010. ISBN: 978-0-470-75440-5.

[32] J Vogt, T Barber, and E Leonardi. Flow field phenomena about lift and downforce generating cambered aerofoils in ground effect. In *Proceedings of 16th Australasian Fluid Mechanics Conference, Gold Coast, Australia*, 2007.

[33] J Zerihan and X Zhang. Aerodynamics of a single element wing in ground effect. *Journal of Aircraft*, 37(6):1058–1064, 2000.

[34] E Genua. *A CFD Investigation into Ground Effect Aerodynamics*. Doctoral thesis, Delft University of Technology, 2009.

[35] J Lindsey. An investigation into induced drag and ground effect. Masters thesis, Durham University, 2011.

[36] M Ahmed and S Sharma. An investigation on the aerodynamics of a symmetrical airfoil in ground effect. *Experimental Thermal and Fluid Science*, 29(6):633–647, 2005.

[37] M Ahmed, T Takasaki, and Y Kohama. Experiments on the aerodynamics of a cambered airfoil in ground effect. In *44th AIAA Aerospace Sciences Meeting and Exhibit, Reno, Nevada*, pages 1–17, January 2006.

[38] X Zhang and J Zerihan. Turbulent wake behind a single element wing in ground effect. In *10th International Symposium on Applications of Laser Techniques to Fluid Mechanics, Lisbon, Portugal*, pages 1–12. Center for Innovation, Technology and Policy Research, January 2000.

[39] S Mahon and X Zhang. Computational analysis of pressure and wake characteristics of an aerofoil in ground effect. *Journal of Fluids Engineering*, 127(2):290–298, 2005.

[40] W Jasinski and M Selig. Experimental study of open-wheel race-car front wings. *SAE Technical Paper*, (983042):2549–2557, 1998.

[41] X Zhang and J Zerihan. Edge vortices of a double element wing in ground effect. *Journal of aircraft*, 41(5):1127–1137, 2004.

[42] V Galoul and TJ Barber. A study of an inverted wing with endplates in ground effect. In *16th Australasian Fluid Mechanics Conference (AFMC)*, pages 919–924. School of Engineering, The University of Queensland, 2007.

[43] L Roberts, J Correia, M Finnis, and K Knowles. Investigation of forcing boundary layer transition on a single-element inverted wing in ground effect. In *The International Vehicle Aerodynamics Conference*, pages 199–211. Woodhead Publishing, 2014.

[44] Y Kuya, K Takeda, X Zhang, S Beeton, and T Pandaleon. Flow separation control on a race car wing with vortex generators in ground effect. *Journal of Fluids Engineering*, 131(12):121102–1–121102–8, 2009.

[45] W Bastedo and T Mueller. Spanwise variation of laminar separation bubbles on wings at low reynolds number. *Journal of aircraft*, 23(9):687–694, 1986.

[46] A Smith. High-lift aerodynamics. *Journal of Aircraft*, 12(6):501–530, 1975.

[47] C Wenzinger. Pressure distribution over a NACA 23012 airfoil with a NACA 23012 external-airfoil flap. *NACA Report*, 614:1–15, 1937.

[48] X Zhang and J Zerihan. Aerodynamics of a double-element wing in ground effect. *AIAA journal*, 41(6):1007–1016, 2003.

[49] S Mahon and X Zhang. Computational analysis of a inverted double-element airfoil in ground effect. *Journal of fluids engineering*, 128(6):1172–1180, 2006.

[50] D Jeffrey, X Zhang, and D Hurst. Aerodynamics of gurney flaps on a single-element high-lift wing. *Journal of Aircraft*, 37(2):295–301, 2000.

[51] X Zhang, AE Senior, and A Ruhrmann. Vortices behind a bluff body with an upswept aft section in ground effect. *International journal of heat and fluid flow*, 25(1):1–9, 2004.

[52] R Dominy. Aerodynamics of grand prix cars. *Proceedings of the Institution of Mechanical engineers, Part D: Journal of Automobile Engineering*, 206(4):267–274, 1992.

[53] D Neuhart and O Pendergraft Jr. A water tunnel study of gurney flaps. *NASA Technical Memorandum*, (4071):1–19, November 1988.

[54] J Zerihan and X Zhang. Aerodynamics of gurney flaps on a wing in ground effect. *AIAA journal*, 39(5):772–780, 2001.

[55] C Jang, J Ross, and R Cummings. Numerical investigation of an airfoil with a gurney flap. *Aircraft Design*, 1(2):75–88, 1998.

[56] D Sims-Williams, A White, and R Dominy. Gurney flap aerodynamic unsteadiness. *Sports Engineering*, 2(4):221–234, 1999.

[57] X Zhang, J Zerihan, A Ruhrmann, and M Deviese. Tip vortices generated by a wing in ground effect. In *Proceedings of the 11th International Symposium on Applications of Laser Techniques to Fluid Mechanics*. Citeseer, 2002.

[58] S Diasinos, T Barber, and G Doig. Influence of wing span on the aerodynamics of wings in ground effect. *Proceedings of the Institution of Mechanical Engineers, Part G: Journal of Aerospace Engineering*, 227(3):569–573, 2013.

[59] A Senior and X Zhang. The force and pressure of a diffuser-equipped bluff body in ground effect. *Journal of fluids engineering*, 123(1):105–111, 2001.

[60] A Ruhrmann and X Zhang. Influence of diffuser angle on a bluff body in ground effect. *Journal of fluids engineering*, 125(2):332–338, 2003.

[61] S Mahon, X Zhang, and C Gage. The evolution of edge vortices underneath a diffuser equipped bluff body. In *12th International Symposium on Applications of Laser Techniques to Fluid Mechanics, Lisbon, Portugal*, pages 1–10. Center for Innovation, Technology and Policy Research, July 2004.

[62] L Puglisevich and G Page. Large eddy simulation of the flow around a diffuser-equipped bluff body in ground effect. In *ASME 2011 International Mechanical Engineering Congress and Exposition*, pages 313–322. American Society of Mechanical Engineers, 2011.

[63] L Jowsey and M Passmore. Experimental study of multiple-channel automotive underbody diffusers. *Proceedings of the Institution of Mechanical Engineers, Part D: Journal of Automobile Engineering*, 224(7):865–879, 2010.

[64] L Jowsey. *An Experimental Study of Automotive Underbody Diffusers*. Doctoral thesis, Loughborough University, 2013.

[65] R Knowles, A Saddington, and K Knowles. Simulation and experiments on an isolated racecar wheel rotating in ground contact. In *4th MIRA International Vehicle Aerodynamics Conference, Warwick, UK*, pages 16–17, 2002.

[66] R Knowles. *Monoposto Racecar Wheel Aerodynamics: Investigation of Near-Wake Structure and Support-Sting Interference*. Doctoral thesis, Cranfield University, 2005.

[67] J McManus and X Zhang. A computational study of the flow around an isolated wheel in contact with the ground. *Journal of Fluids Engineering*, 128(3):520–530, 2006.

[68] A Saddington, R Knowles, and K Knowles. Laser doppler anemometry measurements in the near-wake of an isolated Formula One wheel. *Experiments in fluids*, 42(5):671–681, 2007.

[69] A Mears, R Dominy, and D Sims-Williams. The flow about an isolated rotating wheeleffects of yaw on lift, drag and flow structure. In *4th MIRA International Vehicle Aerodynamics Conference, Warwick, UK, October*, 2002.

[70] J Heyder-Bruckner. *The Aerodynamics of an Inverted Wing and a Rotating Wheel in Ground Effect*. Doctoral thesis, University of Southampton, 2011.

[71] J Fackrell. *The aerodynamics of an isolated wheel rotating in contact with the ground*. Doctoral thesis, Imperial College London (University of London), 1974.

[72] J Axerio, G Iaccarino, E Issakhanian, K Lo, C Elkins, and J Eaton. Computational and experimental investigation of the flow structure and vortex dynamics in the wake of a Formula 1 tire. *SAE Technical Paper*, (2009-01-0775):1–9, 2009.

[73] A Sprot. *Open-Wheel Aerodynamics: Effects of Tyre Deformation and Internal Flow*. Doctoral thesis, Durham University, 2013.

[74] D Hetherington. *Interference of Supports Used for Ground Vehicle Wind Tunnel Testing*. Doctoral thesis, Durham University, 2006.

[75] A Sprot, J Minto, D Sims-Williams, and R Dominy. Aerodynamic investigation on the effect of varying through-hub flow on a Formula One front wheel assembly. *SAE International Journal of Passenger Cars - Mechanical Systems*, 4(1):929–944, 2011.

[76] S Clark. An analog for the rolling pneumatic tire under load. Technical report, University of Michigan, College of Engineering, 1965.

[77] A Mears. *The aerodynamic characteristics of an exposed racing car wheel*. Doctoral thesis, Durham University, 2004.

[78] A Sprot, D Sims-Williams, and R Dominy. The aerodynamic characteristics of a fully deformable Formula One wind tunnel tyre. *SAE International journal of passneger cars. Mechanical systems*, 5(2):1026–1041, 2012.

[79] Fédération Internationale de l'Automobile. *2015 FIA Formula 1 Sporting Regulations*, 2015.

[80] S Diasinos, T Barber, E Leonardi, and S Hall. A two-dimensional analysis of the effect of a rotating cylinder on an inverted aerofoil in ground effect. In *Proceedings of the 15th Australian Fluid Mechanics Conference*, 2004.

[81] W Kellar, S Pearse, and A Savill. Formula 1 car wheel aerodynamics. *Sports Engineering*, 2(4):203–212, 1999.

[82] S Diasinos and A Gatto. Experimental investigation into wing span and angle-of-attack effects on sub-scale race car wing/wheel interaction aerodynamics. *Experiments in Fluids*, 45(3):537–546, 2008.

[83] S Diasinos. *The aerodynamic interaction of a rotating wheel and a downforce producing wing in ground effect*. Doctoral thesis, University of New South Wales, 2009.

[84] Fondtech. Fondtech facilities, fondtech 1 - technical details. `http://www.fondtech.eu/site/index.php/wind-tunnel-facilities-fondtech/wind-tunnel-facilities`. [Online; accessed 20/9/2013].

[85] M Soso and P Wilson. Aerodynamics of a wing in ground effect in generic racing car wake flows. *Proceedings of the Institution of Mechanical Engineers, Part D: Journal of Automobile Engineering*, 220(1):1–13, 2006.

[86] N Barrett. The aerodynamic influences on Formula 1 car overtaking. Masters thesis, Durham University, 2012.

[87] J Correia, L Roberts, M Finnis, and K Knowles. Aerodynamic characteristics of a monoposto racing car front wing operating in high turbulence conditions. In *The International Vehicle Aerodynamics Conference*, pages 225–236. Woodhead Publishing, 2014.

[88] R Dominy and G LeGood. The use of a bluff body wake generator for wind tunnel studies of NASCAR drafting aerodynamics. *SAE International Journal of Passenger Cars - Mechanical Systems*, 1(1):1404–1411, 2008.

[89] J Howell. Catastrophic lift forces on racing cars. *Journal of Wind Engineering and Industrial Aerodynamics*, 9(1):145–154, 1981.

[90] R Dominy, A Ryan, and D Sims-Williams. The influence of slipstreaming on sports prototype race car performance. *Proceedings of the Institution of Mechanical Engineers, Part D: Journal of Automobile Engineering*, 214(8):887–894, 2000.

[91] `https://www.mulsannescorner.com`. [Online; accessed 14/6/2014].

[92] R Perry and D Marshall. An evaluation of proposed Formula 1 aerodynamic regulations changes using computational fluid dynamics. In *26th AIAA Applied Aerodynamics Conference*, pages 1–17, 2008.

[93] P Bearman and T Morel. Effect of free stream turbulence on the flow around bluff bodies. *Progress in aerospace sciences*, 20(2):97–123, 1983.

[94] P Roach. The generation of nearly isotropic turbulence by means of grids. *International Journal of Heat and Fluid Flow*, 8(2):82–92, 1987.

[95] R Huang and H Lee. Effects of freestream turbulence on wing-surface flow and aerodynamic performance. *Journal of aircraft*, 36(6):965–972, 1999.

[96] P Devinant, T Laverne, and J Hureau. Experimental study of wind-turbine airfoil aerodynamics in high turbulence. *Journal of Wind Engineering and Industrial Aerodynamics*, 90(6):689–707, 2002.

[97] K Swalwell. *The effect of turbulence on stall of horizontal axis wind turbines*. Doctoral thesis, Monash University, 2005.

[98] P Newnham. *The influence of turbulence on the aerodynamic optimisation of bluff body road vehicles*. Doctoral thesis, Loughborough University, 2007.

[99] O Mankowski. *The Wind Tunnel Simulation and Effect of Turbulent Air flow on Automotive Aerodynamics*. Doctoral thesis, Durham University, 2013.

[100] O Mankowski, D Sims-Williams, and R Dominy. A wind tunnel simulation facility for on-road transients. *SAE International Journal of Passenger Cars - Mechanical Systems*, 7(3):1087–1095, 2014.

[101] D Schröck, N Widdecke, and J Wiedemann. Aerodynamic response of a vehicle model to turbulent wind. In *Progress in Vehicle Aerodynamics and Thermal Management-Proceedings of the 7th FKFS Conference*, 2009.

[102] A Cogotti. Generation of a controlled level of turbulence in the pininfarina wind tunnel for the measurement of unsteady aerodynamics and aeroacoustics. *SAE Technical Paper*, (2003-01-0430), 2003.

[103] A Cogotti. Update on the Pininfarina turbulence generation system and its effects on the car aerodynamics and aeroacoustics. *SAE Technical Paper*, (2004-01-0807), 2004.

[104] A Cogotti. Evolution of performance of an automotive wind tunnel. *Journal of Wind Engineering and Industrial Aerodynamics*, 96(6):667–700, 2008.

[105] S Watkins, J Saunders, and P Hoffmann. Turbulence experienced by moving vehicles. part i. introduction and turbulence intensity. *Journal of wind engineering and industrial aerodynamics*, 57(1):1–17, 1995.

[106] D Sims-Williams. Cross winds and transients: reality, simulation and effects. *SAE International Journal of Passenger Cars - Mechanical Systems*, 4(1):172–183, 2011.

[107] M Docton. *The Simulation of Transient Cross Winds on Passenger Vehicles*. Doctoral thesis, Durham University, 1996.

[108] O Mankowski, D Sims-Williams, R Dominy, B Duncan, and J Gargoloff. The bandwidth of transient yaw effects on vehicle aerodynamics. *SAE International Journal of Passenfer Cars - Mechanical Systems*, 4(1):131–142, 2011.

[109] A Gaylard, N Oettle, B Duncan, and J Gargoloff. Effect of non-uniform flow conditions on vehicle aerodynamic performance. In *Progress in Vehicle Aerodynamics and Thermal Management, Proceedings of the 9th FKFS Conference*, pages 63–78, 2013.

[110] A Gaylard, N Oettle, J Gargoloff, and B Duncan. Evaluation of non-uniform upstream flow effects on vehicle aerodynamics. *SAE International Journal of Passenger Cars - Mechanical Systems*, 7(2):692–702, 2014.

[111] A D'Hooge, R Palin, L Rebbeck, J Gargoloff, and B Duncan. Alternative simulation methods for assessing aerodynamic drag in realistic crosswind. *SAE International Journal of Passenger Cars - Mechanical Systems*, 7(2):617–625, 2014.

[112] `http://www.cd-adapco.com/cfdImage/external-aerodynamic-analysis-renault-r28-2`. [Online; accessed 5/5/2015].

[113] D Sims-Williams and R Dominy. The design of a new wind tunnel for vehicle aerodynamics research. In *4th MIRA International Vehicle Aerodynamics Conference, Warwick, UK*, 2002.

[114] D Sims-Williams and R Dominy. The design of an open-jet wind tunnel for model testing. *SAE Technical Paper*, (2002-01-3340), 2002.

[115] M Gillan. Keynote speech. 2nd International Forum Future Automotive Aerodynamics, December 2013.

[116] Sauber F1 Team. Model motion system - f1 wind tunnel explained 4/8, 2014.

[117] L Sterken, L Löfdahl, S Sebben, and T Walker. Effect of the traversing unit on the flow structures behind a passenger vehicle. In *The International Vehicle Aerodynamics Conference*, pages 91–99. Woodhead Publishing, 2014.

[118] J Barlow, W Rae, and A Pope. *Low-Speed Wind Tunnel Testing*. John Wiley & Sons, New York, 3 edition, 1999. ISBN: 978-0-471-55774-6.

[119] P Parker and R DeLoach. Structural optimization of a force balance using a computational experiment design. *AIAA Paper*, 540:1–12, 2002.

[120] S Gorlin and I Slezinger. *Wind Tunnels and Their Instrumentation*. Israel Program for Scientific Translations;[available from the US Department of Commerce, Clearinghouse for Federal Scientific and Technical Information, Springfield, Va.], 1966. ISBN: 9780706504323.

[121] B Ewald. Multi-component force balances for conventional and cryogenic wind tunnels. *Measurement Science and Technology*, 11(6):R81–R94, 2000.

[122] ARA. Aircraft research association website, 2013. http://www.ara.co.uk/services/experimental-aerodynamics/test-technologies-and-services/model-load-measurement/.

[123] R Rhew. Nasa langley research center strain gage balance design concepts. In *NASA CONFERENCE PUBLICATION*, pages 525–542. NASA, 1999.

[124] M Dubois. Six-component strain-gage balances for large wind tunnels. *Experimental Mechanics*, 21(11):401–407, 1981.

[125] BFR Ewald. The development of electron beam welded, strain-gaged wind-tunnel balances. *Journal of Aircraft*, 16(5):349–352, 1979.

[126] Smiths Metal Centres. Datasheets, 2013. http://www.smithmetal.com/.

[127] Fylde Electronic Laboratories Ltd. *FE-579-TA Bridge Amplifier Manual*. 49/51 Fylde Road, Preston, PR1 2XQ.

[128] BFR Ewald, P Giesecke, L Polansky, and T Preusser. Fully automatic calibration machine for internal 6-component wind tunnel balance including cryogenic balances. In *Instrumentation in Aerospace Simulation Facilities, 1989. ICIASF'89 Record., International Congress on*, pages 470–476. IEEE, 1989.

[129] D Smith. An efficient algorithm using matrix methods to solve wind-tunnel force-balance equations. NASA TN D-6860, NASA Lewis Research Center, 1972.

[130] Perrinn Ltd. Perrinn CFD database, July 2016. http://www.perrinn.com.

[131] Fédération Internationale de l'Automobile. Official speed trap figures, 2015. http://www.fia.com/events/fia-formula-1-world-championship/season-2015/formula-one.

[132] EXA Corporation. *EXA PowerFLOW 5.0 User's Guide*. 55 Network Drive, Burlington, MA, USA.

[133] S Cyr, K-D Ih, and S-H Park. Accurate reproduction of wind-tunnel results with cfd. *SAE Technical Paper*, (2011-01-0158), 2011.

[134] S Kandasamy, B Duncan, H Gau, F Maroy, A Belanger, N Gruen, and S Schäufele. Aerodynamic performance assessment of BMW validation models using computational fluid dynamics. *SAE Technical Paper*, (2012-01-0297), 2012.

[135] R Palin, V Johnston, S Johnson, A D'Hooge, B Duncan, and J Gargoloff. The aerodynamic development of the Tesla model S-part 1: Overview. *SAE Technical Paper*, (2012-01-0177), 2012.

[136] W Toet. Aerodynamics and aerodynamic research in formula 1. *The Aeronautical Journal*, 117(1187):1–26, 2013.

[137] M Giles and R Cummings. Wake integration for three-dimensional flowfield computations: Theoretical development. *Journal of aircraft*, 36(2):357–365, 1999.

[138] G Brune. Quantitative three-dimensional low-speed wake surveys. In *The Fifth Symposium on Numerical and Physical Aspects of Aerodynamic Flows;*, pages 1–13. California State University, NASA, 1992.

[139] D Hunt, R Cummings, and M Giles. Determination of drag from three-dimensional viscous and inviscid flowfield computations. *AIAA Paper*, pages 97–2257, 1997.

[140] D Hunt, R Cummings, and M Giles. Wake integration for three-dimensional flowfield computations: Applications. *Journal of aircraft*, 36(2):366–373, 1999.

[141] A Ryan. *The Simulation of Transient Cross-Wind Gusts and Their Aerodynamic Influence on Passenger Cars*. Doctoral thesis, Durham University, 2000.

[142] F Ganzevles, A de Bruin, and W Puffert-Meissner. A quantitative analysis of viscous and lift-induced drag components from detailed wake measurements behind a half-span model. Technical report, Nationaal Lucht-en Ruimtevaartlaboratorium, 2002.

[143] A Carre, M Cordero-Graciaa, M Gómeza, and J Ponsinb. Wake-integral method for drag prediction. In E Oñate, J Oliver, and A Huerta, editors, *11th World Congress on Computational Mechanics, Barcelona, Spain*, July 2014.

[144] S McBeath. Dynamic flow fields: CFD study of generic 2013 formula 1 car. *Racecar Engineering Magazine*, 25(10):46–52, October 2015.

[145] D Acheson. *Elementary Fluid Dynamics*. Oxford University Press, 1990. ISBN: 978-0198596790.

[146] D Giaiotti and F Stel. The rankine vortex model. *PhD Course on Environmental Fluid Mechanics-ICTP/University of Trieste*, 2006.

[147] D Fabre, D Sipp, and L Jacquin. Kelvin waves and the singular modes of the lamb–oseen vortex. *Journal of Fluid Mechanics*, 551:235–274, 2006.

[148] Automobile Club de l'Ouest (ACO). *Réglement Technique pour Prototype LMP1 2015*, 2014. `http://www.24h-lemans.com/wpphpFichiers/1/1/ressources/Pdf/2015/24-heures-du-mans/regulations/2015-technical-regulations-lm-p1.pdf`.

[149] INDYCAR. *Technical Specifications 2016*, 2015.

[150] Racecar-Engineering. `http://www.racecar-engineering.com/`. [Online; accessed 20/5/2016].

[151] Fédération Internationale de l'Automobile. *2017 FIA Formula 1 Technical Regulations*, 2016.

# Appendix A

# Published Work

The following is a list of work published during the completion of this research:

### Conference Proceedings

1. Newbon J, Dominy R, and Sims-Williams D. Investigation into the effect of the wake from a generic Formula one car on a downstream vehicle. In *IMechE International Vehicle Aerodynamics Conference, Loughborough, UK*. October 14–15 2014.

2. Newbon J, Sims-Williams D and Dominy R. Analysis of the impacts of Formula 1 car wakes on the aerodynamic performance of a following vehicle. In *Second International Conference in Numerical and Experimental Aerodynamics of Road Vehicles and Trains, Göteborg, Sweden*. June 21–23 2016.

3. Kremheller A, Moore M, LeGood G, Sims-Williams D, Newbon J, Lewis R. The effects of transient flow conditions on the aerodynamics of an LCV concept using CFD and wind tunnel experiments. In *IMechE International Vehicle Aerodynamics Conference, Coventry, UK*. Sept 21–22 2016.

### Journal Papers

1. Newbon J, Dominy R, and Sims-Williams D. CFD investigation of the effect of the salient flow features in the wake of a generic open-wheel race car. *SAE International Journal of Passenger Cars – Mechanical Systems*. 2015; 8 (2015-04-14).
   (Also in *SAE World Congress, Detroit, Mi, USA*. April 21–23 2015.)

2. Newbon J, Sims-Williams D and Dominy R. Aerodynamic analysis of Grand Prix cars operating in wake flows. *SAE International Journal of Passenger Cars – Mechanical Systems*. 2017; 10 (2017-01-1546).
   (Also in *SAE World Congress, Detroit, Mi, USA*. April 4–6 2017.)

# Appendix B

# Experimental Methodology

Calibration of the $4\times$ 70N wheel sting load cells was performed by Harry Kounenis and Dr David Sims-Williams. Before calibration each corner was paired with a strain gauge amplifier, either a Fylde FE-579 or a generic amplifier constructed of stock RS components. The individual calibrations were performed by incrementally hanging masses up to a total of 3kg, then removing to check for hysteresis and zero shift, with the results shown below.

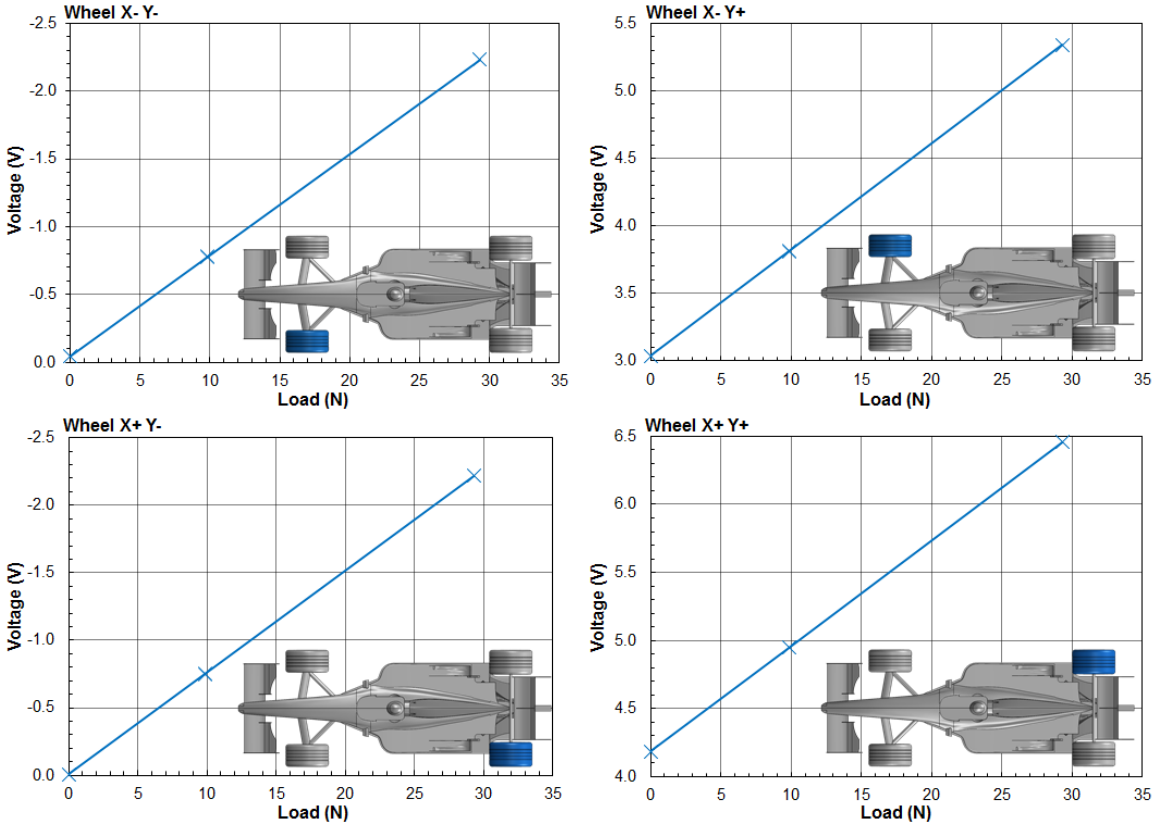


**Figure B.1:** Wheel sting load cell calibration.

Wheel load cell repeatability was calculated using the same method as the internal 6-component balance, Chapter 2. The greatest error occurring on the X+Y- load cell, albeit the error is low, $C_{D\,error} \approx \pm 0.002$.

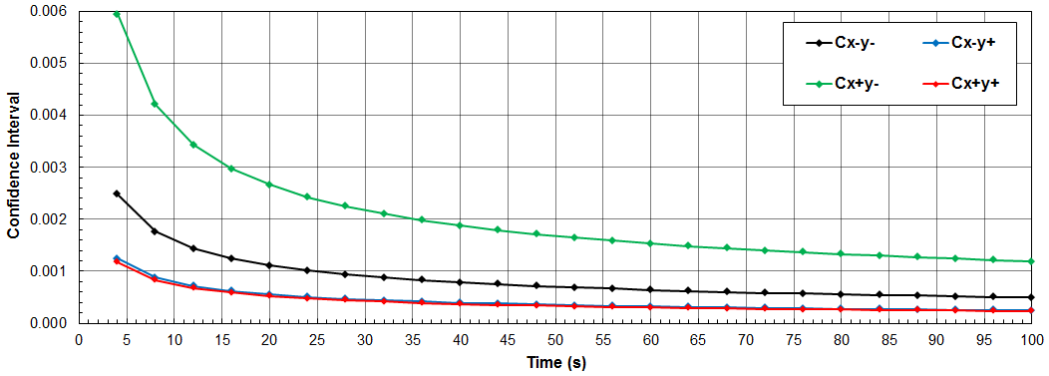


**Figure B.2:** Wheel load cell confidence interval.

**Table B.1:** 25% Formula 1 wind tunnel model, pressure tapping co-ordinates.

| Front Wing Centreline Upper | | |
|---|---|---|
| x (mm) | y (mm) | z (mm) |
| 22.500 | 0.000 | 37.310 |
| 28.896 | 0.000 | 39.703 |
| 33.747 | 0.000 | 39.838 |
| 38.598 | 0.000 | 39.800 |
| 38.598 | 0.000 | 39.800 |
| 46.653 | 0.000 | 39.414 |
| 49.917 | 0.000 | 39.146 |
| 53.151 | 0.000 | 38.831 |
| 56.385 | 0.000 | 38.480 |
| 77.406 | 0.000 | 36.225 |

| Front Wing Centreline Lower | | |
|---|---|---|
| x (mm) | y (mm) | z (mm) |
| 28.896 | 0.000 | 32.040 |
| 33.747 | 0.000 | 30.391 |
| 38.598 | 0.000 | 29.306 |
| 45.066 | 0.000 | 28.469 |
| 48.300 | 0.000 | 28.257 |
| 51.534 | 0.000 | 28.164 |
| 54.768 | 0.000 | 28.180 |
| 79.023 | 0.000 | 31.220 |

| Front Wing Quarter-Span Upper | | |
|---|---|---|
| x (mm) | y (mm) | z (mm) |
| 22.500 | 82.500 | 37.310 |
| 28.896 | 82.500 | 39.703 |
| 33.747 | 82.500 | 39.838 |
| 38.598 | 82.500 | 39.800 |
| 38.598 | 82.500 | 39.800 |
| 46.653 | 82.500 | 39.414 |
| 49.917 | 82.500 | 39.146 |
| 53.151 | 82.500 | 38.831 |
| 56.385 | 82.500 | 38.480 |
| 77.406 | 82.500 | 36.225 |

| Front Wing Quarter-Span Lower | | |
|---|---|---|
| x (mm) | y (mm) | z (mm) |
| 28.896 | 82.500 | 32.040 |
| 33.747 | 82.500 | 30.391 |
| 38.598 | 82.500 | 29.306 |
| 45.066 | 82.500 | 28.469 |
| 48.300 | 82.500 | 28.257 |
| 51.534 | 82.500 | 28.164 |
| 54.768 | 82.500 | 28.180 |
| 79.023 | 82.500 | 31.220 |

| Chassis (Upper) Centreline | | |
|---|---|---|
| x (mm) | y (mm) | z (mm) |
| 75.000 | 0.000 | 108.762 |
| 100.000 | 0.000 | 117.109 |
| 125.000 | 0.000 | 124.285 |
| 150.000 | 0.000 | 130.334 |
| 175.000 | 0.000 | 136.812 |
| 250.000 | 0.000 | 144.709 |
| 300.000 | 0.000 | 148.156 |
| 365.000 | 0.000 | 151.098 |

| Chassis (Under) Centreline | | |
|---|---|---|
| x (mm) | y (mm) | z (mm) |
| 278.062 | 0.0000 | 29.280 |
| 304.312 | 0.0000 | 26.018 |
| 330.562 | 0.0000 | 20.577 |
| 356.812 | 0.0000 | 15.000 |

| Sidepod Upper/Cockpit Side | | |
|---|---|---|
| x (mm) | y (mm) | z (mm) |
| 555.000 | -92.500 | 132.768 |
| 580.000 | -92.500 | 130.981 |
| 605.000 | -92.500 | 128.814 |
| 630.000 | -92.500 | 124.389 |
| 655.000 | -92.500 | 123.832 |

| Rear Diffuser | | |
|---|---|---|
| x (mm) | y (mm) | z (mm) |
| 972.50 | 99.000 | 17.500 |
| 986.50 | 95.000 | 21.000 |
| 1000.5 | 90.500 | 23.920 |
| 1014.5 | 86.500 | 26.510 |
| 1028.5 | 82.000 | 29.000 |
| 972.50 | 64.000 | 17.500 |
| 986.50 | 61.000 | 21.000 |
| 1000.5 | 57.500 | 23.920 |
| 1014.5 | 55.000 | 26.510 |
| 1028.5 | 52.500 | 29.000 |
| 1080.5 | 19.000 | 44.010 |
| 1094.5 | 20.000 | 50.130 |
| 1108.5 | 21.000 | 57.640 |
| 1080.5 | 0.0000 | 44.010 |
| 1094.5 | 0.0000 | 48.930 |
| 1108.5 | 0.0000 | 52.950 |
| 278.062 | 0.0000 | 29.280 |
| 304.312 | 0.0000 | 26.018 |
| 330.562 | 0.0000 | 20.577 |
| 356.812 | 0.0000 | 15.000 |

| Underbody | | |
|---|---|---|
| x (mm) | y (mm) | z (mm) |
| 451.81 | 0.0000 | -2.5000 |
| 478.06 | 0.0000 | -2.5000 |
| 504.31 | 0.0000 | -2.5000 |
| 530.56 | 0.0000 | -2.5000 |
| 556.81 | 0.0000 | -2.5000 |
| 583.06 | 0.0000 | -2.5000 |
| 609.31 | 0.0000 | -2.5000 |
| 635.56 | 0.0000 | -2.5000 |
| 661.81 | 0.0000 | -2.5000 |
| 688.06 | 0.0000 | -2.5000 |
| 714.31 | 0.0000 | -2.5000 |
| 740.56 | 0.0000 | -2.5000 |
| 740.56 | 0.0000 | -2.5000 |
| 793.06 | 0.0000 | -2.5000 |
| 819.31 | 0.0000 | -2.5000 |
| 845.56 | 0.0000 | -2.5000 |
| 871.81 | 0.0000 | -2.5000 |
| 898.06 | 0.0000 | -2.5000 |
| 898.06 | 0.0000 | -2.5000 |
| 898.06 | 0.0000 | -2.5000 |
| 451.81 | 42.500 | 0.0000 |
| 478.06 | 42.500 | 0.0000 |
| 504.31 | 42.500 | 0.0000 |
| 530.56 | 42.500 | 0.0000 |
| 556.81 | 42.500 | 0.0000 |
| 583.06 | 42.500 | 0.0000 |
| 609.31 | 42.500 | 0.0000 |
| 609.31 | 42.500 | 0.0000 |
| 661.81 | 42.500 | 0.0000 |
| 661.81 | 42.500 | 0.0000 |
| 714.31 | 42.500 | 0.0000 |
| 714.31 | 42.500 | 0.0000 |
| 766.81 | 42.500 | 0.0000 |
| 793.06 | 42.500 | 0.0000 |
| 793.06 | 42.500 | 0.0000 |
| 845.56 | 42.500 | 0.0000 |
| 871.81 | 42.500 | 0.0000 |
| 898.06 | 42.500 | 0.0000 |
| 924.31 | 42.500 | 0.0000 |
| 924.31 | 42.500 | 0.0000 |
| 504.312 | 85.000 | 12.500 |
| 504.312 | 85.000 | 12.500 |
| 504.312 | 85.000 | 12.500 |
| 530.562 | 85.000 | 12.500 |
| 556.812 | 85.000 | 12.500 |
| 583.062 | 85.000 | 12.500 |

| Underbody (Continued) | | |
|---|---|---|
| x (mm) | y (mm) | z (mm) |
| 609.312 | 85.000 | 12.500 |
| 635.562 | 85.000 | 12.500 |
| 661.812 | 85.000 | 12.500 |
| 688.062 | 85.000 | 12.500 |
| 714.312 | 85.000 | 12.500 |
| 740.562 | 85.000 | 12.500 |
| 766.812 | 85.000 | 12.500 |
| 793.062 | 85.000 | 12.500 |
| 819.312 | 85.000 | 12.500 |
| 845.562 | 85.000 | 12.500 |
| 871.812 | 85.000 | 12.500 |
| 898.062 | 85.000 | 12.500 |
| 924.312 | 85.000 | 12.500 |
| 950.562 | 85.000 | 12.500 |
| 504.312 | 85.000 | 12.500 |
| 504.312 | 85.000 | 12.500 |
| 504.312 | 85.000 | 12.500 |
| 530.562 | 85.000 | 12.500 |
| 556.812 | 85.000 | 12.500 |
| 583.062 | 85.000 | 12.500 |
| 609.312 | 85.000 | 12.500 |
| 635.562 | 85.000 | 12.500 |
| 661.81 | 127.50 | 12.500 |
| 688.06 | 127.50 | 12.500 |
| 714.31 | 127.50 | 12.500 |
| 740.56 | 127.50 | 12.500 |
| 766.812 | 85.000 | 12.500 |
| 793.062 | 85.000 | 12.500 |
| 819.312 | 85.000 | 12.500 |
| 845.562 | 85.000 | 12.500 |
| 871.812 | 85.000 | 12.500 |
| 898.062 | 85.000 | 12.500 |
| 924.312 | 85.000 | 12.500 |
| 950.562 | 85.000 | 12.500 |

# Appendix C

# Effects on a Following Vehicle (Experimental)

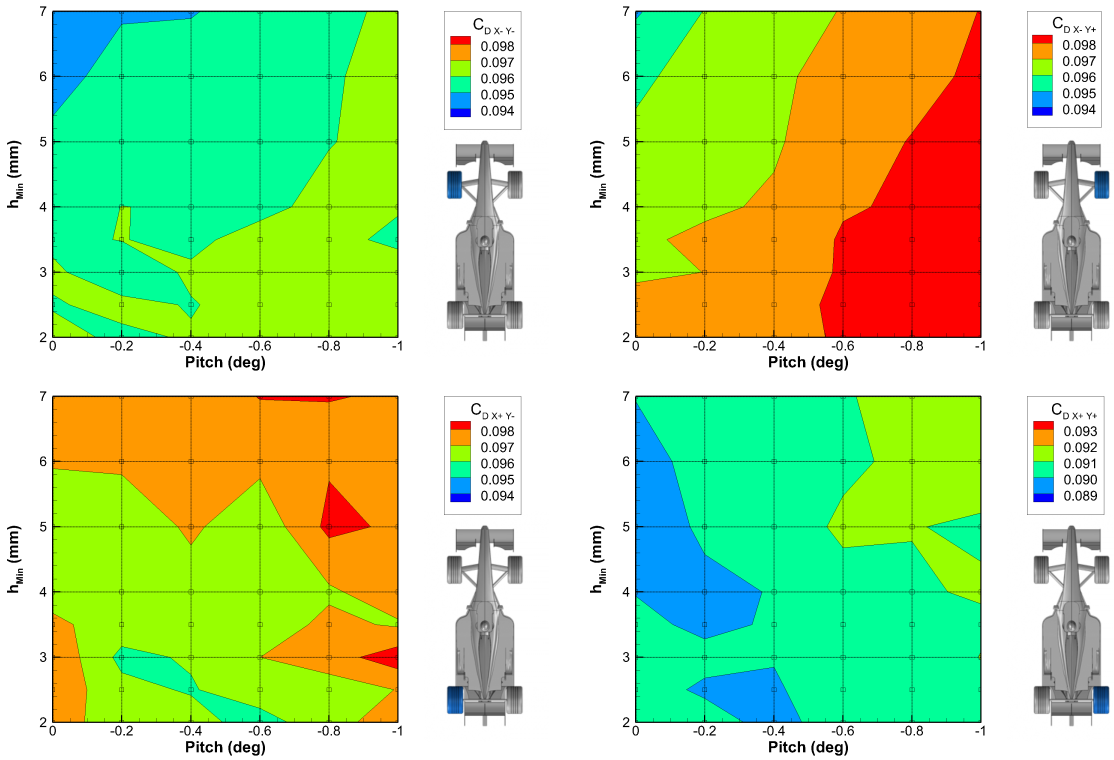


**Figure C.1:** Freestream individual wheel drag loads.

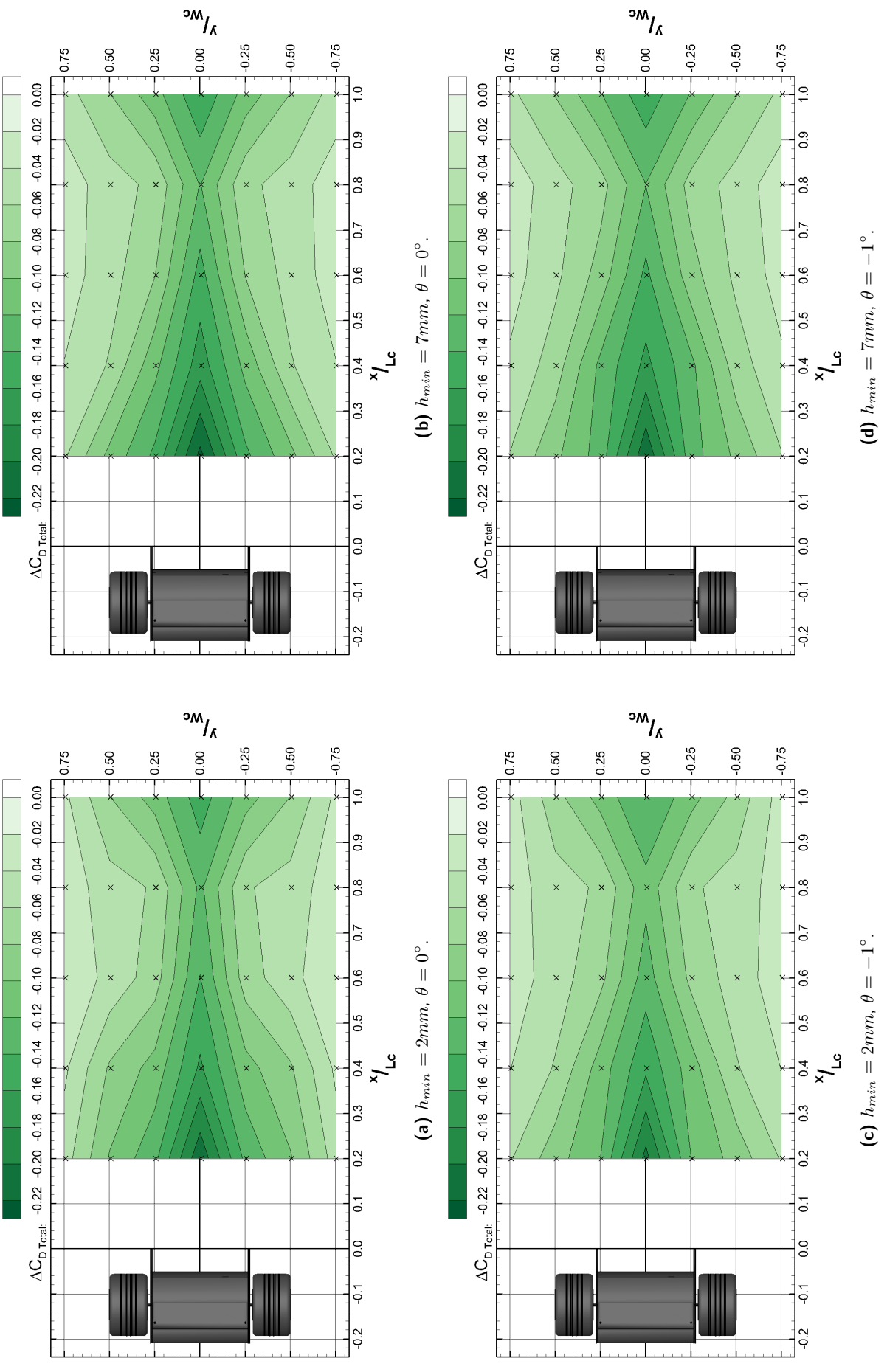


**(a)** $h_{min} = 2mm$, $\theta = 0°$.

**(b)** $h_{min} = 7mm$, $\theta = 0°$.

**(c)** $h_{min} = 2mm$, $\theta = -1°$.

**(d)** $h_{min} = 7mm$, $\theta = -1°$.

**Figure C.2:** Effect of upstream wake on drag ($C_D$) for the different car postures tested.

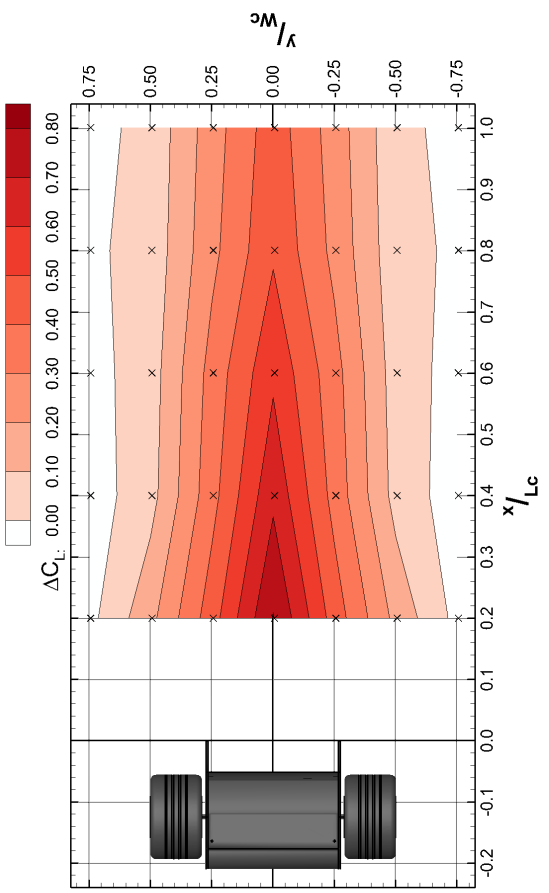


**(a)** $h_{min} = 2mm$, $\theta = 0°$.

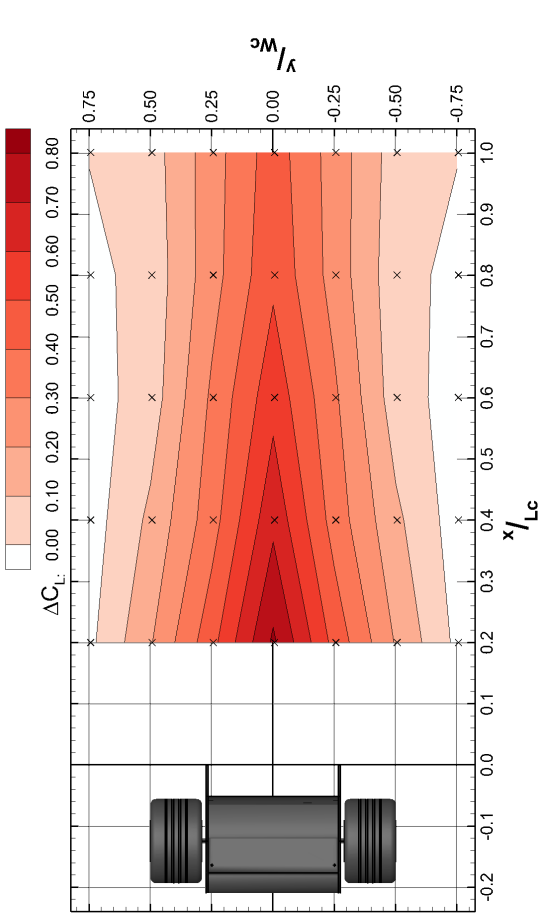


**(b)** $h_{min} = 7mm$, $\theta = 0°$.

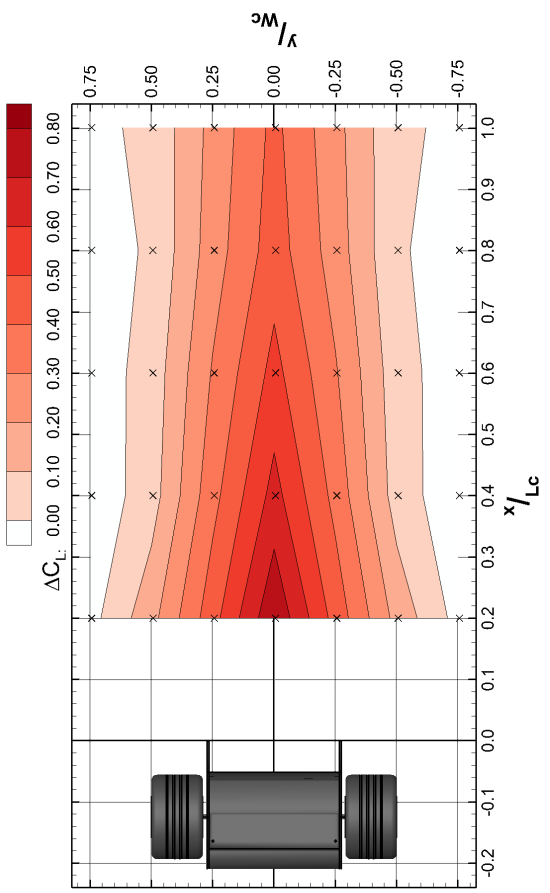


**(c)** $h_{min} = 2mm$, $\theta = -1°$.

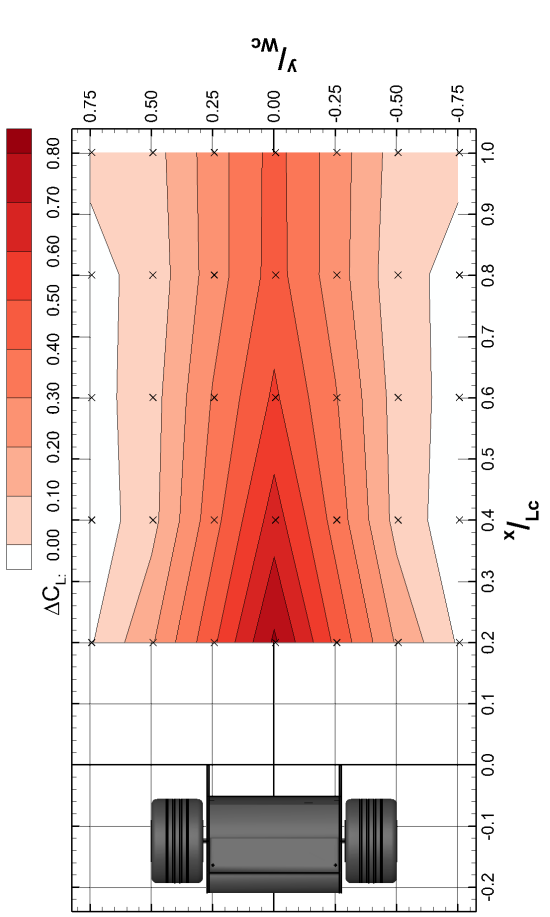


**(d)** $h_{min} = 7mm$, $\theta = -1°$.

**Figure C.3:** Effect of upstream wake on downforce ($C_L$) for the different car postures tested.

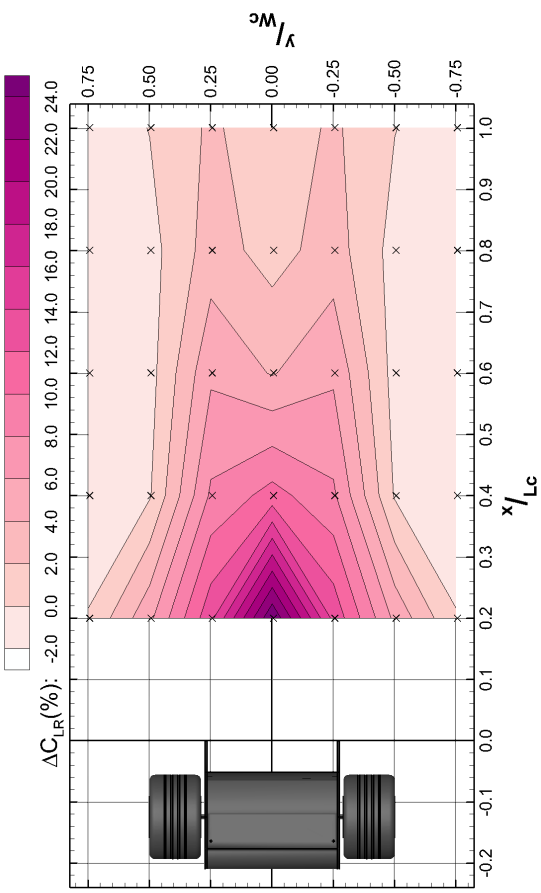


**(a)** $h_{min} = 2mm$, $\theta = 0°$.

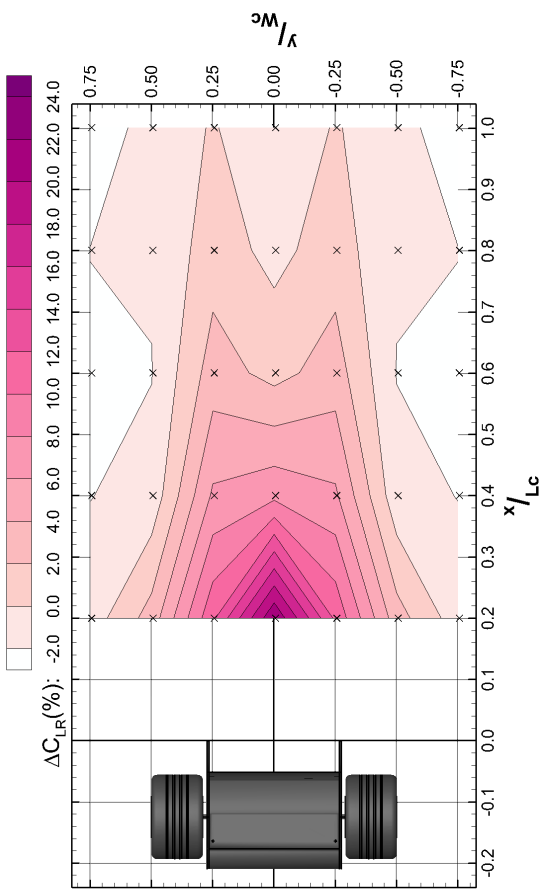


**(b)** $h_{min} = 7mm$, $\theta = 0°$.

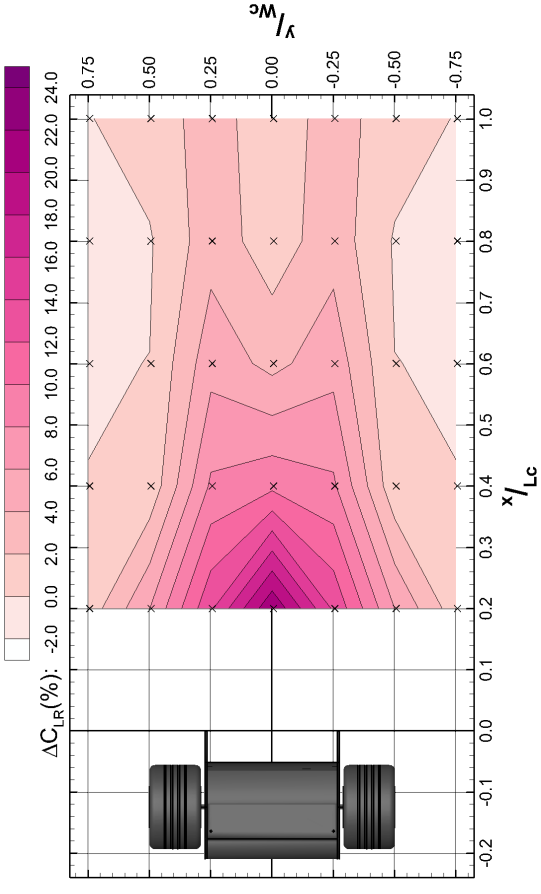


**(c)** $h_{min} = 2mm$, $\theta = -1°$.

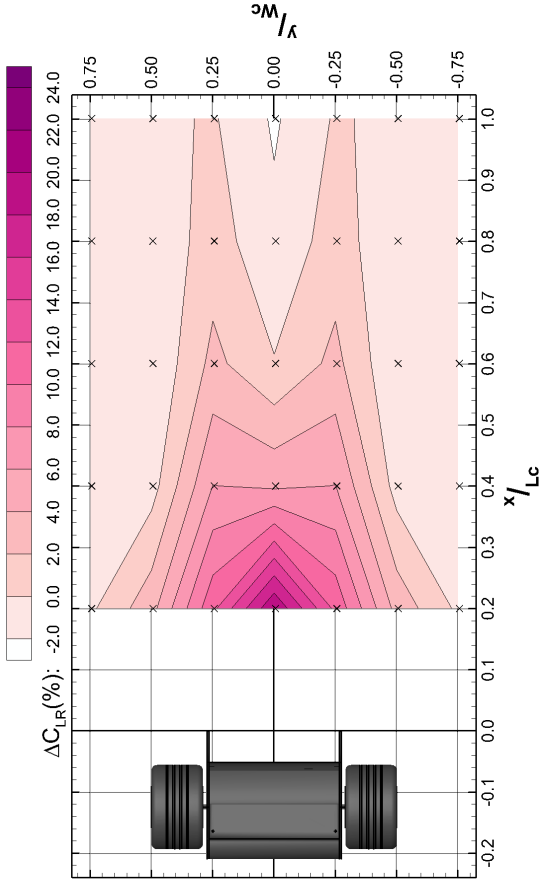


**(d)** $h_{min} = 7mm$, $\theta = -1°$.

**Figure C.4:** Effect of upstream wake on aerodynamic balance ($C_{LR}$) for the different car postures tested.

# Appendix D

# Computational Methodology

```
// CONSTANTS
U_infty = 25 <<m/sec>>;
P_infty = 101325 <<Pa>>;
density = 1.225 <<kg/m^3>>;
q_infty = 0.5 * density * (U_infty^2);
Po_infty = P_infty + q_infty;

t_cycle = 0.043 <<sec>>; // period of table time signal
t_floor = floor(t, t_cycle);
t_star = t - t_floor;

// VARIABLES - FROM CFD PLANES
P  = table_lookup("Inlet", InletTable.y, InletTable.z, t_star, 0);
Po = table_lookup("Inlet", InletTable.y, InletTable.z, t_star, 1);
ux = table_lookup("Inlet", InletTable.y, InletTable.z, t_star, 2);
uy = table_lookup("Inlet", InletTable.y, InletTable.z, t_star, 3);
uz = table_lookup("Inlet", InletTable.y, InletTable.z, t_star, 4);
qx = 0.5 * density * ux^2;
qyz = 0.5 * density * (uy^2 + uz^2);

// INLET COPNDITIONS - STATIC PRESSURE & VELOCITY
P_inlet = P;
ux_inlet = ux;
uy_inlet = uy;
uz_inlet = uz;
```

**Figure D.1:** PowerFLOW equations for imposed wake periodic inlet boundary conditions.

```
# UNSTEADY INLET CONDITIONS
# full inlet grid
# trilinear sampling
uniform

numMeasurements = 5

measurementUnit 0 "Pa"
measurementUnit 1 "Pa"
measurementUnit 2 "m/sec"
measurementUnit 3 "m/sec"
measurementUnit 4 "m/sec"

numlines={216, 461, 43}

iunit="mm"
junit="mm"
kunit="sec"

ibase = 5
iincr = 10
jbase = -2300
jincr = 10
kbase = 0
kincr = 0.001

# Data
# Format: igridline jgridline kgridline P Po ux uy uz
0 0 0 101324 101708 25.059300 -0.001754 0.001664
0 1 0 101324 101708 25.059700 -0.001775 0.001700
0 2 0 101324 101708 25.060200 -0.001795 0.001737
0 3 0 101324 101708 25.060600 -0.001815 0.001774
0 4 0 101324 101708 25.061000 -0.001835 0.001810
...
0 220 0 101316 101374 8.567820 0.046236 4.574760
0 221 0 101319 101369 8.432390 0.235398 3.043580
0 222 0 101319 101369 8.443190 0.240125 3.000450
0 223 0 101319 101369 8.873670 0.317550 1.512810
0 224 0 101319 101370 9.043850 0.339269 1.100690
0 225 0 101318 101366 8.807640 0.332505 0.820560
0 226 0 101315 101354 8.042690 0.309427 -0.392120
0 227 0 101314 101354 8.037780 0.307688 -0.412699
0 228 0 101310 101353 8.177330 0.225346 -1.457070
0 229 0 101310 101353 8.196050 0.219775 -1.565950
0 230 0 101309 101355 8.443170 0.210817 -1.703730
...
215 456 42 101324 101708 25.033700 -0.000467 0.002379
215 457 42 101324 101708 25.033500 -0.000471 0.002335
215 458 42 101324 101708 25.033300 -0.000475 0.002291
215 459 42 101324 101708 25.033100 -0.000479 0.002247
215 460 42 101324 101708 25.032900 -0.000484 0.002203
```

**Figure D.2:** Example of wake sample table.

# Appendix E

# Computational Results

The following figures are the absolute surface pressure contours for the downstream vehicle cases presented in Chapter 6. Each figure corresponds to a surface contour of $\Delta C_P$ in the main text.

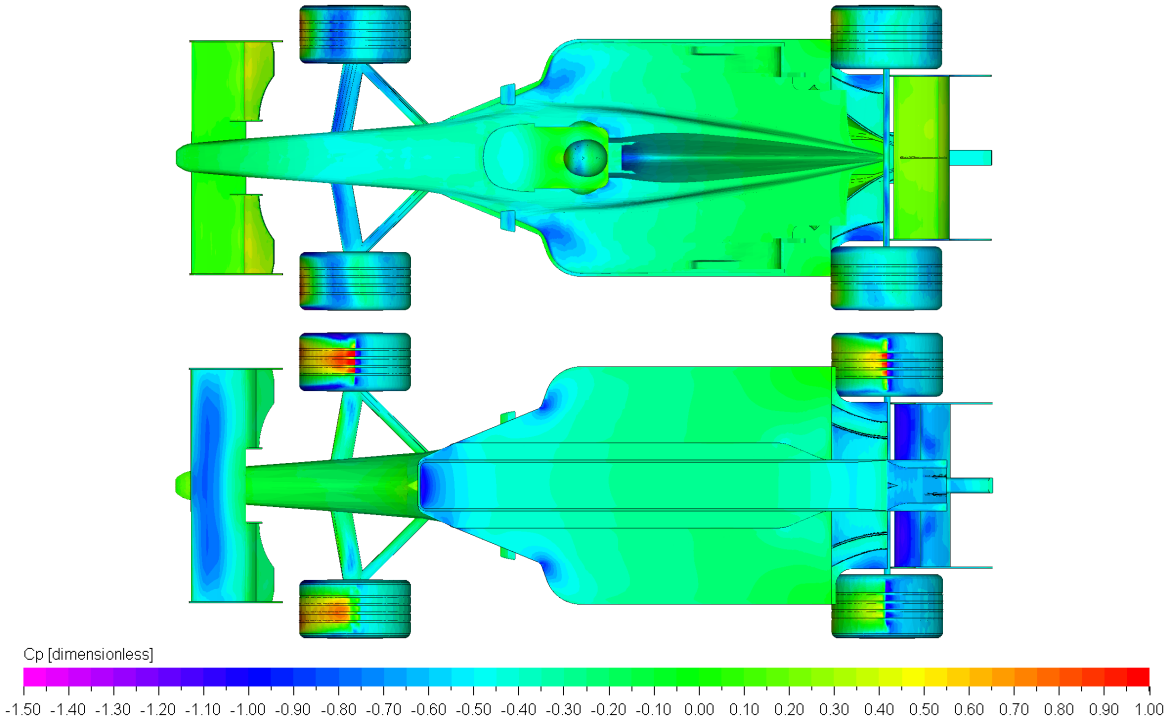


**Figure E.1:** Surface pressure distribution for following vehicle with upstream bluff bodied wake generator.

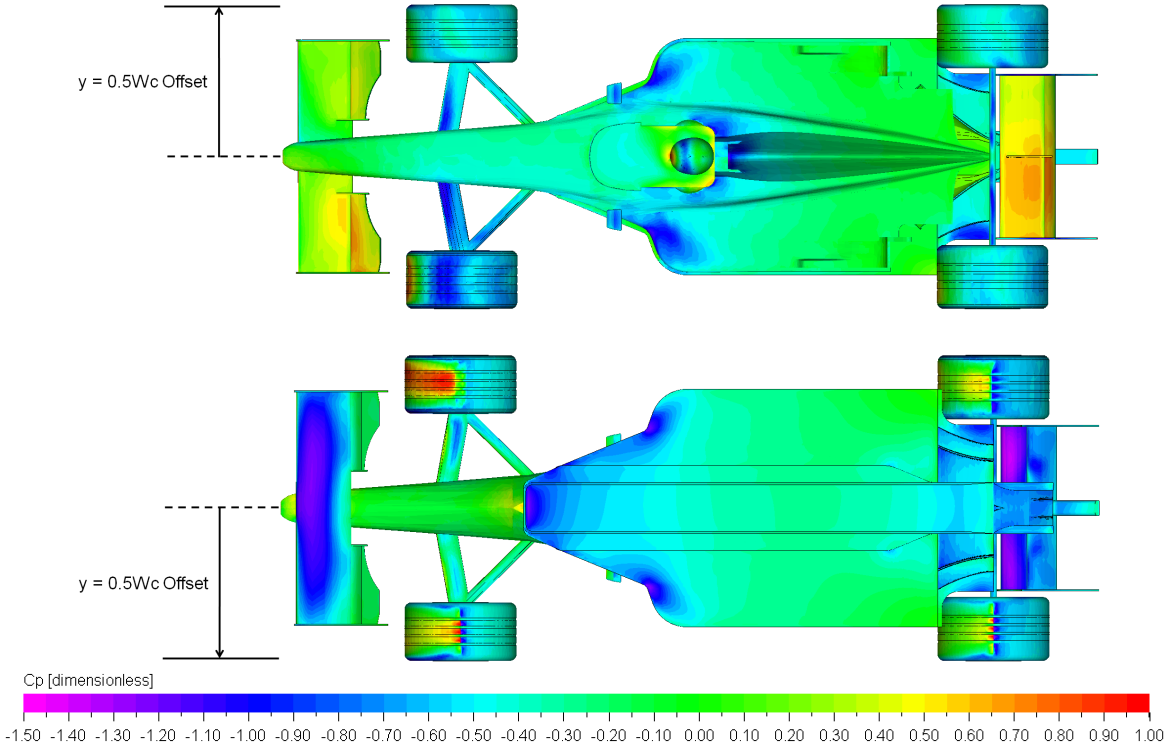


**Figure E.2:** Surface pressure distribution for following vehicle, $1L_C$ separation with $0.5W_C$ offset.

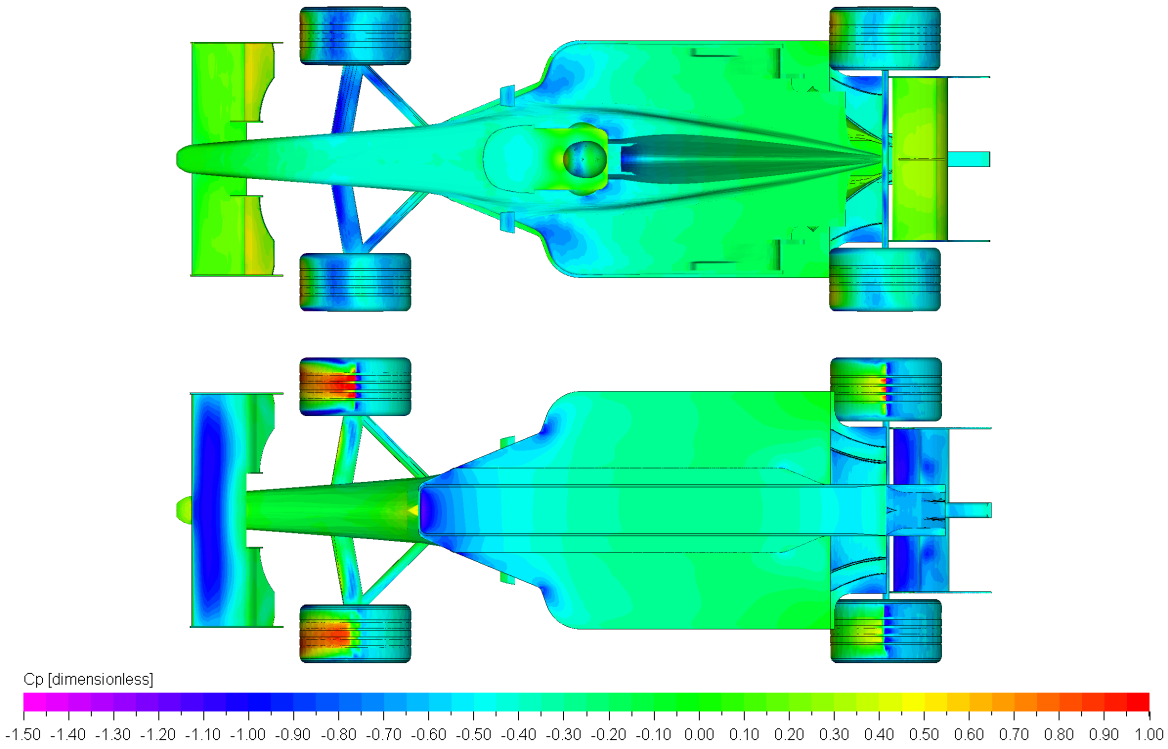


**Figure E.3:** Surface pressure distribution for following vehicle, with a $2L_C$ separation and no lateral offset.

# Appendix F

# Effect of Increasing Vehicle Track on the Wake

In the main text of this thesis, all studies investigate the wake of the car, either its effect on another vehicle or the propagation and decay in isolation. Methodologies, especially in CFD, sought to ignore the geometry of the upstream vehicle from the and focus instead on the effect of different wake parameters. A key proposal in the regulations for 2017 [151] is a return to $2m$ wide cars, last allowed in 1997. The reduction of track from $2m$ to $1.8m$ coincided with the introduction of grooved tyres in an attempt to reduce cornering velocities; the grooves reduced tyre contact patch area, while the track change reduced downforce by increasing the interactions between wheel wakes the body, in particular the underbody.

This is a simple geometry change to examine in the wind tunnel, achieved by sliding the wheel stings outward, figure F.1, though proposals for 2017 also include an increase of front and rear tyre widths of $55mm$ and $75mm$.

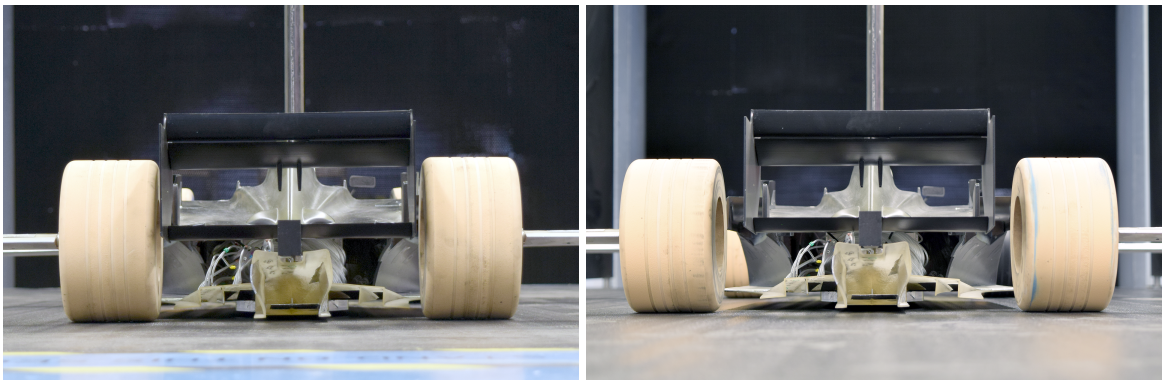

**(a)** 1.8m Wide Car **(b)** 2.0m Wide Car

**Figure F.1:** 25% Formula 1 car with narrow and wide wheel tracks.

The effect of the wider track on the car forces are shown in figure F.2. The downforce of the car is greater for all tested conditions, this is not coincidental as one of the reasons for the narrow track was to reduce the capability of the car to generate downforce. Improvements in downforce are greater with increased car pitch, especially at low ride heights, though only by $-C_L = 0.065$. The increase of downforce is relatively constant at $0°$ pitch, $-C_L = 0.01$. The downforce increase is coupled with a change of the aerodynamic balance, mainly a reduction of downforce acting at the rear axle. This could be related to reduced interactions between the front wheels and wing, resulting in improved front wing performance both on-surface near the endplates and in the wake. Balance shifts further rearwards at lower ride heights, and with increased pitch, where the front wing is lowest to the ground and front wing downforce will be greatest.

As well as increased downforce, body drag also increases by between $0.008 < \Delta C_D < 0.018$. The effective blockage of the body will increase when the wheels are further outboard, exposing more of the car to the onset flow. As the car is also generating more downforce it is evident that induced drag will also grow. Drag increase for the most part is greater than the downforce increase so the lift-to-drag radio of the car deteriorates for most conditions tested. Only the $\theta = 0.4°$ and $\theta = 0.4°$ conditions improved relative to the narrower car, and then only below $h_{min} = 3mm$.

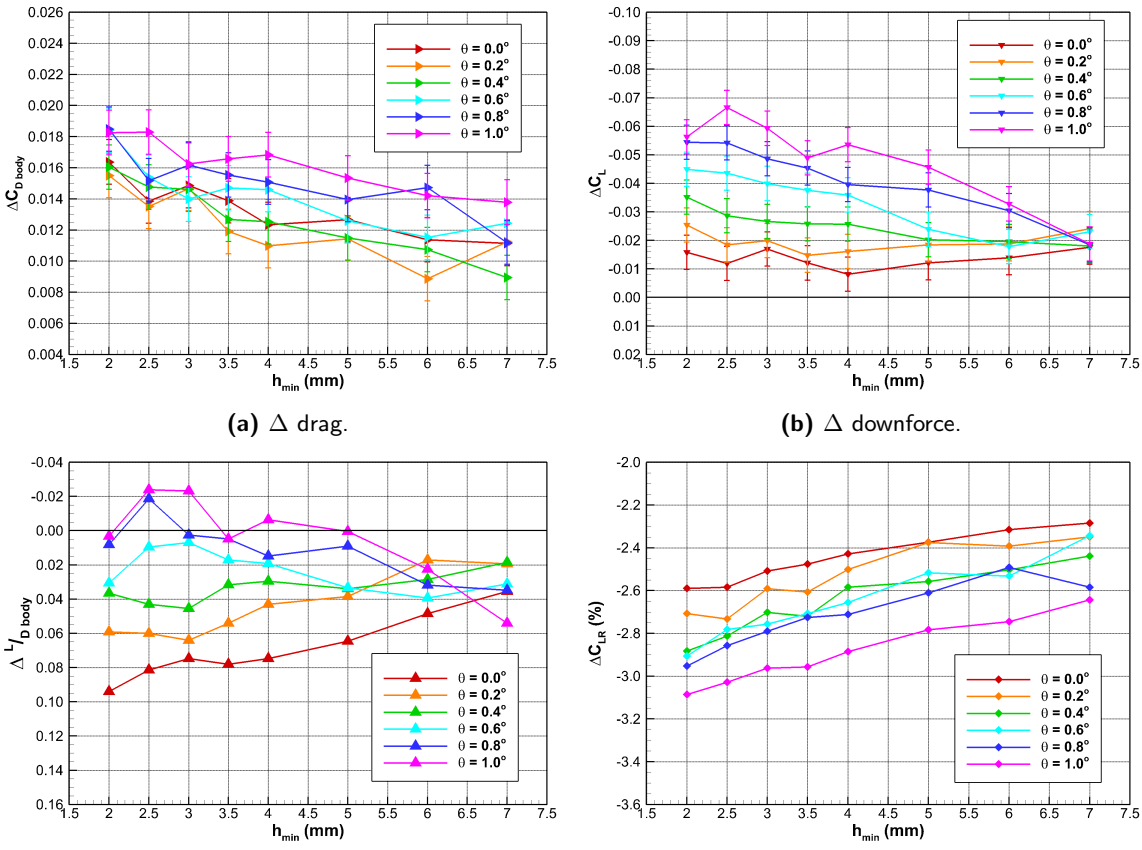


**(a)** Δ drag.

**(b)** Δ downforce.

**(c)** Δ lift-to-drag

**(d)** Δ aero-balance

**Figure F.2:** Effect of car track width on vehicle forces.

As would be expected, given the rationale behind the change to $1.8m$ vehicle track, the rear wing tip vortex is stronger, with a lower pressure core, when the wheels are further outboard, figure F.3. There is also a reduction of base pressure ($C_P$) in the immediate wake of the car ($x = 1.1L_C$), possibly indicating lower pressure at the diffuser exit. Increasing the track also increases the width of the stagnation pressure deficit, proportionally with the track width and below axle height seen in figure F.4a.

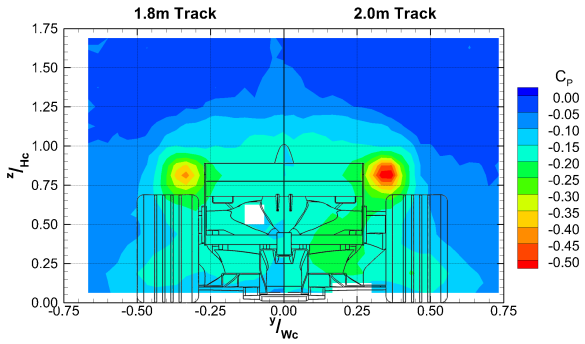


**Figure F.3:** Contours of $C_P$ in wake at $x = 1.1L_C$ comparing 25% Formula 1 track widths.

Due the stronger wing tip vortex, by $x = 1.25L_C$ (figure F.4b) the width of the stagnation pressure deficit in the wake of the $2m$ car is as narrow towards the centreline (on the 'mushroom stalk') than is the $1.8m$ car. As the wake continues the stagnation pressure is swept to surround the vortex cores, with a very similar wake to the $1.8m$ car beyond $x = 1.5L_C$. The only visual difference being the low pressure region, from the low static pressure in the vortex core, just outboard of the rear wing tips. The result on a downstream vehicle would therefore not be any different.

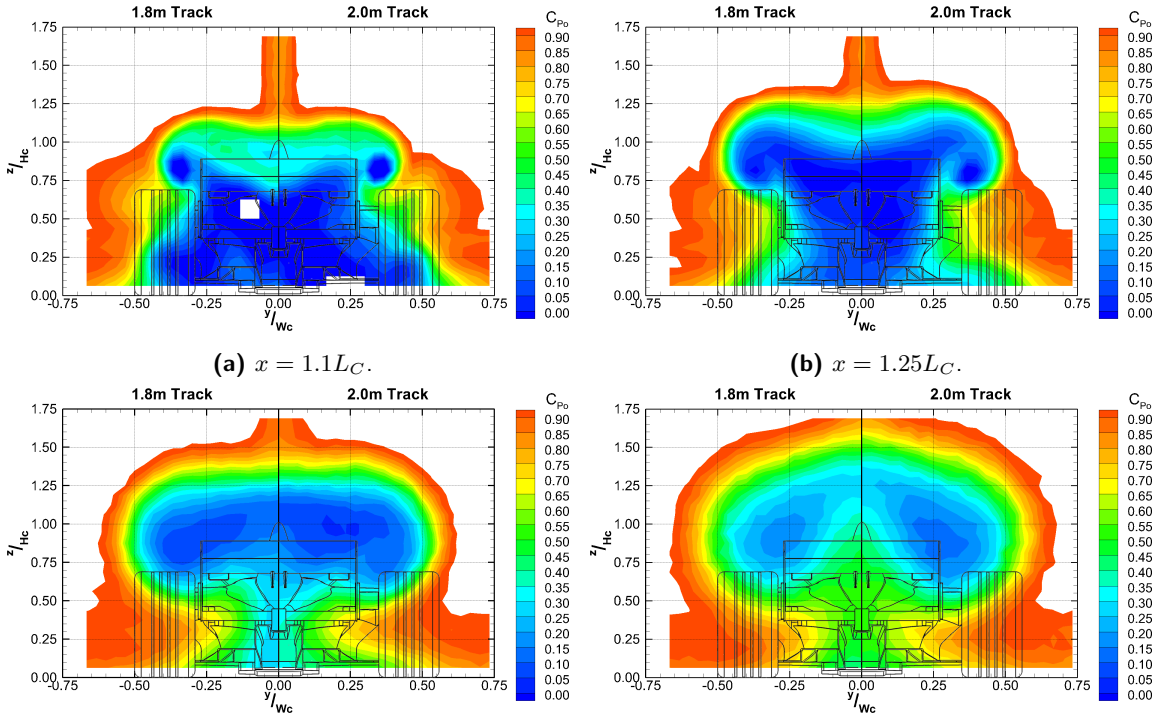


**(a)** $x = 1.1L_C$.

**(b)** $x = 1.25L_C$.

**(c)** $x = 1.50L_C$.

**(d)** $x = 1.75L_C$.

**Figure F.4:** Contours of total pressure deficit ($C_{P_O}$) in aake comparing 25% Formula 1 track widths.

3D ISO surfaces ($C_{Po} = 0.2$) of the wake, figure F.5, show that the strengthened wing tip vortex pair of the $2m$ car is more isolated from the rest of the wake. The wake under the vortex cores also seems to decay more rapidly than the $1.8m$ wide car. The wake low down affects the front wing and underbody of a downstream vehicle, so reducing wake deficits in this region is beneficial to a following vehicle. This is contrary to what would be expected, considering increasing the track increases vehicle drag. This vehicle is also not optimized for a wider track, which could reduce some of the total drag, and increase efficiency of underbody and wing profiles.

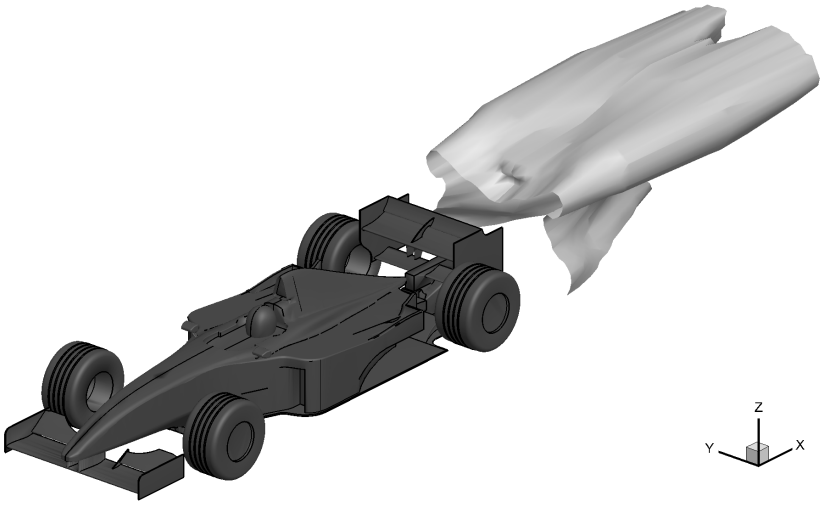


**(a)** $1.8m$ wide.

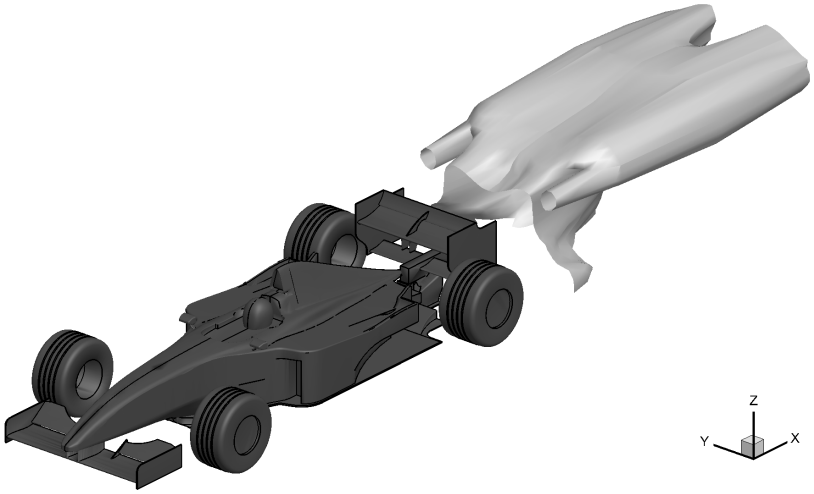


**(b)** $2.0m$ wide.

**Figure F.5:** Iso surfaces of $C_{P_O} = 0.2$ in wake.